
UNIVERSITY OF LIVERPOOL

# Dynamic petrology and rheology of ascending magma during lava dome eruptions: Effusive–explosive activity

*Thesis submitted in accordance with the requirements of the University of Liverpool for the degree of Doctor of Philosophy*

by

**Paul Anthony Wallace**

May 2019

# Declaration of authorship

I, Paul Anthony Wallace, declare that this thesis entitled "Dynamic petrology and rheology of ascending magma during lava dome eruptions: Effusive–explosive activity" and the work presented in it is my own. I confirm that:

- This thesis was completed as part of a research degree at the University of Liverpool;
- The material contained in this thesis has not been presented, nor is currently being presented, either wholly or in parts, for any other degree or qualifications;
- Where I have consulted published studies, this have been clearly referenced;
- Where the work was part of a collaborative effort, I have made clear what others have done and what I have contributed myself;
- Parts of this thesis have been published or in preparation for publication as:
    - **Wallace, P.A.**, Kendrick, J.E., Ashworth, J.D., Miwa, T., Coats, R., De Angelis, S.H., Mariani, E., Utley, J.E.P., Biggin, A., Kendrick, R., Nakada, S., Matsushima, T., and Lavallée, Y. (published in *Journal of Petrology*). **Petrological architecture of a magmatic shear zone: A multidisciplinary investigation of strain localisation during magma ascent at Unzen Volcano, Japan**.
    - **Wallace, P.A.**, De Angelis, S.H., Hornby, A.J., Kendrick, J.E., von Aulock, F.W., Clesham, S., Hughes, A., Utley, J.E.P., Hirose, T., Dingwell, D.B., and Lavallée, Y. (published in *Geochimica et Cosmochimica Acta*). **Frictional melt homogenisation during fault slip: Geochemical, textural and rheological fingerprints.**
    - **Wallace, P.A.**, Lamb, O.D., De Angelis, S., Kendrick, J.E., Hornby, A.J., Díaz-Moreno, A., von Aulock, F.W., Lamur, A., Utley, J.E.P., Rietbrock, A., Chigna, G., and Lavallée, Y. (in preparation for *Earth and Planetary Science Letters*). **Integrated constraints on explosive eruption intensification at Santiaguito dome complex, Guatemala.**

Signed:

Paul Anthony Wallace

# Thesis Abstract

Lava dome eruptions are one of the most hazardous forms of intermediate volcanic activity, with their ability to switch from benign effusive to catastrophic explosive eruption style with little precursory warning. Such behaviour can be attributed to a complex interplay between deep and shallow magmatic processes which alter the rheological, physical and chemical state of the magma, and its propensity to erupt. A comprehensive understanding of such processes is thus paramount for deciphering causes for different eruptive behaviours. This thesis aims to address three distinct processes, all of which are deemed a common phenomenon at lava dome volcanoes and can have an integral role in magma ascent dynamics in shallow volcanic conduits: (1) magma shearing, (2) fault friction and (3) magma recharge.

During the ascent of high-viscosity magma, crystallisation and volatile exsolution favours a non-Newtonian response, which promotes localisation of stress and strain near the conduit margins, leading to the formation of discrete shear zones. The impact and role of strain localisation during magma ascent was investigated through a detailed petrological survey of a shear zone developed at the margins of the 1994–1995 lava spine at Unzen volcano (Japan). A multidisciplinary approach combining field observations, microtextures, crystallography and magnetics was deployed, which was supplemented by the first high-temperature, high-velocity rotary shear experiment to simulate the processes involved during shear. I show that crystals can effectively monitor stress conditions during magma ascent through the viscous–brittle transition, with viscous remobilisation, crystal plastically and comminution all systematically increasing with shear intensity at the conduit margins. I suggest evidence for a thermo-mechanical response due to strain localisation (shear/frictional heating) which triggered disequilibrium conditions leading to mineral reactions, altered rock magnetic properties and compacted the original porous network. The range of deformation textures recorded can have a profound effect on magma outgassing and the style of surface activity.

Strain localisation can lead to seismogenic magma failure proceeded by faulting and slip along fracture planes. In particular, frictional sliding near the conduit margins can cause localised melting (by frictional heating) and impose an important rheological control on slip dynamics, acting as a lubricant or viscous brake that controls magma ascent in the upper conduit. Frictional melting is a non-equilibrium process, involving the selective melting of mineral phases and the softening of a glass at the glass transition. I present a detailed, systematic experimental investigation demonstrating the importance of host-rock mineralogy on the mechanical, geochemical, textural and rheological evolution of a frictional melt. The presence of hydrous minerals, such as amphibole, have the most influential role due to their lower melting point, generating heterogeneous mafic melts with lower viscosities that promote slip. In contrast, when amphibole is absent, frictional melts are more compositionally homogenous with higher viscosities resulting in higher shear resistance during slip. Understanding frictional properties with respect to mineralogy may aid in constraining flow behaviour in the shallow volcanic conduit that can impact activity at the surface.

Regular, small-to-moderate gas-and-ash explosions at Santiaguito dome complex (Guatemala) have previously been attributed to shear and frictional processes. However, in 2015–2016, eruptive activity intensified to larger, less frequent ash-rich explosive activity. I present a unique, multiparametric dataset that integrates petrological and geochemical signatures of the eruptive products with a rich geophysical dataset to assess the cause for a shift in eruption style. I provide evidence for a magma recharge event, resulting in changes in ash componentry, mingling textures, bulk compositional changes, alteration of groundmass microlite textures that occur concordantly with a deeper explosion source in the conduit revealed by seismicity. The integrated observations imply a switch from shallow shear-driven fragmentation to deeper gas overpressure fragmentation, intensifying local hazards. These observations not only aid in understanding Santiaguito's ongoing dynamic activity, but may also assist in deciphering complex shifts in eruption style at many active volcanoes.

# Contents

# List of Figures

**CHAPTER 1**



**CHAPTER 2**

**CHAPTER 3**



**CHAPTER 4**



**CHAPTER 5**

# List of Tables

**CHAPTER 2**



**CHAPTER 3**



**CHAPTER 4**

# Acknowledgements

I would firstly like to say a massive thanks to my supervisors, Yan and Jackie. Your combined friendship and guidance over the last four years have been invaluable. You have not only opened the door for my scientific career, but your passion for science, innovation and fearlessness of going into the unknown has been inspirational to watch over the past years. Jackie, your relentless effort, support, advice and encouragement has been truly awesome, and I can't thank you enough for the time you have dedicated to support me over the last four years. I could not have asked for better mentors and role models. I look forward to the many more collaborations throughout our careers. I also want to thank Sarah H. De Angelis, an honorary supervisor and fellow amphibole enthusiast. Over the last few years you have provided much guidance of which I am most grateful for. Not only have we had excellent discussions with regards research, but your friendship has been most valuable. Our trip to Alaska is one of the biggest highlights of my PhD and I couldn't have wished to have spent it with a greater person.

I'd like to thank my office buddies, Guðjón (aka. my work wife) and James A., for being such great friends throughout. Guðjón, have you found me a job in Iceland yet? I will be your 6-figure baby sitter any day $$$ ;-). To everyone in the experimental volcanology group at Liverpool, both past and present (Silvio, Felix, Adrian, Oliver, Anthony, Becky, Guðjón, Jenny, Josh and Amy) – you have all made my experience at Liverpool truly incredible and I look forward to creating many more great memories with each of you. Thank you for all for the great discussions we have had throughout the last years and I hope we continue to produce great science together for many more years to come. A special thanks to Amy for giving me a bed and a roof towards the end of my PhD, I am truly indebted. I also want to thank all my non-volcanology friends (of which there are too many to name), it has been a privilege sharing this journey with you all.

As well as my friends and colleagues in Liverpool, I would like to thank the many external collaborators over the last four years for the fruitful scientific discussions and assistance.

Furthermore, the work within this thesis would not have been possible without the financial support of the European Research Council, which has also allowed me to travel around the world for fieldwork and conferences.

And last, but far from the least, to my parents. No words can describe how much I owe you, love you and I am truly indebted to everything you have done to support me since day one.

# Chapter 1 Introduction

## 1.1. MOTIVATION

Volcanic eruptions are the surface expression of dynamic Earth. Volcanoes connect Earth's interior to the surface, acting as agents for the evolution of the atmosphere, the hydrosphere and biosphere, and bringing a combination of fear and fascination. Human populations can reap societal benefits and economic welfare from active volcanism, including fertile soils, geothermal energy, ore deposits and tourism, while also providing inspiration to artists. However, these awe-inspiring phenomena are more renowned for their destructive force and direct threat to those living in close proximity. During the past 10,000 years, over 1500 terrestrial volcanoes have been active (Siebert *et al.*, 2010), amongst which, approximately 575 of these have experienced at least one eruptive episode and continue to be active today (Tilling, 2005, 2008). The catastrophic 1902 Mount Pelée eruption (Martinique) was a landmark for volcanology, where, for the first-time, scientists began to elucidate the cause behind such devastating events. However, it was not until the 1980's, following the Mount St. Helens eruption (Washington State, USA), that volcanology matured to its current state, as one of the most interdisciplinary scientific fields (Cashman & Sparks, 2013). Owing to a rapidly growing population, volcanoes pose a potential hazard for ~58 million people estimated to live within 10 km of an active volcano, although up to ~600 million people could be affected by volcanic activity (Small & Naumann, 2001; Brown *et al.*, 2015). With an increasing population and increased dependence on infrastructure in the 21$^{st}$ century, mitigating the risks associated with volcanic unrest forms a non-trivial task for volcanologists and public officials. In the past 500 years, 275,000 volcano-related fatalities have been recorded due to primary effects (e.g., pyroclastic flows), although many more unrecorded, and despite our best efforts this number continues to grow (Tilling, 2005, 2008; Auker *et al.*, 2013).

Our understanding of volcanic eruptions has greatly improved in the last two decades (e.g., Cashman & Sparks, 2013) owing to advancement in monitoring techniques (e.g., seismometers, tilt meters, gas sensors), a plethora of observational and analytical datasets (i.e., geophysical, geochemical and petrological), and improved communication for impending eruptions and rapid transfer of knowledge. Precursory monitored signals have improved our ability to forecast when an eruption may take place; however, assessing how the eruption will proceed at the surface still remains a challenging task. Reducing the vulnerability to volcanic activity thus requires a comprehensive understanding of the physical processes that regulate them.

Volcanoes vary significantly in both morphology and eruption style. Magma composition has a fundamental control, which can range from mafic (iron- and magnesium-rich) to intermediate and silicic (silica-rich) composition. Intermediate–silicic volcanoes represent some of the most iconic landforms, with relatively steep-sided cones formed from continuous deposition of viscous lava flows (i.e., sticky causing a high flow resistance) and are renowned for their structural instability (e.g., the 1980 Mount St. Helens sector collapse; Voight, 2000; Sherrod *et al.*, 2008; Reid *et al.*, 2010) and explosive eruptions (e.g., 1991 Mount Pinatubo; Lynch & Stephens, 1996). The biggest challenge posed by intermediate–silicic volcanoes is their unpredictability in eruption style, ranging from benign effusive episodes to catastrophic explosions, and occasionally, both simultaneously. In particular, lava dome eruptions represent one of the most hazardous forms, renowned for their ability to switch from effusive to explosive activity with little precursory warning (e.g., Fink & Griffiths, 1998). Approximately 6% of all volcanic eruptions are dome-building, of which 95% of these have experienced an explosive episode (Calder *et al.*, 2015 and references therein). Detailed field, experimental, analytical and theoretical investigations of eruptive products have demonstrated that shallow magmatic processes are essential factors that regulate eruption style due to their ability to influence the chemical, rheological and physical properties of the magma (Fink *et al.*, 1992; Sparks, 1997; Voight *et al.*, 1999; Castro *et al.*, 2002; Allen & McPhie, 2003; Gonnermann & Manga, 2005; Mueller *et al.*, 2005; Tuffen & Dingwell, 2005; Lavallée *et al.*, 2007; Hale & Wadge, 2008; Yamamoto *et al.*, 2008; Cordonnier *et al.*, 2009; Lavallée *et al.*, 2013; Pallister *et al.*, 2013; Kendrick *et al.*, 2014a; Hornby *et al.*, 2015). Owing to the unpredictability of intermediate volcanic activity, specifically lava dome eruptions, improved forecasting and management of their hazards demands a better understanding of the processes that take place during magma ascent and thus forms the overarching motivation of this thesis.

In this thesis, the following questions will be addressed:

1) What is the impact of strain localisation on the geochemical, rheological and physical properties of magma as it ascends in the volcanic conduit at lava domes?
2) What thermo-mechanical effects does strain localisation have on the petrological architecture of magma?
3) Can crystals be used as effective deformation markers during magma ascent?
4) How important is mineral assemblage on the frictional properties of magma?
5) Can magma shearing and friction regulate shifts in eruption style at lava domes?
6) What effect does magma recharge have on shallow conduit processes and eruption style (effusive vs. explosive)?

## 1.2. LAVA DOME ERUPTIONS

Lava domes are mounds of viscous lava that extrude and accumulate around an active vent (e.g., Fink & Bridges, 1995). Although lava domes generally erupt passively in the form of effusive dome growth, they represent one of the most challenging volcanic crises to manage owing to the range of hazards generated, including impulsive transitions to explosive activity (vulcanian to sub-plinian; e.g., Cashman, 1992; Stix *et al.*, 1997; Hammer *et al.*, 1999; Sparks, 2003a; Clarke *et al.*, 2007), dome collapse events (e.g., Voight *et al.*, 2000), pyroclastic flows (e.g., Sato *et al.*, 1992; Calder *et al.*, 1999), block-and-ash flows (e.g., Cole *et al.*, 2002), tephra/ash fall (e.g., Baxter *et al.*, 1999) and lahars following heavy rain (e.g., Sparks & Young, 2002). Magma rheology has a fundamental role on lava dome morphology and its style of activity, with strain localisation during magma ascent and associated thermomechanical discontinuities having a significant impact (see section 1.5). Lava domes are typically associated with magmas exhibiting a high viscosity, causing the dome to grow in one of two ways, endogenously or exogenously. Endogenous dome growth occurs when the dome increases in size by internal expansion, while exogenous dome growth takes place when magma pieces through the dome's exterior surface (i.e., the carapace) causing the dome to grow externally via accumulation of lava flows and other extruded material. Lava domes can grow relatively fast (days–weeks), while activity at a single dome can last up to several decades, although their growth is often interrupted by intermittent explosive episodes or dome collapses. Well known examples of dome-building systems (Fig. 1.1) and eruptions include: Mount St. Helens, Washington, USA (1980–1986 and 2004–2008; Swanson & Holcomb, 1990; Sherrod *et al.*, 2008); Soufrière Hills Volcano, Montserrat (1995–present; Sparks & Young, 2002); Unzen volcano, Japan (1991–1995; e.g., Nakada *et al.*, 1999), Volcán de Colima, Mexico (1998–present; e.g., Varley *et al.*, 2010); and Santiaguito dome complex, Guatemala (1922–present; e.g., Rose, 1972; Harris *et al.*, 2003). Extensive studies of these systems have highlighted that dome growth is controlled by the complex evolution in the chemical, petrological, rheological, and mechanical properties of the magma as it ascends in the volcanic conduit (Cashman, 1992; Goto, 1999; Nakada & Motomura, 1999; Nakada *et al.*, 1999; Sato *et al.*, 1999; Venezky & Rutherford, 1999; Luhr, 2002; Harris *et al.*, 2003; Blundy & Cashman, 2005; Holtz *et al.*, 2005; Iverson, 2008; Kohno *et al.*, 2008; Noguchi *et al.*, 2008b; Pallister *et al.*, 2008; Kennedy *et al.*, 2009; Cichy *et al.*, 2011; Avard & Whittington, 2012; Lavallée *et al.*, 2012b; Scott *et al.*, 2012; Cashman & Blundy, 2013; Kendrick *et al.*, 2013b; Gaunt *et al.*, 2014; Cassidy *et al.*, 2015; Hornby *et al.*, 2015; Rhodes *et al.*, 2018). Their eruptive products display a range of deformation structures and petrological textures suggesting a complex interplay between deep and shallow magmatic processes that can be used to unravel the story of magma storage and ascent.

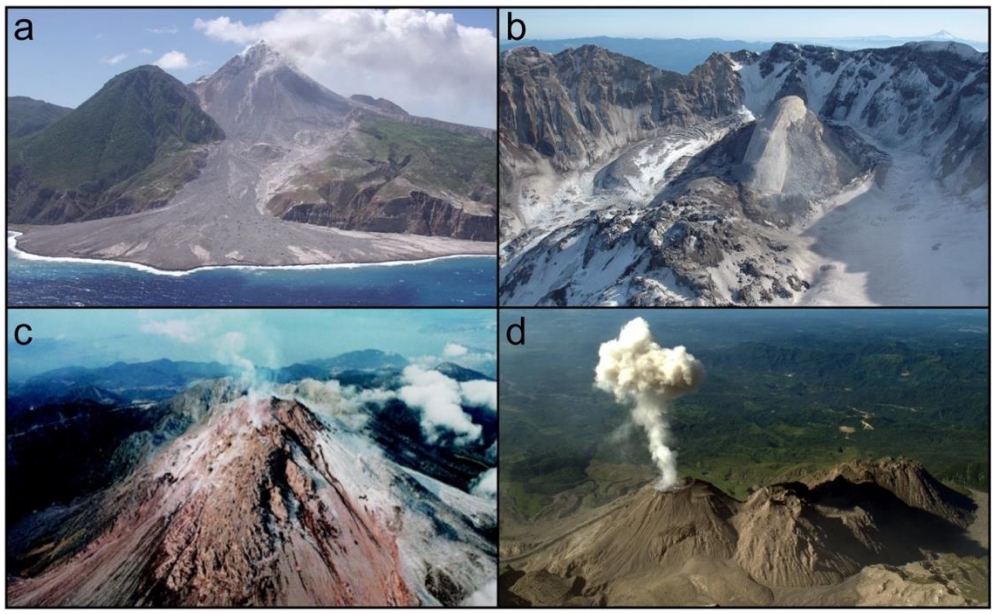


***Figure 1.1*** *– Classic examples of lava domes. (a) Soufrière Hills Volcano, Montserrat (Wadge et al., 2014), (b) Mount St. Helens, Washington DC, USA (credit: S. Schilling, USGS), (c) Unzen volcano, Japan (Nakada et al., 1999), and (d) Santiaguito dome complex, Guatemala (credit: O. Lamb).*

Lava dome eruptions are regulated by a combination of magma rheology and their ability to degas (e.g., Lavallée *et al.*, 2013); the competition between outgassing and dome pressurisation is integral to the style of dome activity (e.g., Sparks, 1997). If gas accumulates faster than the rate of gas escape, then pore overpressures develop and the magma will fragment causing an explosion (e.g., Self *et al.*, 1979). In contrast, if the rate of gas accumulation is lower than the rate of gas loss then the lava will erupt passively, either as a dome, a flow or spine (e.g., Melnik & Sparks, 2002; Watts *et al.*, 2002; Sparks, 2003b). Outgassing takes place through permeable structures that can develop by bubble coalescence (e.g., Klug & Cashman, 1996), collapse of magma foams (e.g., von Aulock *et al.*, 2017) or deformation of magma as it ascends in the conduit, including fracture networks, conduit margin shear zones or permeable wall rocks (Eichelberger, 1995; Tuffen & Dingwell, 2005; Kendrick *et al.*, 2013a; Heap *et al.*, 2015; Farquharson *et al.*, 2016a). Strain localisation can influence the outgassing efficiency by causing pore dilation (e.g., Gaunt *et al.*, 2014), compaction (e.g., Kendrick *et al.*, 2013a; Ashwell *et al.*, 2015) and/or anisotropy (Farquharson *et al.*, 2016b) near the conduit margins (Fig. 1.2a; Lavallée *et al.*, 2013). Furthermore, permeable pathways may infill (e.g., tuffisite veins; Castro *et al.*, 2012; Kendrick *et al.*, 2016) and/ or heal (i.e., fracture-healing; Tuffen *et al.*, 2003; Lamur *et al.*, 2019), which can facilitate pressurisation and favour explosive activity. Another mechanism for explosive activity at lava

domes is shear-induced fragmentation (Papale, 1999; Gonnermann & Manga, 2003), attributed to high strain conditions at the conduit margins causing brittle failure and slip causing intermittent development of outgassing pathways (e.g., Tuffen *et al.*, 2003; Lavallée *et al.*, 2008; Castro *et al.*, 2012); this mechanism has been used to explain gas-and-ash explosions at Santiaguito dome complex, Guatemala (Fig. 1.2b–d; e.g., Bluth & Rose, 2004; Johnson *et al.*, 2008; Sahetapy-Engel *et al.*, 2008; Lavallée *et al.*, 2015a). Thus, the style of activity is strongly influenced by the development or destruction of permeable pathways in the shallow volcanic conduit. Integrating petrological signatures of erupted products with geophysical monitoring signals (e.g., seismicity, infrasound, gas sensors, thermal data) may provide further information about shallow conduit processes (e.g., magma influx, gas fluxing, fragmentation depths; Blundy & Cashman, 2001; Edmonds *et al.*, 2009; Johnson *et al.*, 2014).

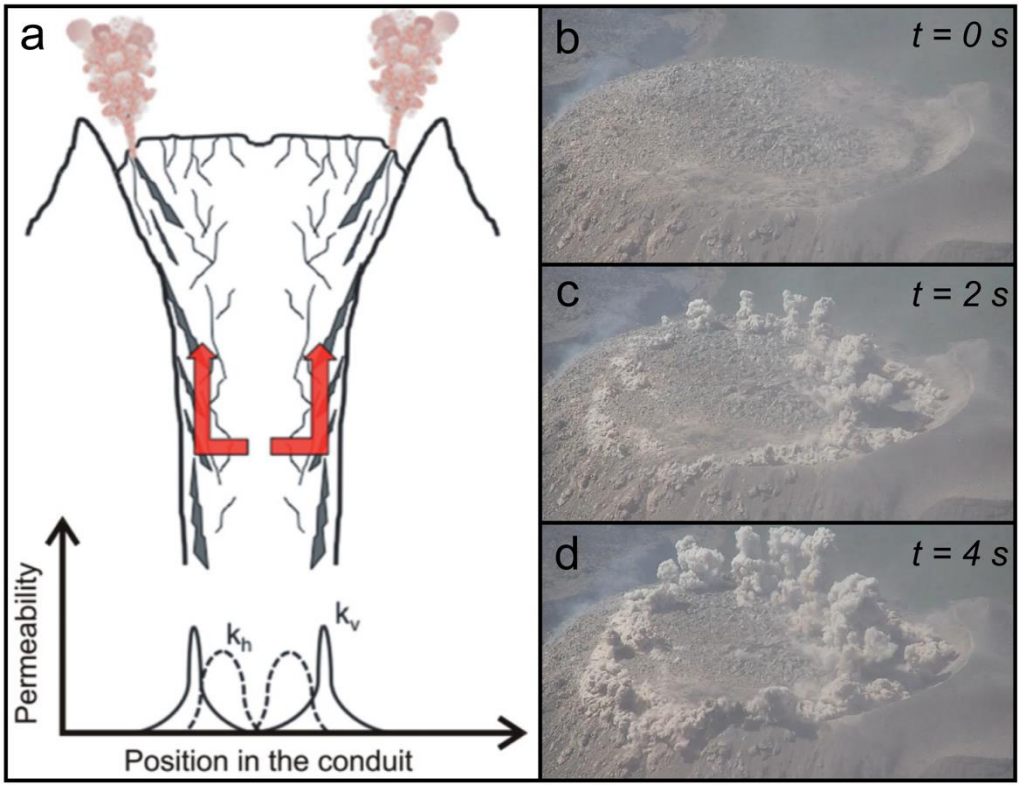


***Figure 1.2*** *– Architecture of shear-induced fracture networks and permeable outgassing pathways at the conduit margins (from Lavallée et al., 2013). Strain localisation near the conduit margins and subsequent failure promotes lateral outgassing ($K_h$) followed by vertical gas ascent ($K_v$) along anisotropic fracture planes to the surface. (a) Conduit margin fracturing and slip is believed to be the cause for gas-and-ash explosions at Santiaguito dome complex, Guatemala, which is supported by visual observations of gas-and-ash venting along ring fractures within the dome (b–d; from Johnson et al., 2008).*

## 1.3. PETROLOGICAL CONSTRAINTS ON MAGMA STORAGE AND ASCENT

In order to provide a comprehensive assessment of eruption style during dome building eruptions, an understanding of the processes that occur as magma is transported from a deep (several km) storage region to the surface is required. The physical, chemical and textural characteristics of eruptive products form an archive of the processes that take place during magma storage and ascent. Geophysical imaging combined with numerical models are commonly used to constrain magma storage regions (e.g., seismic tomography; Paulatto *et al.*, 2012). However, new advances such as muon imaging techniques have given greater insights into the internal structure of volcanic systems (Macedonio & Martini, 2010); yet these techniques are rare, thus petrological tools are extensively used for such purposes (e.g., Cashman & Blundy, 2013; Stechern *et al.*, 2017; Stock *et al.*, 2018). Petrological assessment of magma storage conditions prior to an eruption come from compositions of phenocrysts (e.g., Cashman & Blundy, 2013; Costa *et al.*, 2013; Scott *et al.*, 2013; Kiss *et al.*, 2014), their growth zonations (e.g., Huppert *et al.*, 1982; Cassidy *et al.*, 2016; Ubide & Kamber, 2018) and comparison of natural mineral assemblages to those created in experiments (i.e., phase equilibria; e.g., Barclay *et al.*, 1998; Rutherford & Devine, 2003; Holtz *et al.*, 2005; Blundy & Cashman, 2008; Gualda *et al.*, 2012). The processes regulating magma storage regions are highly complex with magma mixing/ mingling (e.g., Nakamura, 1995; Venezky & Rutherford, 1999; Murphy *et al.*, 2000; Couch *et al.*, 2001), assimilation of the country rock (e.g., Tepley *et al.*, 2000) and compositional stratification of storage regions (e.g., Scott *et al.*, 2013) believed to be common. Magma stored in the sub-volcanic plumbing system has long been portrayed as a body of liquid-rich (>50%) melt within a magma chamber (Daly, 1911). However, increasing evidence from eruptive products (e.g., entrained fragments of crystal-rich enclaves) and geophysical signals of active volcanic systems have caused a paradigm shift away from large liquid-rich magma reservoirs to an extensive storage region comprising liquid-poor (5–15%), crystal-laden (85–95%) mush zones (e.g., Cashman *et al.*, 2017; Holness *et al.*, 2019).

Magma recharge events (typically of mafic composition) that trigger an eruption have frequently been reported at intermediate volcanic systems, where the intrusion of hotter, less viscous magma interacts with a cooler, more evolved and crystal-rich magma (e.g., Murphy *et al.*, 2000). The destabilisation by new magma can generate convection driven by heat, causing the remobilisation of the crystal-mush zone resulting in a mobile and eruptible magma that contains crystals with different origins (e.g., Huppert & Sparks, 1984; Nakamura, 1995;

Couch *et al.*, 2001; Burgisser & Bergantz, 2011; Larrea *et al.*, 2013; Cooper & Kent, 2014; Klemetti & Clynne, 2014; Bergantz *et al.*, 2015).

Conditions of magma storage, particularly temperatures and pressures, can be obtained through the application of chemical thermodynamics, which allows the assessment of magma in both equilibrium and disequilibrium states (e.g., Richet & Ottonello, 2010). Quantification of these intensive variables can be determined by geothermobarometry where chemical equilibrium is reached following a reaction involving two or more phases (Blundy & Cashman, 2008; Putirka, 2008). Thermometry (temperature-sensitivity) relies on reactions with high enthalpy changes that are commonly brought about by exchange reactions between different phases (e.g., Fe and Mg exchange). Barometers (pressure-sensitivity) require reactions involving high volume changes through net transfer of components from a reactant phase to a product phase. Based on these principles, it can provide useful information on the conditions of magma crystallisation. Subsequently, a range of geothermobarometers have been developed for such purposes, for example plagioclase-melt (Putirka, 2008), amphibole-plagioclase (Holland & Blundy, 1994) and two-pyroxene (Putirka, 2008), which have been calibrated experimentally from known equilibrium pressure and temperature conditions in the laboratory. New and pre-existing geothermobarometers are frequently being developed to improve accuracy of pressure and temperature estimates. In particular, amphibole is a widely used tool to estimate conditions of pre-eruptive magma conditions (e.g., Rutherford & Hill, 1993; Browne & Gardner, 2006; Ridolfi *et al.*, 2010; De Angelis *et al.*, 2015) due to their composition and texture being highly sensitive to many magmatic variables (e.g., pressure, temperature, $H_2O$ content, oxidation state ($fO_2$)). Ridolfi *et al.* (2010) and Ridolfi and Renzulli (2012) demonstrated that due to this sensitivity, amphibole composition alone can be used as an estimate for physical and chemical conditions in calc-alkaline magmas, allowing construction of empirical thermobarometric equations. These equations include estimates for: (1) temperature, which is strongly influenced by Si and Ti concentration; (2) pressure, dependent on total Al content; (3) $fO_2$ from Mg and Ti content; and (4) dissolved melt $H_2O$ content, which is most sensitive to Al concentration. This model has been validated by comparing it to other geothermobarometers and seismic data of magma storage, and subsequently has been widely used to constrain conditions of crystallisation at many intermediate volcanic systems (e.g., Scott *et al.*, 2012; Shane & Smith, 2013; Kiss *et al.*, 2014; Nagasaki *et al.*, 2017).

Mineral reactions with the surrounding melt can provide information about magma ascent processes. For example, amphibole is a ubiquitous hydrous mineral in many subduction-related volcanic systems that forms within a hydrous melt and crystallises within the deeper magmatic system where water contents are high (up to several wt.% $H_2O$) as they

are yet to exsolve. When forced out of their stability zone (i.e., in disequilibrium with the surrounding melt), they breakdown to form a reaction rim of anhydrous mineral phases (pyroxene, plagioclase and Fe-Ti oxides). Textures of amphibole reaction rims (thickness, mineralogy and grain size/shape) have been investigated to reconcile the process driving their destabilisation, such as decompression (e.g., Rutherford & Hill, 1993; Browne & Gardner, 2006; Buckley *et al.*, 2006), heating (e.g., Murphy *et al.*, 2000; Rutherford & Devine, 2003) and oxidation (e.g., Garcia & Jacobson, 1979). Isothermal decompression experiments (Rutherford & Hill, 1993; Browne & Gardner, 2006) were the first to successfully replicate amphibole breakdown rims by reducing the amount of $H_2O$ in the melt, which demonstrated that rim thickness may be used as a proxy for magma ascent rates and resulted in a calibrated model that is still extensively used today (Rutherford & Hill, 1993). However, decompression driving such a reaction may be considered an oversimplification, with a more recent experimental investigation (De Angelis *et al.*, 2015) highlighting that breakdown rims can also form by heating the magma above its stability field and on much shorter timescales (hours rather than days for decompression; Fig. 1.3). Consequently, owing to their high sensitivity, a range of processes that trigger thermal instabilities in the shallow volcanic conduit, particularly in dome-building systems, may cause amphibole to destabilise (see Chapter 2).

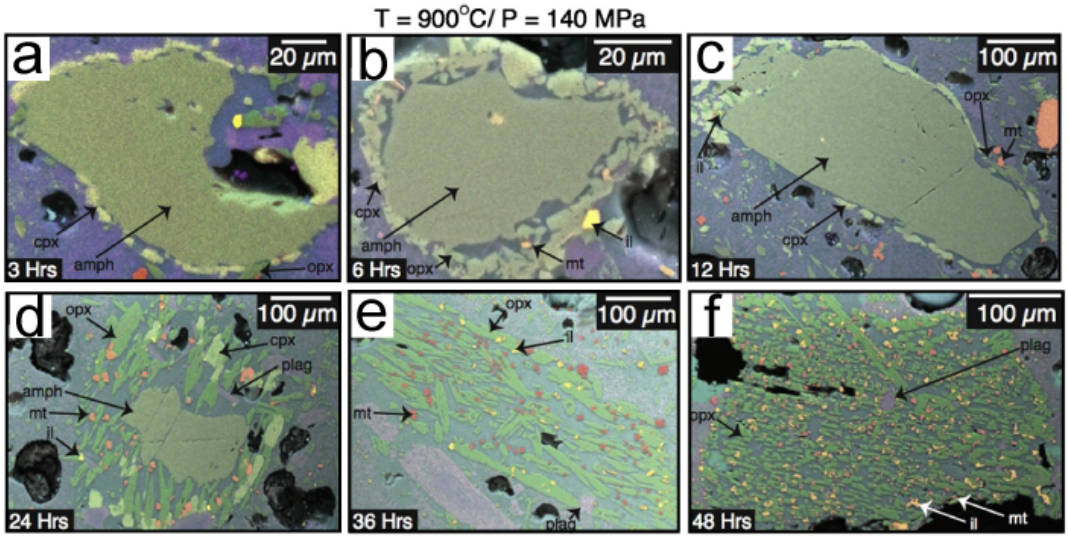


***Figure 1.3*** *– Experimental heating-induced amphibole reaction rims (from De Angelis et al., 2015). For the experiments, amphiboles were held within their stability field (870 ºC and 140 MPa) for 24 hours for equilibration, and then heated for either 10, 30 and 50 ºC and held for a further 3–48 hours. (a–f) Mineral X-ray maps for the experiments heated 30 ºC above the amphibole stability field and held for 3–48 hours. Breakdown rims formed within 3 hours and completely broke down to pseudomorphs after 36 hours, demonstrating the importance of temperature on amphibole destabilisation.*

The most fundamental process that takes place during magma ascent is volatile exsolution of the melt phase (i.e., degassing), driven primarily by decompression, as volatiles are less soluble at lower pressures (e.g., Papale *et al.*, 2006). For silicate melts, $H_2O$ is the dominant volatile species (up to several wt.%; e.g., Carmichael, 2002) along with less abundant $CO_2$, $SO_2$ and Cl (e.g., Wallace, 2005); the extent of degassing is thus controlled by the amount of $H_2O$ in the melt during ascent (e.g., Dingwell *et al.*, 1996). During decompression, the exsolution of these volatiles causes nucleation and growth of bubbles and crystallisation (Sparks, 1978; Tait *et al.*, 1989), which has a drastic effect on magma rheology at low pressures (<2 km depth; e.g., Dingwell, 1996). For crystallisation to take place, volatile exsolution causes an increase in the stability of anhydrous minerals (particularly plagioclase) by increasing their liquidus temperature relative to the temperature of the magma (Kirkpatrick, 1981), termed effective undercooling ($\Delta T$), which promotes the formation of groundmass microlites (e.g., Cashman, 1992; Geschwind & Rutherford, 1995; Hammer *et al.*, 1999; Hammer *et al.*, 2000). Over the past two decades, extensive experimental investigations (Hammer & Rutherford, 2002; Couch *et al.*, 2003; Brugger & Hammer, 2010) have linked the amount of $\Delta T$, decompression style and plagioclase microlite textures. These experiments importantly demonstrated that these textures are reproducible on eruptive timescales (e.g., Geschwind & Rutherford, 1995). The rate of decompression, and thus volatile exsolution, has been shown to be influential to crystallisation kinetics (i.e., crystal nucleation and growth), and it is reported that magma ascent rate has an integral role on eruption style (effusive or explosive; e.g., Toramaru *et al.*, 2008; Cassidy *et al.*, 2015; Cassidy *et al.*, 2018). When the melt experiences a higher $\Delta T$, crystal nucleation dominates leading to the formation of numerous small microlites, while a lower $\Delta T$ favours crystal growth, resulting in fewer but larger microlites (Mollo & Hammer, 2017). Additionally, experiments have related feldspar crystal shape to $\Delta T$, where crystals change from equant/ tabular to more elongate/ acicular with increasing $\Delta T$ (Hammer & Rutherford, 2002; Couch *et al.*, 2003).

Naturally, many studies have compared the groundmass textures of eruptive products (i.e., crystal size, shape, abundance), particularly of volcanic ash, with these experimentally calibrated models to infer pre-eruptive conduit processes prior to and during an eruption, including magma ascent rate, decompression path (i.e., continuous, single-step or multi-step) and volatile content (e.g., Cashman & Blundy, 2000; Hammer *et al.*, 2000; Noguchi *et al.*, 2008b; Toramaru *et al.*, 2008; Miwa *et al.*, 2009; Preece *et al.*, 2013; Cassidy *et al.*, 2015; Preece *et al.*, 2016). However, temperature changes due to magma ascent processes in the volcanic conduit are unconstrained by these models. In particular, crystallisation during magma ascent can release latent heat (Blundy *et al.*, 2006), which could contribute up to 100 ºC temperature rise, further influencing petrological reactions and subsequent textures.

## 1.4. MAGMA RHEOLOGY

Rheology is a term used to describe how a material flows under given stress conditions. The processes that take place in a volcanic conduit influence its rheological behaviour, owing to magmas' physicochemical changes that alter the dynamics of magma ascent. The volcanic dilemma, to flow or blow, is commonly attributed to a change in magma rheology (Dingwell, 1996). Magmas are comprised of silicate melts which are viscoelastic liquids (i.e., exhibit properties of both a viscous body and elastic solid), following the theoretical notion of Maxwell (1867), that abides to the timescales of structural relaxation (Dingwell & Webb, 1989). The boundary between the liquid and glassy state of a melt is known as the glass transition ($T_g$), which is a compositionally-unique kinetic barrier that varies as a function of temperature and strain rate (Dingwell & Webb, 1989; Webb & Dingwell, 1990). At low strain rates (or long timescales) the melt behaves as a Newtonian liquid, while higher strain rates (or short timescales that approach the timescales of structural relaxation) it forces the melt to behave as a glass, causing brittle failure. This phenomenon illustrates silicate melts' temperature and strain-rate dependence of viscosity (Fig. 1.4), a concept that has been invoked in many eruptive scenarios to contribute to the ductile-brittle transition in magmas, particularly fragmentation during explosive eruptions (e.g., Gonnermann & Manga, 2003).

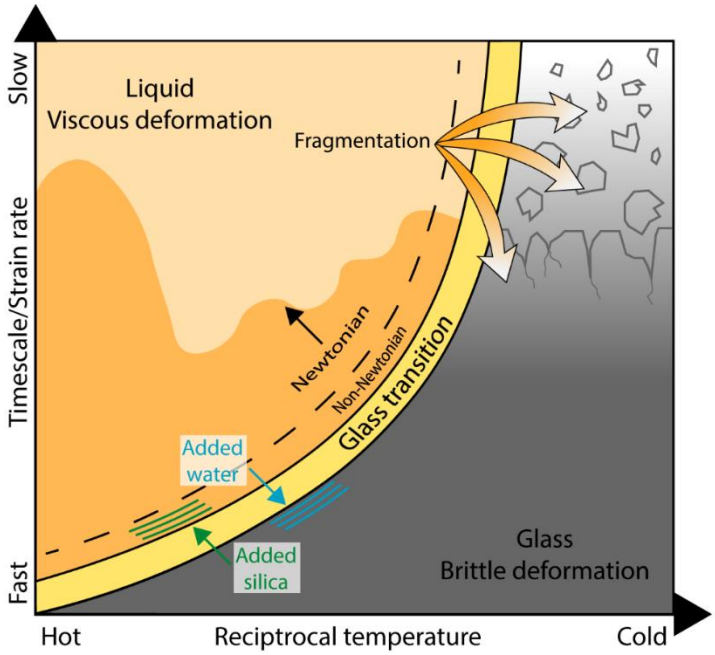


***Figure 1.4*** *– Illustration of the glass transition ($T_g$) in strain rate (time-reciprocal) temperature space (modified from Dingwell, 1996). The liquid state refers to when a melt is relaxed, and deformation is slower (low strain rates) than the timescale of structural relaxation. During faster deformation (high strain rates) the timescale of structural relaxation is approached, resulting in an elastic response of the melt and a shear-thinning, non-*

*Newtonian behaviour, eventually leading to brittle failure. Variations in silica and water content also influence the position of $T_g$, highlighting the importance of degassing (loss of water) and crystallisation (increase in silica) on the melt's mechanical behaviour during magma ascent.*

Composition and volatile content (particularly $H_2O$) of the melt have a large influence on melt viscosity, with decreasing silica content and increasing water content favouring viscous flow over brittle failure (Dingwell, 1996; Giordano *et al.*, 2008). The viscosity of silicate melts can vary over several orders of magnitude (from $10^1$ to $10^{12}$ Pa.s.); experimentally calibrated models for constraining the non-Arrhenian, temperature-dependence of melt viscosity for a range of compositions has consequently been generated (Hess & Dingwell, 1996; Giordano *et al.*, 2008).

During transport through the crust, magma evolves from a single-phase melt (although sometimes with rare bubbles and crystals) to a multi-phase mixture through the addition of suspended crystals and bubbles owing to volatile exsolution, which can interact to bring complex rheological changes and a non-Newtonian rheology. The influence of bubbles on magma rheology depends on their ability to interact during flow. If they behave as rigid objects they can increase viscosity, but if they are able to deform freely, they may reduce viscosity (e.g., Manga *et al.*, 1998; Lejeune *et al.*, 1999; Llewellin & Manga, 2004). However, magmas feeding lava dome eruptions are commonly crystal-rich (>50% crystallinity) with low porosity (<35%) that results from relatively slow extrusion rates and extensive degassing in the shallow conduit (Nakada & Motomura, 1999; Cashman & Blundy, 2000; Kueppers *et al.*, 2005; Lavallée *et al.*, 2012b). Crystals represent rigid suspensions that can cause complexities to rheological flow laws, fundamentally increasing magma viscosity (e.g., Lejeune & Richet, 1995; Stevenson *et al.*, 1996; Caricchi *et al.*, 2007; Lavallée *et al.*, 2007; Cordonnier *et al.*, 2009; Costa *et al.*, 2009). Crystal fraction has a significant control on rheological dynamics, where melts with low crystal fractions behave as Newtonian fluids converting to non-Newtonian once a maximum packing fraction is reached (Caricchi *et al.*, 2007; Cordonnier *et al.*, 2009; Cordonnier *et al.*, 2012; Moitra & Gonnermann, 2015). The maximum packing fraction represents a critical threshold in which crystals can interact and hamper flow, causing a non-linear increase in viscosity (e.g., Einstein, 1906; Roscoe, 1952). The extent of crystal interaction is dependent on their shape, size and distribution (e.g., Saar *et al.*, 2001; Mueller *et al.*, 2011; Picard *et al.*, 2011). In particular, particle aspect ratio exerts a strong control on the maximum packing fraction. Crystals with higher aspect ratios (i.e., elongate) can create a locking effect allowing crystals to interact at lower packing fractions, having a greater impact on the viscosity than more equant crystals (Mueller *et al.*, 2010;

Mueller *et al.*, 2011). However, magmas typically contain crystals with different shapes and sizes (i.e., from phenocrysts and microlites). Such polydispersity can have a large effect on rheology, yet quantifying the role of polydisperse suspensions remains an area of active research (e.g., Cimarelli *et al.*, 2011; Mader *et al.*, 2013).

At high crystallinities (>50%), typical of dome lavas, crystals begin to interact via partitioning strain and adopt a single rheological law and a shear-thinning rheology (viscosity decreases with strain rate; Caricchi *et al.*, 2007; Lavallée *et al.*, 2007; Costa *et al.*, 2009; Mueller *et al.*, 2010; Mader *et al.*, 2013). Rheological models have subsequently been developed that link magmas' non-Newtonian behaviour with crystal content and strain rate (Fig. 1.5; Caricchi *et al.*, 2007; Costa *et al.*, 2009). In particular, a rheological law for the non-Newtonian behaviour of crystal-rich dome lavas was developed by Lavallée *et al.* (2007), derived from parallel plate experiments on natural samples, demonstrating the strain-rate dependence of viscosity at eruptive temperatures. Such models have further been developed to assess failure criteria for crystalline dome lavas at a range of strain rates, temperatures and porosities (e.g., Cordonnier *et al.*, 2009; Cordonnier *et al.*, 2012; Lavallée *et al.*, 2012b; Coats *et al.*, 2018). Although these rheological models do not take into account natural dispersity of crystal sizes and shapes, they give a first order relationship across a broad range of strain rates and crystal fractions, which have greatly improved our understanding of magma ascent dynamics in the volcanic conduit during dome-building eruptions.

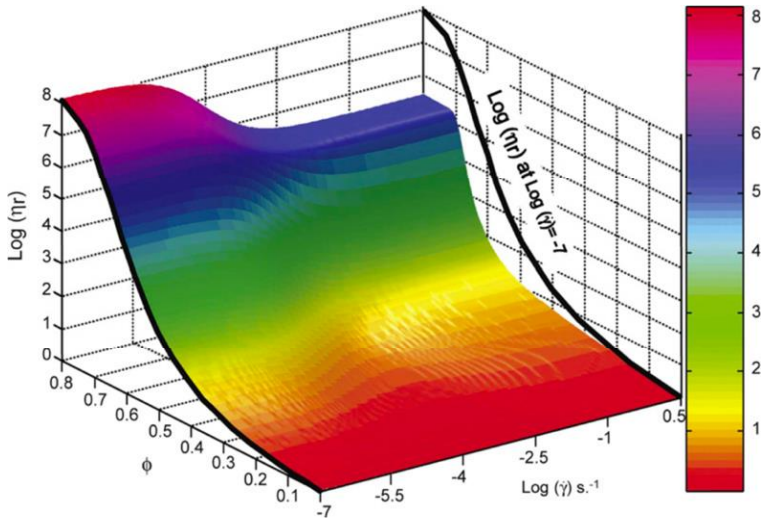


***Figure 1.5*** *– Effect of crystal fraction (ϕ) and strain rate (γ) on the relative viscosity (ηr) of magmas (from Caricchi et al., 2007). The colour bar denotes ηr. The rheological model shows that with increasing crystal fraction the ηr increases, while an increase in γ causes a decrease in ηr causing a shear-thinning, non-Newtonian behaviour. Crystal-bearing magmas, such as those at lava domes, are thus ideal candidates for strain localisation in high strain regions of the volcanic conduit during magma ascent.*

## 1.5. STRAIN LOCALISATION, MAGMA SHEARING AND FRICTION

A consequence of magmas' non-Newtonian, shear-thinning rheology is that it promotes strain localisation in regions of most stress, causing crystals and bubbles to rearrange and deform (Lavallée *et al.*, 2007; Okumura *et al.*, 2009; Petford, 2009; Wright & Weinberg, 2009). The ascent of high viscosity, crystal-laden magma facilities the localisation of stress and strain near the conduit margins which generates a velocity gradient across the conduit resulting in a "plug flow" style ascent (e.g., Llewellin & Manga, 2004; Hale, 2007; Hale *et al.*, 2007). Marginal shear zones may develop in such regions, which are then subjected to a range of transient deformation modes as magma ascents through the viscous-brittle transition, preserving evidence for strain within bubbles and/ or crystals. Magma shearing is deemed as a pervasive process that can take place across the entire width of a conduit, albeit to varying extents, and may propagate to great depths in the conduit (Costa *et al.*, 2007; Cashman *et al.*, 2008). Strain localisation in the volcanic conduit has previously been assessed using vesicle shapes preserved in rapidly quenched eruptive products (i.e., pumice clasts; Wright & Weinberg, 2009; Dingwell *et al.*, 2016); elongated, sheared vesicles have been interpreted to be the result of high strain rates near the conduit margins. However, during the slow extrusion of dome lavas, these textures are likely to be erased as a result of relaxation timescales, where surface tension takes over in the absence of shear causing deformed bubbles to relax to a spherical shape (e.g., Rust & Manga, 2002) or a simplified network (e.g., Kennedy *et al.*, 2016). Consequently, assessing strain conditions in the volcanic conduit during dome-building eruptions remains problematic.

Crystals may also act as indictors of stress concentration (e.g., Deubelbeiss *et al.*, 2011). Strain conditions during viscous flow have previously been assessed by the preferential orientation of crystals within a melt (e.g., Castro *et al.*, 2002; Picard *et al.*, 2011), while in the brittle regime crystals can fracture and comminute under high stresses (e.g., Allen & McPhie, 2003; Cordonnier *et al.*, 2009; Forien *et al.*, 2011). However, prior to failure in high strain conditions, crystals may exhibit a permanent deformation by deforming plasticity, as evidenced in many tectonic, mylonitic shear zones (e.g., Vernon, 2000; Selverstone *et al.*, 2012) and plutonic intrusions (e.g., Murray, 1979; Vernon & Paterson, 1993; Zibra *et al.*, 2012). Crystal plasticity is a permanent strain that develops when a shear stress exceeds a crystal's yield stress causing the formation and accumulation of dislocations in a crystal's lattice (Fig. 1.6; e.g., Poirier, 1995; Brewer *et al.*, 2006). A recent experimental study by Kendrick *et al.* (2017) highlighted crystal plasticity in extrusive lavas may be used as an outlet for strain during magma ascent through the viscous–brittle transition in the volcanic conduit. Crystal plasticity is a relatively new concept in the context of volcanic eruptions and has yet

to be explored at outcrop scale; however, its systematic variation as a function of imposed strain conditions reveals a potential for using it to unravel the extent of strain localisation during magma ascent and eruption (see chapter 2).

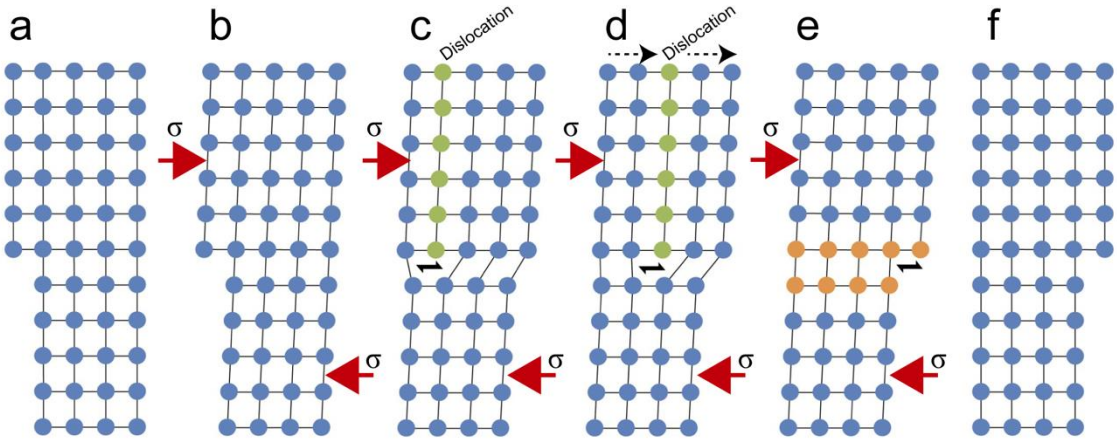


***Figure 1.6*** *– Schematic of a dislocation in a crystal lattice leading to crystal plastic deformation (from Kendrick et al., 2017). The development of a dislocation involves: (a) isostatic stress and no deformation; (b) elastic strain caused by differential stress; (c) the crystal lattice yields causing a dislocation to form; (d) the dislocation migrates along the lattice under continued stress, leaving internal distortions, and eventually passes through (e); (f) differential stress removed and elastic strain recovered. If a dislocation passes all the way through the crystal lattice, no internal distortion would be recorded. A quantification of crystal plasticity requires dislocations to move and accumulate within the lattice (c–d) without passing all the way through (e-f).*

The mechanical work associated with shear deformation may be converted to viscous shear heating, defined as the dissipation of viscous energy in the liquid state (Ockendon, 1979). Shear heating has previously been reported to generate > 100 ºC temperature rise in areas of most strain generating contrasts in viscosity within the magma (Rosi *et al.*, 2004; Mastin, 2005; Costa *et al.*, 2007; Hale *et al.*, 2007). Additionally, rheological experiments by Hess *et al.* (2008) recorded increased magma temperatures with increased applied stress due to shear heating, and measured rates of a few ºC/s in highly viscous melt (from $10^8$ to $10^{12}$ Pa.s.) when subjected to strain rates exceeding $10^{-3}$ $s^{-1}$. A thermal input associated with shear heating may cause a physical and chemical alteration of the magma and thus play a role in defining eruption style by altering magma flow dynamics in the conduit (e.g., Polacci *et al.*, 2001; Costa & Macedonio, 2003; Hale, 2007). Evidence for shear heating has previously been reported to take place in the conduit during explosive eruptions (e.g., Polacci *et al.*, 2001; Rosi *et al.*, 2004), relating different degrees of vesicle deformation and crystallinity of pumice

clasts to being derived from different regions of the conduit. Such a process has been theoretically constrained and modelled assuming magma ascent through a pipe-like conduit geometry (Hale *et al.*, 2007), yet the thermal impact of magma shearing on eruption dynamics remains elusive, raising questions on the thermal budget of magma during ascent in the shallow conduit (see chapter 2).

Magma failure is integral for dome-building eruptions. Magma can either fail by forming localised fractures in regions of high strain, or fragment via decompression if pore pressures overcome magma strength, leading to an explosive eruption (e.g., Gonnermann, 2015). Fracture formation takes place during strain localisation forcing magma to encounter the brittle regime, which prevents pressure accumulation and facilitates outgassing if connected to the surface (e.g., Smith *et al.*, 2001; Gonnermann & Manga, 2003; Spieler *et al.*, 2004; Tuffen *et al.*, 2008; Smith *et al.*, 2011; Lavallée *et al.*, 2013). If fractures propagate to the surface the lava may extrude in a near solid-state as a lava spine that forces through the dome carapace bounded by fault zones (e.g., Cashman *et al.*, 2008; Kennedy *et al.*, 2009; Kendrick *et al.*, 2012; Pallister *et al.*, 2013; Hornby *et al.*, 2015). Spines typically form either at the beginning of an eruptive phase, forcing relics of old, degassed lava out of the conduit, or at the end of an eruptive phase when extrusion rate slows down causing viscosity to increase (e.g., Nakada *et al.*, 1999). Classic examples of lava spines (Fig. 1.7) include those that formed during the 1902 eruption of Mount Pelée, Martinique (e.g., Tanguy, 2004), the 2004–2008 eruption of Mount St. Helens (e.g., Sherrod *et al.*, 2008; Pallister *et al.*, 2013), and the 1991–1995 eruption of Unzen volcano (e.g., Nakada *et al.*, 1999). Spines that protract from a lava dome are structurally unstable, thus are prone to collapse, exposing remnants of the dome interior and providing a unique opportunity to assess syn-eruptive conduit processes (e.g., Nakada *et al.*, 1999). Structures and textures of the 2004–2008 Mount St. Helens lava spine indicated pure brittle deformation during extrusion at sub-solidus conditions, evidenced by extensive marginal fractures, tensile dilation, comminution, and cataclastic gouge layers (Cashman *et al.*, 2008; Kennedy *et al.*, 2009; Kendrick *et al.*, 2012; Pallister *et al.*, 2013), yet further microstructural evidence suggested rapid heating by frictional processes may have been involved (Kendrick *et al.*, 2012).

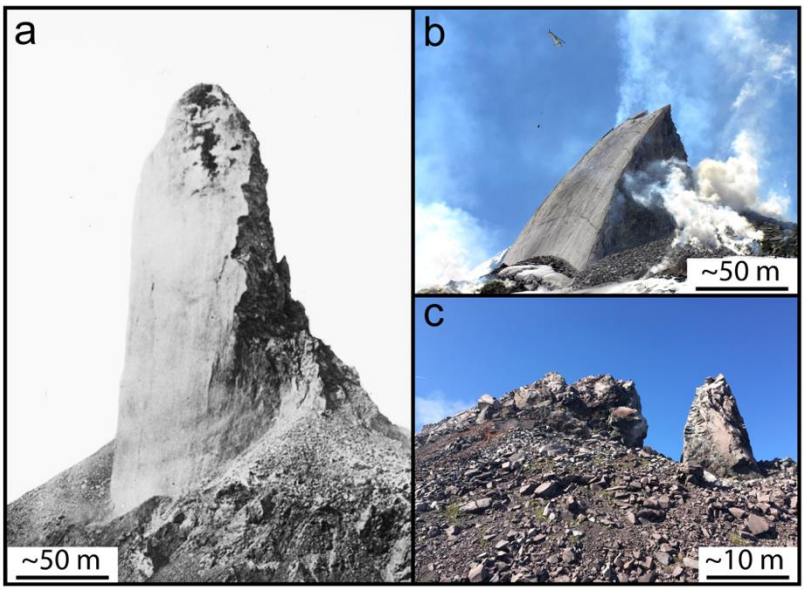


***Figure 1.7*** *– Photographs of lava spines. (a) The 1902 lava spine from Mt. Pelée, Martinique, which reached a maximum height of 305 m before it collapsed in 1903 (from Lacroix, 1904). (b) 2004–2008 Mount St. Helens lava spine (credit: D. Dzurisin, USGS). (c) Unzen volcano lava spine which extruded towards the end of the 1991–1995 eruption.*

Magma ascent during dome-building eruptions has been observed to take place in cyclic behaviour due to frequent shallow seismicity emitted from the upper conduit (e.g., Voight *et al.*, 1999; Iverson *et al.*, 2006; Neuberg *et al.*, 2006; Iverson, 2008; Johnson *et al.*, 2014; Lamb *et al.*, 2015). These seismic signals are often accompanied by tilt cycles due to elastic deformation of the edifice causing the dome and/ or edifice to seemingly inflate and deflate (e.g., Neuberg *et al.*, 2006; Johnson *et al.*, 2014; Lavallée *et al.*, 2015a; Neuberg *et al.*, 2018). Failure of magma and cyclic faulting in regions of strain localisation (i.e., conduit margins) is considered to modulate such a process, facilitating ascent in a piston-like manner with traction at the conduit walls (e.g., Iverson *et al.*, 2006; Neuberg *et al.*, 2006; Lensky *et al.*, 2008; Neuberg *et al.*, 2018). Seismogenic failure and the formation of fault planes near the conduit margins facilitates slip and friction, which ultimately dictate magma ascent in the shallow conduit (e.g., Lavallée *et al.*, 2008; Kendrick *et al.*, 2014b; Lavallée *et al.*, 2015b). Extreme frictional work during co-seismic slip along fault planes can rapidly raise magmatic temperatures by several hundred degrees (i.e., frictional heating) causing local melting of the adjoining rocks (e.g., Carslaw & Jaeger, 1959), termed frictional melts, which then follow a temperature path during cooling and occasionally quenching rapidly to a glass. Evidence of frictional melting is preserved in the geologic record as pseudotachylyte (sometimes termed frictionite) and is likely a common product of viscous magma ascent in volcanic conduits feeding lava domes (Fig. 1.8; e.g., Kendrick *et al.*, 2012; Kendrick *et al.*, 2014a).

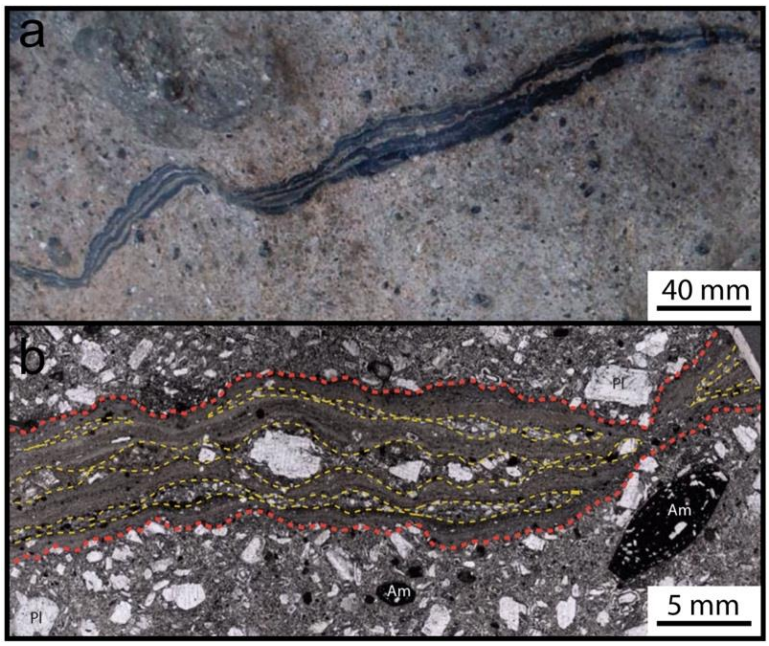


***Figure 1.8*** *– Shear band hosting pseudotachylyte layers from Soufrière Hills Volcano, Montserrat (from Kendrick et al., 2014a). (a) Metre-sized andesitic block from a block-and-ash flow displaying a shear band that cuts through the host rock with interlayered bands of pseudotachylyte and cataclasite formed by friction of viscous magma in the conduit. (b) Photomicrograph of the shear band and pseudotachylyte (red lines), along with lenses of cataclasite (yellow lines). Labelled minerals include plagioclase (Pl) and amphibole (Am).*

However, the preservation of frictional melts and pseudotachylytes in volcanic systems is poor owing to the high ambient temperatures in volcanic conduit and low stability of glass, which promotes crystallisation, thus overprinting distinguishing features (e.g., Kendrick *et al.*, 2012; Kirkpatrick & Rowe, 2013). In the absence of visible melt filaments (from individual breakdown of minerals; e.g., Lavallée *et al.*, 2012a), microtextures, such as a reduction in crystal size (e.g., Kendrick *et al.*, 2012) accompanied by rounding of the crystal edges (e.g., Lin, 1999), have previously been given in evidence for frictional comminution and melting. Furthermore, magnetic analyses of a material have also been shown to provide useful information on its thermal history by the alteration of magnetic minerals (such as magnetite and haematite; e.g., Nakamura *et al.*, 2002; Ferré *et al.*, 2005; Freund *et al.*, 2007; Kendrick *et al.*, 2012). Demagnetisation is the most significant process, which can be caused by reheating events (such as frictional heating) that raise the magma above its Curie temperature. Additionally, chemical alteration of the magnetic minerals by hydrothermal activity (gas and fluid migration) or oxidation can also impact rock magnetic properties (e.g., Krása & Herrero-Bervera, 2005; Bouligand *et al.*, 2014; Geuna *et al.*, 2014).

High-velocity rotary shear experiments on igneous rocks have demonstrated frictional melting can take place after a fraction of a second or just a few centimetres of slip and control slip properties, either acting as a lubricant (e.g., McKenzie & Brune, 1972; Tsutsumi & Shimamoto, 1997) or viscous brake (e.g., Koizumi *et al.*, 2004; Kendrick *et al.*, 2014b). A frictional melt's ability to act as a brake or lubricate has been demonstrated to be dependent on its rheological properties (e.g., Lavallée *et al.*, 2012a; Hornby *et al.*, 2015). As described in section 1.4, the rheological behaviour of a silicate melt is strongly controlled by composition, along with temperature and strain rate (Hess & Dingwell, 1996; Giordano *et al.*, 2008). Due to the rapid heating involved, frictional melting is a disequilibrium process and involves the selective melting of the constituent mineral phases (e.g., Scott & Drever, 1953; Sibson, 1975; Spray, 1992; Lin & Shimamoto, 1998). Subsequently, a hierarchy of common-rock forming minerals susceptible to frictional melting was constructed (Fig. 1.9; Spray, 1992). In volcanic rocks, hydrous minerals (e.g., amphibole), when present, are the most likely to preferentially melt due to their lower melting point compared to the rest of the mineral assemblage (e.g., plagioclase, pyroxene, quartz, Fe-Ti oxide), which may impact the compositional and rheological evolution of the frictional melt (e.g., Hornby *et al.*, 2015). Additionally, extrusive volcanic rocks typically consist of a glass, which, due to its dependence on the glass transition (Fig. 1.4), may impact the frictional 'melting' (or remobilisation) process (Lavallée *et al.*, 2015b). The ability of melt to act as an effective brake can cause slip to halt, potentially leading to cyclic failure and slip, termed stick-slip, generating a characteristic drumbeat seismicity commonly recorded during magma ascent at lava domes (e.g., Tuffen *et al.*, 2003; Neuberg *et al.*, 2006; Lensky *et al.*, 2008; Kendrick *et al.*, 2014b), particularly during the pulsatory extrusion of lava spines (e.g., Iverson *et al.*, 2006; Pallister *et al.*, 2013; Hornby *et al.*, 2015; Lamb *et al.*, 2015). In contrast, melts may lubricate fracture planes and facilitate magma ascent and expulsion. Thus, understanding the role slip and frictional melts requires detailed investigation of the contributing mineral phases during the melting process (see chapter 3).

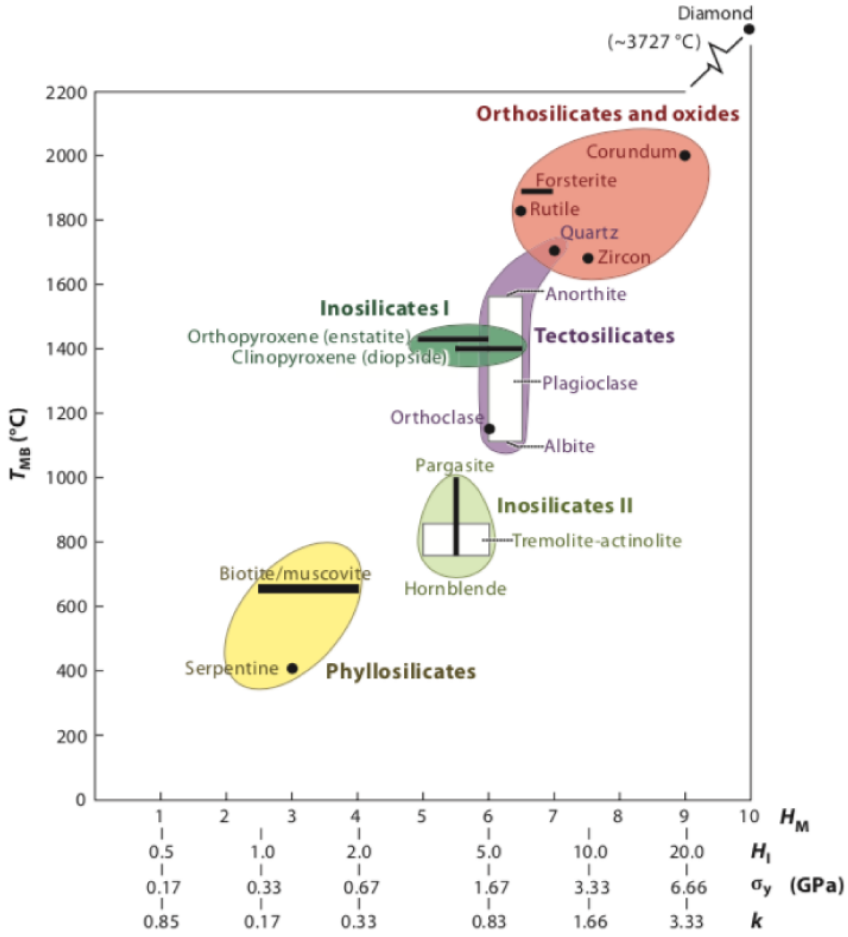


***Figure 1.9*** *– Mineral hierarchy for frictional melting susceptibility (from Spray, 2010). The approximate melting temperature versus Mohs hardness ($H_M$), indentation hardness ($H_I$), yield strength ($\sigma_y$) and shear yield strength (k) for common rock-forming mineral phases.*

## 1.6. AIMS OF THE THESIS

This thesis aims to constrain the impact of strain localisation on the geochemical, rheological and physical evolution of magma as it ascends in the volcanic conduit, and importantly to assess its role on eruption style. The focus is directed to crystal-rich, intermediate (andesite–dacite) lava domes where enigmatic shifts from effusive–explosive activity are common. Eruptive products from both effusive and explosive activity are analysed structurally, chemically and petrographically (Chapters 2, 3 and 4), while natural processes are replicated by laboratory experimentation (Chapters 2 and 3). The thesis also aims to highlight the importance of multidisciplinary datasets (including petrological, geochemical, rheological, crystallographic, microstructural, magnetics, geophysical, and experimentation) in gaining a compressive assessment of magmatic processes (Chapters 2 and 4).

The thermo-mechanical response of magma in the shallow conduit (e.g., in shear and fault zones) remains elusive, with shear and frictional heating deemed a likely phenomenon during magma ascent. However, the role of thermal instabilities during shearing on the petrological architecture of the magma remains poorly constrained, which may alter magma permeability, outgassing efficiency and drive different modes of dome activity. Controls on the different deformation mechanisms as magma is transported in the shallow conduit (viscous, plastic and brittle) will be assessed in the field and by microstructural analysis. Lava spine extrusion following the 1991–1995 eruption at Unzen volcano (Nakada *et al.*, 1999) provided the unique opportunity to assess *in-situ* the role of pre-eruptive conduit processes that are archived within the spine (Chapter 2). In recent years, efforts have focused on the viscous and brittle contributions, with little attention on the plastic regime, which may provide new insights on stress conditions in the conduit (Kendrick *et al.*, 2017). Crystal plasticity is quantified by electron backscatter diffraction (EBSD), with the aim to drive EBSD as a useful tool in volcanology. The data gathered will provide insights into rheological changes that occur as magma ascends in the conduit and demonstrate the importance of crystals as they may act as an indicator of strain (Chapter 2 explores this in detail).

Faulting and friction in the shallow volcanic conduit can dictate magma ascent style preceding an eruption. Extensive experimental studies have demonstrated the role of frictional melts on slip properties, acting as a lubricant or brake. In geological environments, frictional melts are silicate melts, thus like magmas, their behaviour is viscosity-dependent, which, in turn, is influenced by composition (along with temperature and strain rate). As frictional melting is defined as a selective mineral melting processes (Spray, 1992), it is apparent that the mineral assemblage of the host material is an essential factor that determines slip progression. Yet, the impact of mineralogy on a frictional melt's chemical, textural and

rheological evolution remains relatively unexplored. Chapter 3 aims to address the importance of mineral assemblage on frictional melt properties by experimental and geochemical investigation, which will provide new insights on magma ascent dynamics controlling lava dome eruptions.

The thesis will then move away from thinking specifically about strain localisation and apply our understanding of these processes to a constrain a shift in eruption intensity at Santiaguito dome complex, Guatemala, by integrating observations of petrological and geochemical signatures of explosive products (ash and bombs) with geophysical (seismic and infrasound) and thermal monitoring (Chapter 4). Regular, small-to-moderate gas-and-ash explosions at Santiaguito have previously been attributed to shear-driven processes at the conduit margins (e.g., Johnson *et al.*, 2008; Sahetapy-Engel *et al.*, 2008; Lavallée *et al.*, 2015a; Fig. 1.2), yet a shift to less frequent, larger ash-rich explosions in 2015–2016 (as reported by Lamb *et al.*, 2019) highlights the need to evaluate the magmatic plumbing system as a whole and the explosion mechanisms in play.

## 1.7. THESIS STRUCTURE

Following this introduction chapter, which has provided a background to the thesis topic, the thesis moves onto the original research that was collected for this thesis. The thesis presented is paper-based, thus readers are referred to each individual chapter for details on the analytical and experimental techniques used.

Chapters 2–4 are stand-alone papers presented in a logical order starting with pre-eruptive conduit processes (Chapter 2: Magma shearing; Chapter 3: Frictional melting) that can alter the magma's physical and chemical properties and influence eruption style, followed by a unique case study that marks a transition from effusive to explosive activity (Chapter 4: Santiaguito dome complex). Each manuscript has been reformatted for consistency throughout the thesis, with all references compiled at the end of the thesis in the bibliography. As these chapters are stand-alone published papers, there will be repetition of some key concepts and analytical methods used.

Chapter 5 provides a succinct summary of the results from each chapter and discusses the implications of these new findings on a broader scale, along with future directions for this research topic. Following the bibliography, Appendices (I–III) of supplementary figures for Chapters 2–4 are provided. Large supplementary data tables are provided as Electronic Appendices on CD, attached to the inside back cover of this thesis.

## 1.8. STATUS OF PAPERS AND CO-AUTHOR CONTRIBUTIONS

**CHAPTER 2**

**Manuscript title:** Petrological architecture of a magmatic shear zone: A multidisciplinary investigation of strain localisation during magma ascent at Unzen Volcano, Japan

**Authors:** Paul A. Wallace[1], Jackie E. Kendrick[1], Takahiro Miwa[2], James D. Ashworth[1], Rebecca Coats[1], James E.P. Utley[1], Sarah Henton De Angelis[1], Elisabetta Mariani[1], Andrew Biggin[1], Rhodri Kendrick[1], Setsuya Nakada[2], Takeshi Matsushima[3] and Yan Lavallée[1]

**Affiliations:**

[1] *Department of Earth, Ocean and Ecological Sciences, 4 Brownlow Street, University of Liverpool, Liverpool L69 3GP, UK*

[2] *National Research Institute for Earth Science and Disaster Resilience, Ibaraki, 305-0006 Japan*

[3] *Institute of Seismology and Volcanology, Faculty of Science, Kyushu University, Shin'yama 2-5643-29, Shimabara, Nagasaki, 855-0843 Japan*

**Journal:** *Journal of Petrology*

**Review process:** Peer reviewed

**Status:** Published

**DOI:** 10.1093/petrology/egz016

**Date published:** 13th March 2019

**Author contributions:**

- Paul A. Wallace – Primary investigator, primary author, fieldwork, data collection, data analysis, manuscript preparation
- Jackie E. Kendrick – Field assistance, data collection, data analysis, discussion, manuscript review, funding
- Takahiro Miwa – Field assistance, discussion
- James D. Ashworth – Field assistance, discussion
- Rebecca Coats – Field assistance
- Sarah H. De Angelis – Discussion
- Elisabetta Mariani – Manuscript review, funding
- James E.P. Utley – Data collection, Manuscript review
- Andrew Biggin – Data collection, discussion, manuscript review
- Rhodri Kendrick – Data collection
- Setsuya Nakada – Discussion, manuscript review
- Takeshi Matsushima – Field assistance, manuscript review
- Yan Lavallée – Field assistance, discussion, manuscript review, primary funding

## CHAPTER 3

**Manuscript title:** Frictional melt homogenisation during fault slip: Geochemical, textural and rheological fingerprints

**Authors:** Paul A. Wallace[1], Sarah H. De Angelis[1], Adrian J. Hornby[1,3], Jackie E. Kendrick[1], Stephen Clesham[1], Felix W. von Aulock[1], Amy Hughes[1], James E. P. Utley[1], Takehiro Hirose[2], Donald B. Dingwell[3] and Yan Lavallée[1]

**Affiliations:**

[1] *Department of Earth, Ocean and Ecological Sciences, 4 Brownlow Street, University of Liverpool, Liverpool L69 3GP, UK*

[2] *Kochi Institute for Core Sample Research (KCC), Japan Agency for Marine-Earth Science and Technology (JAMSTEC), 200 Monobe-otsu, Kochi, Nankoku 783-8502, Japan*

[3] *Department of Earth and Environment, Ludwig-Maximilians-Universität München (LMU-Munich), Theresienstrasse 41/III, 80333 Munich, Germany*

**Journal:** *Geochimica et Cosmochimica Acta*

**Review process:** Peer reviewed

**Status:** Published

**DOI:** 10.1016/j.gca.2019.04.010

**Date published:** 17th April 2019

**Author contributions:**

- Paul A. Wallace – Primary investigator, primary author, data collection, data analysis, manuscript preparation
- Sarah H. De Angelis – Data collection, data analysis, discussion, manuscript review
- Adrian J. Hornby – Data collection, discussion, manuscript review
- Jackie E. Kendrick – Data collection, discussion, manuscript review
- Felix W. von Aulock – Data collection, manuscript review
- Stephen Clesham – Data collection
- Amy Hughes – Data collection
- James E.P. Utley – Data collection
- Takehiro Hirose – Discussion, manuscript review
- Donald B. Dingwell – Discussion, manuscript review, funding
- Yan Lavallée – Data collection, discussion, manuscript review, primary funding

## CHAPTER 4

**Manuscript title:** Integrated constraints on explosive eruption intensification at Santiaguito dome complex, Guatemala

**Authors:** Paul A. Wallace[1], Oliver D. Lamb[1,2], Silvio De Angelis[1], Jackie E. Kendrick[1], Adrian J. Hornby[1,3], Alejandro Díaz-Moreno[1], Felix W. von Aulock[1], Anthony Lamur[1], James E.P. Utley[1], Andreas Rietbrock[1,4], Gustavo Chigna[5], Yan Lavallée[1]

**Affiliations:**

[1] *Department of Earth, Ocean and Ecological Sciences, 4 Brownlow Street, University of Liverpool, Liverpool L69 3GP, UK*

[2] *Department of Geological Sciences, University of North Carolina at Chapel Hill, Chapel Hill, NC, USA*

[3] *Department of Earth and Environment, Ludwig-Maximilians-Universität München (LMU-Munich), Theresienstrasse 41/III, 80333 Munich, Germany*

[4] *Geophysical Institute, Karlsruhe Institute of Technology, Karlsruhe, Germany*

[5] *Instituto Nacional de Sismologia, Vulcanologia, Meteorologia, e Hydrologia (INSIVUMEH), Guatemala City, Guatemala*

**Journal:** *Earth and Planetary Science Letters*

**Status:** In Preparation

**Author contributions:**

- Paul A. Wallace – Primary investigator, primary author, data collection, data analysis, manuscript preparation
- Oliver D. Lamb – Fieldwork, data collection, data analysis, discussion, manuscript review
- Silvio De Angelis – Fieldwork, data collection, discussion, manuscript review, funding
- Jackie E. Kendrick – Fieldwork, data collection, discussion, manuscript review
- Adrian J. Hornby – Fieldwork, data collection, discussion, manuscript review
- Alejandro Díaz-Moreno – Data analysis, discussion, manuscript review
- Felix W. von Aulock – Fieldwork, data collection, manuscript review
- Anthony Lamur – Fieldwork, data collection, discussion, manuscript review
- James E.P. Utley – Data collection
- Andreas Rietbrock – Discussion, manuscript review
- Gustavo Chigna – Fieldwork
- Yan Lavallée – Fieldwork, discussion, manuscript review, funding

# Chapter 2 Petrological architecture of a magmatic shear zone: A multidisciplinary investigation of strain localisation during magma ascent at Unzen Volcano, Japan

## ABSTRACT

Shearing of magma during ascent can promote strain localisation near the conduit margins. Any mechanical and thermal discontinuities associated with such events may alter the chemical, physical and rheological stability of the magma, and thus its propensity to erupt. Lava spines can record such processes, preserving a range of macroscopic and microscopic deformation textures, attributed to shearing and friction, as magma ascends through the viscous-brittle transition. Here, we use a multidisciplinary approach combining petrology, microstructures, crystallography, magnetics and experimentation to assess the evidence, role and extent of shearing across a marginal shear zone of the 1994–1995 lava spine at Unzen volcano, Japan. Our results show that crystals can effectively monitor stress conditions during magma ascent, with viscous remobilisation, crystal plasticity and comminution all systematically increasing towards the spine margin. Accompanying this, we find an increase in mineral destabilisation in the form of pargasitic amphibole breakdown displaying textural variations across the shear zone, from symplectitic to granular rims towards the spine margin. In addition, the compaction of pores, chemical and textural alterations of interstitial glass, and magnetic variations all change systematically with shear intensity. The strong correlation between the degree of shearing, crystal deformation and disequilibrium features, together with distinct magnetic properties, implies a localised thermal input due to shear and frictional processes near the conduit margin during magma ascent. This was accompanied by late-stage or post-emplacement fluid- and gas-induced alteration of the gouge, as well as oxidation and glass devitrification. Understanding and recognising evidence for strain localisation during magma ascent may, therefore, be vital when assessing factors that regulate the style of volcanic eruptions, which may provide insights into the cryptic shifts from effusive to explosive activity as observed at many active lava domes.

## 2.1. INTRODUCTION

The characteristics of erupted lavas reflect a complex series of magmatic events from crystallisation, crystal segregation, chemical speciation, magma mixing, ascent, degassing, eruptive shearing and deposition. Strain localisation during the ascent of high viscosity magmas at lava domes may have an influential role on many pre-eruptive conduit processes as well as eruption dynamics. The ability for strain to preferentially localise during magma ascent is favoured by the magma's non-Newtonian response, following crystallisation (e.g., Lejeune & Richet, 1995) and gas exsolution (e.g., Llewellin & Manga, 2004). This, in turn, can promote a transition from a Poiseuille to plug-like flow (Hale, 2007; Hale *et al.*, 2007), facilitating the formation of discrete shear zones near conduit margins (Hale & Wadge, 2008; Lavallée *et al.*, 2013) which may be more (Gaunt *et al.*, 2014) or less permeable (Kendrick *et al.*, 2013a) than the bulk of the magma. Where marginal shear zones with relatively high permeabilities (Gaunt *et al.*, 2014) surround a relatively dense, degassed magma core, temporal sealing of these regions may cause gas pressure to accumulate below the plug and consequently fragment causing explosive activity and/or dome destabilisation (Voight *et al.*, 1999; Mason *et al.*, 2006; Clarke *et al.*, 2007; Lensky *et al.*, 2008; Michaut *et al.*, 2009; Kennedy *et al.*, 2010; Ashwell *et al.*, 2015; Farquharson *et al.*, 2016b; Heap *et al.*, 2017). Upon ascent, magma may encounter the viscous-brittle transition, beyond which, faulting processes can dominate (Kendrick *et al.*, 2012). If faulting extends to the surface, it may result in the extrusion of a lava spine piercing through the dome carapace, contributing to the exogenous growth of dome-building eruptions (Mount St. Helens, USA – e.g., Cashman *et al.*, 2008; Soufrière Hills volcano, Montserrat – e.g., Melnik & Sparks, 2002; Unzen volcano, Japan – e.g., Nakada *et al.*, 1999; and Mont Pelée, Martinique – e.g., Tanguy, 2004). Hence, a lava spine provides a relic of magma shearing and faulting processes in the shallow volcanic conduit.

Understanding the processes involved in spine extrusion may aid in constraining the complexities associated with ongoing eruptions at lava domes. Many lava domes are crystal-rich. Crystals have the propensity to physically interact within the flowing magma by partitioning strain (e.g., Caricchi *et al.*, 2007; Lavallée *et al.*, 2007; Picard *et al.*, 2011), promoting strain localisation (Cordonnier *et al.*, 2009; Lavallée *et al.*, 2012b; Lavallée *et al.*, 2013), and, as such, preserve deformation textures (e.g., Kendrick *et al.*, 2017). The interaction of crystals has been observed and parameterised in many experimental investigations (e.g., Caricchi *et al.*, 2007; Cordonnier *et al.*, 2009; Forien *et al.*, 2011; Picard *et al.*, 2011), being portrayed as acting to localise stress, forming a rigid network. However, stress concentration (e.g., Deubelbeiss *et al.*, 2011) may result in plastic deformation of the crystalline phase (Kendrick *et al.*, 2017) and even fracturing (Lavallée *et al.*, 2007; Cordonnier *et al.*, 2009;

Forien *et al.*, 2011; Coats *et al.*, 2018) as magma undergoes the viscous-brittle transition. This characteristic suggests crystal plasticity and fracturing of crystals (also termed comminution when induced by shear) may play roles in accommodating strain, and that crystals in erupted lavas can act as deformation markers of shallow volcanic processes. Until now, the extent of crystal plasticity in extrusive lavas has yet to be explored at outcrop scale, and its role remains unquantified.

Previous investigations on the mechanical processes of spine growth at Mount St. Helens observed multiple forms of evidence supporting brittle deformation at the conduit margin (e.g., Kennedy *et al.*, 2009), resulting in a 1–3 m thick mantle of gouge dominated by tensile fracturing, granulation and cataclasis, all thought to form at sub-solidus conditions at <1 km depth (Cashman *et al.*, 2008; Pallister *et al.*, 2013). The products revealed no microstructural evidence of subsequent annealing, high-temperature viscous flow or solid-state crystal plasticity (Cashman *et al.*, 2008; Kennedy *et al.*, 2009), although solid-state sintering has been attributed to the lithification of fault gouge at the spine margin (Ryan *et al.*, 2018). However, Kendrick *et al.* (2012) examined the latest spine at Mount St. Helens, finding evidence for the role of rapid heating in the form of textural and microstructural evolution, complemented by geochemical, mineralogical, kinetic and magnetic analyses of the sheared region of the spine 7 margin.

It has become increasingly recognised, via theoretical models (e.g., Costa & Macedonio, 2003; Mastin, 2005; Vedeneeva *et al.*, 2005; Hale *et al.*, 2007), experimentation (Hess *et al.*, 2008; Lavallée *et al.*, 2012a; Kendrick *et al.*, 2014b; Hornby *et al.*, 2015) and detailed petrological constraints (e.g., Rosi *et al.*, 2004; Wright & Weinberg, 2009), that shear and/or frictional heating in areas of strain localisation may locally raise magmatic temperatures. Shear heating is a thermodynamic response to the dissipation of viscous energy (Ockendon, 1979); similarly, fault friction can also generate substantial thermal input (Carslaw & Jaeger, 1959). The plug-like flow that characterises the extrusion of lava domes makes them more susceptible to these thermal effects, contributing to shifts in rheology that dictate magma ascent dynamics. It has been proposed, based on numerical modelling, that temperature rises of >100 ºC near the conduit margins are attainable due to viscous deformation (Rosi *et al.*, 2004; Mastin, 2005; Costa *et al.*, 2007; Hale *et al.*, 2007). In contrast, fault friction, although localised on narrow planes, can generate a temperature rise of several hundred degrees (e.g., Lavallée *et al.*, 2012a; Kendrick *et al.*, 2014b; Hornby *et al.*, 2015; Lavallée *et al.*, 2015a). Such temperature increases could alter the magmas physical and chemical properties; in detail, heating could: drive mineral reactions (e.g., De Angelis *et al.*, 2015), melt crystalline phases (e.g., Kendrick *et al.*, 2014b), re-set magnetic properties (e.g., Kendrick *et al.*, 2012), trigger vesiculation (Lavallée *et al.*, 2015a), lower interstitial melt

viscosity (e.g., Hornby *et al.*, 2015), redistribute and collapse pores (e.g., Laumonier *et al.*, 2011) altering degassing pathways (e.g., Kendrick *et al.*, 2014a; Ashwell *et al.*, 2015), and more efficiently heal fractures (e.g., Tuffen *et al.*, 2003; Lamur *et al.*, 2019). In glass-bearing rocks at lower temperatures, a thermal input could push them above the glass transition temperature ($T_g$), a kinetic barrier that is dependent on the timescales of structural relaxation where the glass softens to a melt (Dingwell & Webb, 1989; Webb & Dingwell, 1990), enabling viscous remobilisation (e.g., Hornby *et al.*, 2015; Lavallée *et al.*, 2015a). Although becoming increasingly explored through laboratory experiments, few studies have documented the effects of shear or frictional heating in shallow volcanic conduits from a physical volcanology perspective (Smith *et al.*, 2001; Rosi *et al.*, 2004; Tuffen & Dingwell, 2005; Kendrick *et al.*, 2012; Kendrick *et al.*, 2014a; Hornby *et al.*, 2015; Lavallée *et al.*, 2015a). Recognising evidence for strain localisation and the related thermal feedback processes should not be overlooked when assessing dome longevity and could contribute to cryptic shifts in eruption style (Sparks, 1997; Cashman & Sparks, 2013; Cassidy *et al.*, 2018).

Spine extrusion during the closing of the 1991–1995 lava dome eruption and subsequent quiescence at Unzen volcano, Japan, provided the unique opportunity to explore the occurrence, extent and role of shearing on crystal deformation and thermal disequilibrium during magma ascent. Here, we present the first systematic study of the mineralogy, microstructures, crystal size and shape distribution, mineral stability, and magnetic properties across a sheared margin of Unzen lava spine, where we explore the results in the context of syn-emplacement deformation and subsequent alteration. The data are complemented by the first high-temperature high-velocity rotary shear experiment on volcanic materials to simulate the conditions during eruptive shear.

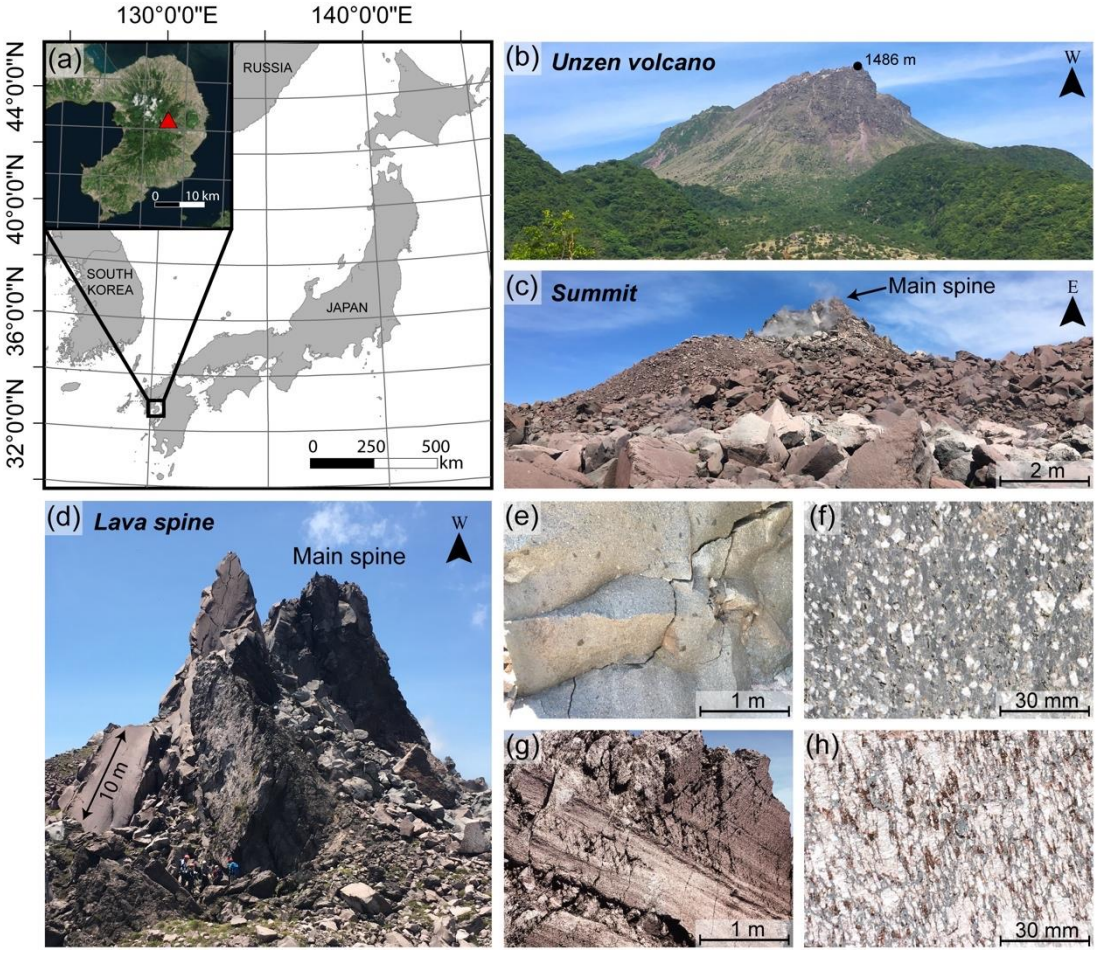


***Figure 2.1*** *– Unzen volcano and lava dome heterogeneity. (a) Map showing the location of Unzen volcano in southwestern Japan (created using ArcGIS® software by Esri™ under copyright © license; Esri, 2015). The inset shows the Shimabara Peninsula with Unzen volcano denoted with a triangle (Esri, 2009). (b) View of the eastern side of Unzen lava dome. (c) Dome summit displaying large, polygonal blocks with a range of deformation textures and variable degrees of oxidation. The lava spine can be seen having extruded from the top of the dome. (d) Eastern side of the 1994–1995 lava spine revealing multiple, broken segments and larger in-situ slabs, with the main spine residing in the background. (e) Example of an undeformed dome block with no macroscopic deformation, little alteration and negligible oxidation. (f) Close-up textures of an undeformed block consisting of large, euhedral, white plagioclase phenocrysts, along with dark amphibole and biotite crystals. (g) Example of a highly deformed dome block with moderate oxidation, consisting of shear bands and conjugate fractures. (h) Close-up textures of an extremely deformed block consisting of smeared plagioclase phenocrysts and elongated, oxidised amphibole crystals.*

### 2.1.1. Overview of the 1991–1995 dome eruption

Unzen volcano is a stratovolcano located in southwest Japan on the Shimabara Peninsula (Fig. 2.1a). Since its formation ca. 500 ka, its historical activity consists dominantly of thick lava flows, domes, and their subsequent collapse deposits, which range from andesites to dacites, and notably lacks extensive explosive episodes (Hoshizumi *et al.*, 1999; Nakada *et al.*, 1999). The latest eruption took place between 1991–1995 following 198 years of dormancy, leading to the growth of a dacitic lava dome (Fig. 2.1b) with eruptive products having a narrow compositional variability of 64.5–66.0 wt % $SiO_2$ (Nakada & Motomura, 1999). A full description of the 1991–1995 dome-building eruption has been given by Nakada *et al.* (1999) and is briefly summarised here. On 20 May 1991, a dacitic lava dome appeared for the first time at Unzen volcano after persistent phreatic and phreatomagmatic activity several months prior (Nakada & Motomura, 1999; Nakada *et al.*, 1999). The eruption lasted ~4 years and was the most voluminous in Unzen's history, being temporally characterised by two styles of dome growth; exogenous and endogenous. Exogenous growth occurred when effusion rates were high from May 1991 to November 1993 (Nakada *et al.*, 1995; Nakada & Motomura, 1999), which contributed to the formation of 13 lava lobes (Sato *et al.*, 1992; Nakada & Fujii, 1993; Nakada & Motomura, 1999; Nakada *et al.*, 1999) and repetitive dome collapse events generating block-and-ash flows and pyroclastic density currents (Yamamoto *et al.*, 1993; Miyabuchi, 1999; Ui *et al.*, 1999; Sakuma *et al.*, 2008). The dome grew endogenously when effusion rates waned (from November 1993 onwards) causing rhythmic inflation-deflation cycles (Nakada & Motomura, 1999; Nakada *et al.*, 1999). By mid-October 1994 to mid-February 1995 exogenic growth resumed as a lava spine extruded from the western limits of the endogenous crater (Fig. 2.1c and d; Nakada & Motomura, 1999; Nakada *et al.*, 1999; Saito & Shikawa, 2007). Spine growth was accompanied by tilt cycles and shallow swarms of seismicity in 40–60 hour cycles (Nakada *et al.*, 1999; Yamashina *et al.*, 1999; Umakoshi *et al.*, 2008), attributed to pressure fluctuations (Hendrasto *et al.*, 1997; Kohno *et al.*, 2008) or traction during fault-controlled pulsatory magma ascent (Hornby *et al.*, 2015; Lamb *et al.*, 2015). The spine extruded obliquely at an angle of ~45° towards the east-south-east, consistent with the inclined nature of the conduit (Umakoshi *et al.*, 2001; Kohno *et al.*, 2008; Tanaka, 2016), with a final dimension of 150 m long, 30 m wide and 60 m high (Nakada *et al.*, 1999). After the eruption ended, cooling contraction of the underlying dome led to partial collapse of the spine leaving behind dissected blocks that are detached from the main spine (Fig. 2.1d; Nakada *et al.*, 1999).

### 2.1.2. Magma feeding the 1991–1995 eruption

Based on petrographic evidence of the erupted products, the 1991–1995 eruption has been interpreted to be the result of magma mixing that took place within a ~7–8 km deep magma reservoir (e.g., Nakamura, 1995; Venezky & Rutherford, 1999; Holtz *et al.*, 2005; Kohno *et al.*, 2008; Sato *et al.*, 2017). The abundance of disequilibrium textures, including reversely zoned plagioclase and hornblende phenocrysts, diffusion profiles of magnetite phenocrysts, biotite reaction rims consisting pargasitic amphiboles and embayed quartz, has suggested interaction of two compositionally contrasting magmas (e.g., Nakada & Fujii, 1993; Nakamura, 1995; Nakada & Motomura, 1999; Venezky & Rutherford, 1999). These observations, along with experimental investigations, demonstrated that mixing involved a high-temperature (~1050 ºC) aphyric andesite and a low-temperature (~790 ºC) crystal-rich rhyodacite, resulting in a mixed 870–900 ºC dacite (Venezky & Rutherford, 1999; Holtz *et al.*, 2005). Most phenocrysts are interpreted to have derived from the low-temperature end-member, while the groundmass assemblage is believed to be representative of a post-mixed melt (Nakada & Motomura, 1999; Cichy *et al.*, 2011). The common occurrence of mafic enclaves further supports this model and has placed constraints on the different residence times between the different magmas involved (Sato *et al.*, 2017). Fe-Ti oxide re-equilibration experiments have suggested that mixing took place a few weeks before the start of the eruption (Venezky & Rutherford, 1999), and that continuous or intermittent mixing may have taken place throughout the eruptive period (e.g., Nakamura, 1995; Venezky & Rutherford, 1999; Holtz *et al.*, 2005). Although mixing likely continued during ascent from the magma reservoir (Nakada & Motomura, 1999), the Unzen Scientific Drilling Project demonstrated that the conduit from ca. 1 km depth consisted of a thoroughly mixed dacite (Goto *et al.*, 2008).

## 2.2. METHODS

### 2.2.1. Sample collection

To explore evidence for strain localisation and its implications for the mineralogical signature of ascending magma, the focus of the study was directed to two intact shear zones (Fig. 2.2a and Fig. 2.3a). Outcrop 1 (Fig. 2.2a), located ~60 m east of the main spine (Latitude: 32.761313º Longitude: 130.299826º), represents a quasi-continuous gradation across a faulted margin of the spine. The shear zone is elongated towards the south-south-east (158º) with a dimension of 4.5 m long, 3.7 m wide and 2.5 m high. Based on the nature and degree of deformation observed, the shear zone was subdivided into four structurally discrete units (see results section "Field observations" for description), including: gouge (Fig. 2.2b); a "high shear" zone (Fig. 2.2c, d and e); transitioning to a "moderate shear" zone (Fig. 2.2f and g);

and a relatively undeformed core termed “low shear” (Fig. 2.2h and i) believed to be representative of the spine interior. Samples were collected along a transect of this shear zone (A–H in Fig. 2.2a), with all petrological and geochemical analysis in this study focusing exclusively to outcrop 1. For textural comparison, an undeformed dome block was collected from the talus (i.e., not from the spine), which represented a material that was extruded immediately prior to spine growth and thus acts as a suitable baseline (Fig. 2.2j). Outcrop 2 (Fig. 2.3a) is the end-on exposure of a dissected portion of the east side of the main spine (Latitude: 32.761350° Longitude: 130.299444°), measuring >20 m wide by ~20 m high, and consisting of a relatively intact interior, grading to a fractured and highly sheared zone with a sharp boundary to a narrow gouge layer bordered on the other side by a breccia (as described in Hornby *et al.*, 2015). This outcrop was used exclusively to assess magnetic variations across the faulted margin of the spine, along with loose blocks from the gouge, highly sheared and host (near-pristine spine interior) which were selected at outcrop 2 (Fig. 2.3b, c and d). All samples collected from outcrop 1 and 2 were thin sectioned perpendicular to the principle shear direction for petrographic analysis. Principle shear was characterised in each outcrop using *in-situ* textural fabrics (e.g., lineations, elongated crystals, Riedel fractures) that reveal consistent orientations within the high shear zones with respect to the position of the gouge, with both outcrops displaying the oblique upward shear motion of the extruded spine.

### 2.2.2. Geochemistry

Whole-rock geochemistry (across outcrop 1) was determined by X-ray Fluorescence (XRF) on a PANalytical Axios Advanced XRF spectrometer at the University of Leicester. Major elements were measured on glass beads fused from ignited powders using a sample to flux ratio of 1:5 (80% Li metaborate: 20% Li tetraborate). Results are reported as component oxide weight percent and have been recalculated to include loss on ignition (LOI). Trace elements were analysed using 32 mm diameter pressed powder pellets produced by mixing 7 g of fine ground sample powder with 12–15 drops of a 7 % polyvinyl alcohol solution (Mowiol 8-88). Relative precisions and accuracies are better than 1–2 % for all major elements and better than 5 % for trace elements based on repeat analyses of international reference materials (BH-1 microgranodiorite, JR-1 rhyolite and BCR-1 basalt).

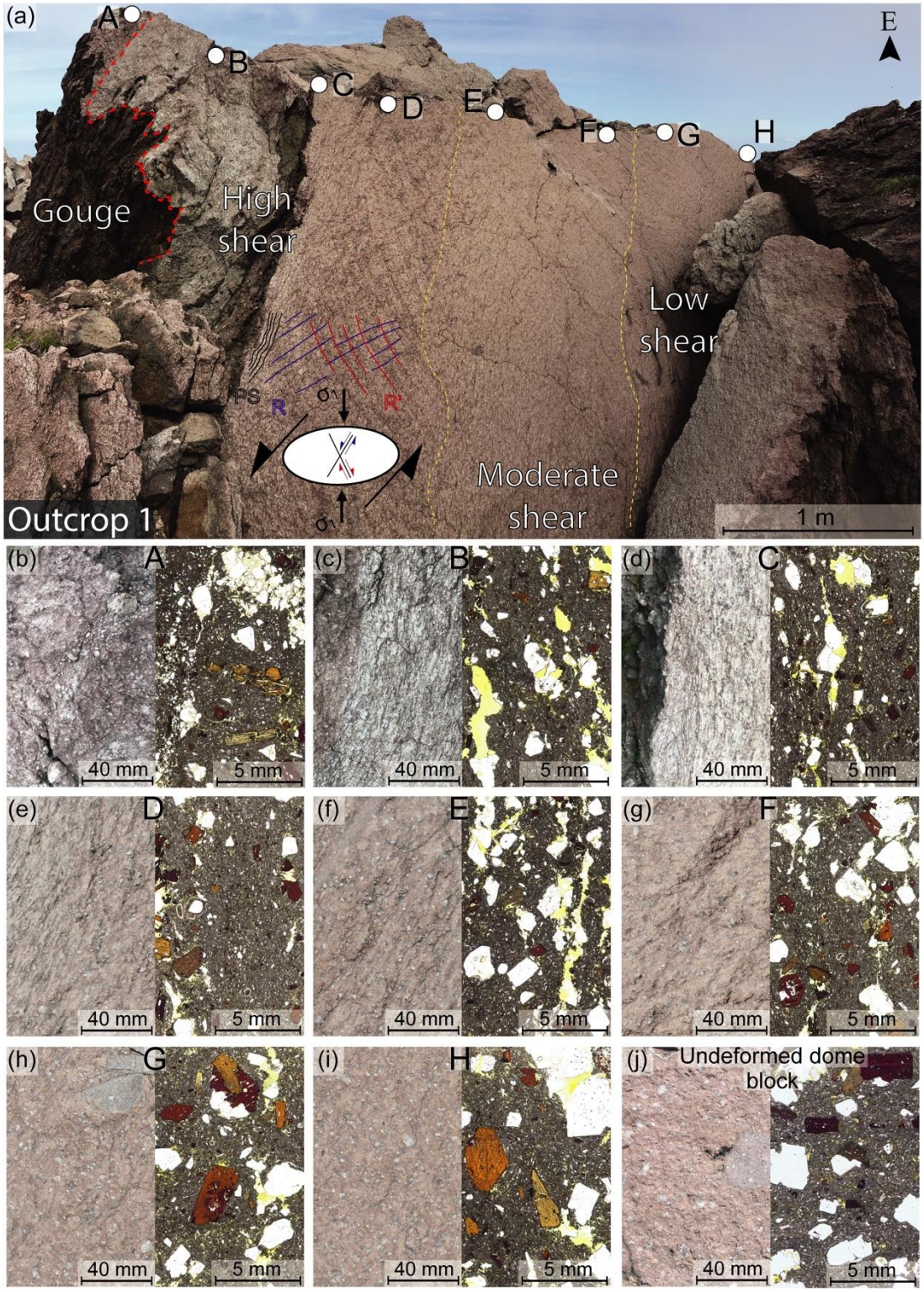


***Figure 2.2*** *– Field and textural observations of outcrop 1 marginal shear zone of Unzen lava spine. (a) Photograph of the shear zone, which has been separated into four zones according to style and intensity of deformation, along with sample collection locations (points A–H). On the surface of the high shear zone, principle shear lineations (PS), and Riedel shear textures (R and R') are visible, consistent with an upward movement of the spine. In panels (b–j), the left-hand side is the outcrop surface and the right-hand side is the corresponding plane*

*polarised light photomicrograph. (b) Gouge; a well-consolidated, reddish gouge layer consisting of cataclastic deformation textures in the form of abundant crystal fragments, larger intact clasts and surface fractures. (c–e) High shear zone, displaying strong lineations and elongated white filaments that decrease in intensity from (c) to (e). Photomicrographs in (c) and (d) show these filaments are comprised of plagioclase phenocryst fragments, with the elongated yellow-green area representing voids where some fragments were removed. Fragments of amphibole are also observed within the groundmass. (f–g) Moderate shear zone, individual crystals are more visible, representing larger fragments, and elongated filaments of plagioclase crystals are less apparent. Lineations are less intense, although still visible on the outcrop surface. (h–i) Low shear zone, a smooth outcrop surface with negligible deformation, consisting of intact, euhedral plagioclase and amphibole phenocrysts. (j) Undeformed dome block, consisting of large, euhedral plagioclase and amphibole phenocrysts, closely resembling the low shear zone.*

### 2.2.3. Electron Microprobe (EPMA)

Major element composition of the interstitial glass (from outcrop 1) was determined using a Cameca SX-5 field-emission electron probe microanalyser (EPMA) at the University of Oxford. Element abundances were determined using wavelength dispersive spectroscopy (WDS) with TAP, PET and LIF crystals. Standards for calibration of the spectrometers included a range of silicates and oxides (e.g., albite for Na, Si, Al; wollastonite for Ca). Analyses were performed using a 15 kV accelerating voltage, 5 nA beam current and a defocused spot size of 5 μm. Due to a 5 μm spot size being used on glass, the concentrations of alkalis, namely Na and K, may show minor reduction; however, owing to the abundance of microlites and devitrified glass filaments, the use of a defocused 10 μm beam would have yielded higher inaccuracies. Major elements have a relative precision better than 3 % and an accuracy better than 5 %, except Na which was better than 10%, based on repeat analyses of KN-18 glass standard (comendite obsidian, Kenya). Our results are consistent with compositions reported by Nakada and Motomura (1999) for partly devitrified.

### 2.2.4. Automated SEM-EDS (QEMSCAN)

Mineral distribution and quantitative phase modality (of outcrop 1) was acquired using QEMSCAN (Quantitative Evaluation of Minerals by SCANning electron microscopy), an automated SEM-EDS system. It uses specially configured conventional SEM hardware and advanced, highly adaptable software, manufactured by FEI. Each analysis was performed on

an uncovered, polished and carbon coated thin section using a QEMSCAN WellSite at the University of Liverpool operating with a 15 kV accelerating voltage and ~5 nA beam current. Two Bruker energy dispersive X-ray spectrometers (EDS) recorded the discrete secondary X-rays emitted by the sample excited by the electron beam (within an interaction volume of ~10 $\mu m^3$), which are processed to identify and quantify the elements present and output a chemical composition. The chemistry recorded is matched to known compositions for minerals, glasses and other chemically distinct phases. These phase compositions are stored in an extensive mineral database, referred to as a species identification protocol (SIP), which can be added to, and edited by, the user (see Gottlieb *et al.*, 2000). The system cannot measure any crystallographic features, thus cannot differentiate between amorphous, crystalline or any chemically identical polymorphs (e.g., quartz, cristobalite and tridymite). Data were collected in field-scan mode collecting X-rays in an automated raster pattern at a specified step size (Gottlieb *et al.*, 2000; Pirrie *et al.*, 2004). For bulk mineralogy, whole thin section scans were performed with X-rays collected at 20 μm intervals, and to assess groundmass mineralogy a 2 μm step size was used. The electron beam dwells at each point until sufficient X-rays are collected by the detectors to allow for successful phase matching (set to collect 1000 X-rays per point). A re-calibration of the system was performed after every sample exchange from the machine. Data processing and interpretation were performed using iDiscover software, which stitches the resulting data to form a continuous colour image of the sample, where each colour represents a different phase. Mineral statistics were obtained from the sum of the number of pixels of each phase and were normalised on a pore-free basis to provide a quantitative 2-D modal mineralogy (e.g., Pirrie *et al.*, 2004; Ayling *et al.*, 2012). The resolution (10 μm or 2 μm) did not influence the calculated mineralogy as there was no change in the beam operating conditions (i.e., interaction volume), only the spacing between analyses. Any phases smaller than the beam's interaction volume are not identified individually but incorporated with the chemistry of its surroundings (e.g., crystals less than ~2 μm in diameter surrounded by glass). Although 100 % reproducibility of a different thin section of the same material is unlikely (simple thin section effect), precision errors based on repeat scans after removing and reinserting the same thin section produced standard deviations <0.39 for all phases.

### 2.2.5. Image acquisition and analysis

#### *2.2.5.1. Optical and scanning electron microscopy (SEM)*

Optical microscopy enabled the identification and comparison of the major phases and any microstructural variations across the samples. Plane polarised light (PPL) images and whole thin section scans were acquired using a Leica DM2500P microscope, at a magnification of 2.5x, and a Leica DFC295 camera with a pixel resolution of 5 x 5 µm. SEM analysis was conducted using a Philips XL30 tungsten filament scanning electron microscope and Hitachi TM3000 at the University of Liverpool. Thin sections were carbon coated and imaged using the Philips XL30 with a 20 kV beam, a working distance of 25 mm and a spot size of 5 µm, while the Hitachi TM3000 used a 15 kV beam and 10 mm working distance, both operating in backscattered electron (BSE) mode.

#### *2.2.5.2. Plagioclase crystal size- and shape-distribution*

Whole thin section photomicrographs (from outcrop 1) collected in PPL were used to determine crystal size and shape variations of plagioclase phenocrysts across the shear zone to quantify crystal fracturing. The analysis was carried out using the National Institute of Health (NIH) ImageJ software package (Schneider *et al.*, 2012), where scans were converted to binary images, replacing all plagioclase crystals with black pixels and all other phases, including pores, with white pixels. To prevent misidentification of plagioclase with quartz in the binary conversion process, QEMSCAN maps were used as a guide to ensure all black pixels were correctly identified as plagioclase. Measurements were made on phenocrysts above a detection limit of 0.01 $mm^2$ ensuring all crystals above this size fraction were measured and shapes were accurately represented. Crystal size measurements included major and minor axis length (using the "fit ellipse" tool) and total area. Crystal shape was determined using the "shape descriptors" tool (circularity, aspect ratio, roundness and solidity). Circularity of each phenocryst in the thin section was calculated using: $\mathbf{Circularity} = \mathbf{4\pi(A/p^2)}$, where **A** is crystal area and **p** is the perimeter. Circularity values range from 0–1, with 1 indicating a perfect circle, becoming more elongate as values approach 0.

#### *2.2.5.3. Groundmass pargasite reaction rims*

High-magnification BSE images of pargasitic amphibole crystals in the groundmass were collected from each section of outcrop 1 shear zone (gouge, high shear, moderate shear and low shear zones in Fig. 2.2a) and the undeformed dome rock (Fig. 2.2j). Reaction rim thickness variations were quantitatively assessed using ImageJ. The sizes of the pargasite

crystals were determined using the longest axis, and when permitted, using the C-axis. Due to the irregular and patchy occurrence of breakdown rims within a single crystal, the thickest part of the rim was measured. Data were collected for >30 pargasite crystals from each zone, ensuring coverage of the whole thin section to avoid misrepresentation.

### 2.2.6. Electron Backscatter Diffraction (EBSD)

Permanent internal deformation of a crystal lattice can provide useful insights into the stress conditions that a material has been exposed to during its history. Crystal plasticity is an isovolumetric deformation process derived from external forces exceeding the yield stress of a crystal lattice (Poirier, 1995), manifesting in a permanent strain by generating internal stranded dislocations. Dislocations cause a distortion of the crystal lattice structure and this distortion can be measured by electron backscatter diffraction (EBSD) in the SEM as a crystallographic "misorientation" angle (Prior *et al.*, 1999; Prior *et al.*, 2009). The angular resolution of the technique is ±0.5º (e.g., Mariani *et al.*, 2009). Crystal lattice orientation mapping for the identification and quantification of crystal plasticity was carried out across outcrop 1 shear zone samples using a CamScan X500 CrystalProbe field-emission gun (FEG) SEM using the AZtec EBSD acquisition software from Oxford Instruments HKL. Analyses were performed using a 20 kV accelerating voltage and 30 nA beam current. The electron beam source column is tilted at 70º relative to the sample surface. EBSD maps were collected on plagioclase and biotite phenocrysts and plagioclase microlites. The area coverage of phenocryst maps was dependent on the size of the target crystal, whereas microlites were analysed within a ~150 x 120 µm area from 2 or more locations within the same thin section to ensure accurate representation of each sample (see Fig. A1.1 for the mapped areas). Acquisition of the data was performed using Oxford Instruments HKL AZtec EBSD software using step sizes from 0.15–0.4 µm for microlites and 2 µm for phenocrysts. Minerals were identified using energy dispersive point analyses (EDS) to determine their chemistry and mapped by EBSD using the appropriate crystallographic match units for each of the phases investigated. For statistical representation, >40 plagioclase microlites from each section of the shear zone were analysed. Minerals were indexed using all 12 bands, 70 reflectors, 120 Hough resolution, band edges and 4 x 4 binning. Data processing was carried out in CHANNEL 5 software by Oxford Instruments HKL. Individual crystals in the EBSD maps were subjected to a "texture component" analysis, where each pixel (each EBSD data point) is colour-coded according to the degree of misorientation of the crystal lattice relative to a selected reference pixel. All reference pixels were selected from one end of the crystal as this more accurately reflects the relative distortion across the crystal and depicts the maximum misorientation.

Similarly, misorientations were measured as profiles along the length of a crystal to give a quantitative description of the deformation experienced. For each crystal, the length and width were recorded, as well as the "maximum misorientation" along the major axis from the misorientation profile. "Misorientation per micron" values were determined by dividing the maximum misorientation by the long axis length of the crystal following the method of Kendrick *et al.* (2017). Through using the mean misorientation per micron, we can model the amount of lattice distortion expected in a plagioclase microlite for a given crystal length from each section of the shear zone.

### 2.2.7. Thermal analysis

The kinetic and thermal properties of the Unzen lava spine were measured using differential scanning calorimetry (DSC), performed on a Netzsch simultaneous thermal analyser (STA) Jupiter 449 F1 at the University of Liverpool, using a single sapphire crystal for calibration of specific heat capacity ($C_p$). $C_p$ as a function of temperature was calculated using DSC, which can provide a thermal history of the sample, in particular, a quantification of the glass transition temperature ($T_g$). Due to the high crystallinities of Unzen spine lavas and thus the low proportion of pristine glass to obtain a well-defined $T_g$ measurement, spine material was lightly crushed into mm-sized fragments and groundmass dominated grains were selectively plucked to increase the glass:crystal ratio and provide a more reliable $T_g$ value. Lightly crushed, phenocryst-free sample chips (38 mg) of low shear material from outcrop 1 (Fig. 2.2i) were placed in a lidded platinum crucible (with a single hole in the centre of the lid) and heated at 10 $^{o}$C.min$^{-1}$ to 1000 $^{o}$C with a continuous 20 mL.min$^{-1}$ argon flow. The onset of the $T_g$ interval is defined by an exothermic deflection (increase) in the DSC and $C_p$ curves (e.g., Gottsmann *et al.*, 2002).

### 2.2.8. Magnetic properties

Magmas that have undergone extensive shearing and faulting are ideal candidates to display magnetic anomalies due to alignments of the magnetic carriers (Hayman *et al.*, 2004) or a heating event associated with such processes (Nakamura *et al.*, 2002; Ferré *et al.*, 2005). The temperature dependent bulk magnetic susceptibility was measured on crushed chips (~140 g per measurement) from loose, *in-situ* blocks from outcrop 2 shear zone (undeformed host rock, Fig. 2.3b; highly sheared coherent lava, Fig. 2.3c; gouge, Fig. 2.3d). These were measured in an Agico MFK1-FA Kappabridge with CS4/CS-L high/low-temperature attachments to measure the change in magnetic susceptibility across the

temperature range of -200 to 700 ºC (using 4–5 repeats of each sample to verify the results). To complement the laboratory measurements a Bartington MS2 surface scanning probe to measure magnetic susceptibility was utilised on the lava dome to non-destructively measure the *in-situ* distribution of susceptibility, with each measurement taken over a 20 cm circular area. Our measurements were performed across two transects of the spine margin shear zone (Fig. 2.3a) and on a selection of loose dome blocks that were categorised as either undeformed or deformed. A Magnetic Measurements Variable Field Translation Balance (MMVFTB) was further utilised to measure the Isothermal Remanent Magnetisation (IRM), backfield, hysteresis and thermomagnetic signal to identify magnetic grains and their domain states. Here, 4 or 5 measurements were made from crushed powder (~100 g per measurement) of the host, high shear and gouge material. The MMVFTB dataset was analysed using the RockMagAnalyzer software by Leonhardt (2006).

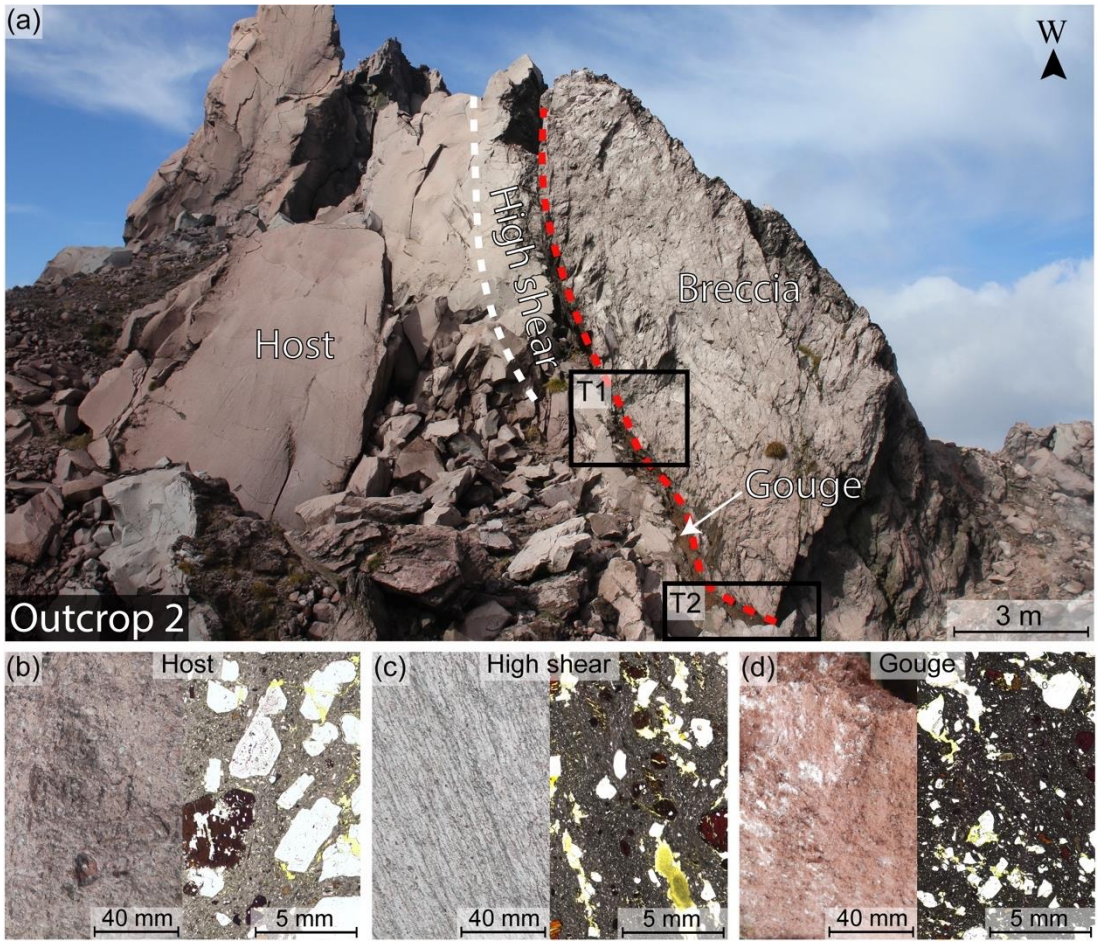


***Figure 2.3*** *– Photograph of outcrop 2 shear zone used for the investigation of magnetic properties of Unzen lava spine. (a) The shear zone is an end-on exposure of the eastern section of the spine, subdivided into four discrete units (host, high shear zone, gouge and breccia), as described by Hornby et al. (2015). The outlined areas (T1 and T2) are the locations of two*

*transects across the shear zone margin where field magnetic measurements were taken. In panels (b–d), the left-hand side is the outcrop surface and the right-hand side is the corresponding plane polarised light photomicrograph. (b) The host material represents an undeformed interior of the spine, akin to the low shear zone of outcrop 1. (c) High shear zone, consisting of elongated, white filaments similar to those observed in outcrop 1 and fragments of broken crystals. (d) A red, cataclastic gouge layer (~0.6 m wide) situated between the high shear zone and breccia, dominated by finely comminuted crystals.*

### 2.2.9. Experimental simulation

Experimental investigations on the co-existence of contrasting deformation textures in volcanic rocks (i.e., viscous, ductile and brittle) have primarily focused on the rheological implications associated with crystal interactions (e.g., Picard *et al.*, 2011). These experiments provide useful insights into magma behaviour under varying stress conditions in the volcanic conduit, which can influence bulk magma rheology. To explore the role of magma shearing within a volcanic conduit and assess materials' textural response to such a process, we experimentally recreated conduit margin processes using a high-temperature, high-velocity rotary shear (HVR) apparatus. The experiment was performed on a second-generation HVR at the University of Liverpool (see Hirose & Shimamoto, 2005 for details of the first-generation HVR) using the natural, undeformed dome rock (as seen in Fig. 2.2j) as the starting material. The experiments involved the preparation of two 24.98 mm diameter plane parallel cylindrical cores with a 9 mm hollow centre, designed to create a ~8 mm wide annulus that would minimise any variations in slip rate across the contact surface. The two cores were placed inside the experimental apparatus, each connected to a separate piston so that during the experimental run one core would remain stationary and the other would rotate. Before placing the cores in direct contact, they were enclosed within a furnace and heated to 600 ºC at a rate of 10 $^{o}C.min^{-1}$. This temperature was chosen for two reasons: 1) it represents a reasonable low-end temperature estimate of spine extrusion (with no recorded data available), which is also equivalent to temperatures estimated for the volcanic conduit at Mount St. Helens during faulting (Pallister *et al.*, 2013) and moreover, 2) it was below the solidus and $T_g$ thus any textural features observed could be directly related to shear and frictional heating and not the initial heating stage. After allowing ~30 minutes for thermal equilibration, a controlled axial load was applied and held constant using an air actuator on the non-rotating piston, corresponding to a normal stress of 2 MPa applied across the sample interface. The other piston and sample were rotated at 1150 rpm, equating to an equivalent slip rate of 1 m $s^{-1}$ in direct shear (for sample geometry, see Shimamoto & Tsutsumi, 1994; Hirose &

Shimamoto, 2005), analogous to conduit conditions previously estimated at Unzen volcano (Hornby *et al.*, 2015). The torque, axial load and sample shortening (using an externally-mounted strain-gauge with 10 mm scale) were measured for the duration of the experiment and used to calculate the continuous slip rate, normal stress and shear stress at 100 Hz. During the experimental run, the samples were recorded using a FLIR X6000sc infrared thermographic camera through a sapphire window of the furnace at a pixel resolution of 90 x 90 μm and 30 frames per second to monitor the temperature change due to frictional and shear heating along the simulated shear zone. It should be noted that these recorded temperatures only depict that of the sample surface and may slightly underestimate the slip zone's internal temperature.

## 2.3. RESULTS

### 2.3.1. Field observations

#### *2.3.1.1. Lava dome blocks*

Lava blocks on the talus and summit of Unzen lava dome are extremely heterogeneous (Fig. 2.1c). The characteristic differences of these blocks come most noticeably from their varying degrees of deformation, ranging from relatively undeformed (Fig. 2.1e and f) to complex deformation fabrics (i.e., sheared; Fig. 2.1g and h). All blocks display varying degrees of discolouration from pale grey to reddish-brown (Fig. 2.1c). Blocks that were classified as undeformed were distinguished by their massive nature (Fig. 2.1e), consisting of large, euhedral phenocrysts of plagioclase and amphibole, in addition to lacking any systematic textural anisotropy (Fig. 2.1f). Deformed or sheared blocks were characterised by the presence of at least one (but typically a combination) of the following: flow bands, systematic fractures (often conjugate), alignment of crystals or pores, and, in extreme cases, smeared plagioclase crystals visible to the naked eye (Fig. 2.1g and h). The porosity of these blocks is also quite variable, consistent to the porosity range of 8–33 % constrained for Unzen dome rocks (Kueppers *et al.*, 2005; Coats *et al.*, 2018), reiterating the heterogeneity of its deposits. The size of the blocks and proportion of sheared to undeformed material varies depending on the distance from the summit, which is observed succinctly on the western side of the dome (Fig. 2.1c). At the base of the talus, dome blocks are smallest (~1–2 m), more uniform in size and are typically undeformed. Further up the dome, blocks become larger (~2–4 m) with an increasing proportion of blocks hosting shear textures. The summit shows the most heterogeneity, exposing multiple shear zones, cataclastic structures and sintered breccia either as fallen slabs surrounding the spine or larger in-situ units (Fig. 2.1d).

*2.3.1.2. Lava spine shear zones*

Detailed structural surveys of the spine (Fig. 2.1d) in autumn 2013 and summer 2016 revealed an abundance of contemporaneous deformation fabrics at the margins including evidence for the co-existence of dilatational and compactional shear zones. Outcrop 1 shear zone (Fig. 2.2a) can be separated into four discrete zones based on lateral variations in the style and intensity of deformation:

- Gouge: A <0.2 m thick, well-consolidated gouge layer is agglutinated onto the outcrop's western limit. The gouge is matrix-supported (i.e., a groundmass to crystal ratio of ~60:40) and dominated by cataclastic deformation (Fig. 2.2b) including conjugate fractures, trails of broken grains, clusters of angular crystal fragments (e.g., plagioclase and amphibole) and a poorly sorted reddish matrix consisting of ostensibly sintered finer material (<2 mm). Rounded dacitic clasts up to 15 mm in diameter are incorporated into the gouge, distinguished by their pale-yellow groundmass and structural integrity (Fig. 2.2b).

- High shear zone: Directly adjoining the gouge, the high shear zone takes the form of a narrow (0.1–0.2 m wide) region comprised of undulated white-yellow porphyritic filaments/lenses surrounded by a reddish-brown groundmass that runs parallel to the gouge contact (Fig. 2.2c and d). Optically, these filaments appear to be partially filled with remnant fragments of broken crystals, commonly plagioclase, with any excavated fragments leaving behind elongated voids. These filaments were traceable on two sides of the outcrop (A–C and C–H in Fig. 2.2a), which revealed a planar orientation of NEE-SWW and provided a principle shear direction of NNW-SSE. These elongated filaments grade into a 0.5 m wide zone displaying principle and Riedel shear lineations on the outcrop's external surface (between sample D and E in Fig. 2.2a), indicative of the upwards sinistral motion of the spine. In this section of the high shear zone, crystal filaments become less clear and individual crystals are more visible (Fig. 2.2e). However, all crystals within the high shear zone take the form of broken, angular fragments that rarely exceed 1 mm and are often aligned in the extrusion direction (optical images in Fig. 2.2c–e), with no crystals remaining intact.

- Moderate shear zone: A ~2 m thick zone which displays a reduction in principle shear intensity and lacks secondary Riedel features (E and F in Fig. 2.2a). Cataclastic structures are less intense, although still a predominant appearance. Crystals are significantly more visible, representing larger fragments compared to those observed in the high shear zone (up to 2 mm), although they still display alignment in the

extrusion direction. Rare elongated mafic enclaves (top left of Fig. 2.2f) are also observed, which were not visible at outcrop scale in the high shear zone, likely owing to their extreme flattening and the overprint of principle shear lineations.

- Low shear zone: The moderate shear zone grades into a >1.5 m thick section consisting of negligible deformation. It has a smooth, reddish external surface and displays large (up to 5 mm), euhedral phenocrysts of plagioclase, amphibole and biotite, with little sign of fractured or aligned crystals. Mafic enclaves (up to 40 mm) are also present (Fig. 2.2h), being texturally similar to those in the moderate shear zone but more circular. This zone is comparable to the undeformed, non-spine dome rock, both at outcrop and thin section scale (Fig. 2.2j).

Outcrop 2 (Fig. 2.3a), previously described by Smith *et al.* (2001) and Hornby *et al.* (2015), has been divided into four separate units. A <0.6 m wide red gouge layer (Fig. 2.3d) is mantled by a poorly-sorted, >6m thick massive fault breccia (right in Fig. 2.3a). Lenses of highly sheared coherent lava are embedded into the gouge and elongated parallel to the gouge-breccia contact. A ~2 m wide high shear zone (Fig. 2.3a and c), texturally similar to that of outcrop 1 (Fig. 2.2c and d), lies to the left of the gouge, consisting of 20–40 mm elongated white filaments within a reddish-grey groundmass. Adjacent to this highly sheared region, a >8 m thick, relatively undeformed unit represents the core of the lava spine (termed host in Fig. 2.3a). Although here the dacite consists of large euhedral phenocrysts (up to 5 mm; Fig. 2.3b), with textures similar to those observed in the low shear zone of outcrop 1 (Fig. 2.2i), occasional high-porosity shear bands that extend up to 2 m in length run sub-parallel to the spine margin (see Smith *et al.*, 2001).

### 2.3.2. Bulk chemical heterogeneities

Bulk-rock chemistry of the lava spine reveals a dacitic composition (65.4–65.9 wt % $SiO_2$) with only subtle variations across the shear zone that are close to the analytical limit. Yet, it may be possible to distinguish each zone in Figure 2.2a (gouge, high, moderate and low shear) from individual major and trace elements (Table 2.1). For major components, the gouge has the lowest concentration of $SiO_2$ and $Na_2O$, and highest $Fe_2O_3$ and MgO contents; directly in contact, the high shear zone has the highest $SiO_2$ and $K_2O$. The low shear zone has the highest CaO and $Na_2O$, together with the lowest $Fe_2O_3$, MgO and $K_2O$. The moderate shear zone falls compositionally intermediate between these zones. Trace elements may reflect further variations between each zone. For example, the gouge reveals highest levels of Rb and Zr, with the low shear zone having the least. The high shear zone can be distinguished by the

lowest Sr content and highest La and Ce, while the low shear zone can be identified by the highest Sr.

***Table 2.1*** *– Whole-rock chemical analyses of major and trace elements from outcrop 1 shear zone*

| **Sample:** | **A** | **C** | **E** | **H** |
|---|---|---|---|---|
| **Rock type:** | Lava spine | Lava spine | Lava spine | Lava spine |
| **Zone:** | Gouge | High shear | Moderate shear | Low shear |
| *(wt.%)* | | | | |
| **$SiO_2$** | 65.41 | 65.88 | 65.71 | 65.55 |
| **$TiO_2$** | 0.70 | 0.66 | 0.62 | 0.62 |
| **$Al_2O_3$** | 15.49 | 15.34 | 15.30 | 15.58 |
| **$Fe_2O_3$*** | 5.04 | 4.87 | 4.74 | 4.68 |
| **MnO** | 0.10 | 0.10 | 0.10 | 0.10 |
| **MgO** | 2.45 | 2.40 | 2.38 | 2.29 |
| **CaO** | 4.50 | 4.51 | 4.61 | 4.61 |
| **$Na_2O$** | 3.57 | 3.58 | 3.61 | 3.65 |
| **$K_2O$** | 2.52 | 2.56 | 2.49 | 2.47 |
| **$P_2O_5$** | 0.06 | 0.10 | 0.09 | 0.09 |
| **LOI** | 0.17 | 0.11 | 0.18 | 0.26 |
| **Total** | 100.01 | 100.11 | 99.83 | 99.90 |
| *(ppm)* | | | | |
| **Ba** | 498.06 | 480.96 | 464.98 | 477.13 |
| **Ce** | 23.41 | 51.93 | 38.11 | 43.00 |
| **Cu** | 20.75 | 20.57 | 28.52 | 21.55 |
| **La** | 20.93 | 25.47 | 21.32 | 22.20 |
| **Nb** | 13.85 | 13.53 | 13.67 | 13.38 |
| **Rb** | 86.88 | 84.63 | 83.50 | 82.06 |
| **Sc** | 11.43 | 13.38 | 12.31 | 10.99 |
| **Sr** | 289.38 | 286.58 | 293.35 | 304.13 |
| **V** | 80.73 | 86.91 | 87.58 | 91.18 |
| **Y** | 16.47 | 17.32 | 18.38 | 17.12 |
| **Zn** | 48.81 | 45.59 | 47.42 | 45.98 |
| **Zr** | 152.47 | 144.15 | 145.65 | 140.29 |

*Major and trace elements measured by XRF.*

** Total Fe as $Fe_2O_3$.*

### 2.3.3. Mineralogy and petrography

The dacitic spine is porphyritic, consisting of phenocrysts and microphenocrysts (27–29 area %) of plagioclase (17–21 area %), amphibole (3.5–6.0 area %), biotite (2 area %) and quartz (1.5–3.5 area %). The groundmass contains 50–60 area % microlites of plagioclase, pargasitic amphibole, polymorphs of silica, pyroxene, Fe-Ti oxides and minor accessory minerals, set in a partially devitrified, peraluminous rhyolitic interstitial glass (ca. 79 wt % $SiO_2$). Plagioclase dominates the mineral assemblage, occurring as phenocrysts up to 5 mm long, tabular and equant microlites in the groundmass, mineral inclusions within hornblende phenocrysts, and as a breakdown product of hydrous mineral phases (i.e., amphibole and biotite). Two types of amphibole are found in the dacite; hornblende as phenocrysts and pargasite as microphenocrysts and microlites in the groundmass. The hornblendes occasionally display reaction rims, often patchy, consisting of pyroxene, plagioclase and Fe-

Ti oxide microlites. Pargasite forms ellipsoidal crystals with occasional hollow cores and/or concentric zoning. Pargasites located in the spine shear zone display breakdown rims, which have not been reported in any other Unzen lava products from the eruption (e.g., Sato *et al.*, 1999). Biotite takes the form of large, tabular phenocrysts, often with distinct coarse-grained reaction rims of pargasite, plagioclase and pyroxene. Reaction rims on both hornblende and biotite phenocrysts are not exclusive to the spine and were also observed in pyroclastic flow deposits throughout the eruption (Nakada & Motomura, 1999), thus are not attributed to spine processes. Quartz often appears as resorbed fragmented phenocrysts (up to 2 mm) embedded within the groundmass (e.g., bottom left of photomicrograph in Fig. 2.2f). Fe-Ti oxides (magnetite and ilmenite) appear as rare microphenocrysts and small acicular microlites in the groundmass. Orthopyroxene and clinopyroxene are found either as groundmass microlites or within breakdown rims of biotite and amphibole. All samples reveal silica-rich patches in the groundmass, either filling voids or as a by-product of glass devitrification.

Variations in mineral abundance across the shear zone were assessed by QEMSCAN analysis. The resulting data are expressed as colour-coded maps, providing a visual distribution of chemically discrete phases (Fig. 2.4 and Fig. 2.5) and through isolating each phase a quantitative comparison can be made across the shear zone (Table 2.2). All samples consist of the same mineral assemblage, although subtle differences in both bulk (phenocrysts plus groundmass phases, Fig. 2.4) and groundmass phases (Fig. 2.5) are observed. Bulk plagioclase content is highest in the low shear zone (40.2 area %), with a systematic decrease in the moderate and high shear zone (37.2 and 34.4 area %, respectively), increasing slightly in the gouge (37.7 area %). Amphibole displays a similar pattern, although to a lesser extent owing to its lower abundance. Bulk biotite and pure silica-phases show an opposite trend, both being lowest in the low shear zone and highest in the gouge. Total bulk glass content shows a subtle increase from the low shear zone to high shear zone (32.0–36.3 area %), with the gouge having significantly less glass than anywhere else in the outcrop (24.6 area %). However, it is important to note that these observed bulk mineralogical variations should be taken with some caution, owing to the natural heterogeneity of Unzen lava, plus the possible effect of highly fractured minerals being removed during sampling or thin section preparation of highly deformed material. This is observed by comparing field textures and photomicrographs of the high shear zone (Fig. 2.2c and d), which show the potential loss of plagioclase evacuating elongated voids.

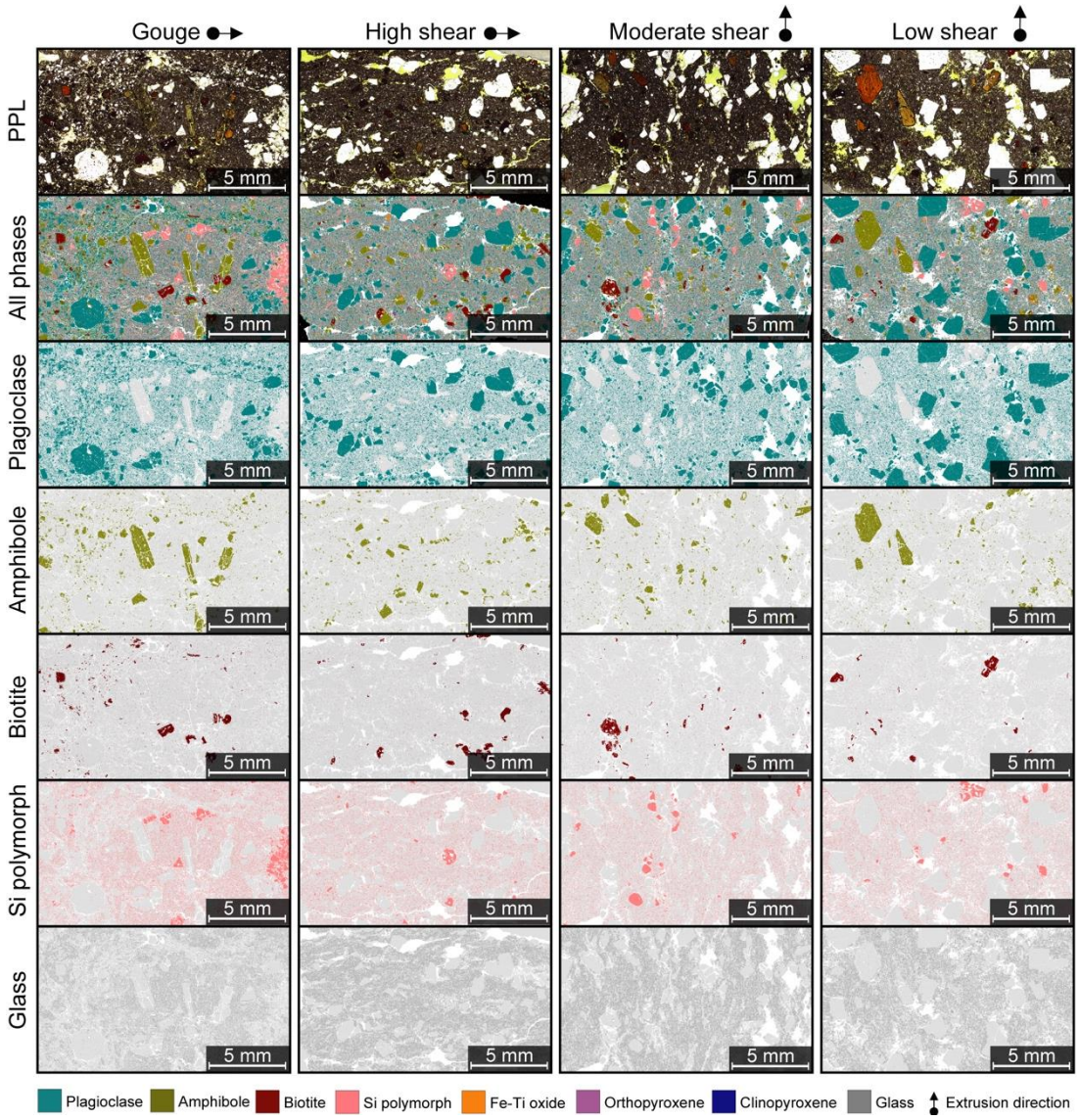


***Figure 2.4*** *– QEMSCAN mineral distribution maps of the gouge, high shear, moderate shear and low shear zones from outcrop 1. Top row panels are whole thin section scans taken in plane polarised light (PPL), followed by QEMSCAN maps with all phases highlighted and each colour representing a different mineral or glass phase (pore space in white). The bottom five rows are maps of individual phases isolated providing a clearer assessment of the variations across the shear zone and allowing a quantitative comparison of their modality (see Table 2.2). Arrows denote the extrusion direction. Note: Si polymorphs represent all* $SiO_2$ *phases, including quartz phenocrysts and groundmass silica phases.*

Within the groundmass (Fig. 2.5), similar quantities of plagioclase microlites are observed in both the low and high shear zones (27.3 and 28.5 area %, respectively). Plagioclase abundance in the gouge groundmass is higher relative to the other zones (33.1 area %), which also corresponds to the presence of angular plagioclase fragments as remnants of phenocryst comminution. Groundmass amphibole (pargasite) also has minimal variation between the low and high shear zone (3.9 and 3.2 area %, respectively), although the gouge displays a subtle increase (4.9 area %). Pyroxene microlites have a similar abundance across the shear zone (all <2 area % for combined ortho- and clinopyroxene). The most significant difference is observed within the Si polymorphs (Fig. 2.5). The low and high shear zones have a similar textural arrangement of large, isolated silica-patches (up to 50 μm) with a minor variation in abundance between them (17.0 and 14.8 area %, respectively). In the gouge, these larger silica-patches are absent, with the groundmass being dominated with small (<10 μm), more abundant (21.4 area %) silica-rich phases that are interconnected with the interstitial glass. These micron-sized silica-patches in the gouge correspond to its lower interstitial glass content (Table 2.2).

***Table 2.2*** *– Bulk mineralogy and groundmass phase abundance of outcrop 1 derived from QEMSCAN*

| **Sample:** | | **A** | | **C** | | **E** | **H** | |
|---|---|---|---|---|---|---|---|---|
| **Rock type:** | | Lava spine | | Lava spine | | Lava spine | Lava spine | |
| **Zone:** | | Gouge | | High shear | | Moderate shear | Low shear | |
| | | Bulk | G.mass | Bulk | G.mass | Bulk | Bulk | G.mass |
| **Phases (area % of solid fraction)** | **Plagioclase** | 37.7 | 33.1 | 34.4 | 28.5 | 37.2 | 40.2 | 27.2 |
| | **Amphibole** | 9.3 | 4.9 | 6.6 | 3.2 | 6.8 | 7.7 | 3.9 |
| | **Biotite** | 3.3 | 1.2 | 2.7 | 0.7 | 2.5 | 1.9 | 0.9 |
| | **Si polymorph*** | 18.4 | 21.4 | 14.1 | 14.8 | 12.3 | 12.1 | 17.0 |
| | **Orthopyroxene** | 1.1 | 1.3 | 1.1 | 1.3 | 0.9 | 0.9 | 1.5 |
| | **Clinopyroxene** | 0.8 | 0.6 | 0.7 | 0.3 | 0.7 | 0.8 | 0.3 |
| | **Fe-Ti oxide** | 0.7 | 0.4 | 0.7 | 0.4 | 0.7 | 0.7 | 0.5 |
| | **Apatite** | 0.1 | 0.0 | 0.1 | 0.1 | 0.2 | 0.2 | 0.2 |
| | **Interstitial glass$** | 24.6 | 33.5 | 36.3 | 47.7 | 35.2 | 32.0 | 45.6 |
| | **Boundary phases#** | 4.0 | 3.6 | 3.3 | 3.0 | 3.5 | 3.5 | 2.9 |
| | **Total** | 100.0 | 100.0 | 100.0 | 100.0 | 100.0 | 100.0 | 100.0 |
| **Porosity (area %)** | | 16.1 | 19.2 | 13.2 | 13.0 | 19.0 | 22.4 | 18.7 |

*All mineral phases and glass abundances are normalised on a pore-free basis.*

** combines all $SiO_2$ polymorphs (including quartz and cristobalite).*

*$ includes any partially devitrified glass and associated groundmass $SiO_2$ phases smaller than the beams interaction volume (~10 $\mu m^3$).*

*# denotes when the beam interacts at the boundary between 2 or more phases.*

The porous network of the shear zone shows significant heterogeneities (Fig. 2.4, Fig. 2.5 and Table 2.2). The 2D bulk porosity, visualised and quantified for each section of the shear zone by QEMSCAN (white in Fig. 2.4), is highest in the low shear zone (22.4 area %), slightly reduced in the moderate shear zone (19.0 area %) and lowest in the high shear zone (13.2 area %). Interestingly, the porosity of the gouge (16.1 area %) is higher than the high shear zone but less porous than the low shear zone. The pores in the moderate and high shear zones are found as elongated voids, typically localised around fractured plagioclase phenocrysts, and less commonly amphiboles; this coincides with the relative decrease in plagioclase and amphibole in these zones (Fig. 2.4 and Table 2.2). By incorporating these porosity values with the bulk mineralogy abundances (i.e., combined and normalised to 100 area %), the decrease in plagioclase and amphibole abundance from the low shear to high shear zone is significantly lower. Groundmass porosity also shows a similar reduction from the low shear to high shear zone (Fig. 2.5 and Table 2.2). In the low shear zone, pores are >10 μm in diameter and are commonly connected to form a permeable porous network, equating to a porosity of 18.7 area %. Pores in the high shear zone groundmass are significantly lower in both abundance (13.0 area %) and size (mostly <10 μm diameter), with the majority of pores being unconnected. The gouge groundmass porosity is slightly higher than low shear zone (19.2 area %), being derived from a combination of small (<5 μm diameter) isolated pores and localised microfractures located between broken plagioclase fragments (Fig. 2.5).

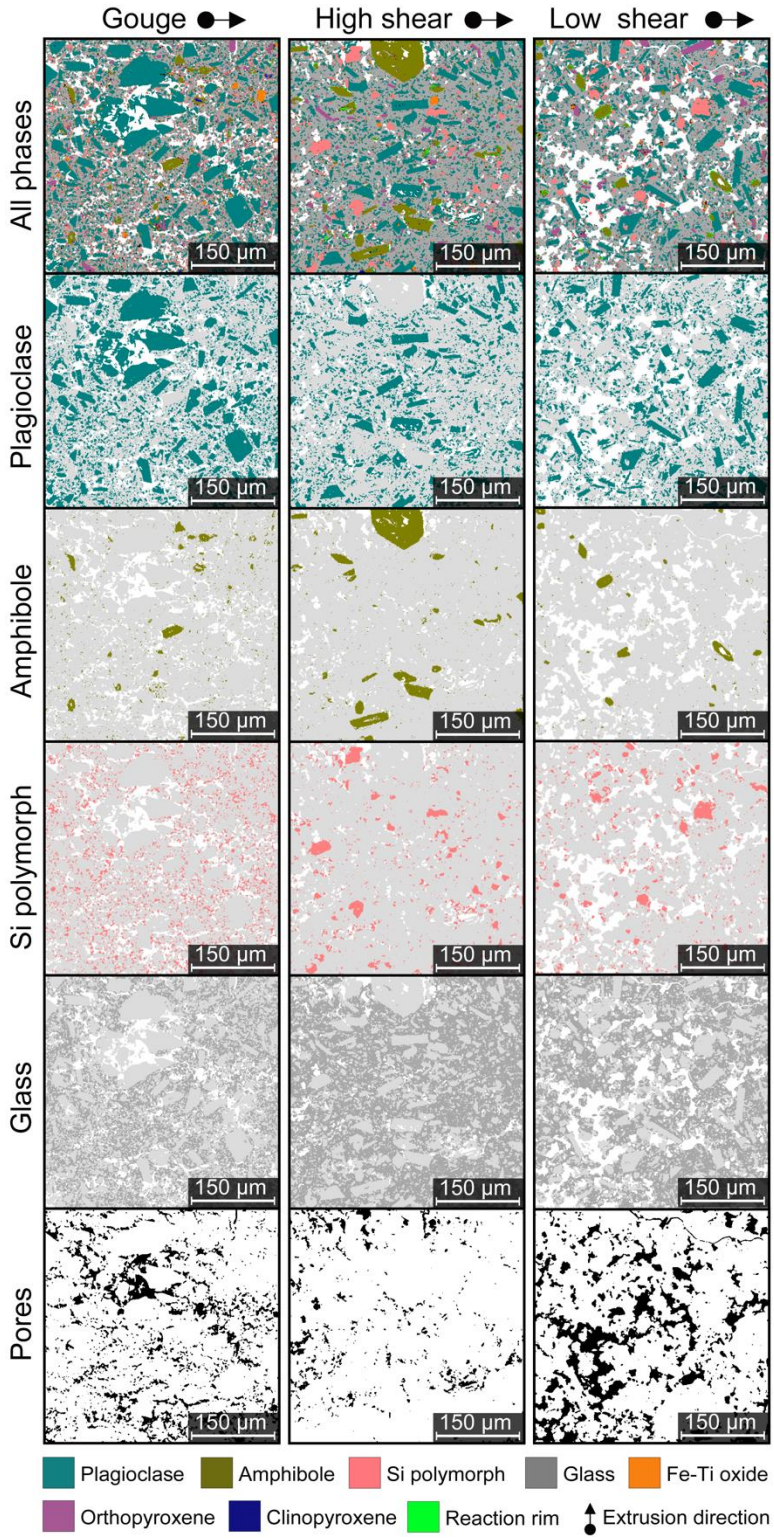


***Figure 2.5*** *– Groundmass mineralogy, glass and porosity textures of the gouge, high shear and low shear zones using QEMSCAN. Plagioclase microlites are equant and tabular; they are randomly orientated in the low shear zone and preferentially aligned in the extrusion direction in the high shear zone, while the gouge consists of angular fragments derived from broken phenocrysts. Groundmass amphibole (pargasite) is present in all three zones as*

*ellipsoidal microlites, with occasional hollow cores. Si polymorphs in the groundmass of the low shear and high shear zone are discrete, isolated crystals often filling or surround pores, while in the gouge these are smaller and localised within the interstitial glass. These inherent differences are reflected in the glass variation, with the gouge being glass-poor relative to the high and low shear zones. Pores in the low shear zone are abundant and irregular shaped, often connected to form a permeable pathway, whereas the high shear pores are smaller, less abundant and typically isolated with no connectivity. The pores within the gouge sit intermediate between the low and high shear zone.*

### 2.3.4. Crystal deformation

#### *2.3.4.1. Banding, alignment and crystal failure*

Crystal deformation is a dominant feature of the spine due to crystals' ability to record textures during transport and bulk viscous flow of the magma. Crystal alignment in the high shear zone is a characteristic feature seen most notably by the preferential orientation of plagioclase microphenocrysts and microlites with their major axis aligned parallel to extrusion direction, in addition to larger crystals displaying pressure shadows (labelled PS in Fig. 2.6a). These aligned microlites appear to be localised within flow bands that envelope larger phenocryst fragments. In the moderate shear zone (Fig. 2.6b), crystal alignment is still present, although subtle, with no evidence of banding or pressure shadows, whereas the low shear zone comprises of freely suspended and randomly oriented crystals (Fig. 2.6c).

In order to investigate crystal deformation due to shearing, we focus on plagioclase owing to its high abundance and previously reported high sensitivity to stress (e.g., Cordonnier *et al.*, 2009; Picard *et al.*, 2011). The change in size and shape of plagioclase phenocrysts were investigated using thin section scans and binary maps (Fig. 2.7a; see Electronic Appendix 1.1 for full quantitative data). Results show a reduction in crystal size with increasing shear (Fig. 2.7b), which can be qualitatively seen in the binary phase maps (Fig. 2.7a), with the low shear zone hosting larger, more euhedral crystals which systemically become more fractured towards the shear zone margin. Average plagioclase circularity measurements of samples from the low and moderate shear zone oscillate between 0.48–0.58. Circularity values for plagioclase crystals in sample C and D of the high shear zone (Fig. 2.7c) show a slight decrease in circularity compared to crystals within the moderate shear zone (sample E in Fig. 2.7c), although they still fall within the range recorded in the low shear zone. Where the high shear zone is directly adjacent the gouge (sample B in Fig. 2.7c) plagioclase crystals have the lowest circularity values (mean 0.44), with the gouge displaying an abrupt increase (mean 0.56), which corresponds to the sharp boundary as observed at outcrop scale (Fig. 2.2a).

Qualitatively, amphibole (the second most abundant phenocryst phase) reveals a similar reduction in size across the shear zone (Fig. 2. 4 and 2.7a).

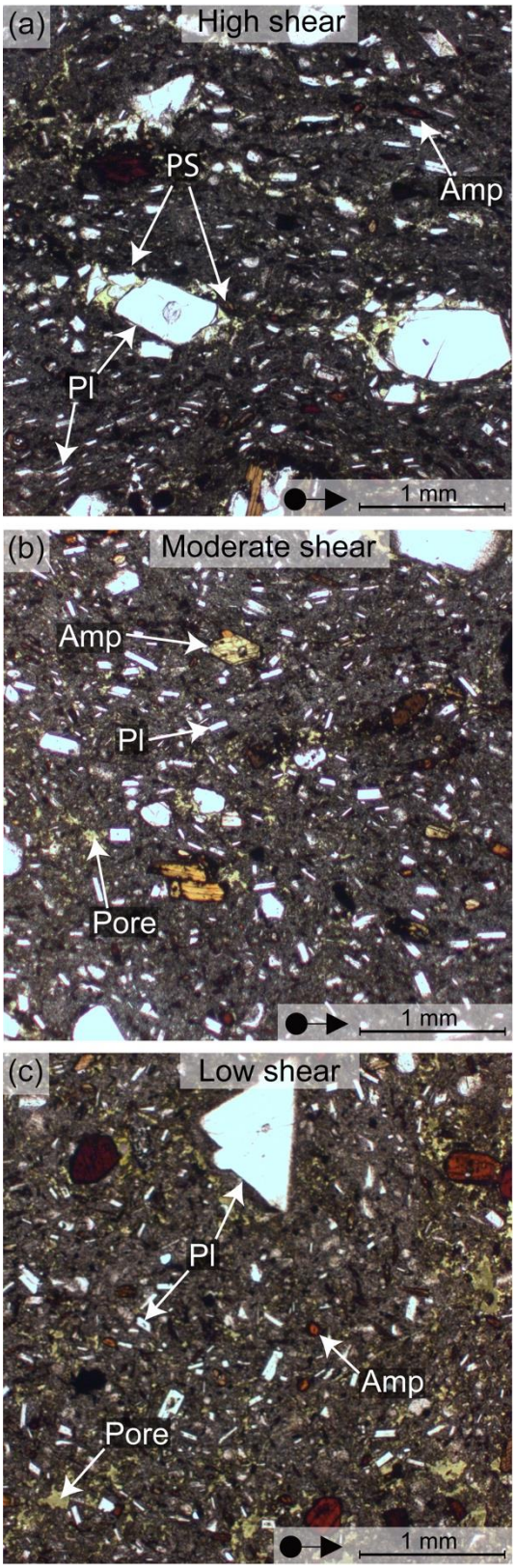


***Figure 2.6*** *– Photomicrographs in plane polarised light of comparative groundmass flow textures from high, moderate and low shear zones. (a) Tabular microlites and microphenocrysts of plagioclase (Pl) and amphibole (Amp) in the high shear zone have a strong preferential alignment in the extrusion direction, localising as flow bands that envelope larger crystal fragments resulting in pressure shadows (PS) at the tips of the crystal fragments. (b) The moderate shear zone has only minor alignment of tabular crystals, while the low shear zone (c) displays a random orientation of tabular crystals. Pores (yellow-green dye) are also systematically smaller in size and lower in abundance from the low shear to high shear zone.*

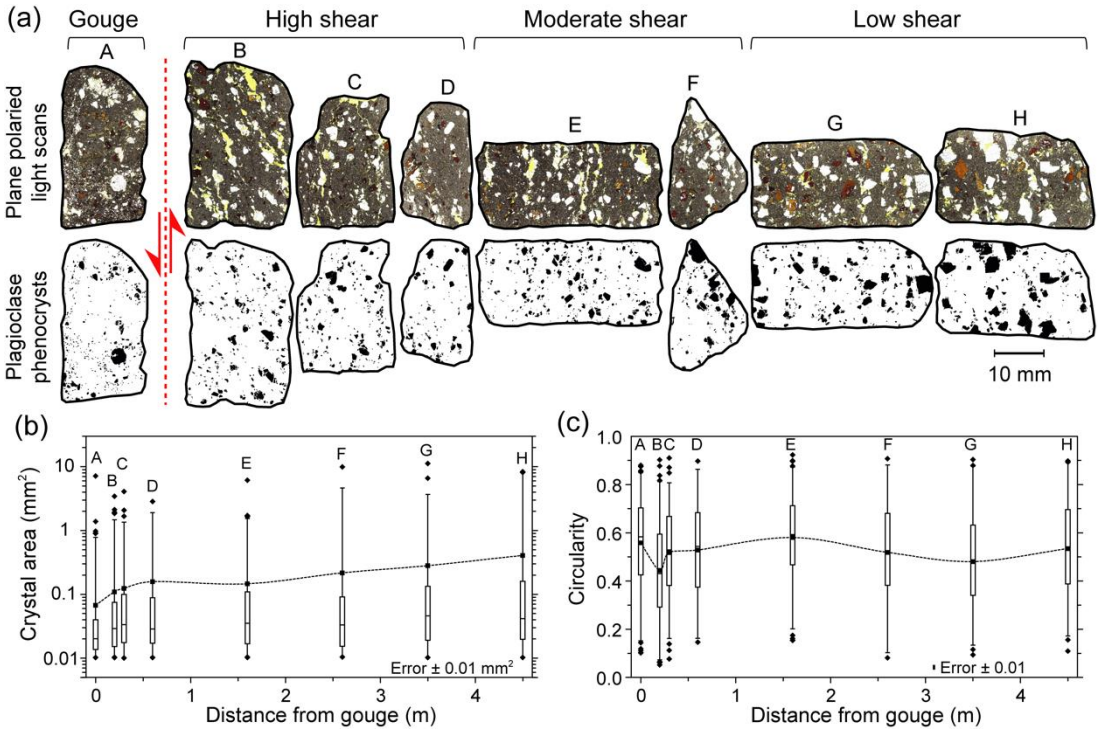


***Figure 2.7*** *– Crystal size and shape distribution of plagioclase phenocrysts across the shear zone. (a) Plane polarised light thin section scans of each sample (A–H) across the shear zone and binary images of plagioclase phenocrysts (>0.01 mm$^2$) used for quantification. Each sample represents between 150–550 crystals depending on the number of phenocrysts present. Plagioclase phenocrysts size variation (b) and circularity variation (c) are shown with distance from the gouge. Both box plots show 25$^{th}$ and 75$^{th}$ percentile, the median value and whiskers outlining the 1–99% range. Diamonds represent outliers within the dataset and squares are the mean value per sample connected by the dashed line. Errors were calculated from repeat thresholding of the crystals and re-analysis.*

### *2.3.4.2. Biotite and plagioclase lattice distortion*

EBSD was performed on both phenocryst and microlite phases across the shear zone. Crystal plasticity is the distortion of a crystal's lattice owing to its rotation brought about by the movement and accumulation of dislocations, which is quantified as a misorientation (Brewer *et al.*, 2006); the higher the misorientation value, the more distorted the crystal lattice. The variation in misorientation within a single crystal can be seen using colour-coded, texture component maps with the colours representing the relative distortion, or misorientation, of the crystal lattice with respect to a selected reference pixel. Misorientation maps on broken segments of a once intact plagioclase phenocryst from the gouge (segment 1–3 in Fig. 2.8a) reveal negligible plastic deformation, with all segments rarely exceeding a 1$^o$ misorientation despite being fragmental. However, analysis of biotite phenocrysts reveals an overwhelming

abundance of plastic deformation. This is a common feature in the high shear zone and gouge, where up to 60° of relative lattice distortion is observed (Fig. 2.8b). In some cases, biotite crystals have exceeded their plastic limit, causing the crystal to fracture in the areas of most lattice distortion (Fig. 2.8b). In the high shear zone, biotite plasticity is proceeded by brittle failure along shear bands, with plasticity remaining in the intact segments (Fig. 2.8c). Biotite plasticity is less common in the moderate shear zone, and not observed in the low shear zone or core of the spine.

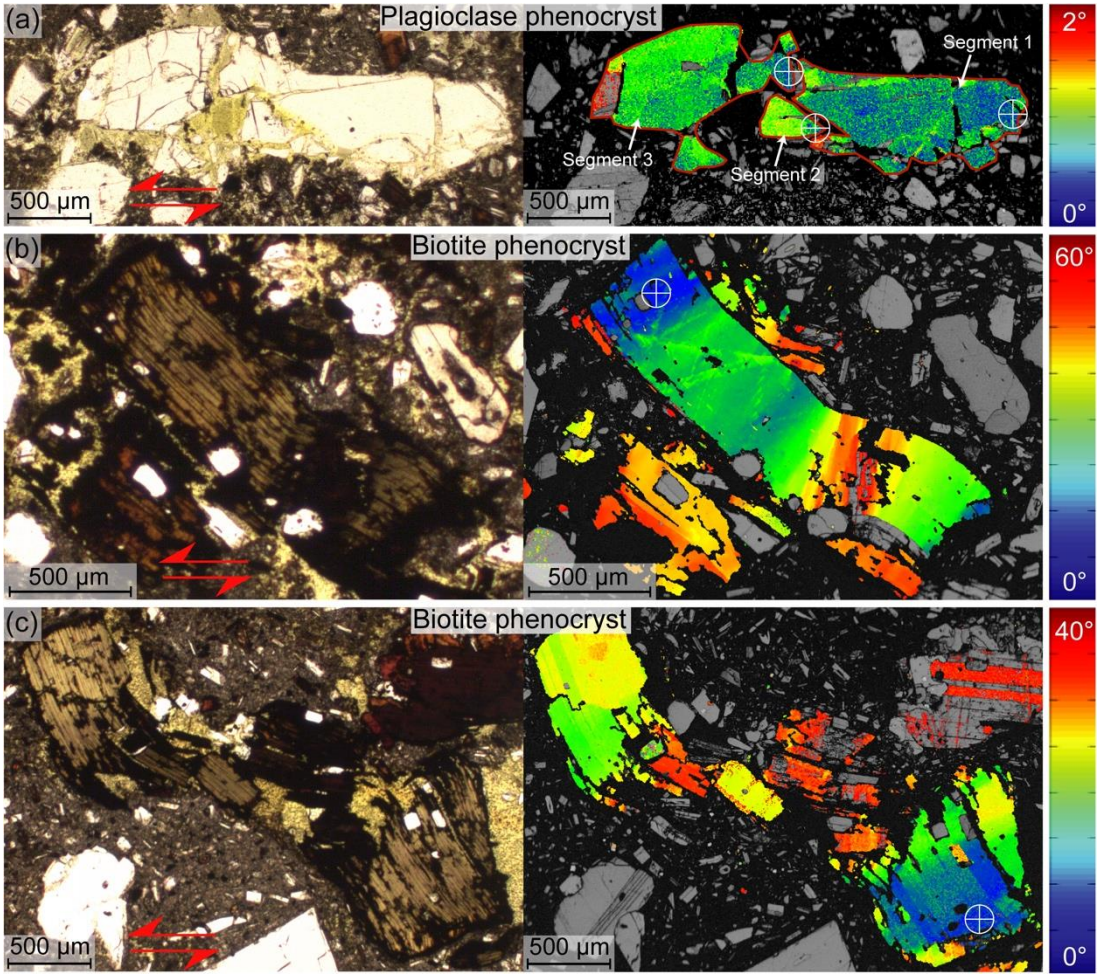


***Figure 2.8*** *– Plastic deformation of plagioclase and biotite phenocrysts measured by electron backscatter diffraction (EBSD). For each panel (a–c), the left-hand side shows a plane polarised light photomicrograph of the crystal analysed and on the right-hand side is the corresponding band-contrast misorientation map overlain by a texture component map. Colours represent the amount of misorientation relative to a selected point along the crystal, with an angular resolution of ± 0.5º. All reference points were chosen at one end of the crystal in order to observe the maximum misorientation along the crystal's major axis and are labelled in (a–c) with a white circle and cross. (a) Three fractured segments of a single plagioclase phenocryst from the gouge (Fig. 2.2b) displaying negligible internal deformation*

*across each. Unlike plagioclase, biotite phenocrysts display extensive plastic deformation throughout the high shear zone. (b) A plastically deformed biotite crystal from the high shear zone (Fig. 2.2d), revealing a partial tear upon reaching its plastic limit in areas of highest lattice distortion. (c) A biotite phenocryst that deformed plastically in the high shear zone (Fig. 2.2d), producing an S-C style fabric and rupture along a shear band parallel to the extrusion direction, forming fragments with variable plasticity.*

In contrast to plagioclase phenocrysts, plastic deformation of plagioclase microlites within the spine shear zone is evident (Fig. 2.9a). The advantage of studying microlites is that it provides a statistically robust dataset and any potential data bias due to internal heterogeneities within a single thin section can be removed by analysing multiple areas within the same sample. Accurately quantifying the degree of lattice distortion in plagioclase microlites involved manually drawing misorientation transects from one end of each crystal to the other (T1 and T2 in Fig. 2.9a). Through compiling the maximum misorientation angles from microlites within each section of the shear zone (Electronic Appendix 1.2), lateral differences were identified. The unimodal distributions of lattice misorientations (Fig. 2.9b) show a shift towards higher angles from low to high shear zone and gouge. The low and moderate shear zones show that most microlites have <2º misorientation. The high shear zone and gouge reveal a broader microlite misorientation distribution with lattice distortions of >9º. Through calculating the misorientation per micron for each microlite (after Kendrick *et al.*, 2017) we can remove any bias that would be caused by comparing microlites of different lengths (Fig. 2.9c). We find that the mean and maximum misorientation per micron increases systematically from the low to high shear zone, with the gouge being slightly lower than the high shear zone. Using the mean misorientation per micron for each section of the shear zone (squares in Fig. 2.9c) and multiplying these by an infinite crystal length, we can provide a modelled estimation for the degree of lattice distortion for a given crystal length (line gradients in Fig. 2.9d). These modelled misorientation estimates reveal that microlites of the same length from each section of the shear zone, are more likely to display a higher degree of plasticity in the gouge and higher shear zone (Fig. 2.9d). EBSD analysis on the undeformed, non-spine dome rock (Fig. 2.2j) shows that microlites exhibit the lowest misorientation values (Fig. 2.9d) and are comparable to those located in the low shear zone of the spine.

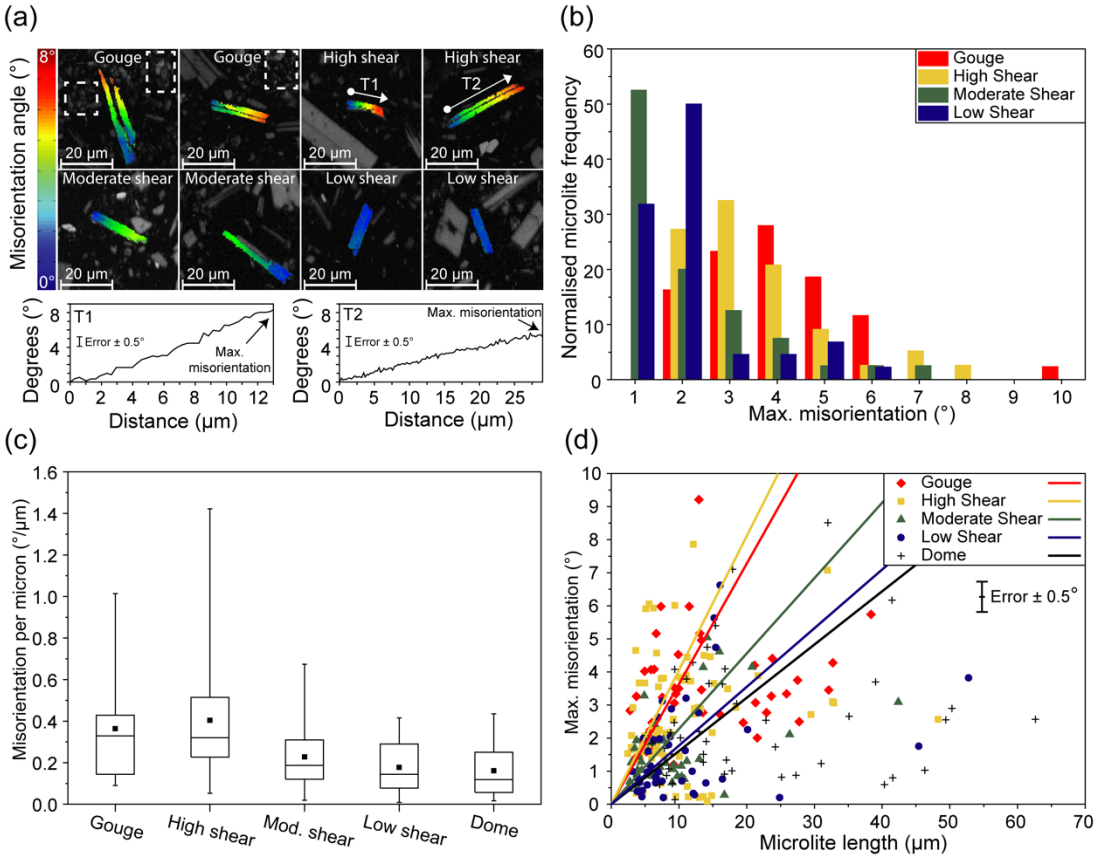


***Figure 2.9*** *– Plastic deformation of plagioclase microlites across the shear zone. (a) Greyscale band contrast maps with plagioclase microlites subjected to a texture component analysis. The colour gradient displays the relative misorientation across a single microlite grain, thresholding to display up to 8º lattice distortion, and visualised by drawing misorientation transects along the crystal's axis from blue to red (T1 and T2). All misorientation angles have a resolution error of ±0.5º. The dashed outlined areas in the gouge indicate crystalline silica phases owing to glass alteration. (b) Normalised frequency histogram of crystal plastic distortion from each section of the shear zone, binned every 1º misorientation. (c) Box plot of the intensity of plastic deformation represented by the misorientation per micron. The box highlights the 25$^{th}$ and 75$^{th}$ percentiles (the bottom and top of the boxes, respectively) and the whiskers show the data range. The horizontal line in the box marks the median value and the square represents the mean for each section of the shear zone. (d) Maximum misorientation within a single plagioclase microlite versus its length. The gradients of the lines represent the modelled degree of crystal lattice distortion for a given crystal length in each section of the shear zone. These misorientation gradients were modelled by multiplying the mean misorientation per micron, as shown in (c), by an infinite crystal length. Plagioclase microlites in the undeformed dome block were also analysed for comparison.*

### 2.3.5. Magnetic signatures

A portable magnetic susceptibility meter was utilised on the lava dome to non-destructively measure the *in-situ* distribution of susceptibility across two transects of the spine margin shear zone at outcrop 2 (Fig. 2.3a, Fig. 2.10a and 2.10b) and to measure a selection of loose dome blocks. The field measurements showed magnetic susceptibility values on the spine range between 0.27–7.21 $x10^{-4}$ (SI) from more than 200 measurements, with the highest values seen in the undeformed spine host material and lowest values in the high shear zone and gouge (Fig. 2.10a and b). Field magnetic susceptibility measurements on loose blocks on the dome, categorised as undeformed and deformed, showed values in close agreement (Figure 2.10c; mean 3.14 and 5.85 $x10^{-4}$ SI [range 1.29–6.53 and 3.04–10.05], respectively). Moreover, magnetic susceptibility measured in the laboratory using a Magnetic Measurements Ltd Variable Field Translation Balance (VFTB) on samples from the undeformed host rock, high shear zone, and gouge (Fig. 2.3b–d), also match closely (Figure 2.10c; Table 2.3). The bulk susceptibility, measured in an Agico MFK1-FA Kappabridge, also showed a similar relationship, where the undeformed host has the highest susceptibility, with the high shear zone having a slightly lower bulk susceptibility and gouge the lowest. The temperature-dependence of the bulk susceptibility was also distinct between each zone (Fig. 2.10d). The host rock produced sharply dropping reversible curves indicative of a single, low coercivity phase of low-Ti titanomagnetite; in contrast, the high shear and, especially, the gouge produced less reversible curves with shallower, less abrupt drops at high-temperature that suggests an alteration of the magnetic carrier (Fig. 2.10d).

The VFTB data were analysed using the RockMagAnalyzer software (Leonhardt, 2006), from which Curie temperatures ($T_C$; Table 2.3) were identified from the thermomagnetic curves (see Fig. A1.2 for curves) using the method of Moskowitz (1981). For each sample set, only one Curie temperature was identified, and these correspond well to the terminal decrease of bulk susceptibility (Fig. 2.10d), being 521 ºC in the undeformed host, 507 ºC in the highly sheared rock and 544 ºC in the gouge.

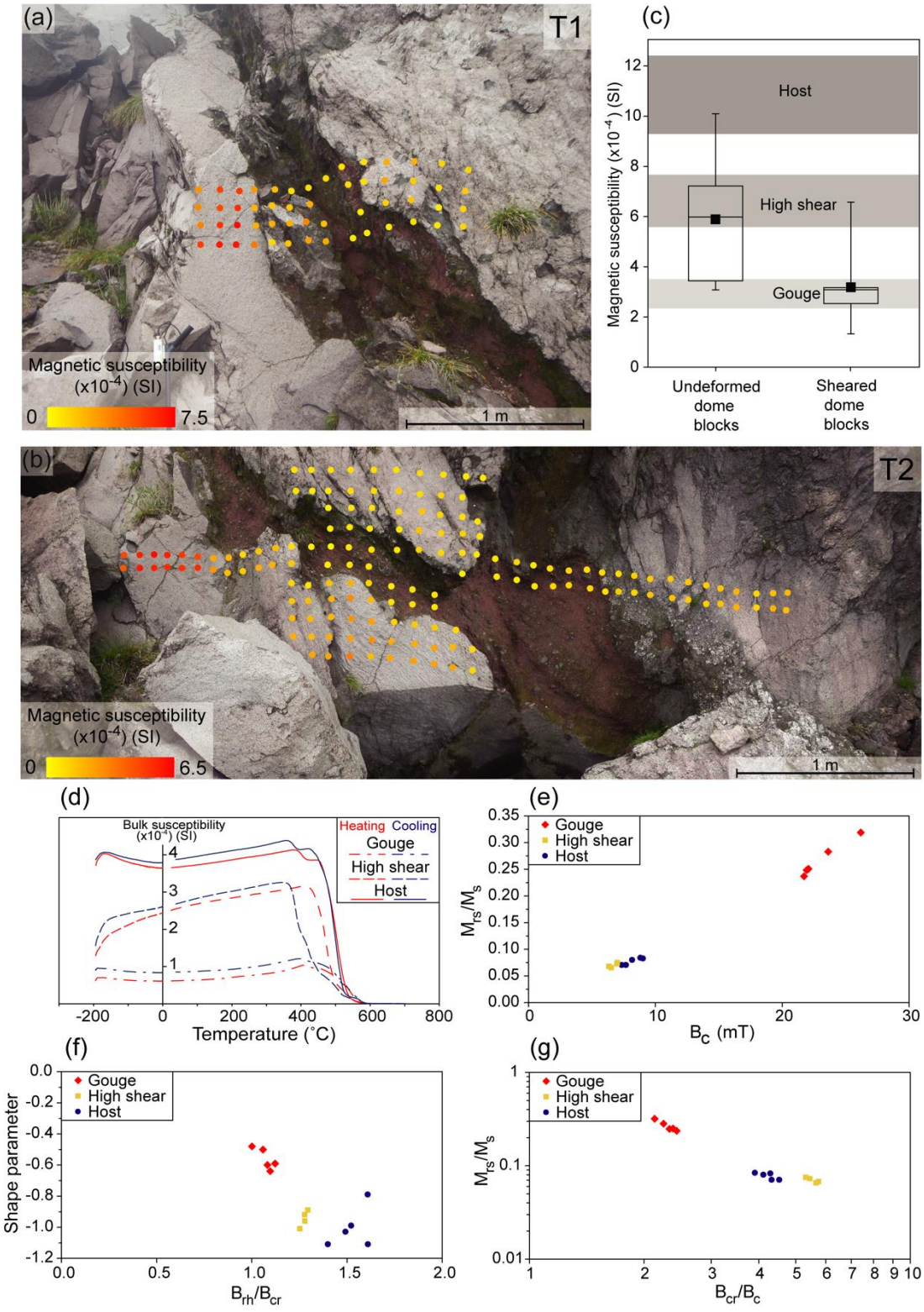


***Figure 2.10*** *– Field and laboratory magnetic susceptibility measurements. (a, b) Magnetic susceptibility across two different transects of the spine margin at outcrop 2 (T1 and T2 in Fig. 2.3a), measured using a Bartington portable magnetic susceptibility meter. The undeformed host rock (left in both panels) has the highest susceptibility, gradually decreasing through the highly sheared area to the lowest values in the red gouge layer and finally slightly*

*higher values in the fault breccia on the right of the gouge. (c) Box plot of field magnetic susceptibility measurements of pristine (undeformed) and sheared (deformed) loose dome rocks, which show values that are comparable to transects in (a) and (b). These are compared to laboratory magnetic susceptibility measurements (marked grey zones; measured using a VFTB) on the host rock, highly sheared coherent lava and gouge. (d) Temperature-dependent bulk susceptibility during heating and cooling cycles (measured using a Kappabridge) for the three rock types. Susceptibility is highest in the host, intermediate in the highly sheared zone and lowest in the gouge, and the magnetomineralogy and stability are distinguishable. (e) Comparison of the ratio of saturation remanence and saturation magnetisation ($M_{rs}/M_s$) to the coercive force ($B_c$), showing that the gouge has significantly different remanence carriers. (f) Day plot combining hysteresis and backfield data showing each section of the shear zone has discrete differences. (g) $M_{rs}/M_s$ against the coercivity ratio ($B_{rh}/B_{cr}$) reinforces the disparate evolution of the high shear and gouge from the host lava.*

Isothermal Remanent Magnetisation (IRM) and backfield curves show each zone almost fully saturates at 200 to 300 mT (see Fig. A1.3 and A1.4 for raw data). Quantitatively, the S300 parameter, a measure of the degree of saturation at 300 mT (Bloemendal *et al.*, 1992), records subtle differences between the host, high shear and gouge zones (0.99, 0.96 and 0.92, respectively; Table 2.3), but with all values close to 1. The dominant magnetic phase is low coercivity titanomagnetites. Coercivity of remanence values ($B_{cr}$; Table 2.3) are lowest in the undeformed material (35 mT), slightly higher in the highly sheared material (37 mT) and significantly higher in the gouge (53 mT). Higher associated ratios of saturation remanence to saturation magnetisation ($M_{rs}/M_s$) and coercive force ($B_c$; Fig. 2.10e), in addition to a contrasting morphology of the hysteresis curves (see Fig. A1.5), also highlights a distinct difference between the gouge and other zones of the spine; in particular, $B_c$ values for host material consistently plot between the high shear zone and gouge. Further differences are recorded by calculating the shape parameter ($\sigma_{hys}$) from the hysteresis curve, which shows that all samples are "potbellied" to different degrees. Plotting $\sigma_{hys}$ against the coercivity ratio ($B_{rh}/B_{cr}$) highlights a systematic change from the host, high shear zone and gouge material (Fig. 2.10f, after Fabian, 2003). Henkel plots (Henkel, 1964) supplement this information, incorporating backfield and IRM data (i.e., remanence data) to identify the presence of a demagnetising field arising either from multi-domain (MD) effects or magnetostatic interactions between single-domain grains (see Fig. A1.6 for raw data). Samples are plotted against ideal Stoner-Wohlfarth particles, or uniaxial non-interacting single-domain particles (Wohlfarth, 1958), and although the gouge plots closest to this line, all plot below the line, and as such all remanence carriers from each section of the shear zone deviate from this ideal

behaviour. Hysteresis and backfield data can be combined into a Day plot (Day *et al.*, 1977) to examine the domain state of the magnetic carriers. All sample sets are repeatable, and plot in distinctly different areas (Fig. 2.10g). Although all points fall within the pseudo-single-domain (PSD) region for pure magnetite (Dunlop, 2002), the Day plot again indicates the tendency for gouge to be considerably more single-domain-like, with the host rock again falling between the highly sheared zone and the gouge.

***Table 2.3*** *– Laboratory-based magnetic properties of outcrop 2 shear zone: Magnetic susceptibility, Curie temperature, degree of saturation and coercivity of remanence*

| Magnetics measurement: | Sample no.: | Host | High shear | Gouge |
|---|---|---|---|---|
| **Magnetic susceptibility ($10^{-4}$ SI units)** | 1 | 9.70 | 6.11 | 1.85 |
| | 2 | 8.97 | 5.21 | 2.25 |
| | 3 | 12.10 | 7.22 | 2.46 |
| | 4 | 10.70 | 6.39 | 3.10 |
| | 5 | 9.24 | – | 2.98 |
| | *Average* | 10.14 | 6.23 | 2.53 |
| **Curie Temperature, $T_C$ (°C)** | 1 | 522 | 509 | 552 |
| | 2 | 509 | 507 | 559 |
| | 3 | 533 | 506 | 555 |
| | 4 | 520 | – | 521 |
| | 5 | – | – | 533 |
| | *Average* | 521 | 507 | 544 |
| **Degree of saturation, S300 (at 300 mT)** | 1 | 0.99 | 0.95 | 0.91 |
| | 2 | 0.99 | 0.95 | 0.91 |
| | 3 | 1.01 | 0.98 | 0.91 |
| | 4 | 1.00 | 0.96 | 0.93 |
| | 5 | 0.98 | – | 0.94 |
| | *Average* | 0.99 | 0.96 | 0.92 |
| **Coercivity of remanence, $B_{cr}$ (mT)** | 1 | 33.39 | 36.43 | 55.86 |
| | 2 | 33.66 | 37.29 | 53.17 |
| | 3 | 33.28 | 36.95 | 52.59 |
| | 4 | 38.81 | 38.06 | 51.10 |
| | 5 | 34.55 | – | 52.88 |
| | *Average* | 34.74 | 37.18 | 53.12 |

## 2.3.6. Groundmass textures and glass chemistry

### *2.3.6.1. Amphibole reaction rims*

The two populations of amphibole that are present in the dacitic spine are hornblende phenocrysts and pargasite microphenocrysts and microlites in the groundmass. Reaction rims have previously been identified on hornblende phenocrysts within the pyroclastic deposits of the 1991–1995 eruption (e.g., Nakada & Motomura, 1999), with no reports of rims on groundmass pargasites. Within the spine shear zone, reaction rims on hornblende phenocrysts are similar in appearance to those reported in pyroclastic deposits, thus are not discussed further.

Groundmass pargasite breakdown rims vary from those seen in hornblende phenocrysts, as they show two types of breakdown textures: symplectitic and granular (Fig. 2.11a; see Fig. A1.7 for additional examples). In the low and moderate shear zone, symplectitic rims mantle pargasite, termed so owing to the submicron interconnection of pyroxene, plagioclase and Fe-Ti oxide laths. In the high shear zone, these symplectitic rims are locally surrounded by coarser, detached pyroxene microlites (Fig. 2.11a). Pargasite in the gouge consists exclusively of detached granular rims of pyroxene and Fe-Ti oxides microlites. Minor symplectitic patches are occasionally seen on the inner zone of these detached granular rims, directly in contact with the host pargasite. Within the undeformed dome rock, only minor symplectitic patches are observed, with some pargasite crystals showing no evidence of reaction. To quantify this variation, the maximum thickness of each rim was measured from each section of the shear zone (Fig. 2.11b; Electronic Appendix 1.3). Reaction rims are thickest in the gouge and high shear zone (maximum of 13.8 and 12.7 μm, respectively), and thinnest in the low shear zone and undeformed dome rock (maximum 4.8 μm and 3.2 μm, respectively), with the latter, occasionally displaying no rims. These changes are systematic across the shear zone and undeformed dome rock from: (1) an unreacted pargasite as observed in undeformed dome material; (2) thin symplectitic rims in the low and moderate shear zone; (3) thicker symplectitic rims and the first appearance of granular rims in the high shear zone; (4) pronounced detached granular rims in the gouge.

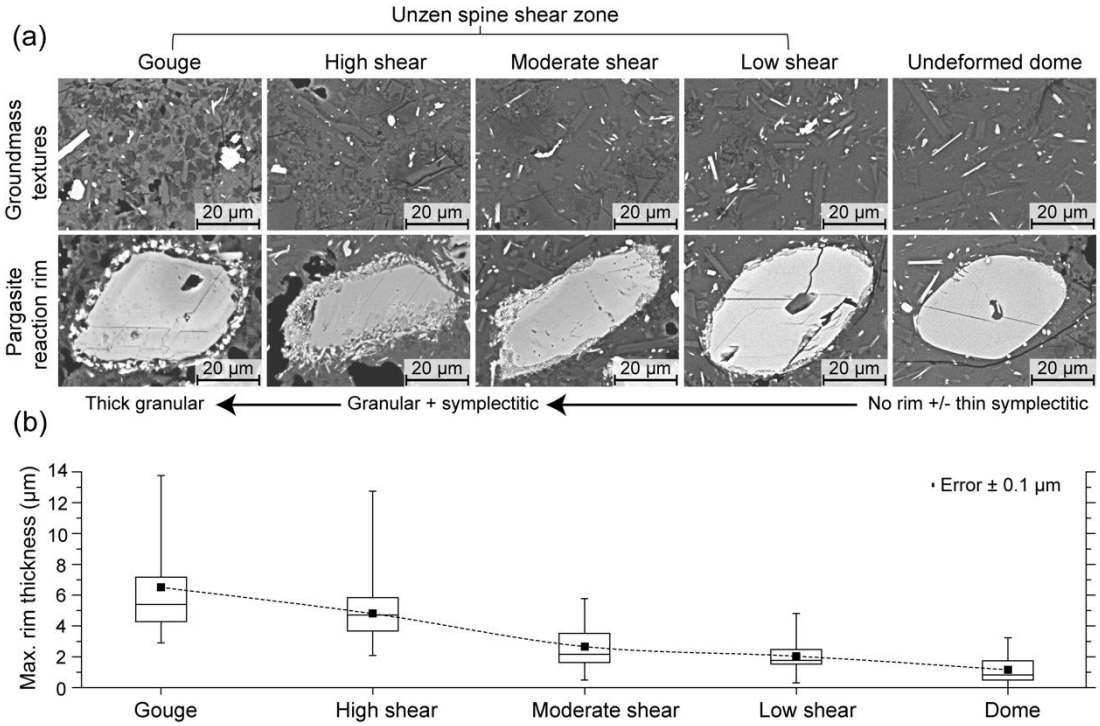


***Figure 2.11*** *– Backscattered electron (BSE) images of the groundmass textures across the shear zone (a) showing the progressive alteration of the groundmass glass and variations in pargasite reactions rims, both compared to the undeformed dome block. In the low shear zone and undeformed dome block, clusters of small, dark grey silica-rich patches are located around microlites. These clusters in the moderate shear zone spread into web-like domains that increase in abundance in the high shear zone. The gouge is textural distinct from the rest of the shear zone, consisting of larger silica-rich patches that are well distributed within the groundmass. Pargasite crystals are surrounded by granular rims in the gouge material, both granular and symplectitic rims in the high shear zone, and symplectitic rims only in the moderate and low shear zones, with the undeformed dome block showing negligible reaction rims. (b) Box plot showing the maximum thickness of pargasite reaction rims for >30 crystal measured per section of the shear zone. The plot shows the 25th and 75th percentiles, data range, median value (horizontal line) and mean value (square). Thickness error was calculated from the pixel resolution of the BSE images. Pargasite rim thicknesses show an average increase towards the gouge.*

*2.3.6.2. Textural, chemical and thermal properties of the interstitial glass*

The solid groundmass of the dacitic lava spine's shear zone consists of 33.5–47.8 area % interstitial glass (Table 2.2). Heterogeneous glass alteration textures are a prominent feature associated with the spine (Fig. 2.11a). In the low shear zone, clusters of fine-grained (<1–2 μm diameter), dark grey, silica-rich phases are observed within the glass, notably localised along plagioclase microlite edges. The moderate shear zone also consists of these silica-rich phases, which appear to be interconnected with web-like intergrowths that radiate in a spherulitic manner. These silica phases and intergrowths are seen most extensively within the high shear zone, where less pristine glass remains relative to the low shear zone. Despite these somewhat systematic differences between the low, moderate and high shear zone, the groundmass of the gouge is texturally different (Fig. 2.11a). The gouge consists of larger (5–10 μm in diameter), subhedral silica phases, often displaying a scaly texture that forms an intercrystalline network around plagioclase microlites, with no web-like intergrowths and only minor interstitial glass remaining (as also recorded by QEMSCAN in Fig. 2.5 and Table 2.2). EBSD band contrast maps of the gouge (Fig. 2.9a and Fig. A1.1), which only detect phases with a definite crystalline structure (i.e., will not detect glass or any other amorphous phases) identify these silica phases as crystalline, likely cristobalite.

***Table 2.4*** *– Composition of the interstitial glass from outcrop 1 shear zone*

| **Sample:** | **A** | **C** | **E** | **H** |
|---|---|---|---|---|
| **Rock type:** | Lava spine | Lava spine | Lava spine | Lava spine |
| **Zone:** | Gouge | High shear | Moderate shear | Low shear |
| *n* | 5 | 8 | 13 | 10 |
| $SiO_2$ | 78.08 (0.75) | 79.64 (0.82) | 80.26 (0.42) | 80.32 (0.38) |
| $TiO_2$ | 0.32 (0.05) | 0.29 (0.02) | 0.28 (0.01) | 0.29 (0.01) |
| $Al_2O_3$ | 11.42 (0.35) | 10.67 (0.51) | 10.42 (0.26) | 10.40 (0.14) |
| FeO* | 0.80 (0.04) | 0.81 (0.11) | 0.73 (0.09) | 0.74 (0.10) |
| MgO | 0.04 (0.01) | 0.06 (0.02) | 0.04 (0.02) | 0.04 (0.01) |
| CaO | 0.22 (0.06) | 0.27 (0.14) | 0.20 (0.06) | 0.18 (0.05) |
| $Na_2O$ | 2.43 (0.15) | 2.04 (0.20) | 2.00 (0.13) | 1.85 (0.06) |
| $K_2O$ | 6.69 (0.24) | 6.22 (0.25) | 6.07 (0.12) | 6.18 (0.17) |
| Total | 100.00 | 100.00 | 100.00 | 100.00 |
| Σ | 99.89 | 99.79 | 100.61 | 99.82 |

*Normalised average compositions of the interstitial glass across the outcrop 1 shear zone. Numbers in parentheses show the standard deviation (1σ) derived from multiple analyses.*

*n, number of microprobe analyses averaged to determine the average glass composition and standard deviation.*

** Total Fe as FeO.*

*Σ, averaged original microprobe totals.*

The groundmass glass is rhyolitic (77–81 $SiO_2$ wt %), with subtle chemical variations between each section of the shear zone (Fig. 2.12; Table 2.4). Interstitial glass of the low and moderate shear zone has similar overlapping compositions for most major elements, particularly in $SiO_2$ (Fig. 2.12a; 79.9–81.3 and 79.8–81.4 wt %, respectively), although some elements in the moderate shear zone display a larger range (e.g., $Al_2O_3$ and $Na_2O$; Fig. 2.12b and c). The high shear zone consists of the most chemically heterogeneous glass; $SiO_2$ extends ~2 wt % below that recorded for the moderate and low shear zone (78.1–80.9 wt %). In contrast, most other elements extend towards higher values, most notably for $Al_2O_3$ and $Na_2O$ (Fig. 2.12b and c), with low concentration elements (e.g., MgO and CaO) residing within the range observed in the moderate and low shear zones. The interstitial glass of the gouge has the least $SiO_2$ (Fig. 2.12a; 77.1–79.1 wt %), but highest $Al_2O_3$, $K_2O$ and $Na_2O$ (Fig. 2.12b and c) with respect to the other zones. MgO (Fig. 2.12d) is lower in the gouge relative to the high shear zone, although it is within range of the moderate and low shear zones. These seemingly systematic chemical changes in the interstitial glass across the shear zone, decreasing in $SiO_2$ from the low and moderate shear zone towards the gouge, and an overall shift towards higher concentrations for other elements, is concordant with the increased appearance of crystalline silica in the groundmass. A simple mass balance using the average glass composition of the low shear zone (Table 2.4) reveals ~6 and ~14 % crystallisation of an $SiO_2$ polymorph (assuming 100 wt % $SiO_2$) is required to change the chemistry to that measured in the high shear zone and gouge, respectively. This is consistent with both the groundmass textures (Fig. 2.11a) and reduction of glass content in the gouge (Fig. 2.5 and Table 2.2). Although no reduction of glass was recorded for the high shear zone, this may be related to the <2 μm silica phases in this region being smaller than the beam's interaction volume (~10 $\mu m^3$) thus being classified as glass in QEMSCAN analysis.

Thermal analysis of the low shear zone groundmass material was performed to collate a thermal history of the magma, and, in particular, an estimation of the temperature at which viscous deformation may ensue, as determined by the glass transition ($T_g$). For the analysis, low shear zone material was used as it was considered to be the most representative of the magma's groundmass prior to deformation and any chemical alteration. A calorimetric $T_g$ value of 790 ºC was obtained (see $C_p$ curve in Fig. A1.8 using a 10 $ºC.min^{-1}$ heating/cooling rate). This value was consistent with the estimated temperature derived from the viscosity model of Giordano *et al.* (2008) using measured glass chemistry (773 ºC) which acts as a viscosity gauge for $10^{12}$ Pa.s.

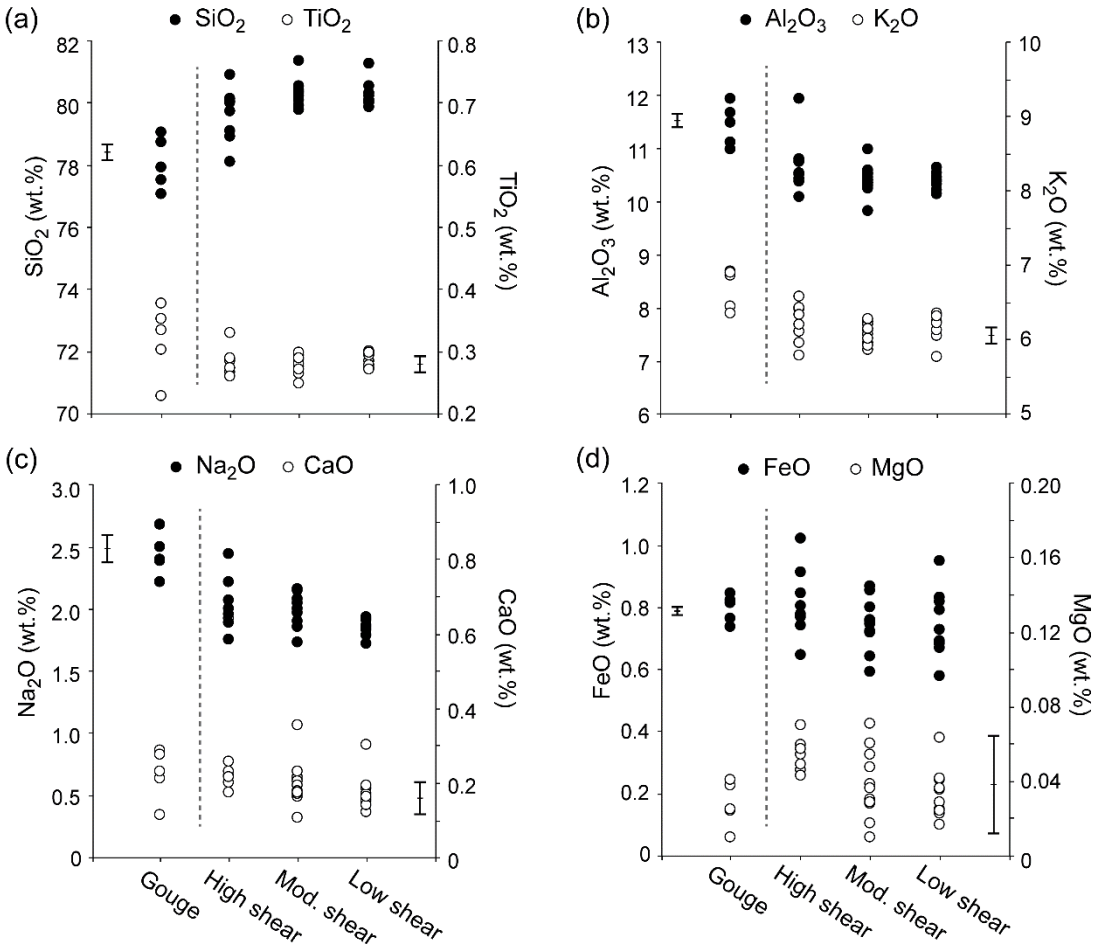


***Figure 2.12*** *– Spatial variation in the interstitial glass composition across the shear zone. (a) $SiO_2$ and $TiO_2$. (b) $Al_2O_3$ and $K_2O$. (c) $Na_2O$ and CaO. (d) FeO and MgO. All values are presented on a volatile-free basis, with totals normalised to 100 wt %. Error bars adjacent to the corresponding component axis denote the relative uncertainty based on repeat analyses of KN-18 glass standard.*

### 2.3.7. Experimental insights

During direct shear at the imposed experimental conditions (2 MPa normal stress and 1 m $s^{-1}$ slip rate), frictional work resulted in a rapid temperature rise of the dacite from 600 ºC to >1150 ºC in ~2 seconds (Fig. 2.13a, b and see Fig. A1.9 for raw mechanical data), permitting localised melting of the rock along a narrow slip plane. After ~5 seconds of slip, a full melt layer had formed causing the heat source to transition from frictional heat to viscous dissipation (i.e., shear heating; e.g., Hirose & Shimamoto, 2005), as recorded by the appearance of shear bands radiating from the slip zone (Fig. 2.13b). Temperature profiles across the simulated shear zone (Fig. 2.13a) reveal a gradual increase in width through time as the temperature exceeds the calorimetric $T_g$. Microtextural observations of the material adjacent to the melt zone show microlites and microphenocrysts are preferentially aligned in the direction of slip (Fig. 2.13c and d). Within this localised region, pores are reduced in both size and abundance, from ~40–100 μm in diameter in the starting material to <10 μm in diameter in the areas directly adjacent to the slip zone (Fig. 2.13e). A closer examination of the textures in the experimental shear zone (Fig. 2.13f) revealed localised reaction rims on pargasite microlites adjacent to the melt zone. Rims closest to the melt zone consist of coarse grained, detached pyroxene microlites (Fig. 2.13g), which become finer grained and more acicular further away (Fig. 2.13h). Pargasite away from the experimental shear zone (i.e., in the starting material) show negligible reaction rims and appear stable in the absence of shearing (Fig. 2.13i). Textural characteristics of the reaction rims in the experimental shear zone are similar to those in the natural gouge and high shear zone of the spine (Fig. 2.13j), while pargasite crystals in the low shear zone are more comparable to the starting material (Fig. 2.11a). Based on the microtextural differences induced across the experimental shear zone, it can be subdivided into discrete zones akin to outcrop 1 shear zone (Fig. 2.2a and Fig. 2.13f): 1) a "low shear zone" with randomly oriented microlites, large open pores and no reaction rims on pargasite microlites; 2) a "moderate shear zone" with the onset of a reduction in porosity and thin reaction rims on pargasites; and 3) a "high shear zone" with strongly aligned tabular microlites, significantly collapsed pores and thick granular reaction rims on pargasite microlites. Using the temperature profile monitored across the shear zone by the thermographic camera, we can estimate the temperature range at which each of these discrete zones (and textures) would have formed (Fig. 2.13a), with the low shear zone between 790–860 ºC, moderate shear zone between 860–980 ºC and high shear zone between 980–1080 ºC, with any bulk melting taking place at >1100 ºC.

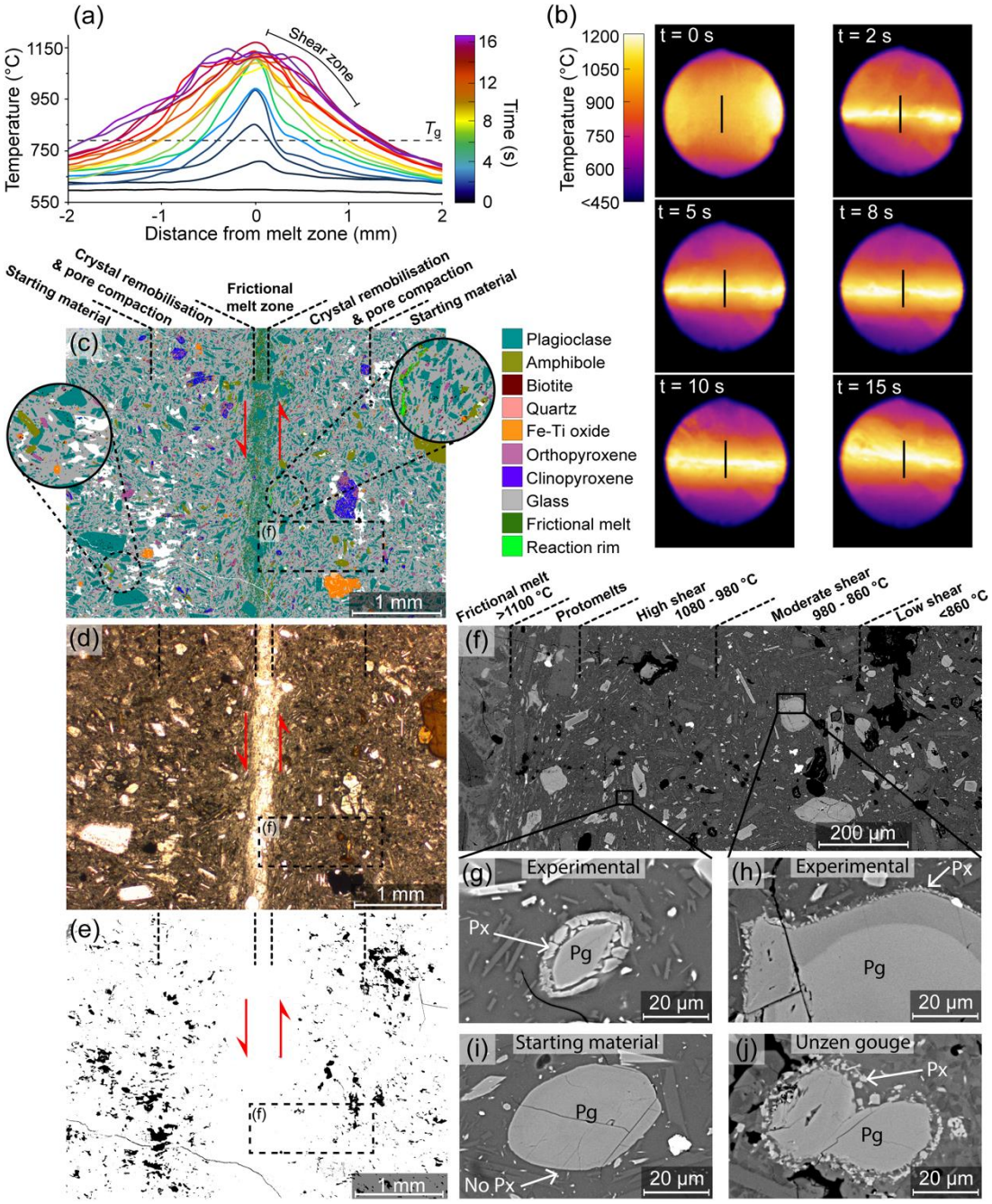


***Figure 2.13*** *– High-temperature, high-velocity rotary shear (HVR) experiment and associated textures of the experimental shear zone. (a) Temperature evolution across a 2 mm transect of the slip zone through time derived from the thermographic recording of the experimental slip zone (b). The dashed line in (a) denotes the calorimetric glass transition (790 ºC) equating to a viscosity of $10^{12}$ Pa.s. (b) After ~10 seconds of slip, shear bands are observed radiating from the slip zone. The line across the slip zone in the thermographic images represents the location of the transect used to obtain the temperature profile in (a). Textural observations in (c), (d) and (e) can be directly compared to the temperature profile above. (c) QEMSCAN map and (d) photomicrograph showing the remobilisation of crystals and their alignment adjacent to the melt zone. (e) Porosity distribution showing pores within the shear zone progressively*

*decrease in size and abundance towards the slip plane. (f) BSE image of the experimental shear zone, being dividing into four zones similar to outcrop 1 shear zone, along with temperature estimates for each zone using the temperature profile in (a). Pargasites (Pg) in the experimental shear zone display pyroxene (px) reaction rims in the areas of elevated temperatures, being granular at the highest temperatures (g) and becoming finer further away (h). (i) Example of a pargasite crystal in the starting material displaying no reaction rim. (j) A pargasite crystal from the gouge displaying a granular rim comparable to (g).*

## 2.4. INTERPRETATION AND DISCUSSION

Direct field studies investigating the textural complexities associated with extruding lavas are in short supply due to the prolonged nature of lava dome eruptions, in addition to the low probability that extruded structures remain well enough preserved to interpret the processes involved effectively (Mount St. Helens – e.g., Pallister *et al*. 2013; Gaunt *et al.* 2014; Unzen volcano – e.g., Smith *et al.*, 2001; Volcán de Colima – e.g., Kendrick *et al.*, 2016; Cordón Caulle – e.g., Castro *et al*., 2013; Tuffen *et al.*, 2013). The quiescence following the 1991–1995 dome-building eruption at Unzen volcano provided this relatively unique opportunity, where remnants of the extruded lava spine and associated marginal shear zones remain intact.

### 2.4.1. Strain localisation and viscous remobilisation

Our observations suggest the formation of these shear zones was a consequence of strain localisation, which in turn was governed by changes in the magma's rheology during its ascent to the surface. Late-stage crystallisation and degassing of the dacitic magma (e.g., Noguchi *et al.*, 2008b; Cichy *et al.*, 2011) will increase viscosity and significantly hamper flow in the conduit, aiding a rheological transition of the magma, causing stress and strain to localise near the conduit margins (Fig. 2.14 panel [1]). A concentration of stress in the high viscosity, crystal-rich magma likely led to the dissipation of viscous energy (shear heating) or friction resulting in a temperature rise (e.g., Lavallée *et al.*, 2008; Kendrick *et al.*, 2014b), which reduced the viscosity of the magma, allowing crystals to align in the direction of flow (i.e., viscously remobilise; Fig. 2.6a), and pores to compact (Fig. 2.5 and Fig. 2.6a–c) reducing permeability (e.g., Kendrick *et al.*, 2014a; Ashwell *et al.*, 2015). The presence of an interstitial glass facilitates viscous remobilisation (e.g., Hornby *et al.*, 2015); when a glass is not present, for example at Mount St. Helens, lava spines extruded in a near-solid state with no high-temperature deformation of this kind observed (Cashman *et al.*, 2008; Kennedy *et al.*, 2009;

Kendrick *et al.*, 2012; Pallister *et al.*, 2013; Ryan *et al.*, 2018). Here, the interstitial glass presents an opportunity to constrain the likely conditions during spine extrusion based on textural evolution, which indicates increasing temperature towards the spine margin (i.e., high shear zone). As experimentally demonstrated here (Fig. 2.13a and f), viscous remobilisation and subsequent crystal rotation and alignment likely took place 200–300 ºC degrees above $T_g$ (980–1080 ºC). Our experiment also constrains an estimated temperature at which the magma in the conduit would remain undeformed (i.e., low shear zone), likely reflecting the temperature of magma that formed the core of the spine (~860 ºC, Fig. 2.13f), which is in close agreement to the post-magma mixing temperatures previously reported (870–900 ºC; Venezky & Rutherford, 1999; Holtz *et al.*, 2005).

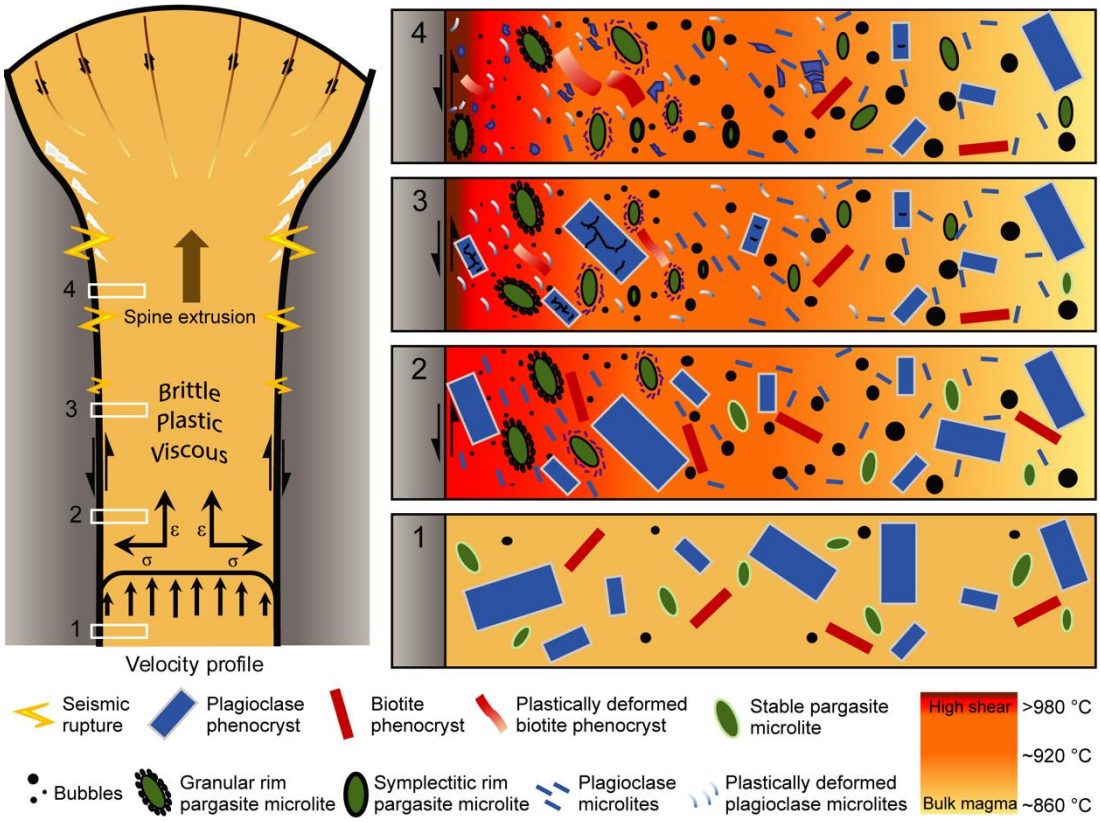


***Figure 2.14*** *– A conceptual model of the shallow conduit at Unzen volcano prior to the extrusion of the 1994–1995 lava spine. Panels 1–4 represent the textural evolution of plagioclase, pargasite, biotite and pores (bubbles) during magma evolution to the surface. The colour gradient across the transects of the conduit represents a temperature profile derived from the rotary shear experiment. During magma ascent (1), an increase in crystallisation and volatile exsolution causes the flow to transition from a Poiseuille flow regime to a plug style ascent. An increase in viscosity of the crystal-rich magma permits strain to localise near the conduit margins causing deformation and formation of shear zones (2).*

*Here, the increase in stress is manifested in the form of crystal rotation and alignment at the conduit margins. A thermal input likely accompanies viscous deformation due to shear heating, which causes a localised higher temperature region towards the conduit margins resulting in the destabilisation of pargasite in the form of granular breakdown rims and pore compaction. As magma ascends further (3), it encounters the viscous-brittle transition, where biotite phenocrysts and plagioclase microlites can accommodate strain by deforming plastically with crystal plasticity increasing towards the conduit margin. With further ascent, magma enters the brittle regime (4) causing strain localisation to be expressed by crystal comminution, which increases towards the conduit margins, where stress and strain are highest. The onset of brittle failure is accompanied by characteristic seismicity, as recorded during the extrusion of many domes and lava spines, where frictional behaviour takes over along the conduit margins. The slow extrusion of the high-temperature viscous spine is envisaged to experience late-stage oxidation, resulting in the formation of symplectitic pargasite breakdown rims accompanied with glass devitrification.*

### 2.4.2. Thermal destabilisation of amphibole

A characteristic effect of disequilibrium conditions is the reaction of mineral phases with the surrounding melt. Hydrous minerals, such as amphibole, are sensitive recorders of such processes and, once forced out of their stability zone, begin to breakdown, forming a rim of anhydrous phases (e.g., Rutherford & Hill, 1993; Browne & Gardner, 2006; De Angelis *et al.*, 2015). Although many factors can cause amphibole decomposition (e.g., decompression, heating, change in melt chemistry, oxidation; Rutherford & Hill, 1993), we investigate the effect of shearing on the dynamic stability of amphibole during magma ascent at Unzen volcano. Within the sheared margins of the lava spine, high-temperature flow appears to influence the stability of pargasitic amphibole, causing localised breakdown rims (Fig. 2.11a). The granular rims are exclusive to the high shear zone and gouge material, often surrounding a symplectitic rim. The symplectitic rims are always in direct contact with pargasite crystals and found across the entire shear zone with varying thickness (Fig. 2.11a). Thus, based on the theoretical understanding of reaction rims growing from the outer edge of the crystal inwards towards the centre (e.g., Browne & Gardner, 2006), the granular rims formed first followed by symplectitic decay. Experimental investigations on heating-induced amphibole reaction rims (De Angelis *et al.*, 2015) are texturally comparable to the granular rims observed in the high shear and gouge regions of the spine. Shear heating in these areas is the likely process that could cause the pargasite to breakdown, occurring contemporaneously with crystal alignment and pore compaction (Fig. 2.14 panel [2]). Similar granular rims also form during

the rotary shear experiment owing to a localised temperature rise brought about by shear heating (Fig. 2.13g and h). Symplectitic rims (Fig. 2.11a) have previously been related to extreme oxidation (i.e., at shallow conditions; Garcia & Jacobson, 1979); however, these textures have been recorded at other lava domes, being located as patches, either on the outer edge of a granular rim (Plechov *et al.*, 2011) or between the granular rim and the host amphibole (Scott *et al.*, 2012), making oxidation inconclusive. Yet, owing to the slow extrusion and cooling of the dacitic spine (Nakada & Motomura, 1999), along with the visual observation of surface reddening across outcrop 1 (Fig. 2.2a) and in blocks on the dome (e.g., Saito *et al.*, 2007), it may imply that the symplectitic rims were the result of late-stage oxidation (e.g., Murphy *et al.*, 2000). Kinetic variations across the shear zone also need to be taken into account due to a localised heat input related to shearing near the spine margin, with symplectitic rims possibly reflecting a kinetic delay (e.g., Scott *et al.*, 2012). Less kinetic inhibition would be expected near the spine margin, leading to the formation of coarser grained reaction rims. However, the coexistence of granular and symplectitic rims on the same pargasite crystal suggests two discrete events were responsible; heating exclusive to the high shear zone, followed by shallower oxidation of the shear zone as a whole (Fig. 2.14 panel [3]).

### 2.4.3. Crystal plasticity as a strain indicator

As magma approaches the viscous-brittle transition, flow behaviour converts from magmatic, viscous flow to near solid-state where fracturing and internal crystal deformation is feasible (Vernon, 2000). Solid-state crystal deformation has been observed to superimpose magmatic flow textures in several plutonic bodies (Murray, 1979; Vernon & Paterson, 1993; Zibra *et al.*, 2012). Typically, eruptive products lack these microstructural textures due to the sustained coexistence of a melt fraction, which may relax stress by adapting to new configurations. However, we show that crystals in magmatic shear zones do not only interact by acting as rigid, brittle bodies but can serve to accommodate strain by deforming plastically and that this plasticity varies systematically with deformation conditions before succumbing to failure. The presence of these deformation textures may be attributed to the low interstitial melt concentrations and the prolonged timescales of magma ascent (~5 months), allowing more time for the crystals to capture the transition from viscous to brittle behaviour. Kendrick *et al.* (2017) experimentally induced plastic deformation within plagioclase microlites present in an andesitic dome lava (from Volcán de Colima, Mexico), highlighting that microlites that were subjected to higher stresses and strains had a higher misorientation (i.e., internal lattice distortion), akin to the systematic variation recorded here across the shear zone of the spine. The increase in crystal plasticity of plagioclase microlites (Fig. 2.9a–d) suggests more stress

and strain were localised and accommodated in these areas (Fig. 2.14 panel [3]). This is further confirmed by the extreme plastic deformation of biotite phenocrysts in the high shear zone (Fig. 2.8b and c), which are akin to mica fish associated with S-C fabrics within mylonitic shear zones in fully crystalline rocks (e.g., Selverstone *et al.*, 2012). It has been observed that yield stresses required for plasticity to initiate decrease with increasing temperature (Poirier, 1995). Therefore, a higher stress and strain at the conduit margins (e.g., Cordonnier *et al.*, 2009; Lavallée *et al.*, 2012b; Lavallée *et al.*, 2013), accompanied with a thermal input due to shear heating and fault friction, would facilitate the observed increase in crystal plasticity towards the spine margin. Additionally, temperature increase could cause a crystal plasticity feedback mechanism, as increasing temperatures would lower the viscosity of the magma in the higher shear zone, enabling further strain to localise and favour yet higher crystal plastic deformation in this region. With more experimentation, building on the work of Kendrick *et al.* (2017), the strain rates required to achieve plastic deformation and failure in different phases could be quantified and thus incorporated into future rheological models.

### 2.4.4. Brittle failure and comminution

During spine extrusion, and once in the transitional brittle regime, crystals can fracture and comminute in areas of higher stress, resulting in a net grain size reduction of phenocrysts towards the spine margins (Fig. 2.14 panel [4]). The cataclastic behaviour, dominantly of plagioclase and amphibole phenocrysts (Fig. 2.4 and Fig. 2.7a), can thus be attributed to brittle deformation during fault slip (e.g., Monzawa & Otsuki, 2003). The point at which brittle failure would take over from viscous and plastic deformation depends on both the temperature and stress (and strain) conditions of the magma (e.g., Allen & McPhie, 2003; Lavallée *et al.*, 2008; Cordonnier *et al.*, 2009; Cordonnier *et al.*, 2012; Coats *et al.*, 2018). Similar brittle textures were observed following uniaxial compression experiments performed on 80 mm by 40 mm cores of natural Unzen dacite at 980 ºC, 1–32 MPa applied normal stress and total strain of 25 % (Cordonnier *et al.*, 2009). These experiments showed that with increasing stress, phenocrysts first cracked, then began to fragment to reduce grain size gradually, and at highest stresses crystal powders formed, with plagioclase and amphibole phenocrysts being the most affected. The decrease in plagioclase circularity in the higher shear zone (sample B, Fig. 2.7b) can be related to initial remobilisation and preferential alignment of the crystals during shear, and subsequent fracturing parallel to the principle shear direction.

Cordonnier *et al.* (2009) reported that following deformation of Unzen lavas under high stresses, finer crystal fragments and powders were commonly removed during thin section preparation, leaving behind voids with some residual fragments. This is in keeping

with our observations that increasing comminution of plagioclase, and to a lesser extent amphibole, caused their systematic reduction in size and abundance due to higher stress conditions at the spine margin (Fig. 2.2c, d, and Table 2.2). Biotite phenocrysts show no such reductions in abundance owing to their ability to deform plastically (Fig. 2.8c and d) and remain cohesive within the high shear zone and gouge. These differences in a crystal's mechanical response to shear may be a partial cause (along with natural heterogeneities) for the subtle variability in bulk rock major and trace elements across the shear zone (Table 2.1); for example, the drop in plagioclase-compatible elements (Sr, Ca, Na, Al) in the high shear zone relative to the low shear zone is consistent with the reduction of plagioclase recorded by QEMSCAN. It is also likely that the conduit wall rock underwent some degree of fracturing, contributing material (along with the high shear zone) to the gouge, and thus causing a further shift in mineralogy (Fig. 2.4, Table 2.1 and 2.2).

Brittle deformation within the conduit margin shear zones is considered to be the cause of the characteristic seismicity (Fig. 2.14) recorded during spine extrusion (Tuffen & Dingwell, 2005; Iverson *et al.*, 2006; Neuberg *et al.*, 2006; Iverson, 2008; Kendrick *et al.*, 2014b; Hornby *et al.*, 2015; Lamb *et al.*, 2015). The depth of the seismic source during spine extrusion at Unzen volcano was constrained to be <500 m (Yamashina *et al.*, 1999; Umakoshi *et al.*, 2008; Lamb *et al.*, 2015), thus the onset of brittle deformation is estimated to occur at a similar depth, perhaps superseding viscous and crystal-plastic behaviour at this depth. Continued fracturing at the conduit margins caused faulting to extend to the surface, allowing the magma to extrude in the form of a lava spine, mantled by cataclastic gouge material and fault breccia.

### 2.4.5. Magnetic response to shear

Magnetic properties of rocks can be highly sensitive to magnetomineralogical changes brought about by, for example, deformation and faulting generating heat (Ben-Zion & Sammis, 2003; Ferré *et al.*, 2005; Freund *et al.*, 2007; Kendrick *et al.*, 2012) or hydrothermal alteration due to flushing through of fluids or gases (Krása & Herrero-Bervera, 2005; Bouligand *et al.*, 2014; Geuna *et al.*, 2014). The magnetic variations across the spine shear zone reveal a disparate history of the magnetic carriers that coincide with the degree of shear. The variation in the reversibility of the magnetic susceptibility curves (Fig. 2.10d) suggests a single, low coercivity phase of low-Ti titanomagnetite ($T_C$ ~530 °C) in the host material; the less reversible curves of the high shear zone and gouge indicate a more distributed range of less stable phases, perhaps with suppressed Curie temperatures. The almost full saturation of the IRM and backfield curves support the predominance of these low

coercivity minerals (Leonhardt, 2006). However, the higher $T_C$, $B_{cr}$, $M_{rs}/M_s$ and $B_c$ values in the gouge (Table 2.3 and Fig. 2.10e) suggests an increasing fraction of higher coercivity magnetite grains. These were likely produced by oxidation of the titanomagnetite in the gouge either through subdividing them further into lamellae of iron-rich and iron-poor end members (i.e., oxyexsolution), or potentially even via conversion to titanohaematite. Interestingly, the undeformed host material consistently plots between the high shear zone and gouge (Fig. 2.10e and g), suggestive of two opposing formation pathways that took place at the spine margin. One event, likely oxidation well above ambient temperatures, influenced the high shear zone and gouge to differing degrees, creating the spread in susceptibility and coercivity ratio (Fig. 2.10a–g). However, the high shear appears to have been influenced by a second factor, potentially a pre- or syn-emplacement re-heating event that shifted the coercive force, and hence domain state in the opposite manner to the gouge (Fig. 2.10e and g). Such a shift in the magnetic carriers could be the result of shear or frictional heating in the laterally limited high shear zone (Fig. 2.3a).

### 2.4.6. Gouge alteration and glass devitrification

The low porosity of the glass-poor gouge, relative to the least sheared region of the spine, suggests that extensive induration of the plastically deformed and comminuted crystal fragments took place (Fig. 2.2b and Fig. 2.4), which would be facilitated by the increased temperature and stress conditions at the conduit margin (e.g., Ryan *et al.*, 2018). However, during its formation and lithification, the gouge is envisaged to have been exposed to prolonged periods of fluid and gas interaction, particularly during slow extrusion and post-emplacement degassing causing alteration, which is visible at outcrop scale due to the red colouration of the gouge (Fig. 2.2b and Fig. 2.3b). The groundmass silica phase within the gouge is somewhat comparable to those found in drilled dacitic dykes retrieved by the USDP-4 Unzen Scientific Drilling Project (Fig. 2.11a; Noguchi *et al.*, 2008a), although the gouge lacks evidence for other alteration phases (e.g., pyrite and alkali-feldspar). One of these dykes (dyke C14) has been interpreted to be the feeder dyke for the 1991–1995 eruption based on its similar texture and composition to the erupted dome lava, but with a distinct overprint of a mosaic of silica-rich grains in the groundmass attributed to hydrothermal alteration by percolating fluids (Noguchi *et al.*, 2008a). Therefore, in addition to the significant difference in rock magnetic parameters of the gouge (susceptibility and coercivity ratio; Fig. 2.10d and e), it suggests that the gouge layer experienced increased interaction with percolating hydrothermal fluids/gases relative to the bulk of the magma in the conduit. Fluids and gases filtrating through magmas and rocks have been seen to influence many petrological,

geochemical and magnetic parameters in volcanic systems (e.g., Krása & Herrero-Bervera, 2005; Salaun *et al.*, 2011; Bouligand *et al.*, 2014; Geuna *et al.*, 2014). Chemical effects are the result of transport of dissolved species either by diffusion or percolating fluids through open pores (Goncalves *et al.*, 2012). Metasomatism of this kind has been observed in many large-scale shear zones (e.g., Wibberley, 1999; Yonkee *et al.*, 2013), thus deciphering the influence of fluid migration during spine extrusion is critical. Porosity measurements (Table 2.2 and Fig. 2.5) across the shear zone reveal a decrease from low shear to high shear, resulting from pervasive compaction in the shear zone occurring at depth. The prevention of fluid access with increasing shear-enhanced compaction will aid in the relative stabilisation of mineral phases, preventing geochemical reactions from taking place (e.g., Wibberley, 1999).

Devitrification of amorphous glass is a common feature observed in many dome lavas (e.g., Mount St. Helens, Pallister et al., 2008; Santiaguito, Scott et al., 2012; Soufrière Hills volcano, Horwell et al., 2013); a solid-state crystallisation process that takes place during the slow cooling of the magma, leading to the formation of crystalline silica ($SiO_2$) phases, commonly cristobalite (e.g., Baxter *et al.*, 1999; Murphy *et al.*, 2000; Horwell *et al.*, 2013). Partially devitrified glass has previously been reported for Unzen lava spine by Nakada and Motomura (1999). The presence of groundmass silica phases in the shear zone, increasing systematically towards the spine exterior (Fig. 2.11a), are likely devitrification products, consistent to those textures observed in other systems (Cashman, 1992; Blundy & Cashman, 2001; Couch *et al.*, 2003; Harford *et al.*, 2003; Horwell *et al.*, 2013). Decompression experiments (Hammer & Rutherford, 2002; Couch *et al.*, 2003) observed similar devitrification textures forming only at very low pressures ($\leq$5 MPa), which led to the proposal that the extent of devitrification could act as a relative estimate for extrusion rate (Scott *et al.*, 2012; Horwell *et al.*, 2013), with increased devitrification during slower extrusion. Thus, devitrification of the spine is consistent with its low extrusion rate and slow cooling (Nakada & Motomura, 1999), and likely coincided with oxidation and the formation of symplectitic rims on pargasite microlites. The high shear zone glass (representing the margin of the spine) is slightly more devitrified (Fig. 2.11a), which could reflect the higher temperatures experienced associated with shear heating that prolonged the cooling period to ambient temperature and consequently influenced the glass chemistry (Fig. 2.12). This is further supported by the higher abundance of more evenly distributed groundmass silica phases in the gouge (Fig. 2.11a), which may have spent a relatively longer amount of time in the conduit than the bulk of the spine due to periodic coupling to the conduit wall.

### 2.4.7. Magma mixing: An added complexity

Evidence for magma mixing is common in the eruptive products at Unzen volcano (e.g., Nakada & Fujii, 1993; Nakamura, 1995; Nakada & Motomura, 1999; Venezky & Rutherford, 1999), including the spine (e.g., biotite reaction rims, mafic enclaves). Pre- and syn-eruptive magma mixing has been documented at other volcanoes, leaving behind petrological and geochemical signatures (e.g., reaction rims on hydrous minerals, reverse zoned crystals, and changes in bulk and glass composition). This brings complications when deciphering the impact of shear and the natural heterogeneities brought about by mixing of the magmas at depth. For example, reaction rims on amphiboles have previously been related to a temperature rise brought about by mixing a lower temperature and higher temperature magma (e.g., Murphy *et al.*, 2000; Rutherford & Devine, 2003; De Angelis *et al.*, 2015). This could be an alternative cause for the pargasite rims observed in the spine shear zone. Additionally, magma mixing can bring about hybridised, compositional heterogeneities in both major and trace elements (e.g., Perugini & Poli, 2012; Morgavi *et al.*, 2013), which could explain the subtle differences in bulk-rock composition across the shear zone. However, magma mixing is deemed an unsystematic, chaotic process, thus, although mixing of two or more magmas could explain the aforementioned differences, their systematic change with shear intensity across the shear zone and the range of complementary deformation indicators suggests otherwise. It has also been suggested that mixing of the magma at Unzen would be near-complete prior to reaching the last kilometre before extrusion (Nakada & Motomura, 1999; Goto *et al.*, 2008), while here we demonstrate that the differences observed across the spine shear zone likely formed within the final kilometre, and thus on a fully mixed magma. Nakada and Motomura (1999) found the bulk-rock composition of the porphyritic dacites from pyroclastic flow deposits collected throughout the 4-year eruption ranged from 64.5–66.0 wt % $SiO_2$, which was related to the natural variation in the abundance of phenocrysts. Consequently, although it is possible to attribute some of the bulk geochemical and mineralogical differences across the shear zone to deformation (fracturing of crystals during magma ascent and some loss of finer fragments forming cavities), inherent variabilities of the magma are expected. Therefore, it is important to consider, particularly for geochemical interpretations, natural variabilities within a mixed magma and refrain from over-interpretation of subtle differences.

## 2.5. IMPLICATIONS FOR ERUPTION STYLE

Shear deformation and strain localisation in the volcanic conduit can regulate eruptive behaviour as demonstrated by the range of characteristic textures that record shallow conduit processes. We relate the combined effect of viscous remobilisation, pore compaction, pargasite destabilisation and variations in magnetic properties to a magmatic heating episode near the conduit margins as a consequence of shearing and friction during magma ascent, manifested here primarily in the high shear zone (see Fig. 2.14). This was likely followed by late fluid-rock alteration, oxidation and glass devitrification of the gouge and, to a lesser extent, high shear regions of the spine.

In volcanic systems, highly fractured materials that reside in the conduit are ideal permeable pathways that facilitate outgassing, and thus reduce explosive potential (e.g., Gaunt *et al.*, 2014; Ashwell *et al.*, 2015). Marginal shear zones with their increased permeable network resulting from fracturing are believed to contribute to such depressurisation, preventing the build-up of excess pressure that can drive explosivity (e.g., Lamur *et al.*, 2017). However, within the shear zone examined here, localised compaction of the magma brought about by an increased temperature resulted in a closure of the original porous network and reduced permeability in these zones. As outgassing proficiency depends on the pore connectivity and permeability anisotropy of the undeformed magma (e.g., Ashwell *et al.*, 2015; Heap *et al.*, 2015; Farquharson *et al.*, 2016b; Colombier *et al.*, 2017; Gonnermann *et al.*, 2017; Lamur *et al.*, 2017), the compaction and closure of pore space in the high shear zone could have caused a shift in the location of outgassing, in this case towards the least sheared material (i.e., the core of the spine). A dilemma, therefore, arises when assessing a magma's ability to fracture (i.e., dilate) or compact in shear zones (Heap *et al.*, 2015), with the competition between the two favouring or limiting the extent of outgassing and therefore likely regulating the style of eruption. For example, explosive activity at Santiaguito volcano, Guatemala, has been attributed to strain localisation and faulting at the conduit margins (Lavallée *et al.*, 2015a), creating a partially open-vent system that regularly seals to build pressure that produces an explosion (Holland *et al.*, 2011; Johnson *et al.*, 2014). Although during the 1991–1995 eruption very limited explosive activity was reported, likely owing to relatively efficient connectivity of the magma's porous network (Nakada & Motomura, 1999; Nakada *et al.*, 1999), this may not be the case for other systems or throughout any other given eruption where shifts from effusive–explosive activity have been observed (Cassidy *et al.*, 2018). Our model suggests magma shearing at the conduit margin could temporally seal gas pathways, by compacting the porous network, creating ideal conditions for explosive activity, a phenomenon that may also be responsible for the frequent shifts in eruption style observed at many other dome-building volcanoes (Voight *et al.*, 1999; Mason *et al.*, 2006; Clarke *et al.*,

2007; Lensky *et al.*, 2008; Michaut *et al.*, 2009; Kennedy *et al.*, 2010; Ashwell *et al.*, 2015; Farquharson *et al.*, 2016b; Heap *et al.*, 2017). Petrological evidence for such a process influencing eruption style may be found in explosive deposits (i.e., ash and bombs); such signatures may include a combination of poorly vesicular clasts accompanied with plastically deformed microlites that show a fluidal or strong alignment, and in extreme cases the appearance of frictional melts.

## 2.6. CONCLUDING STATEMENT

In this study, we integrated multidisciplinary observations made through field examinations, petrology, microstructures, crystallography, magnetics and experimentation, to constrain the impact of shear on the petrological evolution of magma during ascent and spine extrusion at Unzen volcano, Japan. Our results show that crystals can act as an outlet for strain via crystal plasticity, leading the magma towards failure, thus effectively monitoring stress conditions. This accumulation of strain coincides with disequilibrium conditions in the conduit, assisting in mineral decomposition, alteration, crystal alignment, and pore compaction, owing to shear heating near the margin during the late-stages of spine extrusion. This process is overprinted, perhaps by increasing prevalence of dilational shear in the upper conduit, by a narrow gouge layer, characterised by distinct petrographic and magnetic properties typical of gas or fluid-flushing induced alteration, which influences the neighbouring compactional high shear zone to a lesser extent. These deformation microstructures and related processes envisaged in the shallow conduit, especially during the ascent of high viscosity magma, can have a significant effect on the permeable network, altering the outgassing efficiency and extent of fluid-magma interaction during magma ascent, ultimately controlling the style of eruption seen at the surface. For this reason, incorporation of these late-stage processes (i.e., shear heating, crystal plasticity, shear-induced mineral reactions and comminution) into rheological models may assist in constraining the complexities associated with on-going eruptions and thus aid in our understanding of shifts from effusive to explosive activity.

# Chapter 3 Frictional melt homogenisation during fault slip: Geochemical, textural and rheological fingerprints

## ABSTRACT

Volcanic environments often represent structurally active settings where strain localisation can promote faulting, frictional deformation, and subsequent melting along fault planes. Such frictional melting is thermodynamically a disequilibrium process initiated by selective melting of individual mineral phases and softening of volcanic glass at its glass transition as a response to rapid frictional heating. The formation of a thin melt layer on a fault plane surface can drastically accelerate or terminate slip during fault motion. A comprehensive understanding of the physical and chemical properties of the frictional melt is required for a full assessment of slip mechanisms, as frictional rheology depends on the contributions from selectively melted mineral and glass phases as well as the physical effects of restite fragments suspended in the frictional melt. Here, we experimentally investigate the impact of host-rock mineralogy on the compositional and textural evolution of a frictional melt during slip. High-velocity rotary shear (HVR) experiments were performed under controlled, volcanically relevant, coseismic conditions (1 m $s^{-1}$ slip rate and 1 MPa normal stress) using three intermediate dome lavas with contrasting mineral assemblages, sampled from volcanic systems where fault friction is evident: (1) an amphibole-bearing andesite (Soufrière Hills Volcano, Montserrat); (2) an amphibole-poor dacite (Santiaguito dome complex, Guatemala); and (3) an amphibole-free andesite (Volcán de Colima, Mexico). For each sample, five HVR experiments were terminated at different stages of frictional melt evolution, namely: (1) at the onset of melting, (2) upon formation of a steady-state melt layer, and (3) after 5 m, (4) 10 m, and (5) 15 m of slip at steady-state conditions. Progressive mixing and homogenisation of selective, single-phase melts within the frictional melt layer through double-diffusion convection demonstrates the control of melt composition on slip behaviour. Amphiboles melted preferentially, leading to consistently lower shear stress (~1 MPa less than amphibole-pore samples) and pronounced shear-weakening during the frictional melting of amphibole-bearing lavas. The results highlight the implications of mineral assemblages on fault slip, including conduit flow processes, which may influence the explosivity of eruptions, and run-out distances of rapid granular flows.

# 3.1. INTRODUCTION

## 3.1.1. Frictional melting

Frictional melting is a highly dynamic and chemically chaotic phenomenon associated with coseismic faulting and slip as a manifestation of extreme strain localisation (e.g., Sibson, 1975; Allen, 1979; Magloughlin & Spray, 1992; O'Hara, 1992). The presence of a thin melt layer on a narrow slip plane, commonly inferred to be generated at strain rates > $10^{-2}$ $s^{-1}$ and slip velocities > 0.1 m $s^{-1}$, is an important control on slip properties (Spray, 1992). The generation of such melts is a thermomechanical response to energy dissipation associated with the conversion of friction-induced deformation to heat (i.e., frictional heating). This process often results in a quasi-linear melt layer that is preserved in the geologic record as a pseudotachylyte, providing kinematic evidence for coseismic faulting activity (e.g., Shand, 1916; Francis, 1972; Sibson, 1975; Di Toro *et al.*, 2006).

Experimental work has demonstrated the mechanical influence of frictional melting on slip dynamics in geological materials (e.g., Lin & Shimamoto, 1998; Hirose & Shimamoto, 2005; Di Toro *et al.*, 2006; Niemeijer *et al.*, 2011; Kendrick *et al.*, 2014b; Hornby *et al.*, 2015). These studies have highlighted that the evolution of a frictional melt with slip displacement can dictate a material's frictional behaviour. Frictional melts can act as either (1) a lubricant, drastically reducing the frictional resistance during slip (e.g., McKenzie & Brune, 1972; Tsutsumi & Shimamoto, 1997), or (2) a viscous brake, causing slip velocity to wane and seismic slip to terminate (e.g., Koizumi *et al.*, 2004; Kendrick *et al.*, 2014b).

The physical properties of the host material (e.g., surface interface roughness; Nielsen *et al.*, 2010; Harbord *et al.*, 2017) and its constituent minerals (e.g., melting point and shear strength; Spray, 1992) influence the progression of frictional melting. Owing to rapid heating during fault slip, several hundred degrees over a few seconds of slip (e.g., McKenzie & Brune, 1972; Lavallée *et al.*, 2012a; Kendrick *et al.*, 2014b; Hornby *et al.*, 2015), frictional melting is considered a non-equilibrium adiabatic process involving the selective melting of individual mineral phases in the order of their solidus temperatures (e.g., Scott & Drever, 1953; Sibson, 1975; Spray, 1992; Lin & Shimamoto, 1998). In particular, the presence of hydrous phases (e.g., phyllosilicates, amphiboles) can significantly enhance melting probability owing to their lower melting points and the associated release of $H_2O$ (Allen, 1979).

The geochemical signatures of natural pseudotachylytes and experimentally-derived frictional melts demonstrate their derivation from selective melting of the host material (Magloughlin, 1992; O'Hara, 1992; Spray, 1992; Hetzel *et al.*, 1996; Lavallée *et al.*, 2012a; Jiang *et al.*, 2015). Furthermore, it has been proposed that the compositional evolution of

frictional melts may be used to constrain source properties and slip duration (Jiang *et al.*, 2015), but a systematic experimental and geochemical approach has yet to be undertaken.

The shear resistance exerted by frictional melts during slip is strongly influenced by their rheological properties (i.e., viscosity and strain rate; e.g., Hirose & Shimamoto, 2005; Lavallée *et al.*, 2012a; Hornby *et al.*, 2015). Work on the viscosities of multicomponent silicate melts has resulted in a statistically robust dataset over a wide compositional range, all displaying strong non-Arrhenian temperature-dependence and highlighting chemical composition, temperature and strain rate as key controls on rheology (Hess & Dingwell, 1996; Giordano *et al.*, 2008). During frictional melting, only phases with melting temperatures higher than the formation temperature of the melt can survive, leaving a suspension of remnant crystals. Substantial work has demonstrated the influence of suspended crystals on non-Newtonian viscosity and parameterisations have been generated (e.g., Caricchi *et al.*, 2007; Costa *et al.*, 2009; Cimarelli *et al.*, 2011; Lavallée *et al.*, 2012a; Mader *et al.*, 2013).

### 3.1.2. Fault friction in volcanic environments

Volcanic systems display abundant evidence for fault activity. For example, faulting can take place during: (1) the ascent of high-temperature, high-viscosity magma within the shallow volcanic conduit (e.g., Tuffen & Dingwell, 2005; Hale & Wadge, 2008; Kendrick *et al.*, 2012; Lavallée *et al.*, 2013; Wallace *et al.*, 2019); (2) flank instabilities, sector collapses and landslides (e.g., Legros *et al.*, 2000; Bernard & de Vries, 2017); and (3) block collision and sliding in pyroclastic density currents (e.g., Grunewald *et al.*, 2000; Schwarzkopf *et al.*, 2001). In each scenario, the process of frictional melting is material-dependent; thus, magmas with different mineralogical assemblages may have adverse effects on the style of slip and subsequent hazards generated. Differences in mineral assemblages are expected between volcanic systems, although similar differences can be observed within the same system owing to natural heterogeneities or the dynamic nature of the plumbing system. In particular, intermediate volcanic systems can naturally evolve (both continuously and discontinuously) with regards to mineralogy and crystallinity, either reflecting long-term magmatic evolution, magma recharge, or changes in final ascent conditions (e.g., Murphy *et al.*, 2000; Scott *et al.*, 2013). Previous studies have reported that the introduction of hydrous phases into the plumbing system, attributed to an elevated magma-water content at depth, often coincides with an increase in explosivity (e.g., Volcán de Colima, Mexico, Luhr & Carmichael, 1990; Macias *et al.*, 2017). Thus, the question arises as to the importance of the mineral assemblage for frictional properties in volcanic systems.

A complication that arises in the generation of a frictional melt from volcanic rocks is the common presence of a glass phase (e.g., Violay *et al.*, 2014; Lavallée *et al.*, 2015b). Unlike crystalline phases, which must melt to generate a liquid phase, glass exhibits a thermo-kinetic barrier, known as the glass transition temperature ($T_g$), where the glass softens into a liquid without any latent heat of reaction (Dingwell & Webb, 1989). The glass transition temperature increases with heating rate due to the timescales available for structural relaxation, which imposes important controls on fault friction (Lavallée *et al.*, 2015b). For a degassed rhyolitic interstitial glass, common in intermediate extrusive rocks, $T_g$ is typically < 800 ºC at moderate heating rates (e.g., < 10 ºC /min), which is lower than the melting points of the minerals generally present in volcanic rocks. Thus, friction with low heating rates will enable viscous remobilisation of glass at temperatures far lower than mineral melting temperatures, and therefore earlier than mineral melting itself (e.g., Lavallée *et al.*, 2015b). However, during rapid frictional heating, $T_g$ may be encountered at higher temperatures (e.g., ~1000 ºC; Lavallée *et al.*, 2015b) and closer to that of crystal melting temperatures.

Here, we experimentally assess the impact of mineralogy during the frictional melting of intermediate volcanic lavas on the evolutionary dynamics of slip. We highlight the importance of bulk mineralogy on fault properties during shallow-conduit and post-eruptive volcanic processes in high-viscosity systems (e.g., lava domes), which are as yet unaccounted for in current hazard models. A better understanding of frictional melts in systems with contrasting mineral assemblages will improve models for fault slip rheology and magma flow in the conduit, which in turn will aid forecasts of magma behaviour during ascent and the interpretation of early warning geophysical signals. It may also elucidate fault propagation processes at the base of rapid granular flows and help constrain run-out distances during such hazardous events.

## 3.2. MATERIALS AND METHODS

### 3.2.1. Starting material

Three crystal-rich, glass-bearing, intermediate dome lavas from well-characterised, active volcanic systems were chosen for this study: (1) an amphibole-bearing andesite from Soufrière Hills Volcano (SHV), Montserrat; (2) an amphibole-poor dacite from the Santiaguito dome complex (SG), Guatemala; and (3) an amphibole-free andesite from Volcán de Colima (COL), Mexico. Both SHV and COL andesites were collected from dome collapse deposits, while the SG dacite formed part of a lava spine extruded from the El Monje vent. The starting materials where chosen because they are from active volcanic systems renowned for rheological and structural instability, and because they cover a range of mineral assemblages found in intermediate lavas (andesite–dacite).

The whole-rock geochemistry of each rock sample was determined by X-ray Fluorescence Spectrometry (XRF) on a PANalytical Axios Advanced XRF spectrometer at the University of Leicester. Major elements were measured on glass beads fused from ignited powders, and trace elements were measured using pressed powder pellets (Table 3.1). Relative precision and accuracy were better than 1.5% for major elements and 5% for trace elements based on repeat analyses of international reference materials (see Electronic Appendix 2). Mineral abundance statistics were collected using QEMSCAN (Quantitative Evaluation of Minerals by Scanning Electron Microscope) on an automated SEM-EDS (Scanning Electron Microscope-Energy Dispersive Spectrometer) system equipped with two Bruker energy dispersive X-ray spectrometers. QEMSCAN formulates a chemical composition from the X-ray point spectra collected in a raster across a sample and then matches the chemistry to a customisable reference library containing known compositions for minerals and glasses (for more details see, e.g., Gottlieb *et al.*, 2000). Data were collected across an entire polished, carbon-coated thin section from each starting material using a 15 kV accelerating voltage, 5 nA beam current, 10 μm step size, and dwell time sufficient to collect enough X-ray counts for accurate phase identification (defined as 1,000 X-ray counts). The resulting data were combined to produce a false-colour phase distribution map where each colour represents a compositionally discrete phase. Each coloured pixel was summed and normalised on a pore-free basis to provide a quantitative comparison of the mineral modal abundances of each starting material (Table 3.2). Despite precision errors from removing and reinserting the same thin section, standard deviations were better than 0.39 for all phases. QEMSCAN identification is limited to phases larger than the beam's interaction volume (~10 $\mu m^3$); groundmass phases smaller than this cannot be identified individually but are assigned the composition of the surroundings (e.g., crystals less than ~2 μm in diameter are assigned to the

surrounding glass). Consequently, groundmass mineralogy and interstitial glass were quantified separately from point counts of > 1000 points in a 200 × 200 μm area per sample.

***Table 3.1*** *– Geochemical composition of the bulk starting materials (measured by XRF) and interstitial glass (measured by electron probe microanalysis).*

| Location: | Soufrière Hills Volcano | | Santiaguito dome complex | | Volcán de Colima | |
|---|---|---|---|---|---|---|
| Sample: | SHV | | SG | | COL | |
| Rock type: | Andesite | | Dacite | | Andesite | |
| Deposit: | Dome collapse | | Lava spine | | Dome collapse | |
| | Bulk-rock | Glass | Bulk-rock | Glass | Bulk-rock | Glass |
| *(wt.%)* | | *n* 14 | | *n* 9 | | *n* 19 |
| $SiO_2$ | 59.59 | 79.72 (4.82) | 64.44 | 75.65 (1.38) | 62.05 | 77.00 (0.71) |
| $TiO_2$ | 0.60 | 0.29 (0.09) | 0.42 | 0.44 (0.05) | 0.51 | 0.56 (0.06) |
| $Al_2O_3$ | 18.49 | 10.93 (2.91) | 17.66 | 12.27 (0.79) | 17.74 | 11.35 (0.38) |
| FeO* | 6.13 | 1.32 (0.50) | 4.06 | 1.81 (0.46) | 4.58 | 1.86 (0.11) |
| MnO | 0.16 | <lld | 0.14 | <lld | 0.10 | <lld |
| MgO | 2.74 | 0.18 (0.26) | 1.67 | 0.30 (0.27) | 2.83 | 0.16 (0.06) |
| CaO | 7.76 | 2.20 (1.10) | 4.61 | 0.45 (0.29) | 5.59 | 0.48 (0.13) |
| $Na_2O$ | 3.34 | 3.23 (0.63) | 4.79 | 3.88 (0.54) | 4.48 | 4.04 (0.22) |
| $K_2O$ | 0.80 | 1.91 (0.64) | 1.70 | 4.95 (0.34) | 1.32 | 4.27 (0.33) |
| $P_2O_5$ | 0.13 | <lld | 0.21 | <lld | 0.18 | <lld |
| Cl | - | 0.08 (0.04) | - | 0.11 (0.04) | - | 0.12 (0.03) |
| LOI | 0.07 | - | 0.18 | - | 0.15 | - |
| Total[$] | 99.81 | 100.84 | 99.88 | 99.32 | 99.53 | 99.72 |
| *(ppm)* | | | | | | |
| Ba | 214 | - | 805 | - | 618 | - |
| Ce | 26 | - | 26 | - | 30 | - |
| La | 13 | - | 16 | - | 11 | - |
| Nb | 3 | - | 6 | - | 3 | - |
| Nd | 14 | - | 16 | - | 16 | - |
| Pb | 3 | - | 8 | - | 6 | - |
| Rb | 17 | - | 32 | - | 19 | - |
| Sc | 16 | - | 8 | - | 12 | - |
| Sr | 278 | - | 470 | - | 601 | - |
| Th | 2 | - | 2 | - | 1 | - |
| V | 131 | - | 53 | - | 97 | - |
| Y | 24 | - | 17 | - | 14 | - |
| Zn | 56 | - | 73 | - | 53 | - |
| Zr | 99 | - | 154 | - | 124 | - |

*All oxide concentrations for glass are normalised averages of n measurements. Values in parentheses are standard deviations (1σ) from n analyses. See Electronic Appendix 2 for all measurements.*

[$] *Original total*

[*] *All Fe as FeO*

*<lld, below lower limit of detection*

### 3.2.2. Experimental procedure

Frictional melting experiments were performed using a high-velocity rotary shear (HVR) apparatus at the Kochi Core Centre in Japan. Each experiment involved the preparation of two 24.98 mm diameter plane-parallel cylindrical cores with a 9 mm hollow centre, which created an ~8 mm wide annulus to minimise variations in slip rate across the contact surface. The two cores were placed into the experimental apparatus with one core being held stationary and the other rotating. The stationary sample holder was attached to a hydraulic piston that was used to apply a controlled axial stress of 1 MPa, while the other rotated at a constant (coseismically relevant) slip rate of 1 m $s^{-1}$. See Hirose and Shimamoto (2005) for more details of the experimental apparatus. These slip conditions were chosen because they represent realistic estimates for those reported during faulting events, such as at active lava domes (e.g., Johnson *et al.*, 2008; Hornby *et al.*, 2015; Lavallée *et al.*, 2015a), while also providing an ideal timeframe for frictional melting to allow the assessment of melting progression at different stages of slip. For each of the three starting materials, a set of five experiments were performed, with experiments terminated at five different conditions: (1) the onset of melting ($T_m$); (2) immediately after the achievement of steady-state conditions ($T_{ss}$); (3) after 5 m of slip at steady-state conditions ($T_5$); (4) after 10 m of slip at steady-state conditions ($T_{10}$); and (5) after 15 m of slip at steady-state melting conditions ($T_{15}$). All $T_{15}$ experiments were performed first to act as an initial gauge for the shorter slip distance experiments; however, visual monitoring was always used to identify the onset of melting. Steady-state conditions were defined as the attainment of a near-constant value of shear stress and the beginning of sample shortening. All experiments were recorded using an optical camera to track the frictional melting process and correlate it with the mechanical data. At the end of each test, the two cores were welded together by a frictional melt layer. Post-experimental samples were thin-sectioned perpendicular to the slip surface for textural and chemical analysis.

### 3.2.3. Textural & chemical characterisation

#### *3.2.3.1. Scanning electron microscopy & electron probe microanalysis*

Microtextural and geochemical analyses were performed on polished, carbon-coated thin sections for each experiment. Textural assessment of the frictional melt zone was performed using backscattered electron images (BSE) taken on a Philips XL30 scanning electron microscope (SEM) at the University of Liverpool, operated with a 20 kV accelerating voltage, 5 μm spot size and a 10 μm working distance.

The compositions of the different phases present in the starting material (host-rock crystals and interstitial glass), the experimentally generated frictional melt, and any non-melted crystals suspended within the melt zone were determined using a Cameca SX100 electron probe microanalyser (EPMA) at the Ludwig Maximilian University of Munich. Elemental abundances were acquired using wavelength dispersive spectrometers (WDS). Analyses on crystals were performed using a 15 kV accelerating voltage, 20 nA beam current, and a focused (~1 μm) beam. For all glass measurements, a defocussed 10 μm beam was used with a 5 nA beam current. A peak count time of 10 seconds and background count times of 5 seconds were used for all elements, with Na peaks counted first to minimise alkali loss during analysis. Matrix corrections were performed using the PAP procedure (Pouchou & Pichoir, 1984). To ensure accuracy and precision, eight working standards from the Smithsonian collection were utilised throughout the analysis. The full list of reference materials, their measured and known compositions and detection limits, along with the standards used for calibration of the spectrometers can be found in Electronic Appendix 2. All standards were measured regularly to ensure quality. Reproducibility of all elements in the working standards was high, with standard deviations < 0.5. By comparing the measured quantities with the known reference values for each standard, relative accuracies were generally better than 3% for major elements and 20% for minor elements based on multiple repeat analyses. Frictional melt compositions were measured as single points and transects across the width of the slip zone, making sure to avoid remnant crystals. Any melt totals outside 97–102 wt.% were cross-checked with BSE images and discarded in the event of beam interaction with crystal fragments.

### 3.2.4. Synchrotron X-ray spectroscopy

Prior to EPMA, selected major and trace elements of the frictional melt were analysed by high-brightness, micron-scale X-ray spectroscopy using the I18 microfocus spectroscopy beamline at the Diamond Light Source synchrotron, UK. Element maps were produced with a 4 × 3 μm spatial resolution allowing detailed investigation of the extent of frictional melt homogeneity and to investigate mineral susceptibility to contribute to the melt composition. A solid-state detector system enabled the analysis of nine elements per map, of which the focus was on the concentrations of Ca, Fe, K, Ti, Mn, Rb, Sr, Y, and Zr. These elements were chosen because of their different diffusion coefficients and different concentrations in the phases (i.e., minerals and glass), making their distinction straightforward.

### 3.2.5. Frictional melt rheology

The non-Arrhenian, Newtonian temperature-dependence of frictional melt viscosity was estimated using the GRD viscosity model (Giordano *et al.*, 2008). For the viscosity-temperature model, frictional melt compositions obtained by EMPA were imported into the calculator, along with a 0.1 wt.% $H_2O$ and zero fluorine content. These latter values were assumed based on the low water contents expected upon eruption, plus the absence of hydrous phases in the SG dacite and COL andesite (Harford *et al.*, 2003; Reubi & Blundy, 2008; Savov *et al.*, 2008). However, the presence of hydrous amphibole in the SHV andesite makes water content during frictional melting a variable, in addition to fluorine, which can often substitute for hydroxyl ($OH^-$). Although fluorine concentration in SHV amphiboles is reportedly low (0.04–0.06 wt.%; Humphreys *et al.*, 2009), it was demonstrated that this element has a similar viscosity-reduction effect as water with the tendency to remain dissolved within the melt for longer (Giordano *et al.*, 2004). Thus, for simplicity, we assessed the impact of $H_2O$ content on SHV frictional melt viscosity.

Apparent viscosities for the frictional melts were calculated using the recorded mechanical data from the experiments as:

$$\eta_{app} = \frac{\tau}{\dot{\varepsilon}} \tag{3.1}$$

where $\tau$ is the recorded shear stress (in Pa) taken when slip behaviour reached a steady-state condition (i.e., shear stress attained a quasi-constant value), and $\dot{\varepsilon}$ is the strain rate (in $s^{-1}$). Strain rates ($\dot{\varepsilon}$) were calculated as:

$$\dot{\varepsilon} = \frac{2\pi D_e}{dt} \tag{3.2}$$

where $D_e$ is the circumference of the circular trajectory at a given radius (referred to as an equivalent diameter), $d$ is assumed to reflect the thickness of the melt zone (in mm) as measured by optical analysis, and $t$ is slip duration (in seconds). The $D_e$ was calculated as:

$$D_e = \frac{V_e}{R\pi} \tag{3.3}$$

where $R$ is the rotation rate (in $min^{-1}$) and $V_e$ is the equivalent rotation velocity (i.e., displacement rate; in mm per $min^{-1}$). $V_e$ is defined as such that $\tau V_e S$ gives the rate of total frictional work on a fault with area $S$, assuming a constant shear stress on the fault surface after Shimamoto and Tsutsumi (1994):

$$V_e = \frac{4\pi R(D_o^2 + D_i D_o + D_i^2)}{3D_o + D_i} \tag{3.4}$$

where $D_o$ and $D_i$ are the outer and inner diameters (in mm), respectively, of the hollow core sample.

Crystals that remain in the frictional melt may also influence frictional melt viscosity (e.g., Caricchi *et al.*, 2007). This effect was estimated using the empirical relative-viscosity calculator of Costa *et al.* (2009) based on a strain-rate dependent rheology model combined with fitting parameters solved experimentally by Caricchi *et al.* (2007). For input values, a maximum packing fraction of 0.55 was used based on the semi-equant crystal population (Mueller *et al.*, 2011) and a crystal fraction estimated from ImageJ (Schneider *et al.*, 2012) using BSE images of the frictional melt. The relative effect of crystals was added to the calculated temperature-dependence of viscosity for the homogenised frictional melts to produce a modelled apparent viscosity of the suspension.

***Table 3.2*** *– Quantitative mineral modal abundance for the bulk starting materials and the host groundmass.*

| **Location:** | Soufrière Hills Volcano | | Santiaguito dome complex | | Volcán de Colima | |
|---|---|---|---|---|---|---|
| **Sample:** | SHV | | SG | | COL | |
| **Rock type:** | Andesite | | Dacite | | Andesite | |
| **Deposit:** | Dome collapse | | Lava spine | | Dome collapse | |
| *(vol.%)* | Bulk-rock[a] | Groundmass[b] | Bulk-rock[a] | Groundmass[b] | Bulk-rock[a] | Groundmass[b] |
| **Plagioclase** | 52.5 | 27.4 | 63.9 | 38.8 | 67.0 | 30.0 |
| **Amphibole** | 9.3 | 0.0 | 1.5 | 0.0 | 1.1 | 0.0 |
| **Orthopyroxene** | 6.4 | 16.8[d] | 2.9 | 2.6[d] | 6.5 | 3.8[d] |
| **Clinopyroxene** | 2.3 | | 0.3 | | 1.2 | |
| **Si polymorph[c]** | 13.0 | 23.2 | 14.2 | 11.0 | 5.6 | 2.0 |
| **Fe-Ti oxide** | 1.9 | 3.4 | 1.0 | 1.4 | 0.8 | 2.2 |
| **Apatite** | 0.3 | - | 0.4 | - | 0.4 | - |
| **Olivine** | 0.0 | 0.0 | 0.0 | 0.0 | Rare | 0.0 |
| **Glass** | 14.4 | 19.2 | 15.9 | 46.2 | 17.2 | 62.0 |
| **Vesicularity** | 15.2 | 10.0 | 7.0 | 0.0 | 13.7 | 0.0 |
| **Porosity (Pyc)[e]** | 13.0 | n.a. | 9.0 | n.a. | 17.0 | n.a. |

[a] *Bulk mineralogy acquired from QEMSCAN*

[b] *Groundmass mineralogy determined using point counting*

[c] *Combines quartz, cristobalite, and tridymite*

[d] *Groundmass pyroxene abundances combines both orthopyroxene and clinopyroxene.*

[e] *Connected porosities measured by He-pycnometry using cores from each starting material*

## 3.3. RESULTS

### 3.3.1. Characterisation of the starting material

All three starting materials were crystal-rich, porphyritic, and compositionally intermediate lavas (Fig. 3.1, Table 3.1 and Table 3.2). The sample from Soufrière Hills Volcano (SHV) was andesitic (59.6 wt.% $SiO_2$; Fig. 3.1a, b) and consisted of large phenocrysts of calcic-amphibole (i.e., hornblende; 9 vol.%; up to 6 mm), plagioclase (38 vol.%; up to 2 mm), orthopyroxene (5 vol.%; up to 2.5 mm), and minor clinopyroxene, quartz, and Fe-Ti oxides. The groundmass (Fig. 3.1c) was highly crystalline and consisted of plagioclase (27 vol.%), pyroxene (17 vol.%), and minor Fe-Ti oxide microlites (3 vol.%). Silica-rich phases (~5 μm diameter), with characteristic fish-scale cracks (likely cristobalite, a typical byproduct of glass devitrification in SHV lavas; e.g., Horwell *et al.*, 2013), formed the second most abundant groundmass phase (23 vol.%), while an interstitial rhyolitic glass was located between the microlite phases (19 vol.%).

The sample from the Santiaguito dome complex (SG) was dacitic (64.4 wt.% $SiO_2$; Fig. 3.1d, e) and had a similar porphyritic texture (phenocryst size and shape) to that of the SHV andesite (39 vol.% plagioclase and 3 vol.% orthopyroxene); however, amphibole was rare (~1 vol.%). Again, plagioclase microlites dominated the groundmass (39 vol.%; Fig. 3.1f), along with less abundant pyroxene (3 vol.%), Fe-Ti oxides (~1 vol.%), and a silica-rich phase (~10 μm diameter; likely tridymite, as reported for early Santiaguito lavas; e.g., Rose, 1972). These microlites were situated within an unaltered and abundant interstitial rhyolitic glass (46 vol.%).

The sample from Volcán de Colima (COL) was andesitic (62.1 wt.% $SiO_2$; Fig. 3.1g, h) and consisted of plagioclase phenocrysts that were more abundant (47 vol.%) and tabular (length up to 3 mm) than those in the SHV and SG samples. Both orthopyroxene (6 vol.%) and clinopyroxene (2 vol.%) were present as phenocryst phases (both up to 800 μm), in addition to rare quartz and Fe-Ti oxides. Rare, single olivine crystals were also present in the COL andesite, but owing to their infrequent appearance they were unlikely to influence frictional melting processes. Plagioclase dominated the groundmass mineralogy (30 vol.%; Fig. 3.1i) along with a pristine interstitial rhyolitic glass (62 vol.%), and minor pyroxene (4 vol.%) and Fe-Ti oxides (2 vol.%). Minor silica phases (2 vol.%) were occasionally located at the edges of plagioclase microlites.

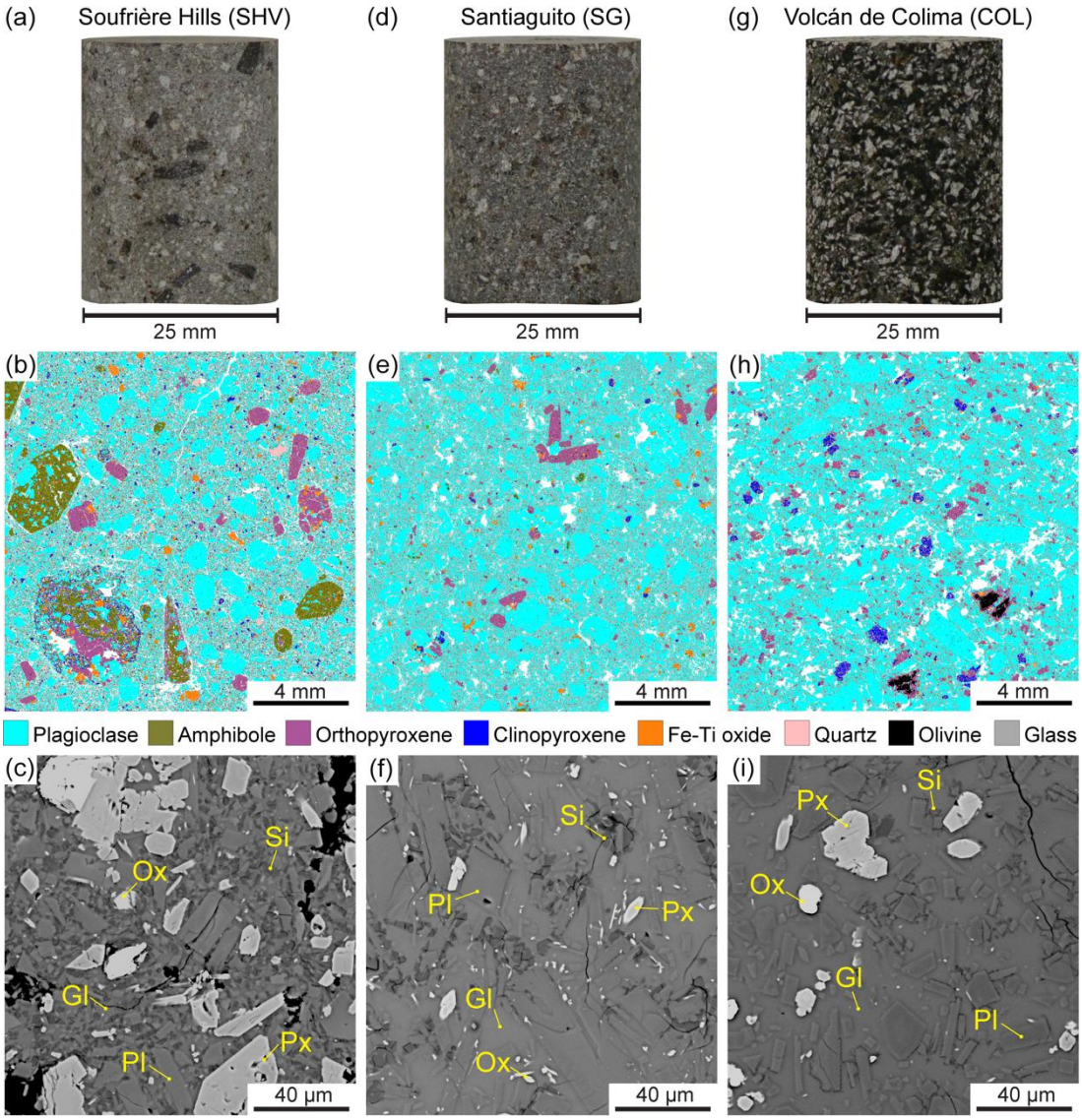


***Figure 3.1*** *– Mineralogical and textural characteristics of the three host materials used in the high-velocity rotary shear (HVR) experiments: Soufrière Hills Volcano (SHV) andesite (a–c), Santiaguito dome complex (SG) dacite (d–f), and Volcán de Colima (COL) andesite (g–i). Panels (a, d and g) are photographs of the cored starting materials, (b, e and h) are QEMSCAN maps used for quantifying bulk-rock phase abundances, where colours identify phases as shown in the key and white indicates pore space, and (c, f and i) are backscattered electron (BSE) images showing groundmass textures. The phases in the groundmass include plagioclase (Pl), pyroxenes (Px), Fe-Ti oxides (Ox), silica polymorphs (Si), and interstitial glass (Gl).*

### 3.3.2. Mechanical behaviour of high-velocity frictional melts

During HVR experiments, frictional melts formed on the slip plane surfaces (Fig. 3.2a). The slip properties of the three sample sets evolved differently (Fig. 3.2b); mechanical data for all experiments are displayed in Appendix II (Fig. A2.1–A2.3). The frictional properties of the SHV andesite were characterised by a sudden increase in shear stress within the first metre of slip. As slip progressed, the shear stress plateaued at 0.50 MPa for ~2 m before it strengthened to a maximum stress of 1.34 MPa at ~10 m of total slip, which coincided with incandescence along the fault contact. This was followed by the growth of melt patches, which eventually coalesced to form a molten zone that extended across the entire slip plane ($T_m$). Upon the formation of a continuous melt layer (at ~10 m of total slip), the SHV andesite exhibited a weakening phase that resulted in a decay of the shear stress of 0.46 MPa (from 1.34 MPa to 0.88 MPa). Further slip was characterised by the shear stress sustaining a steady-state value of 0.88 MPa until the experiment was stopped (from $T_{ss}$ to $T_{15}$). Concurrent with steady-state conditions, continuous axial shortening of the sample at a constant rate of 0.12 mm/s (or 0.12 mm/m) was recorded and resulted in a total shortening of 1.4 mm after $T_{15}$.

The COL andesite and SG dacite showed similar frictional behaviours, despite their differences in bulk-rock composition, and contrasted with the behaviour of the SHV andesite. Both samples displayed an abrupt increase in shear stress during the first few metres of slip, which plateaued at ~0.50 MPa. Shear stress then oscillated around this value for ~9 m before strengthening to a maximum (1.83 MPa for SG and 2.00 MPa for COL) at ~15 m of total slip. Simultaneously, incandescence initiated and melt patches grew, approximately 5 m later than with SHV andesite, which eventually connected to form a single melt layer at ~12 m of total slip ($T_m$). With increased slip distance (> 15 m), both SG and COL samples experienced only minor shear-weakening (0.13 and 0.29 MPa, respectively) and remained at a similar steady-state condition of ~1.70 MPa from $T_{ss}$ to $T_{15}$. Steady-state frictional melting was accompanied by continuous axial shortening at a rate of 0.45 mm/s (or 0.45 mm/m) for both SG and COL samples, almost four times faster than for the SHV andesite, which resulted in a total shortening of 5.3 and 5.5 mm after $T_{15}$, respectively. For all experiments, the distance and time to the onset of melting varied owing to natural mineralogical heterogeneities in the lava samples (Fig. 3.2c; Fig. A2.1–A2.3); thus, for textural and chemical analysis, each frictional melt was normalised with respect to the onset of melting (i.e., $T_m$ = 0 m and 0 s) to allow direct comparison across sample sets.

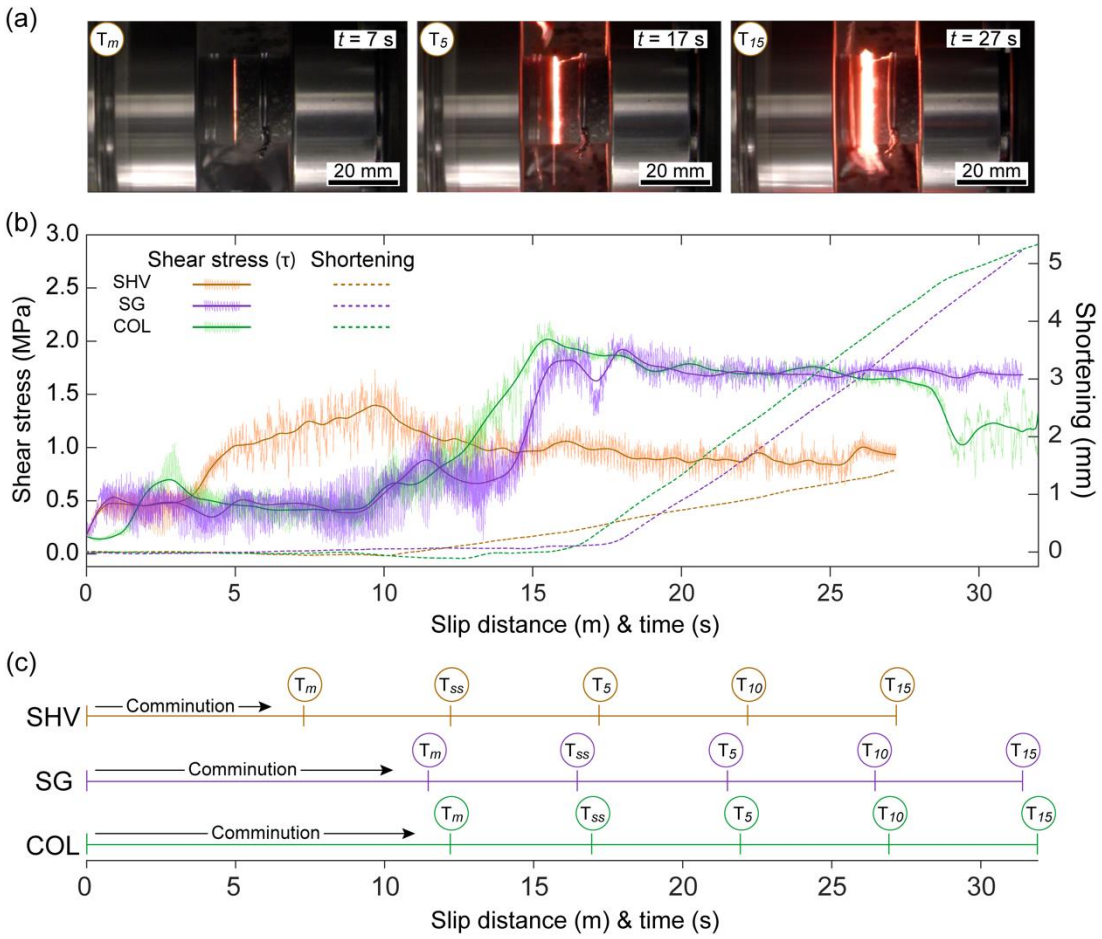


***Figure 3.2*** *– Visual and mechanical observations of frictional melt evolution of the Soufrière Hills Volcano (SHV) andesite, Santiaguito dome complex (SG) dacite, and Volcán de Colima (COL) andesite. (a) Freeze-frames of optical recordings of the simulated fault zone upon stopping the experiment at $T_m$ (melting onset), $T_5$ (5 m of slip at steady-state conditions), and $T_{15}$ (15 m of slip at steady-state conditions). The time (t) refers to the total duration of the experiment. (b) Mechanical data showing the different slip behaviours of the three starting materials, including evolution in shear stress (τ) and experimental sample shortening. Only the mechanical data for $T_{15}$ experiments are displayed for comparison (see Fig. A2.1–A2.3 for all data). (c) Timeline displaying different stages of frictional melting: onset of melting ($T_m$), reaching steady-state conditions ($T_{ss}$), 5 m slip at steady-state ($T_5$), and 10 m slip at steady-state ($T_{10}$), with all data derived from the $T_{15}$ experiment in (b).*

### 3.3.3. Microtextural evolution

SHV andesite produced the thinnest melt zones (0.1–0.4 mm thick), while SG dacite and COL andesite generated thicker frictional melts (0.2–1.0 mm thick). At the onset of melting ($T_m$), the frictional melts exhibited ultra-fine broken crystals (< 5 μm) suspended within a melt that quenched to a glass after the experiment was stopped (Fig. 3.3). These crystal fragments were mineralogically the same as those recorded in the host-rock, except for amphibole, an abundant phase in the SHV andesite, which was not found as a remnant crystal within the entire melt zone. BSE images of the melt zones at $T_m$ showed subtle grey-scale heterogeneities in the frictional melt phase (Fig. 3.3). For frictional melts that reached steady-state ($T_{ss}$), the number of finely suspended clasts had reduced while the melt fraction had increased (Fig. 3.3). Larger crystal fragments (up to 40 μm in diameter), primarily plagioclase, also became more isolated within the melt. From 5 m of steady-state slip onwards ($T_5$–$T_{15}$), all frictional melt zones contained large (up to 80 μm) relic plagioclase fragments that were equant with rounded edges. Partially resorbed rims around these fragments were also a characteristic feature (Fig. 3.3 $T_{10}$ and $T_{15}$). Furthermore, the silica-rich phases observed in the host groundmass of the SHV andesite and SG dacite appear undisturbed in the frictional melts, with their original shape and surficial textures remaining unaltered.

All melt layers contained circular and evenly distributed micro-bubbles, although their sizes and number densities were dependent on the host material involved. The SHV melts displayed consistently large and abundant bubbles that increased in size with slip distance (from < 5 to 14 μm diameter). SG and COL melts showed fewer and smaller bubbles (< 5 μm diameter) with little systematic variation with slip distance. The irregular voids observed in the melt zones (Fig. 3.3) likely reflect an artefact of plucked crystals due to sample polishing and should not be mistaken for vesicles.

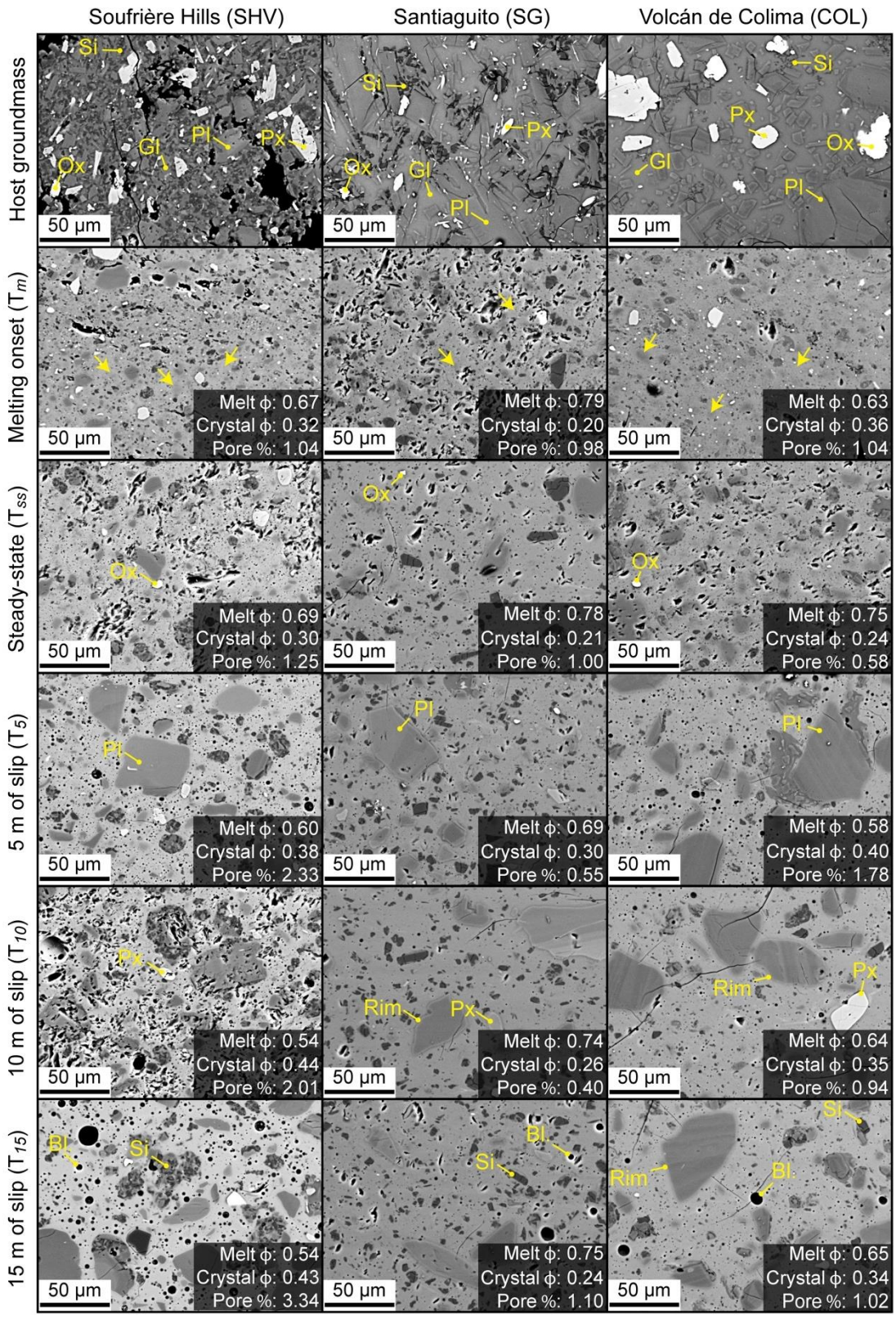


***Figure 3.3*** *– Backscattered electron (BSE) images showing the microtextural evolution of frictional melts from the onset of melting ($T_m$) to 15 m of slip at steady-state conditions ($T_{15}$) for each starting material. The inset text shows the fraction of melt and crystals, along with the percentage porosity of the frictional melt layer (pores/bubbles were defined using a >0.8*

*circularity threshold in imageJ). Labelled phases include: plagioclase (Pl), pyroxenes (Px), Fe-Ti oxides (Ox), silica polymorphs (Si), and interstitial glass (Gl), in addition to bubbles (Bl.) in the melt zone. 'Rim' denotes examples of partially resorbed crystal edges.*

### 3.3.4. Frictional melt compositional variability

The $SiO_2$ concentration of the SHV frictional melts ranged from 54.5 wt.% to 72.3 wt.% (Fig. 3.4a), while the compositions of the SG (Fig. 3.4b) and COL (Fig. 3.4c) frictional melts were more restricted (60.3–72.4 wt.% and 59.5–66.6 wt.%, respectively). Similarly, the ranges in MgO and FeO were 3–4 times larger in the SHV melts compared with the SG and COL melts. For all frictional melts, their composition evolved as slip distance increased, although the style of chemical progression showed a dependence on the starting material. For both the SG and COL melts, as slip distance increased from $T_m$ to $T_{15}$, the variability in melt composition decreased and eventually approached a near-homogeneous equivalent to its bulk-rock composition. Discrepancies between melt composition and the bulk-rock composition were expected, owing to incomplete melting of crystalline fragments (Fig. 3.3). In contrast, the SHV melts became increasingly mafic with time, as reflected by a progressive increase in FeO and MgO. Although compositional discrepancies existed for all frictional melts, binary plots defined a quasi-linear pattern depending on the element oxide (Fig. 3.4). Some element oxide pairs displayed a strong linear relationship (e.g., SHV FeO vs. MgO, SG $SiO_2$ vs. $Al_2O_3$), with compositions located along a classic mixing line between host-rock plagioclase and interstitial glass, while others showed a larger degree of variability away from this trend (e.g., SHV $SiO_2$ vs. $Al_2O_3$, SHV and SG $Al_2O_3$ vs. $Na_2O$). Transects perpendicular to the melt zone were also analysed for compositional variability (Fig. A2.4). These transects recorded a similar trend to that observed in the binary plots, although the higher spatial resolution provided more detail of the extent of melt heterogeneity within a localised area and how it evolved with slip distance. All chemical transects revealed homogenisation towards the bulk-rock composition from $T_m$ to $T_{15}$. However, only in the SHV melt zones that went beyond $T_{ss}$ did the melt composition deviate from that of the bulk-rock, while SG and COL melts maintained a composition close to the precursor material.

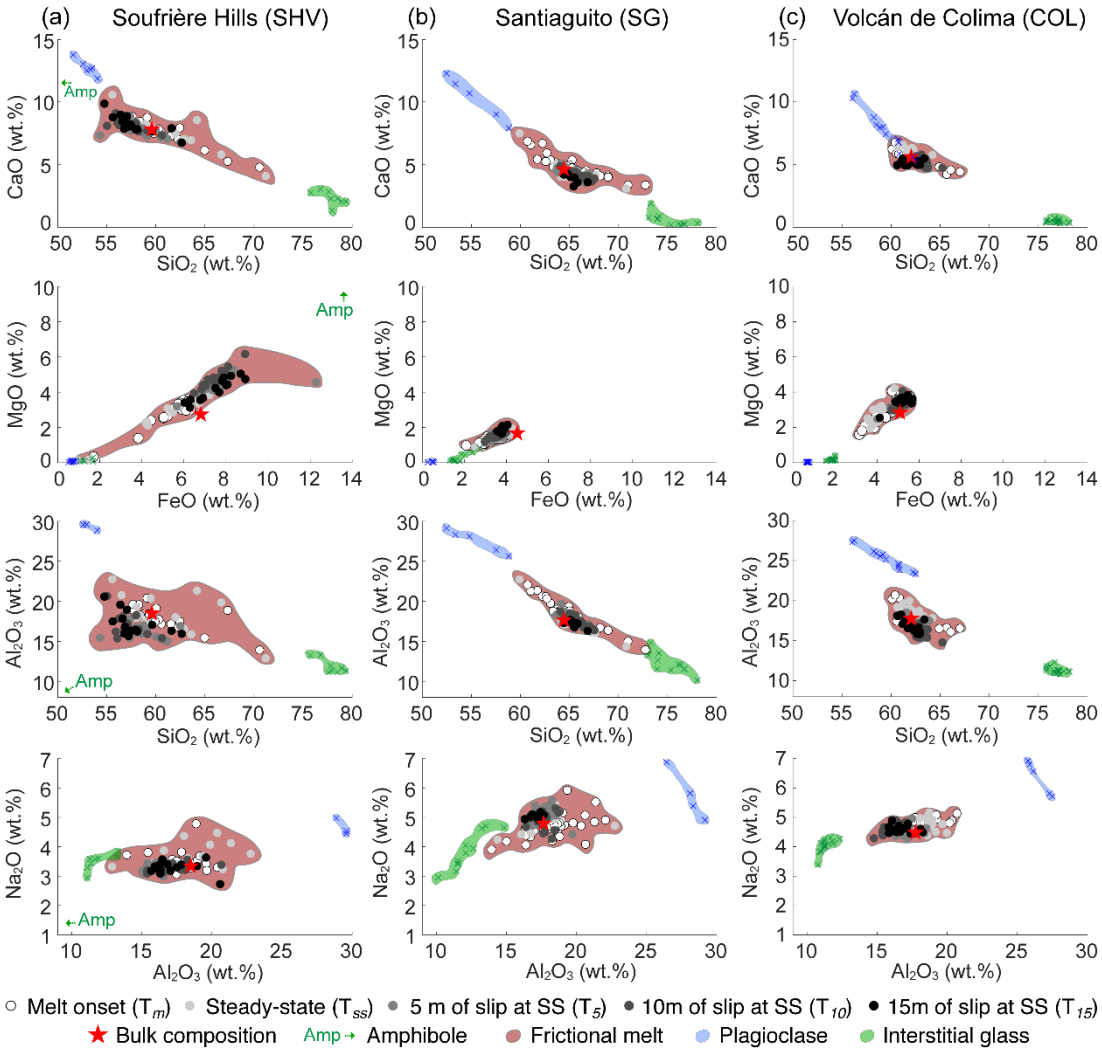


***Figure 3.4*** *– Binary plots showing the evolution in frictional melt composition for representative major element oxides ($SiO_2$, CaO, FeO, MgO, $Al_2O_3$, and $Na_2O$) with increasing slip displacement from the onset of melting ($T_m$) to 15 m of steady-state slip ($T_{15}$). (a) Soufrière Hills Volcano (SHV) andesite, (b) Santiaguito dome complex (SG) dacite, and (c) Volcán de Colima (COL) andesite. For comparison, the composition of host-rock plagioclase, interstitial glass, and amphibole (for SHV only) are plotted, along with the composition of each bulk starting material.*

Evaluating compositional variations through time required careful consideration of all the different components present within the system, as their diffusivities can vary greatly. The standard deviations of concentration across the melt zone for each major element oxide showed an exponential decrease with slip distance (Fig. 3.5). For each starting material, a similar systematic ordering of the decay curves was observed, with $SiO_2$ and $Al_2O_3$ showing the largest variability (Fig. 3.5a, b). This ordering roughly correlated to relative diffusivities of the measured components. The melt derived from the SHV andesite showed the largest standard deviations throughout, with the most homogenous melt compositions at $T_{15}$ being comparable to those at $T_m$ for SG dacite and COL andesite (Fig. 3.5a–f).

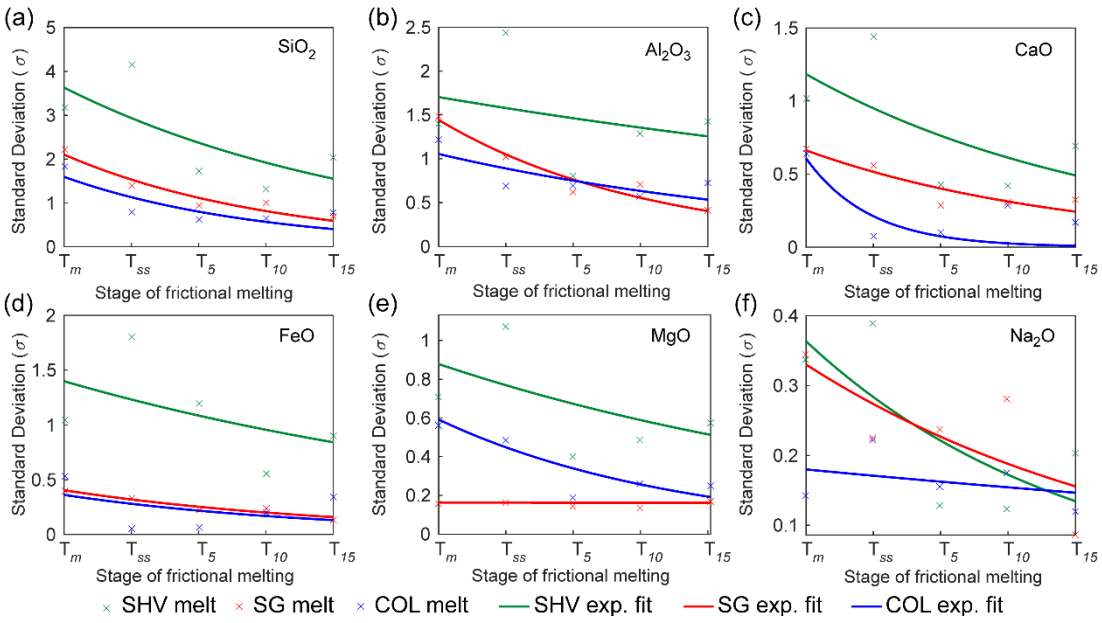


***Figure 3.5*** *– Standard deviations (σ) of compositional variability for the experimental frictional melts as a function of slip distance from the onset of melting ($T_m$) to 15 m of slip at steady-state conditions ($T_{15}$) for the different major components (a–f). The σ for each component decreases with slip duration for all starting materials, modelled using an exponential fit of the data. Frictional melts derived from the Soufrière Hills Volcano (SHV) andesite have the highest σ for all major components, while melts from Santiaguito dome complex (SG) dacite and Volcán de Colima (COL) andesite have the lowest.*

### 3.3.5. Crystal-melt interaction

Areas of interest for electron probe microanalysis (EPMA) and high-resolution synchrotron X-ray spectroscopy were selected, where each crystal phase was in direct contact with the melt zone, to investigate its susceptibility to breakdown and incorporation in the melt zone. Where amphibole crystals were found adjacent to the SHV melt zone, the frictional melt was often twice as thick as anywhere else along the slip plane (Fig. 3.6a). Texturally, amphibole-melt contacts were transitional (Fig. 3.6b), exhibiting: (1) an intact amphibole phenocryst; (2) a partially embayed amphibole, with increased embayment towards the melt zone; and (3) a fully formed frictional melt zone. An EPMA transect across this contact region revealed the direct transfer of amphibole components to the melt, which resulted in a quasi-linear gradational trend for major components (Fig. 3.6c). Components that are low in concentration in these amphiboles (e.g., $Na_2O$) showed only minor influence on melt composition. Element maps along the amphibole-melt contact also depicted the contribution of key elements to frictional melt composition (Fig. 3.6d and Fig. A2.5); in particular, the adjacent melts were enriched with Ca, Fe, and Y, along with minor Ti and Mn. Although K, Sr, Rb, and Zr are incompatible in amphibole, they were still detected in the melt. Fe-Ti oxide crystals in the melt zones appeared less affected by the high temperatures, although they typically showed a subtle halo of Ti-rich melt (Fig. 3.6d).

In contrast to the amphibole-melt relationship, when plagioclase phenocrysts were in contact with the melt zones no embayment textures were observed (Fig. 3.6a); in these areas, the melt layers were often the thinnest (< 50 μm; Fig. A2.6). Plagioclase is similarly abundant in Ca as other phases in the host materials (e.g., amphibole and clinopyroxene), yet its high Sr compatibility allows easy detection and makes its involvement in frictional melt composition distinct. X-ray spectroscopy maps revealed that SG and COL frictional melts were all notably enriched in Sr (Fig. 3.7 and A3.7), although the SHV melts were all relatively Sr poor (Fig. 3.6d, A3.5 and A3.6). Augite (clinopyroxene) and hypersthene (orthopyroxene) were the dominant pyroxene phases in all three host materials (see Electronic Appendix 2). Although pyroxenes are generally similar in composition to amphiboles, importantly they are anhydrous and lacked resorption textures when in contact with the melt zone (Fig. 2.6 and A2.7). In these areas, SG and COL frictional melts were noticeably lower in Ca and Fe and overall less compositionally heterogeneous compared with the SHV melts. Within the SG and COL melts, the contribution of interstitial glass was identified by the high concentration of K, along with zones that showed elevated concentrations of Rb and Zr (Fig. 3.7 and A3.7). However, K, Rb, and Zr were low in concentration in the SHV melts (Fig. 3.6d and Fig. A2.5).

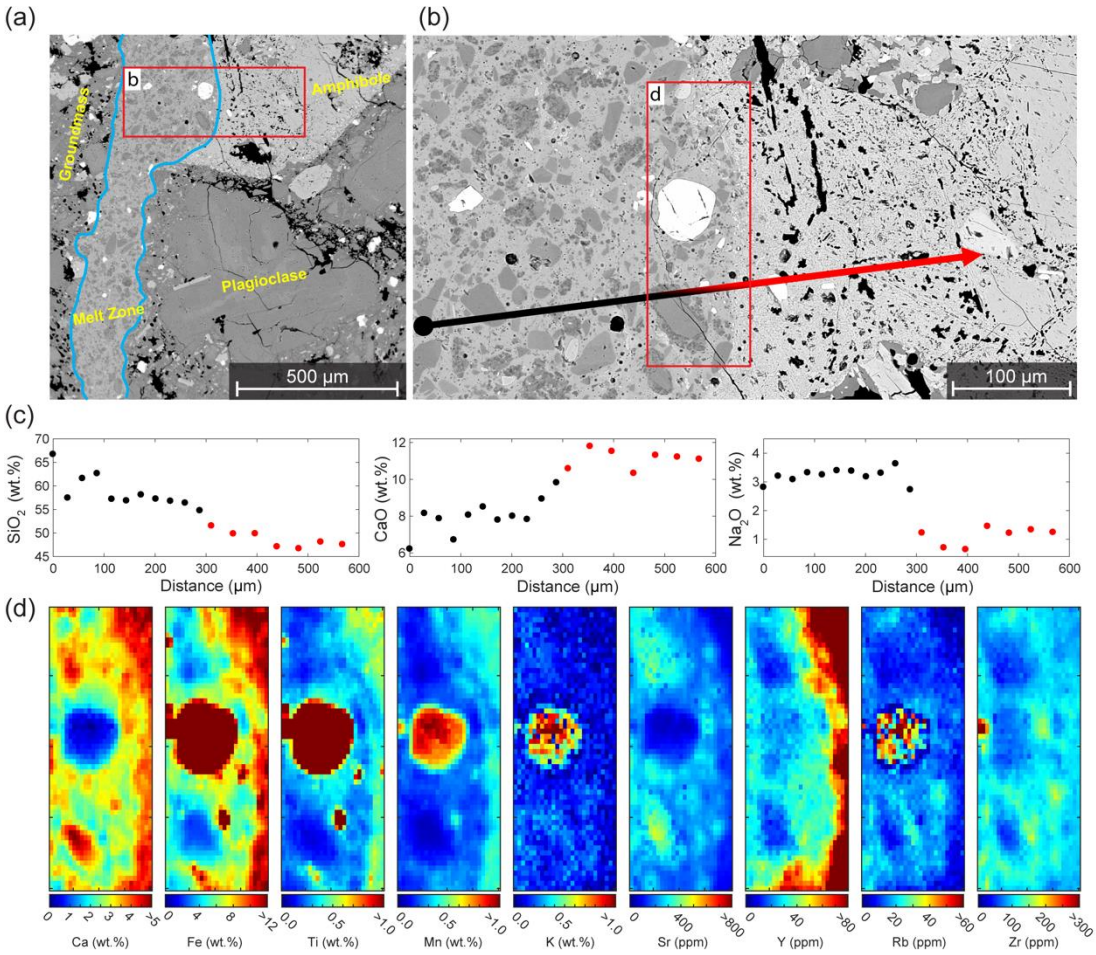


***Figure 3.6*** *– Amphibole-melt interaction during frictional melting of the Soufrière Hills Volcano (SHV) andesite. (a) Backscattered electron (BSE) image of the frictional melt zone after 15 m of slip at steady-state conditions ($T_{15}$), displaying both an amphibole and plagioclase phenocryst on the right side of the melt zone, and groundmass on the left side of the melt zone. (b) BSE image emphasising the nature of the contact between the amphibole and the melt zone displaying textural alteration of the amphibole. (c) Composition of the frictional melt and amphibole phenocryst along the transect labelled by the arrow in (b). (d) Synchrotron X-ray spectroscopy element maps of the amphibole-melt contact as shown in (b).*

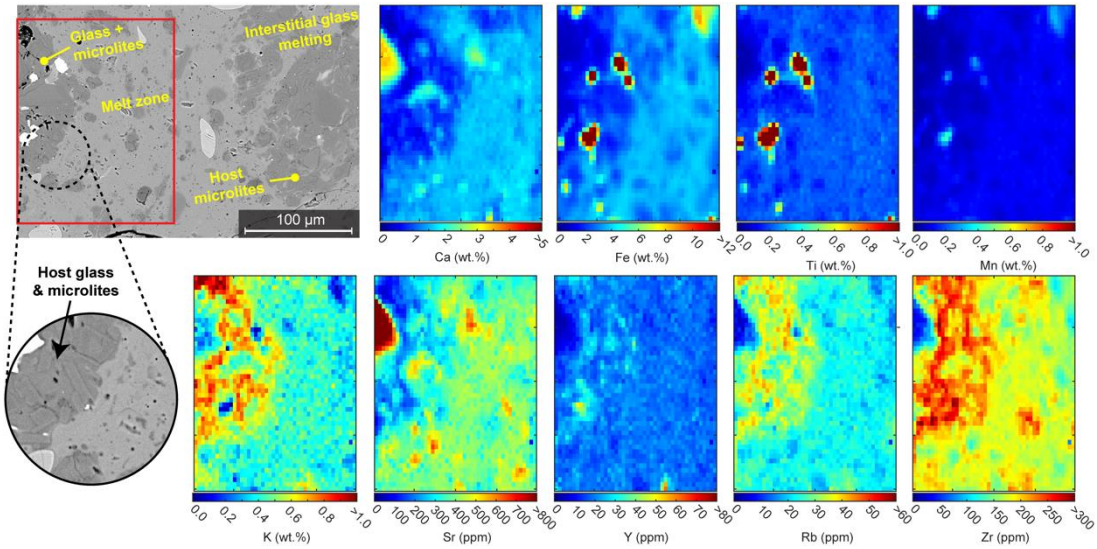


***Figure 3.7*** *– Synchrotron X-ray element maps of Volcán de Colima (COL) andesite frictional melt after 10 m of slip at steady-state conditions ($T_{10}$). The backscattered electron (BSE) image shows the contact between the frictional melt and the host-rock groundmass. The element maps are taken from the outlined area of the BSE image (red box) and depict the contribution of interstitial glass and other groundmass phases to frictional melt composition. Interstitial glass is identified by the highest concentrations of K, Rb, and Zr.*

Mass balance mineral contributions to each frictional melt composition were calculated by applying the adapted least squares petrological mixing program MINSQ (Herrmann & Berry, 2002), using the compositions of host-rock minerals, interstitial glass, and frictional melts from EPMA. Given that the chemical compositions of these phases were expressed as weight percentage of element oxides, modal phase proportions were also calculated as weight percentages. Weight percentages were converted to volume percentages for comparison with measured abundances in the host-rock using the following phase densities (g $cm^{-3}$): amphibole = 3.2, plagioclase = 2.7, clinopyroxene = 3.3, orthopyroxene = 3.5, Fe-oxide = 5.2, quartz (for Si-phases) = 2.6 and glass = 2.4. In the least squares calculations, frictional melt compositions from each experiment were used as the target composition and the host-rock minerals and interstitial glass as the contributing phases. Figure 3.8 shows the major contributing phases for the entire range of compositions measured in each sample suite and how their abundance evolved with slip distance. From these results, calcic-amphibole (hornblende) was shown to be a key component of the SHV melt composition, with the measured melts estimated to have a 0–27 vol.% amphibole contribution (Fig. 3.8a). At the early stages of melting ($T_m$–$T_{ss}$), an average of 6–7 vol.% amphibole was estimated to contribute to the frictional melt composition, but after steady-state melting was achieved, up to 27 vol.% amphibole was incorporated into the melt, consistent with the evolution observed

in the binary plots (Fig. 3.4a). Plagioclase dominated the frictional melt modal compositions in all samples (Fig. 3.8b), albeit under-represented relative to the bulk mineralogy. There was a general decrease in plagioclase abundance and variability with slip distance, which averaged between 43 and 50 vol.% at $T_{15}$ for each starting material. Interstitial glass was the second-most influential phase on melt composition, which appeared to be overrepresented relative to the bulk-rock (Fig. 3.8c). Similar to plagioclase, the contribution range of interstitial glass to melt composition became less variable with slip distance; however, the evolutionary trends between the three sample sets were different. SHV melts showed an average decrease in glass contribution with slip distance (from 43 to 35 vol.%), while the proportions of glass in both SG and COL melts increased (from 31 to 44 vol.% and 31 to 36 vol.%, respectively). All frictional melts showed an increase in orthopyroxene (hypersthene) melting with slip distance (Fig. 3.8d), although SG and COL melts were underrepresented compared with the bulk. Clinopyroxene (augite) had only a minor involvement in the compositions of the SHV and SG melts; however, the COL melts showed a more significant clinopyroxene contribution (Fig. 3.8e), consistent with its occurrence as large phenocrysts in the COL andesite. Fe-Ti oxides represented a minor component of all melt compositions, yet still revealed a subtle increase with slip distance (Fig. 3.8f).

The same least squares model was employed to approximate a theoretical proportion of phases required to further melt and incorporate with the frictional melts to obtain the bulk-rock composition. The measured fraction of homogenised frictional melt (quantified using BSE images) was combined with the compositions of crystal fragments remaining in the melt zone to obtain the following:

$$1\ SHV\ Bulk = 0.53\ Melt + 0.33\ plag + 0.05\ glass\ matrix + 0.06\ qtz + 0.02\ Ti\ mag + 0.02\ opx(Hyp) \pm cpx(Aug) \quad (3.5)$$

$$1\ COL\ Bulk = 0.65\ Melt + 0.24\ plag + 0.08\ qtz + 0.01\ Ti\ mag + 0.02\ opx(Hyp) \pm cpx(Aug) \quad (3.6)$$

$$1\ SG\ Bulk = 0.53\ Melt + 0.29\ plag + 0.13\ qtz + 0.03\ Ti\ mag + 0.02\ opx(Hyp) \pm cpx(Aug) \quad (3.7)$$

These estimated phase proportions were consistent with observations seen in BSE images of the melt zone at $T_{15}$ (Fig. 3.3).

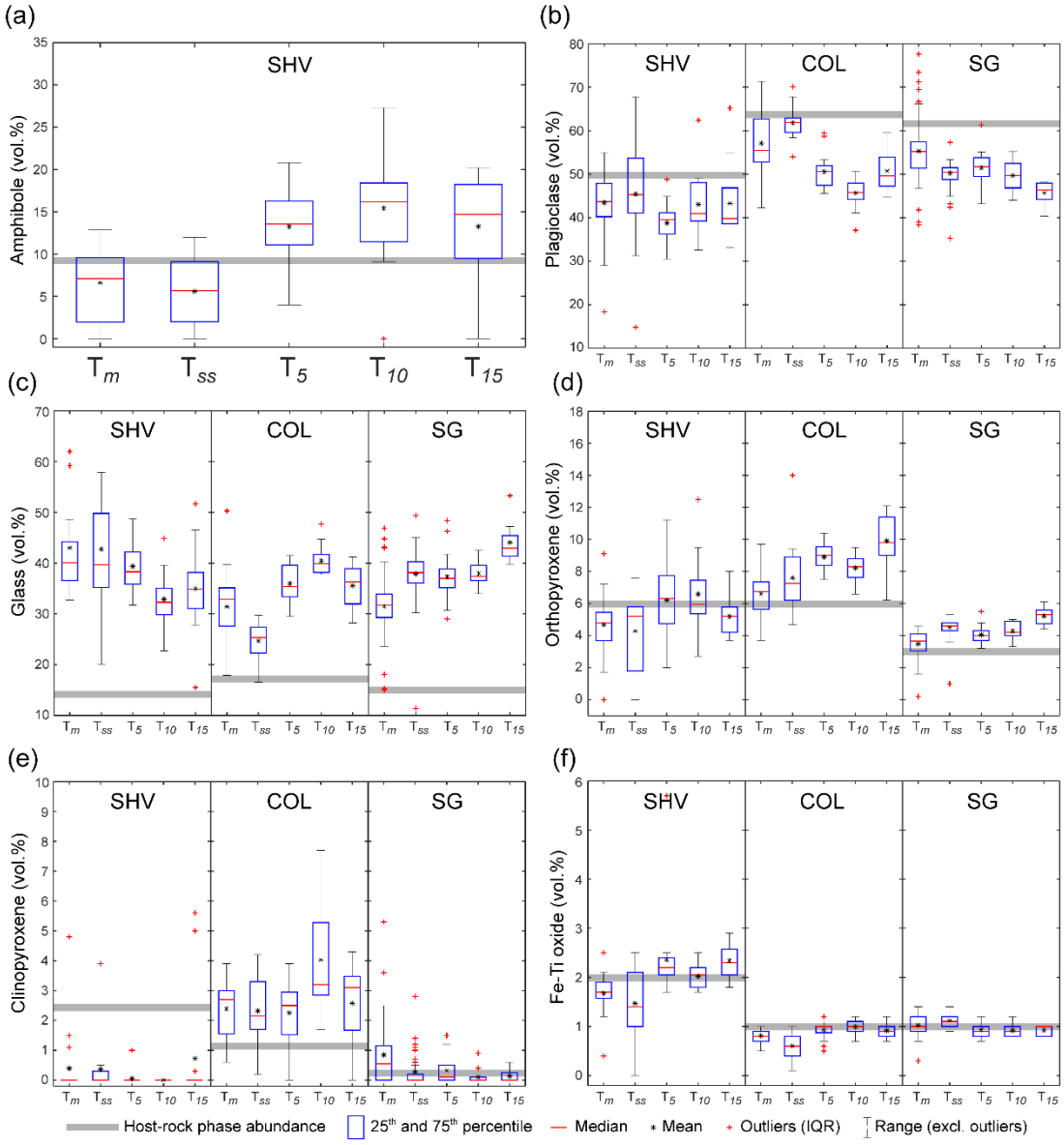


***Figure 3.8*** *– Box plots showing the contribution of the different minerals and glass phases to the frictional melt composition calculated using the least squares petrological mixing program MINSQ (Herrmann & Berry, 2002). The phases contributing to the frictional melt derived from Soufrière Hills Volcano (SHV) andesite, Santiaguito dome complex (SG) dacite, and Volcán de Colima (COL) andesite, include: (a) amphibole (hornblende), (b) plagioclase, (c) interstitial glass, (d) orthopyroxene (hypersthene), (e) clinopyroxene (augite), and (f) Fe-Ti oxides. All estimated phase abundances are compared to the respective abundances of the host rocks. Outliers were detected using the interquartile range (IQR) rule.*

### 3.3.6. Rheological response of frictional melt

Silicate melt viscosity is primarily determined by chemical composition. Frictional melt viscosities were estimated using the empirical equation of Giordano *et al.* (2008). Owing to the large compositional heterogeneities for melts formed between $T_m$ and $T_{ss}$, obtaining a single value for melt viscosity for these melts is challenging. However, the more homogenous melt compositions at $T_{15}$ formed the closest to an equilibrium state, which permitted a more robust approximation for the temperature-dependence of viscosity.

Figure 3.9a–c displays the temperature-viscosity relationships for the homogenised frictional melts for each starting material, plus felsic and mafic melt filaments formed at the onset of melting which act as viscosity end-members. For comparison, viscosities were also calculated for the interstitial glass and molten bulk-rock. The relative effect of solid particles suspended in the melt (estimated using Costa *et al.*, 2009) was added to the temperature-dependence of melt viscosity derived from Giordano *et al.* (2008) to model its apparent viscosity. For the homogenised frictional melts at $T_{15}$ derived from SHV, COL, and SG samples, the presence of crystals added 0.92, 0.63, and 0.36 orders of magnitude to the viscosity, respectively (Table 3.3). Through calculating an apparent viscosity derived from the mechanical data (Eq. 3.1) and comparing these values to the modelled temperature-dependent viscosity curves for each sample (Fig. 3.9a–c), estimates of the temperature range for the frictional melts during steady-state slip were obtained. The SHV melts had an estimated viscosity range of 1.95–2.17 [log Pa s] across a wide temperature range from 1270 ºC (for a crystal-free melt) to 1510 ºC (if the melt contained up to 45 vol.% crystal suspensions; Table 3.3). SG and COL melts revealed overlapping viscosity ranges (of 2.33–2.54 and 2.41–2.73 [log Pa s], respectively), which were consistently higher than the SHV melts. However, estimated temperatures for both SG and COL melts differed significantly from 1400 ºC to 1510 ºC and 1280 ºC to 1440 ºC, respectively. It is important to note that these viscosities, and thus temperature ranges, could be a slight overestimate owing to the possible underestimation of the melt zone thickness (as required for strain rate calculations; Eq. 3.2). Figure 3.9d shows the effect of increasing water content on the temperature-dependent modelled apparent viscosity of the homogenised SHV frictional melt suspension. It demonstrates that if the SHV melts contained water, the modelled apparent viscosities would be lower; thus, the SHV melt zones would require a lower temperature to achieve the apparent viscosities measured using the mechanical data (Eq. 3.1).

***Table 3.3*** *– A summary of the experimental conditions along with mechanical and rheological data measured for each high-velocity rotary shear (HVR) experiment: SHV = Soufrière Hills Volcano andesite; COL = Volcán de Colima andesite; SG = Santiaguito dome complex dacite.*

| Experiment | Max. shear stress (MPa)[a] | Steady-state shear stress (MPa)[a] | Total slip distance (m) | Total shortening (mm) | Melt zone thickness (avg.; mm)[b] | Crystal fraction[c] | RPM | Outer diameter (mm) | Inner diameter (mm) | $V_e$ (Rotation Velocity; m $s^{-1}$)[d] | ($\dot{\varepsilon}$) Strain rate ($s^{-1}$)[e] | Relative viscosity (Log Pa s)[f] | HVR apparent viscosity (Log Pa s)[g] |
|---|---|---|---|---|---|---|---|---|---|---|---|---|---|
| SHV $T_m$ | 1.08 | - | 10.8 | 0.00 | 0.30 | 0.32 | 1043 | 24.94 | 9.32 | 1.00 | 4.1E+03 | 0.55 | - |
| SHV $T_{ss}$ | 1.25 | 0.92 | 16.7 | 0.08 | 0.30 | 0.30 | 1044 | 24.96 | 9.27 | 1.00 | 6.4E+03 | 0.50 | 2.16 |
| SHV $T_5$ | 1.27 | 0.88 | 17.6 | 0.18 | 0.30 | 0.38 | 1044 | 24.97 | 9.29 | 1.00 | 6.8E+03 | 0.72 | 2.11 |
| SHV $T_{10}$ | 1.24 | 0.87 | 25.5 | 0.46 | 0.30 | 0.44 | 1044 | 24.96 | 9.30 | 1.00 | 9.8E+03 | 0.97 | 1.95 |
| SHV $T_{15}$ | 1.34 | 0.88 | 27.2 | 1.43 | 0.30 | 0.43 | 1044 | 24.94 | 9.26 | 1.00 | 1.0E+04 | 0.92 | 1.93 |
| COL $T_m$ | 1.07 | - | 9.30 | 0.01 | 0.25 | 0.36 | 1047 | 24.97 | 9.02 | 1.00 | 4.3E+03 | 0.65 | - |
| COL $T_{ss}$ | 1.12 | 0.73 | 12.1 | 0.01 | 0.55 | 0.24 | 1047 | 24.96 | 9.13 | 1.00 | 2.5E+03 | 0.36 | 2.46 |
| COL $T_5$ | 1.88 | 1.50 | 18.1 | 1.49 | 0.55 | 0.40 | 1044 | 24.97 | 9.25 | 1.00 | 3.8E+03 | 0.79 | 2.60 |
| COL $T_{10}$ | 2.11 | 1.68 | 23.0 | 3.34 | 0.55 | 0.35 | 1047 | 24.98 | 9.19 | 1.00 | 4.8E+03 | 0.63 | 2.54 |
| COL $T_{15}$ | 2.00 | 1.70 | 32.2 | 5.53 | 0.50 | 0.35 | 1044 | 24.95 | 9.20 | 1.00 | 7.4E+03 | 0.63 | 2.36 |
| SG $T_m$ | 1.30 | - | 16.0 | 0.11 | 0.35 | 0.20 | 1046 | 24.96 | 9.12 | 1.00 | 5.2E+03 | 0.28 | - |
| SG $T_{ss}$ | 1.89 | 1.78 | 21.9 | 0.29 | 0.50 | 0.21 | 1044 | 24.99 | 9.18 | 1.00 | 5.0E+03 | 0.30 | 2.55 |
| SG $T_5$ | 1.78 | 1.44 | 21.9 | 1.05 | 0.45 | 0.30 | 1053 | 24.83 | 8.98 | 1.00 | 5.5E+03 | 0.50 | 2.41 |
| SG $T_{10}$ | 1.90 | 1.71 | 27.3 | 3.39 | 0.45 | 0.26 | 1035 | 24.96 | 9.72 | 1.00 | 7.0E+03 | 0.40 | 2.39 |
| SG $T_{15}$ | 1.91 | 1.70 | 31.4 | 5.22 | 0.45 | 0.24 | 1044 | 24.94 | 9.28 | 1.00 | 8.0E+03 | 0.36 | 2.33 |

[a] *Maximum and steady-state shear stress values are an average of the peak and steady-state portion of the curves in Figs. A3.1–A3.3, respectively.*

[b] *Melt zone thickness estimated from optical images and averaged using multiple transects perpendicular to the slip surface; to ensure accuracy, measurements were only taken where melt was is in direct contact with the bulk material on both sides.*

[c] *Crystal fractions quantified using SEM-BSE images of the melt.*

[d] *Equivalent rotation velocities ($V_e$) were used to calculate displacement rates (Eq. 3.4) after Shimamoto and Tsutsumi (1994).*

[e] *Strain rates ($\dot{\varepsilon}$) were calculated for slip during steady-state conditions (Eq. 3.2) using an equivalent diameter ($D_e$; Eq. 3.3), melt thickness, and slip duration.*

[f] *Relative effect of crystals suspended within the frictional melt on melt viscosities were estimated by applying the method of Costa et al. (2009) and the parameterised experimental data of Caricchi et al. (2007), using measured crystal fractions and calculated strain rate data.*

[g] *HVR apparent viscosities were calculated from the mechanical data using Eq. 3.1 for steady-state conditions.*

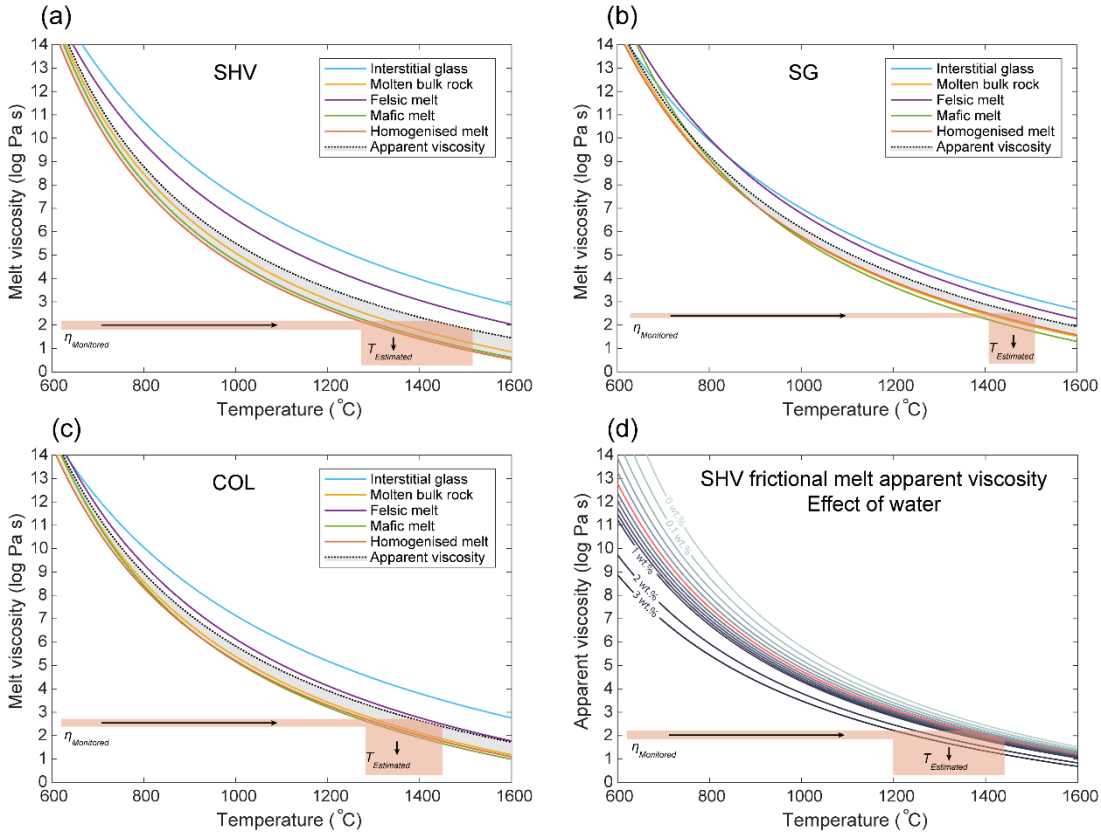


***Figure 3.9*** *– Non-Arrhenian temperature dependence of viscosity of the experimental frictional melts. Viscosities were calculated using the GRD viscosity model of Giordano et al. (2008) for melts derived from the frictional melting of (a) Soufrière Hills Volcano (SHV) andesite, (b) Santiaguito dome complex (SG) dacite, and (c) Volcàn de Colima (COL) andesite. The chemical compositions of the frictional melts, derived by electron probe microanalysis, were used as input parameters, including the most mafic and felsic melts from the onset of melting ($T_m$) and the homogenised frictional melts after 15 m of steady-state slip ($T_{15}$). The relative effect of crystals on melt viscosity was modelled considering crystal fraction and strain rate following the method of Costa et al. (2009); these relative viscosities were added to the homogenised melt curves to produce a modelled apparent viscosity. The modelled apparent viscosities of the frictional melt suspensions were compared with the mechanically constrained apparent viscosities (Eq. 3.1; $\eta_{Monitored}$), providing an estimated temperature of the frictional melt zone ($T_{Estimated}$). (d) Effect of different water contents on the apparent viscosity of SHV frictional melt owing to the presence of hydrous amphibole melting. The red line indicates 0.5 wt.% $H_2O$ based on 27 vol.% amphibole melting for frictional melts at $T_{15}$.*

## 3.4. DISCUSSION

### 3.4.1. Mechanisms driving frictional melting of volcanic rocks

Amongst the many studies that exist on tribological instabilities, dynamic fault slip events are typically described using a rate- and state-dependent friction law (e.g., Dieterich, 1979; Rice *et al.*, 2001; Ohmura & Kawamura, 2007; Popov *et al.*, 2012). Previous experimental investigations on the frictional properties of igneous, metamorphic, and sedimentary rocks have highlighted their dynamic evolution with increasing displacement, a consequence of thermal instabilities brought about by frictional heating and subsequent melting (e.g., Tsutsumi & Shimamoto, 1997; Hirose & Shimamoto, 2005; Di Toro *et al.*, 2011; Niemeijer *et al.*, 2011; Chen *et al.*, 2017; Lockner *et al.*, 2017). Furthermore, the frictional behaviour of both intrusive and extrusive igneous rocks at coseismic slip rates (> 0.1 m $s^{-1}$) has been shown to inherit complex transient regimes in the form of both shear-weakening and strengthening (e.g., Tsutsumi & Shimamoto, 1997; Hirose & Shimamoto, 2005; Kendrick *et al.*, 2014b; Hornby *et al.*, 2015; Chen *et al.*, 2017). Analogous to these reports, the frictional behaviour of the three mineralogically contrasting lavas in the present study can be divided into three discrete stages: (1) an initial steady-state regime; (2) a shear-strengthening regime; and (3) a final shear-weakening to steady-state slip regime. The timing and intensity of each of these stages is material dependent. The SHV andesite experienced only a minor stage 1, lasting just 1–2 m of slip, whereas the SG dacite and COL andesite spent ~10 m at this stage. The transition to stage 2 was similar in all cases, although SG and COL samples continued to strengthen to a higher peak stress and underwent only minor shear-weakening during stage 3. In contrast, the SHV andesite reached a lower shear stress and experienced a more distinct shear-weakening step during stage 3. These observations were similar to previous studies of volcanic rocks, with their differences in slip properties attributed to a contrast in mineral assemblage and the presence of an interstitial glass (Kendrick *et al.*, 2014b). The work of Spray (1992) highlighted the significance of a host material's constituent minerals on frictional properties. Accordingly, a hierarchy of frictional melting susceptibility for a range of common rock-forming minerals was constructed, taking into account their shear strength, fracture toughness and most importantly melting point. Applying this hierarchy to the individual phases of the three lavas in this study, the theoretical order of phases preferentially affected during frictional sliding would be rhyolitic glass ($T_g$ = 740–770 ºC, estimated using Giordano *et al.* (2008) as a viscosity gauge for $10^{12}$ Pa s; Fig. 3.9a–c), calcic-amphibole (hornblende; ~750–1000 ºC), plagioclase ($An_{40}$–$An_{90}$; ~1280–1500 ºC), clinopyroxene (augite; ~1400 ºC), orthopyroxene (hypersthene; ~1425 ºC), Fe-Ti oxides (~1600 ºC), and Si-polymorphs ($SiO_2$; ~1700 ºC). However, due to the fast heating rates involved during

frictional heating and melting, the $T_g$ for the rhyolitic interstitial glass may be momentarily higher than the melting temperature of amphibole.

The marked increase in shear stress at the onset of friction is attributed to the initial interaction of asperities on the slip surfaces, which led to subsequent comminution of the host-rock and likely coincided with minor plucking of minerals. In the SHV andesite, amphibole was the mineral most susceptible to grain size reduction owing to its lower fracture toughness and yield strength (Spray, 1992); for SG and COL samples, the mechanically weakest mineral was plagioclase (Spray, 1992). Additionally, the high abundance of silica phases in the groundmass of the SHV andesite (due to glass devitrification) likely had more of a physical effect at the early stages of slip than an unaltered glass. This micromechanical response resulted in the formation of a cataclastic gouge layer on the contact surface (e.g., Hetzel *et al.*, 1996; Spagnuolo *et al.*, 2016), which acted as a lubricant and permitted minor shear-weakening that led to near steady-state shear stress within the first few metres of slip (e.g., Reches & Lockner, 2010; Lavallée *et al.*, 2014). Frictional heating caused an abrupt shear-strengthening attributed to volumetric expansion of the sample (as seen in the shortening data; Fig. 3.2b) and the first production of a melt on the slip plane. The preferential melting of ultra-fine crystal fragments, due to their larger surface area (Spray, 1992), generated molten patches on the slip surface (Tsutsumi & Shimamoto, 1997; Hirose & Shimamoto, 2005; Chen *et al.*, 2017). These melt patches behaved as a preliminary viscous brake and caused the shear stress to rise to a maximum (Tsutsumi & Shimamoto, 1997; Fialko & Khazan, 2005; Hirose & Shimamoto, 2005). Owing to the ubiquitous occurrence of amphibole in the SHV andesite, this process took place ~5 m (5 s) earlier than in the experiments with the SG dacite and COL andesite. This shorter slip distance required to generate melt could be related to a higher rate of comminution followed by the preferential melting of the amphibole fraction. It has also been postulated that the release of water from the melting of hydrous phases could facilitate this stage (e.g., Allen, 1979; Hetzel *et al.*, 1996). As the temperature increased concurrently with shear stress, melt patches began to coalesce upon increased melting, resulting in a molten layer with abundant crystal fragments, as seen at the onset of melting ($T_m$; Fig. 3.3). With further melting, a fully formed frictional melt separated the two sliding surfaces, owing to an increase in the volume of melt to crystals, until a critical melt fraction is reached (Fialko & Khazan, 2005; Rosenberg & Handy, 2005; Chen *et al.*, 2017). Thickening of the molten layer accompanied by increased melting caused a decrease in shear stress towards a steady-state condition (e.g., Tsutsumi & Shimamoto, 1997), which increased the distance between the two opposing interfaces (referred to as the Stefan problem; e.g., Hirose & Shimamoto, 2005). At this stage, slip behaviour was dependent on the viscosity of the melt, which in turn was influenced by the strain rate in the slip zone. The SHV andesite showed a larger shear-

weakening response (0.46 MPa) compared with SG dacite (0.13 MPa) and COL andesite (0.29 MPa), which matched the variation in estimated frictional melt viscosities for each material (Fig. 3.9; Table 3.3). From this stage on, the ability of the slip zone to sustain a molten layer was determined by the heat produced by shear heating rather than solid friction (Hirose & Shimamoto, 2005). Microstructural evidence of a reduction in finer crystal fragments upon steady-state melting confirmed this (Fig. 3.3), suggesting that intense comminution was no longer in action. Steady-state conditions were marked by a sudden increase in melt production as maximum temperatures were reached. Here, comminution was replaced by tearing of crystals along the slip interface. Consequently, large angular crystal fragments, derived from the host material, became isolated within the molten layer (from $T_{ss}$ onwards; Fig. 3.3) and their outer edges subsequently became rounded by combined attrition and melting (Lin, 1999), a characteristic feature of natural pseudotachylytes (e.g., Sibson, 1975). Melting of the outer edges of plagioclase fragments generated the resorbed rim textures (Fig. 3.3), which demonstrated that these fragments were subjected to temperatures exceeding their equilibrium conditions. The thickening of the melt zone and change in shape of the rock-melt interface towards steady-state conditions was an important characteristic that likely altered the roughness of the fault plane and affected the frictional properties (i.e., flow rheology). Such a change in melt-surface topography was most noticeably brought about by the interaction of amphibole crystals with the melt zone (Fig. 3.6a). Amphibole embayment along with a consistently thicker melt zone adjacent to amphibole crystals provided evidence for its selective melting (e.g., Spray, 1992). Similar textures have been related to the Gibbs-Thomson effect (Hirose & Shimamoto, 2003), by which the local melting temperature of a mineral's external surface—when in contact with the melt zone—is reduced. In contrast, plagioclase crystals showed less textural evidence for melting, expressed as a thinner melt layer where plagioclase phenocrysts are adjacent to the slip zone (Fig. 3.6 and Fig. A2.6). The variation in final melt thickness between each sample set corresponded to the amount of shortening experienced during the experimental run (Fig. 3.2b). However, it is possible that the melt thickness measured may not be fully representative because the melt zone may have been compressed slightly after the experiment ceased, while a normal stress (1 MPa) was still being applied.

### 3.4.2. Selective phase melting and preferential melting of amphibole

Frictional melting has long been portrayed as a disequilibrium selective mineral melting process (Shimamoto & Lin, 1994; Lin & Shimamoto, 1998), yet the influence of discrete phases on the mechanics of frictional melt production during faulting remains an area that is not fully constrained (e.g., Jiang *et al.*, 2015). Here, we relate mechanical and

compositional progression of frictional melting to the presence or absence of amphibole in the host material. Although interstitial glass was more abundant in the SG dacite and COL andesite than in the SHV andesite, it was likely to have a secondary role on the mechanical properties when amphibole was present; this may be a consequence of the high heating rates involved, limiting the timescale of structural relaxation of the glass, and possibly resulted in $T_g$ being higher than the melting point of amphibole (e.g., Dingwell & Webb, 1989; Lavallée *et al.*, 2015b). Previous HVR experiments on the frictional melting of andesites and dacites that were both glass-rich and amphibole-rich (e.g., Kendrick et al., 2014b; Hornby et al., 2015) recorded similar mechanical behaviours to the SHV andesite in this study, supporting the theory that hydrous minerals have a primary control on frictional behaviour. The absence of amphibole fragments hosted within the SHV frictional melt supports the disequilibrium melting model of Spray (1992), where amphibole has the lowest melting point; other studies also reported the lack of ferromagnesian hydrous fragments in experimental melts and natural pseudotachylytes (e.g., Scott & Drever, 1953; Sibson, 1975; Hetzel *et al.*, 1996; Hirose & Shimamoto, 2005; Jiang *et al.*, 2015). The composition of the melts can thus be related to the chemical components that were derived from melting of the different host-rock phases, as revealed by the least squares model (Fig. 3.8).

All melt compositions showed a near-linear relationship between the composition of the interstitial glass and plagioclase (Fig. 3.4), suggesting that these two phases were influential in the melting process. However, a deviation from this trend may have come from either a combination of contrasting mobilities of different chemical elements, referred to as diffusive fractionation (e.g., Perugini *et al.*, 2006; Morgavi *et al.*, 2013; Perugini *et al.*, 2013), or the interaction of mafic minerals (e.g., amphiboles, pyroxenes, and Fe-Ti oxides). The high level of Sr in the SG and COL frictional melts confirms the dominance of plagioclase melting. Additionally, the elevated K, Rb, and Zr concentrations in these melts demonstrates melting of the interstitial glass was integral during frictional melting of SG dacite and COL andesite; this is consistent with the higher abundance of K-rich interstitial glass in their host material. A low concentration of K, Sr, Rb, and Zr in the SHV frictional melts suggests melting of plagioclase and glass was more limited, consistent with less interstitial glass in the host material, as the preferential melting of amphibole proceeded. Interestingly, the composition of the SHV melt at the onset of melting showed only minor amphibole influence based on lower ferromagnesian components (Fig. 3.4); this is supported by the least squares model (Fig. 3.8a). This lack of amphibole contribution was likely due to the absence of amphibole phenocrysts adjacent to or on the slip plane. With slip progression, an overall increase in FeO, MgO, and CaO, along with a slight decrease in $Al_2O_3$, suggests an increased amphibole contribution, which also corresponds to the increase in bubble content. Homogenisation

towards the host's bulk composition, which has been proposed previously (e.g., Spray, 1992; Hirose & Shimamoto, 2005), appeared to be the case upon steady-state melting ($T_{ss}$) due to increased mixing efficiency. However, due to preferential amphibole melting in the SHV andesite, the melt composition became more mafic with time. This contrasts with the interpretation of Jiang *et al.* (2015), who suggested that melts will become progressively more felsic with time if hydrous phases are present. An increased amphibole input was likely the result of the conduction of heat through the sample. High temperatures would have initiated along the fault plane, which would only allow phases exposed to the contact surface to melt (i.e., plagioclase and glass). However, as melting progressed, a strong thermal gradient between the melt zone and the host-rock surface likely formed (e.g., Nielsen *et al.*, 2008). Consequently, any heat being transferred through the host's wall may have been limited to a small distance from the interface where temperatures may not have been high enough to melt most minerals that were directly adjacent to the melt zone. However, as amphiboles have a significantly lower melting temperature compared with the other phases (750–1000 ºC; Spray, 1992), these minerals were likely still affected even if temperatures were a few hundreds of degrees lower than in the melt zone interior. The textures observed in Figure 3.6b confirm this, where amphibole began to melt ~200 µm away from the melt zone. A similar effect has been observed on landslide slip surfaces, in which minerals directly beneath the fault plane had thermally decomposed due to frictional heating (Hu *et al.*, 2018). It is also possible that mafic melt filaments that formed at the onset of melting could have been compromised owing to rapid diffusion related to low viscosities (e.g., Rossi *et al.*, 2017), unlike more felsic filaments with higher viscosities; this may further explain the apparent lack of amphibole signature at the onset. However, the mafic trend with slip progression opens a potential case for amphibole-bearing rocks not being able to (or required to) produce frictional melt temperatures high enough for efficient bulk melting, creating a feedback that encourages mafic compositions.

Compositional trends for the SG and COL melts fit the expected evolution towards homogeneity and bulk-rock composition with increasing slip distance. Although these melts initially had a hybridised composition between plagioclase and interstitial glass, an increase in FeO and MgO with time confirms the melting of pyroxenes. The lack of a CaO trend for these melts suggests the contribution of orthopyroxene to frictional melt composition dominated over clinopyroxene, which corresponds to the relative modal fractions in the host materials. Although clinopyroxene (augite) and orthopyroxene (hypersthene) have similar estimated melting temperatures (~1400 ºC and ~1425 ºC, respectively), orthopyroxene generally has a lower yield strength and shear strength (Spray, 1992), which may have favoured faster comminution and subsequent melting from the onset of slip. The presence of

silica phases suspended in the SHV and SG frictional melts (derived from the host's groundmass; Fig. 3.3) confirms the higher temperatures required to melt them (> 1700 ºC). However, mass balance calculations for the SG frictional melt suggest that some melt filaments required up to 28 vol.% of a pure silica phase to obtain its composition. From the temperature-viscosity model (Fig. 3.9), estimated temperatures of the molten layer rarely exceeded 1500 ºC. However, Lee *et al.* (2017) showed that the melting temperature of quartz could be suppressed by > 200 ºC owing to preferential melting of finer quartz fractions and conversion to a meta-stable β-quartz, referred to as quasi-equilibrium melting.

### 3.4.3. Chaotic mixing and chemical homogenisation during frictional melting

The evolution of frictional melt composition during the progressive melting of chemically discrete phases is governed by a dynamic chaotic mixing phenomenon, akin to magma mixing (e.g., Perugini *et al.*, 2003; De Campos *et al.*, 2011). In recent years, chaotic mixing between mafic and felsic silicate melts has been constrained experimentally to assess the timescales of chemical homogenisation during magma mixing events (e.g., Morgavi *et al.*, 2013; Perugini *et al.*, 2013; Rossi *et al.*, 2017). The diffusivities of the different major elements alone would not permit the chemical exchanges observed over the timescales of frictional melting in our experiments (< 20 s); thus, physical mixing must play a fundamental role. At the onset of melting ($T_m$), the formation of melt filaments within the molten layer generated compositional gradients; via shearing, these filaments began to stretch and fold, which increased the surface area to enhance chemical diffusion. Owing to different element diffusivities, this may have caused a diffusive fractionation resulting in melts with a hybridised composition (Perugini *et al.*, 2006; Perugini *et al.*, 2008; Perugini *et al.*, 2013). In a simple case, the mixing of two melts (with one component) should form linear trends in binary plots (e.g., Fourcade & Allègre, 1981). However, due to the fractal distribution of melt filaments and a frictional melt consisting of more than two end-members with multiple components, a non-linear trend between elements exists (Fig. 3.4), which highlights the complexity involved during chemical mixing of a frictional melt. Consequently, discriminating the effect of diffusive fractionation and the range of chemical filaments involved is a challenging task.

Gradational melt filaments observed in BSE images of the frictional melts (Fig. 3.3 $T_m$) likely represent local areas of immiscibility and incomplete mixing of the different melted phases (termed schlieren). The various compositions of these different filaments suggest that viscosity contrasts would exist within a frictional melt. These viscosity contrasts would have a significant influence on melt filament mixing efficiency (e.g., Sparks & Marshall, 1986), with a larger viscosity contrast taking more time to mix and homogenise (e.g., Morgavi *et al.*,

2013). The large viscosity contrasts expected between amphibole, plagioclase, and interstitial glass filaments could explain the more heterogeneous nature of the SHV melts (Fig. 3.4a). The smaller viscosity contrasts between plagioclase and glass in the SG and COL melts would aid a faster rate of homogenisation (Fig. 3.4b, c). Due to density variations brought about by varying chemical compositions of the melt filaments, mixing during frictional melting can be described as a form of double-diffusion convection, where convection is forced by filaments with juxtaposing diffusivities (Huppert & Sparks, 1984; Hirose & Shimamoto, 2005). In summary, we highlight the complexity involved when attempting to assess chaotic mixing of a frictional melt due to selective phase melting.

### 3.4.4. Rheology

As discussed, the dynamic physicochemical complexity of a frictional melt brings about a convoluted rheological response. It has been well documented that the viscosity of the growing molten layer between two sliding surfaces determines the shear resistance of a melt during slip (e.g., Hirose & Shimamoto, 2005). Consequently, it is the viscosity dependence on melt composition that determines whether a frictional melt will serve as a lubricant or brake (e.g., Koizumi *et al.*, 2004; Hirose & Shimamoto, 2005; Kendrick *et al.*, 2014b). The mafic trend observed in the SHV frictional melts suggests a likely decrease in melt viscosity with slip distance owing to increased amphibole-melt interaction. Heat transfer to the wall rock adjacent to the melt layer can result in a continuous injection of low-viscosity amphibole melt causing the viscosity to be dynamic. However, the more homogenising response of the SG and COL melts suggests a more constant viscosity with time. A constant viscosity may be the cause of the instantaneous transition from peak shear stress to steady-state with little weakening involved (Fig. 3.2b); this was in contrast to the SHV melt, which showed a clear weakening phase before steady-state conditions were achieved.

The presence of crystals and bubbles within a frictional melt can influence the apparent viscosity (Lavallée *et al.*, 2012a; Hornby *et al.*, 2015). Crystals in all the frictional melts increase shear resistance by adding between 0.36 and 0.97 Pa s to the apparent viscosity causing increased strain-rate dependence (Fig. 3.9a–c). However, bubbles may either increase apparent viscosity or have an opposite effect depending on whether the bubbles can resist deformation or deform viscously, respectively (e.g., Bagdassarov & Dingwell, 1992). As highlighted by Lavallée *et al.* (2012a), the low estimated viscosities of the frictional melt imply that bubbles should deform, lowering the apparent viscosity. Yet, bubbles showed no signs of deformation (Fig. 3.3). Undeformed bubbles were previously given as evidence for their formation at the end of sliding (Hirose & Shimamoto, 2005). However, circular bubbles

more likely reflect the relaxation of a low viscosity melt that was dominated by highly isotropic surface tension which brought the bubbles back to spherical once shearing ceased (Rust & Manga, 2002). The increase in bubble content with slip distance in the SHV melt is attributed to elevated water contents due to an increasing input from amphibole melt. With amphibole containing ~2 wt.% $H_2O$ in its structure, a contribution of 27 vol.% amphibole melt (Fig. 3.8a) may have resulted in up to 0.54 wt.% $H_2O$ being transferred to the frictional melt, and thus lowered the modelled apparent viscosity and lowered the estimated temperatures of the SHV melt zone by ~100 ºC (Fig. 3.9d).

The apparent viscosity of a frictional melt suspension is strain-rate dependent and results in dynamic slip mechanics. In nature, slip rates are rarely constant. Considering the non-Newtonian nature of suspensions (e.g., Caricchi *et al.*, 2007; Lavallée *et al.*, 2007), a decrease in slip velocity would result in a reduced strain rate, causing an increase in apparent viscosity; moreover, such slip velocity reduction may promote cooling and further increase the apparent viscosity. These may manifest as a rise in shear stress that exceeds the structural relaxation of the melt causing slip to terminate or melt to rupture (Lavallée *et al.*, 2015b). The slip zone may subsequently heal (e.g., Lamur *et al.*, 2019) and then reactivate following the accumulation of shear stress, resulting in a stick-slip motion (e.g., Koizumi *et al.*, 2004; Kendrick *et al.*, 2014b; Lavallée *et al.*, 2015b; Lockner *et al.*, 2017). Consequently, we infer that host materials bearing a similar mineral assemblage to SG dacite and COL andesite are more likely to form frictional melts that operate as a viscous brake during deceleration of fault slip. On the other hand, in materials bearing a high abundance of hydrous minerals, similar to the SHV andesite, frictional melts would lubricate slip even during deceleration.

## 3.5. IMPLICATIONS FOR VOLCANIC SETTINGS

During the ascent of high-temperature, high-viscosity magma, common during dome-building eruptions, strain localisation along the conduit margins can result in the development of shear zones that experience seismogenic failure as magma encounters the viscous-brittle transition (Neuberg *et al.*, 2006; De Angelis & Henton, 2011; Kendrick *et al.*, 2014a). High strain rates in these regions can lead to frictional melting along the faulted contact and, consequently, dictate ascent dynamics and influence the style of activity at the surface (Kendrick *et al.*, 2014a).

At Santiaguito dome complex (Guatemala), regular gas-and-ash explosions have been attributed to strain localisation and friction during piston-like faulting of a lava plug at the conduit margins due to rapid uplift of the dome, corresponding to a slip velocity of up to 1 m $s^{-1}$ (Johnson *et al.*, 2008). Evidence of frictional melting was recorded by the presence of melt

filaments in erupted ash fragments and frictional marks on blocks forming the dome carapace (Lavallée *et al.*, 2015a). In addition to explosive activity, Hornby *et al.* (2015) reported that frictional melting was a likely process during repetitive slip of an emerging lava spine at Unzen volcano (Japan) following an experimental investigation. The study coupled high-velocity rotary shear experiments with seismic signals recorded during spine growth and constrained a slip velocity of 0.75 m $s^{-1}$. Shear zones that developed at the margins of the lava spine during its extrusion record extensive petrological evidence for localised frictional deformation and subsequent heating (Wallace *et al.*, 2019).

The difficulty we face when identifying pseudotachylytes in volcanic conduits is the high and sustained ambient temperatures (> 500 ºC) which promote slow cooling, crystallisation, hydrothermal alteration, and the metastability of glass. Such post-melting alteration processes can result in chemical, textural, and geophysical overprints that make it difficult to decipher the conditions of frictional melting (e.g., Kendrick *et al.*, 2012; Kirkpatrick & Rowe, 2013).

Fluxes in the abundance of mineral phases have been observed in many volcanic systems, particularly hydrous phases that are attributed to the injection of hydrous magma. Volcán de Colima has experienced such events, where an increased abundance of amphibole was recorded in products erupted in 1818 and from 1869 to 1913. This has been labelled as a potential precursor of explosive activity (Luhr & Carmichael, 1990; Luhr, 2002; Savov *et al.*, 2008; Saucedo *et al.*, 2010). We suggest that the introduction of amphibole could play a fundamental role in altering flow dynamics in the upper conduit by reducing the shear resistance during slip and facilitating explosive behaviour. This is because a lubricating effect could enable a continuous, fast magma ascent in the conduit where less shear resistance takes place near conduit margins. As amphibole-derived frictional melts are less likely to act as viscous brakes during a deceleration in magma ascent rate, they may be less prone to generate permeable fractures. Additionally, our observations that lavas containing amphibole generate frictional melts faster than amphibole-free lavas suggest amphibole-bearing systems are more susceptible to frictional melting. Consequently, the rapid formation of frictional melts in amphibole-bearing systems following short slip events may help seal fault planes that subsequently heal, thus decreasing the permeability of the system. Both these mechanisms promote higher gas overpressures and greater explosivity. If the magma is amphibole-free, frictional melts are less likely to form during very short slip events, and even during prolonged slip frictional melts are more likely to fail and fracture, leading to a pulsatory magma ascent in a stick-slip motion. Thus, frictional melting in amphibole-free systems favours the development of outgassing pathways that relieve the pressure of the system and reduce the explosive potential. However, for hydrous phases to control frictional behaviour, their

abundances would likely need to be above a critical fraction to ensure continuous interaction during frictional melting.

Additionally, rapid granular flows due to collapse events (e.g., landslides, pyroclastic flows, block-and-ash flows) in materials' bearing hydrous minerals could facilitate propagation processes, by decreasing the frictional resistance and thereby increasing the velocity of the flow and its travel distance. Frictional marks on block exteriors from block-and-ash flow deposits have highlighted the highly energetic internal processes taking place within rapid granular flows, where blocks continuously collide and slide past each other (e.g., Grunewald *et al.*, 2000; Schwarzkopf *et al.*, 2001). An investigation of frictional marks found on amphibole-bearing andesitic blocks from Soufrière Hills Volcano (SHV) identified thin pseudotachylyte veins that were compositionally heterogeneous, with $SiO_2$ ranging from 53 to 63.5 wt.% (Grunewald *et al.*, 2000). The pseudotachylyte glass composition had no overlap with that of the bulk-rock composition and was attributed to matrix melting rather than bulk melting of the host andesite. However, from our findings using a similar andesite from SHV, we suggest pure matrix melting was unlikely and these pseudotachylyte-bearing frictional marks represented very short-lived slip where only the onset of selective phase melting took place rather than prolonged slip to achieve a composition comparable to that of the bulk precursor rock. Contrary to the work of Grunewald *et al.* (2000), Schwarzkopf *et al.* (2001) performed a similar chemical analysis on frictional marks imprinted on the surface of andesitic–basaltic-andesite blocks from a block-and-ash flow deposit from Merapi volcano (Indonesia), classifying pseudotachylyte formation as a response to flash melting of the entire rock following frictional contact. This interpretation was based on the consistent compositional overlap of the pseudotachylyte and bulk-rock. From the experiments performed here, the different compositional relationships between the blocks from SHV and Merapi volcano could be explained by either prolonged sliding of blocks at Merapi (several metres of slip to allow the melt to homogenise towards the bulk-rock composition), prolonged incursion to high temperatures (to favour bulk melting), or a different mineral assemblage. Sustained slip between blocks in a block-and-ash flow is highly unlikely owing to the short-lived, chaotic collisions of rotating blocks; thus, we relate these previously assessed chemical observations to their contrasting bulk mineral assemblages, primarily the high abundance of amphibole in the SHV andesite. We thus anticipate our experimental and geochemical findings will also contribute to the improvement of flow models of similar rapid granular flows, including basal faulting during volcanic avalanches (e.g., Legros *et al.*, 2000; Bernard & de Vries, 2017).

## 3.6. CONCLUSIONS

We have experimentally demonstrated the effect of contrasting mineral assemblages on the frictional properties of extrusive volcanic rocks, providing a chemical viewpoint to a physical process. We find that the compositional discrepancies in frictional melts are attributed to selective phase melting during faulting, which, in addition to suspended crystal fragments, have a profound influence on the rheological properties of the melt, consequently controlling the mechanical response to slip. Selective melting preferentially occurs in phases with the lowest melting temperatures and mechanical strength, represented by amphibole in the volcanic rocks studied here. In the presence of amphibole, frictional melts are chemically and rheologically complex heterogeneous liquids. With time, these melts homogenise and evolve simultaneously, moving chemically further away from the bulk-rock towards a more mafic composition as amphiboles further from the fault zone continue to melt preferentially. Consequently, the lower melt viscosities attributed to preferential amphibole melting, likely accompanied by $H_2O$ release, facilitate a lower shear resistance that promotes slip. When amphibole is absent, frictional melts are compositionally more homogenous from the onset and in general homogenise continuously towards the bulk composition. In this case, the rheological response of the melt is dependent on preferential melting of phases with the next lowest melting temperatures and strength (i.e., plagioclase and rhyolitic glass). High modal fractions of these molten phases lead to frictional melt compositions that are closer to the bulk-rock. Selective melts of these phases have higher melt viscosities that cause a stronger shear resistance during slip, which may inhibit slip progression and eventually lead to failure. These findings provide new insights for assessing volcanic processes that involve slip displacement, either by altering conduit flow dynamics, which could impact the style of an eruption (explosive or effusive), or by contributing to the velocities and run-out distances of rapid granular flows.

# Chapter 4 Integrated constraints on explosive eruption intensification at Santiaguito dome complex, Guatemala


## ABSTRACT

Protracted volcanic eruptions may exhibit unanticipated intensifications in explosive behaviour. Santiaguito dome complex, Guatemala, has been characterised by century-long effusion interspersed with small-to-moderate gas-and-ash explosions. During 2015–2016, explosions intensified, generating hazardous ash-rich plumes and pyroclastic flows, thus raising questions over the current state of Santiaguito's magmatic system. Here, we integrate geochemical, petrological and geophysical evidence to evaluate the causes in explosion intensification, providing a unique dataset that captures an enigmatic shift in eruption style. Seismic and infrasound signals reveal progressively longer repose intervals between explosions and deeper fragmentation levels as the magnitude of these events increased. The onset of large explosions is concordant with a relatively fast ascent of deep-sourced, hot, volatile-rich magma, that mingles at shallow depth with the left-over mush under-rooting the pre-2015 lava dome. We interpret that purging by new magma led to consequential changes in the explosion mechanism and energy, intensifying local volcanic hazards. The multiparametric record indicates that geophysical data provide an instantaneous record of eruption intensification, whereas geochemical and petrological changes, which trigger explosion intensifications, are only expressed by examining the eruptive products following eruption.

## 4.1. INTRODUCTION

Subduction-related volcanic systems often exhibit transitions in eruption style over short (mins to days) and long (months to years) timescales. Amongst these, lava domes present one of the most hazardous forms of volcanic activity, with their ability to shift from benign effusive to catastrophic explosive eruption style with little precursory warning (e.g., Mount St Helens, Cashman (1992); Soufrière Hills volcano, Clarke *et al.* (2007); Pinatubo, Hammer *et al.* (1999); Galeras volcano, Stix *et al.* (1993); Stix *et al.* (1997)). Achieving comprehensive understanding of the processes that facilitate one style of activity over the other remains a non-trivial task for real-time hazard assessment and future monitoring efforts. Effective forecasting thus relies on the integration of multi-parametric observations, including geophysical monitoring data and petrological and geochemical signatures of the erupted material. Yet, such interdisciplinary datasets are rare for a single eruption and even more so over a period exhibiting a prolonged transition in eruption style (e.g., Wadge *et al.*, 2014; Stock *et al.*, 2018).

Volcanic eruptions are highly dynamic, both temporally and spatially, that involve a complex interplay between many physico-chemical processes. It is thus envisaged that no single process is responsible for a given eruption style (Cassidy *et al.*, 2018), but rather a feedback associated with multiple competing factors as magma is transported through the Earth's crust. For instance, a shift in activity within, or between, eruptive episodes is commonly attributed to a switch in the degassing-regime from open-system to partially closed-system degassing (e.g., Fink *et al.*, 1992; Stix *et al.*, 1993; Woods & Koyaguchi, 1994; Adams *et al.*, 2006), regulated by a combination of deep (e.g., magma injection, deep convection, mush instabilities and volatile fluctuations; Sparks *et al.*, 1977; Pallister *et al.*, 1992; Murphy *et al.*, 2000; Williamson *et al.*, 2010; Burgisser & Bergantz, 2011) and shallow (e.g., volatile exsolution, degassing, crystallisation, shearing/friction; Hammer *et al.*, 1999; Sparks *et al.*, 2000; Sparks, 2003b; Edmonds, 2008; Lavallée *et al.*, 2012b; Lavallée *et al.*, 2013; Preece *et al.*, 2013; Wallace *et al.*, 2019) magmatic processes that control the composition, physical properties, rheology, and ultimately ascent style of the magma.

The architecture of magma plumbing systems and inferences of deep magmatic processes that influence volcanic activity often come from petrological and geochemical analyses of erupted materials. Information may be archived in the bulk-rock composition and/ or the constituent mineral and glass phases (incl. phenocryst zonations and diffusion profiles, disequilibrium textures, reaction rims on hydrous minerals and melt inclusions). Of particular importance is the ability to constrain magma storage conditions, which are commonly estimated from geochemical analyses via application of experimentally-calibrated geothermobarometers (e.g., Holland & Blundy, 1994; Putirka, 2008; Ridolfi *et al.*, 2010), as

well as deciphering the processes that may overprint these signals during ascent immediately prior to and during eruptions. As magma ascends to the surface, decompression drives volatile exsolution of the melt phase, which in turn influences their petrological and rheological evolution. Melt degassing causes an increase in the liquidus temperature and generates an effective undercooling (difference in temperature between that of the melt and liquidus, $\Delta T$) favouring conditions for microlite crystallisation; thus groundmass textures of eruptive products reflect the ascent history (e.g., Cashman & Blundy, 2000; Noguchi *et al.*, 2008b; Toramaru *et al.*, 2008; Miwa *et al.*, 2009; Preece *et al.*, 2013; Cassidy *et al.*, 2015; Preece *et al.*, 2016). Degassing as well as associated crystallisation increase bulk magma viscosity and may inhibit flow in the upper conduit leading to plug formation (e.g., Lavallée *et al.*, 2012b; Lavallée *et al.*, 2013). The outgassing efficiency of such a plug determines the development of pore pressure in the magmatic column (e.g., Diller *et al.*, 2006; Mueller *et al.*, 2008; Burgisser *et al.*, 2010); if pore pressure induces strain rates that exceed the relaxation rate of magma it can cause the plug to rupture and generate an explosion (Dingwell, 1996). Open-system volcanoes, such as protracted lava dome eruptions, commonly display pulsatory magma ascent associated with cyclic seismicity (e.g., Neuberg *et al.*, 2006; Iverson, 2008; Kendrick *et al.*, 2014b), ground deformation (e.g., Voight *et al.*, 1999; Johnson *et al.*, 2014; Neuberg *et al.*, 2018), gas emission (e.g., Edmonds *et al.*, 2003; Michaut *et al.*, 2013) and explosion (e.g., Gonnermann & Manga, 2003; Johnson *et al.*, 2014; Lavallée *et al.*, 2015a) as a result of complex interplays between magma ascent, petrological and rheological evolution, deformation and gas fluxing through the system. However, during the course of an eruption, the physico-chemical properties of magma in the source region may evolve (due to assimilation, differentiation or magma mixing), thus affecting the balance between the aforementioned pre-eruptive processes, and resulting in a shift in eruptive behaviour (e.g., Melnik & Sparks, 2002). Understanding of the timescale, signs and causes of such changes in the volcanic system remains insufficient for hazard assessment.

In this study, we integrate geophysical observations with petrological and geochemical analyses of the erupted material to characterise a phase of eruption intensification during 2015–2016 at Santiaguito dome complex, Guatemala. Geochemical and microtextural investigations were performed on ash and bombs ejected during Vulcanian explosions across the transition period, and compared with seismic and infrasound signals, to explore the cause behind this shift in eruption style and the implications it had on eruption mechanism.

## 4.2. SANTIAGUITO DOME COMPLEX

### 4.2.1. Eruptive history and explosive activity

Santiaguito is an active dacitic-andesitic dome complex in south-west Guatemala. Following the cataclysmic Plinian eruption of Santa Maria (Fig. 4.1) in 1902, and after 20 years of quiescence, in 1922 extrusion began in the centre of the explosion crater and has been ongoing for the past century from four vents (Rhodes *et al.*, 2018): El Caliente (active during 1922–39 and 1967–present), La Mitad (1939–49), El Monje (1949–58) and El Brujo (1958–86). El Caliente is considered the primary vent as it has remained continuously active (via intense fumarolic activity) even during extrusion from the other vents (Rose, 1972). For the past two decades, Santiaguito's eruptive activity has been characterised by exogenous dome growth, including continuous slow extrusion of blocky lava flows and regular, small-to-moderate gas-and-ash explosions (≤2 per hour) with plume heights rarely exceeding 1–2 km above the vent (Bluth & Rose, 2004; Sahetapy-Engel *et al.*, 2008; Yamamoto *et al.*, 2008; Johnson *et al.*, 2014; Lavallée *et al.*, 2015a; De Angelis *et al.*, 2016). However, from December 2014, these regular explosions (>30 per day) became less frequent, gradually decreasing to <10 per day by July 2015 while their magnitude increased significantly (Lamb *et al.*, 2019). This shift in explosive activity caused excavation of the crater by mid-2016 (Lamb *et al.*, 2019) and generated ash-rich plumes up to 7 km high, before returning to characteristic regular, small-to-moderate explosions in-late 2016 and the growth of a new lava dome within the El Caliente vent.

### 4.2.2. Previous constraints on the magma plumbing system

Petrological and geochemical assessments of extruded lava between 1922–2002 have provided a comprehensive overview of the evolution of the system (Scott *et al.*, 2012; Scott *et al.*, 2013; Andrews, 2014). Whole-rock composition revealed a progressive decrease of ~4 wt.% $SiO_2$ through time (~66 to 62 wt.%; Rose, 1972; Harris *et al.*, 2003; Avard & Whittington, 2012; Scott *et al.*, 2013), attributed to a combination of magma mixing that likely triggered the 1902 eruption, and varying degrees of fractional crystallisation which took place ~25 ka prior (Scott *et al.*, 2013). Magma feeding the Santiaguito dome complex has been constrained to reside between ~12 and ~24 km depth at temperatures ~940–980 ºC (Scott *et al.*, 2012), with no definitive evidence of an additional, shallower reservoir. Based on the extrusion of less evolved magma over the past century, a compositionally, vertically-stratified storage region in the lower crust was proposed, grading from basaltic at depth to dacitic in the shallow region, with the system currently extruding andesite (Scott *et al.*, 2013). The extrusion of this lava has taken place in 7 to 15-year cycles (nine documented) of high and low extrusion

rates, with high extrusion rates taking place over a 3–6 year period and low extrusion rates over a 3–11 year period (Harris *et al.*, 2003; Rhodes *et al.*, 2018); this accompanied by the magma's compositional trend led to the hypothesis that the magma source beneath Santiaguito was depressurising, and was proposed to succumb to complete exhaustion between 2014–2024 (Harris *et al.*, 2003). However, the eruption intensification in 2015–2016 brings questions on the current state of magma storage and ascent processes (Rhodes *et al.*, 2018; Lamb *et al.*, 2019).

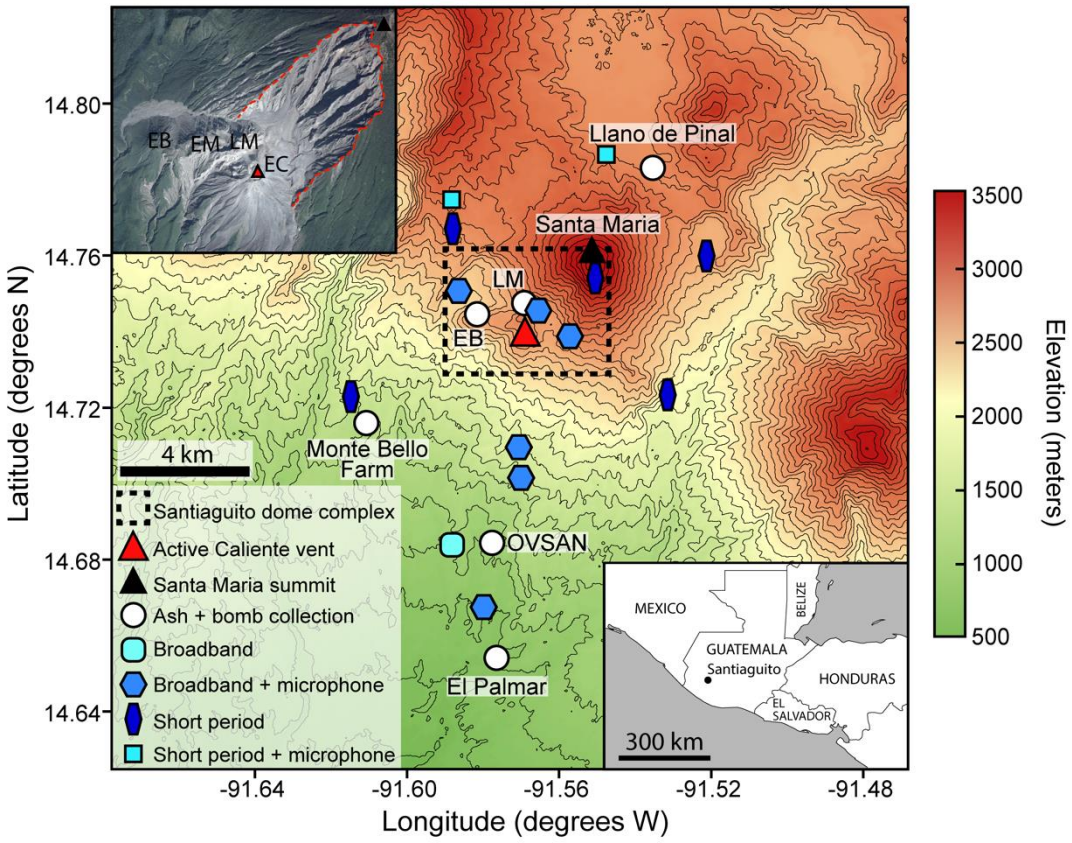


***Figure 4.1*** *– Map of Santiaguito dome complex showing the location of the deployed instrument network and sample collection locations. Bottom right inset of Central America showing the location of Santiaguito in SW Guatemala. Top left insert shows an aerial photograph (sourced from Google Earth CNES/Airbus data © 2018) of the dome complex taken in January 2017 corresponding to the dashed area of the map and the four domes (EC: El Caliente; LM: La Mitad; EM: El Monje; EB: El Brujo). The red dashed line marks the crater scarp on the SW flank of Santa Maria formed by the 1902 eruption.*

## 4.3. METHODS

### 4.3.1. Seismic and acoustic infrasound

A geophysical network, consisting of 11 seismometers (six broadband and five short-period instruments) and five acoustic infrasound microphones located around the dome complex was deployed between November 2014 and May 2017 (Fig. 4.1; see Lamb *et al.* (2019) for further details on the network deployment). A waveform characterisation algorithm, that matches the seismic waveforms from each event with triggered acoustic signals (using infrasound waveform shape, amplitude and frequency), was used to detect individual explosions (Lamb *et al.*, 2019; Bueno et al., in preparation, VINEDA—Volcanic Infrasound Explosions Detector Algorithm). This approach provided a means for tracking the real-time evolution of the intensity and magnitude of explosions across the transition period, recording over 6000 explosion events. For each explosion in the catalogue, the energy of each event was calculated from the seismic waveform using an approach that assumes velocity waveforms are representative of the seismic kinetic energy at a specific location on the volcano. Following Johnson and Aster (2005), seismic energy can be calculated as:

$$E_{seismic} = 2\pi r^2 \rho_{earth} c_{earth} \frac{1}{A} \int S^2 U(t)^2 dt \qquad (4.1)$$

where $r$ is source-to-receiver distance, $\rho_{earth}$ is rock density, $c_{earth}$ is seismic velocity (2150 m $s^{-1}$), $A$ is attenuation, $S$ is seismic site response, and $U$ is the particle velocity. For each explosion, we integrate over a time window that corresponds to the entire duration of the event waveform.

### 4.3.2. Thermal radiance

Near-real-time thermal infrared satellite data was obtained from the non-interactive algorithm MODVOLC (http://modis.higp.hawaii.edu) to assess evidence for surficial temperature changes across the same eruptive period (Wright, 2016). MODVOLC uses low-spatial, high-temporal resolution infrared satellite data (1 km pixel resolution) acquired by the Moderate Resolution Imaging Spectroradiometer (MODIS) to detect thermal anomalies and quantify emitted spectral radiance at a given hotspot using the 3.595 μm infrared region (short-wave) of the electromagnetic spectrum. MODVOLC uses the radiance emitted to estimate the radiant heat flux from the surface (in W) following the method of Wright *et al.* (2016).

### 4.3.3. Eruptive products and characterisation

Ejected ash and bombs from heightened explosive activity in 2015–2016 were periodically sampled from both proximal and distal locations (0.1–10.0 km away) from the active El Caliente vent (Fig. 4.1). Pre-prepared thin sections for ash samples from explosions in January 1968, January 2003, November 2014 and January 2018 were also analysed to assess changes in groundmass microlite textures and glass chemistry for pre- and post-heightened activity (the samples from 2003 and 1968 were provided courtesy of Bill Rose). Collected ash from 2015–2016 was dried in a furnace at 70 ºC for 6 hours and sieved into 6 grain size fractions (1 mm, 0.5 mm, 0.25 mm, 0.125 mm, 0.063 mm and <0.063 mm). Only the 0.25–0.5 mm size fraction was selected for the study to enable direct comparison across the sample suite. Ash componentry analysis was performed using a binocular microscope to quantify the abundance of different clast types based on their physical appearance (counting >300 grains per sample). Two Bombs, from Febuary and April 2016, were thin sectioned and all ash particles were set in a cylindrical resin mount, which were polished and carbon coated for textural and chemical investigation.

Mineralogy and phases abundances were quantified using QEMSCAN (Quantitative Evaluation of Minerals by Scanning Electron Microscopy), an automated SEM-EDS (Scanning Electron Microscopy-Energy Dispersive X-ray Spectroscopy) system (Pirrie *et al.*, 2004). Analyses were performed using 15 KeV accelerating voltage and a ~5 nA beam current, with the beam rastering along the sample at 20 µm intervals. The chemical compositions, determined by EDS, were matched with compositions for known mineral or glass phases stored within a reference library to produce a colour-coded phase distribution map for each ash and bomb sample (see Wallace *et al.* (2019) for more detail). Phase abundances were calculated using the sum of pixels of each coloured phase, normalised on a pore-free basis to enable a quantitative comparison across the sample suite.

### 4.3.4. Geochemistry

Whole-rock major and trace element concentrations were measured by X-ray Fluorescence (XRF) for all ash and bomb samples using a PANalytical Axios Advanced XRF spectrometer at the University of Leicester. Relative precisions and accuracies are better than 1–2% for all major elements and better than 5% for trace elements based on repeat analyses of international reference materials (BH-1 microgranodiorite, JR-1 rhyolite 55 and BCR-1 basalt).

Chemical composition of crystals and interstitial glass were determined using a Cameca SX100 electron microprobe (EPMA) at Ludwig-Maximilians-University in Munich.

Crystal analyses were performed using a 15 kV accelerating voltage, 20 nA beam current, and a focused (~1 μm) beam; all analyses on glass used a 5 nA beam current and a defocussed 10 μm beam. Alkalis were measured first to avoid their migration during the analyses. Eight working standards from the Smithsonian collection (incl. VG-568 rhyolitic glass and Kakanui hornblende) were measured at regular intervals to ensure accuracy and precision. All elements had standard deviations < 0.5 and relative accuracies were generally better than 3% for major elements and 20% for minor elements. Any data with totals outside 97–101 wt.% were excluded from the results.

### 4.3.5. Textural analysis

SEM analysis was conducted using a Hitachi TM3000 operating at 15 kV accelerating voltage and 10 mm working distance, in backscattered electron (BSE) mode. Quantitative microlite texture analysis of juvenile ash (dense brown and transparent clasts) and bombs were conducted on high resolution BSE images. Plagioclase microlites were manually outlined within a 10,000 $mm^2$ area using Adobe Illustrator. The digitised images were converted to high-resolution TIFF files, which were imported to ImageJ for crystal measurements using the best-fit ellipse tool (Schneider et al., 2012). Measurements included the total area analysed, number of crystals per area, total area % of crystals, individual and mean crystal area, and crystal dimensions (long and short axes). From this data, microlite area %, microlite fraction ($\varphi$), and microlite number density ($N_A$, $mm^{-2}$) were calculated. Plagioclase $\varphi$ was calculated on phenocryst-free and mafic microlite-free basis (i.e., area available for plagioclase crystallisation) following the methods of Hammer *et al.* (1999), and $N_A$ was calculated by dividing the total number of whole crystals by the area of groundmass measured. Crystal shapes were determined using *CSDSlice* (Morgan & Jerram, 2006), which objectively converts 2D measurements into known 3D shapes to obtain a short (S), intermediate (I) and long (L) axes.

*CSDCorrections* software (Higgins, 2000) was used to provide 3D crystal size distributions (CSDs) by stereological conversion of the 2D crystal intersections measured in ImageJ. From the CSD data, volumetric plagioclase number densities were calculated using $Nv = n_o \times \frac{-1}{\alpha}$, where $\alpha$ is the slope of a straight CSD curve (in $mm^{-1}$) and $n_o$ is the y-intercept (Blundy & Cashman, 2008). The CSDs can also be used to estimate microlite nucleation rates ($J$) and growth rates ($G$) if crystallisation times ($\tau$) are known (Cashman, 1988; Marsh, 1988): $\alpha = -1/G\tau$ and $J = n_oG$. As crystallisation times ($\tau$) at Santiaguito are unknown, maximum and minimum crystallisation times were estimated from the onset of a change in explosion seismicity (i.e., when explosions first began to increase in magnitude in February 2015) and

repose times between explosions, respectively. As our geophysical network did not extend further back than November 2014, a maximum crystallisation time for microlites in the November 2014 ash was estimated as the onset of lava extrusion in April 2014. Nucleation and growth rates for explosions in 1968 and 2003 were not calculated due to the large uncertainty in crystallisation time.

## 4.4. RESULTS

### 4.4.1. 2014–2017 eruptive activity and associated monitoring signals

Visual monitoring of eruptive activity between 2014 and 2017 (Fig. 4.2a–f) has been compiled from multiple field campaigns, activity reports (Global Volcanism Program) and INSIVUMEH, and are here integrated with the geophysical and thermal signals monitored during this period (Fig. 4.2g). Four phases were identified and these are compared to the pre-2015 observed activity.

#### *4.4.1.1. Pre-2015 activity*

Prior to the deployment of the geophysical network in November 2014, a significant collapse of El Caliente's eastern flank on the 9$^{th}$ April 2014 was followed by the extrusion of a blocky lava flow that eventually halted in December 2014 (Global Volcanism Program, 2015). Regular, small to moderate explosions interspersed this extrusion period; plumes were ash-poor and rose ≤1 km above the vent from arcuate to ring-shaped fractures within an infilled crater (Fig. 4.2a and b). Similar observations were reported for explosions in 2007 by Johnson *et al.* (2008). Explosions in November and December 2014 were low energy (avg. 15 MJ), with repose intervals averaging ~47 minutes, equating to ~30 explosions per day (Fig. 4.2g); thermal heat flux during this time remained consistently low (avg. 15 MW). Integrating these seismic signals with infrasound observations can be used to gain insights into explosion source mechanisms (e.g., Johnson *et al.*, 2004); in particular, time difference between the two signals can be used as a proxy for explosion depths in the conduit (e.g., Hagerty *et al.*, 2000), thus can be temporally assessed across the 2014–2017 period. By comparing seismic and infrasound signals from a number of randomly selected explosion events in late-2014, the delay in arrival times are up to 6 seconds (Fig. 4.2h).

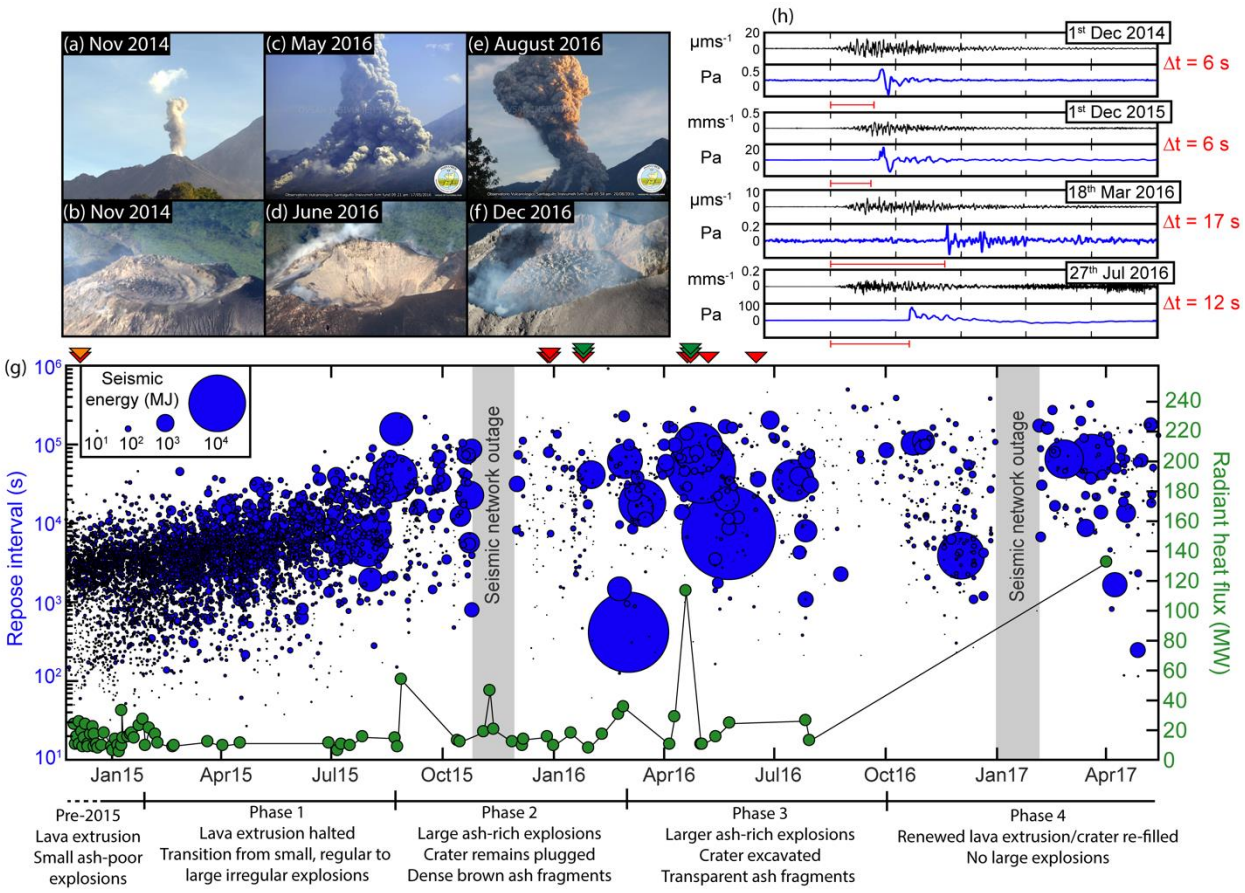


***Figure 4.2*** *– Visual observations and monitored geophysical signals of the 2014–2017 eruptive activity. (a-f) Photographs of explosions from the El Caliente vent through time taken from OVSAN (a, c, e), and the subsequent change in crater morphology taken from Santa Maria summit (b, d, f). (g) Seismic record of explosions as captured by the deployed geophysical network from Nov 2014 to May 2017, showing a change in repose intervals (left vertical axis) and energy of individual explosions (bubble sizes) across the transition period. The satellite radiant heat flux data (green circles and right vertical axis), as derived from MODVOLC, overlays the seismic data (g). The coloured arrows located above seismic time sequence in (g) indicate eruption dates for the samples analysed: lava flow (orange), ash (red), bombs (green). (h) Comparison of selected seismic and acoustic infrasound signals displaying larger delays in arrival times for explosion events in phase 3.*

#### *4.4.1.2. Phase 1: February–September 2015*

The regular, small-to-moderate explosions from late-2014 continued until February 2015. From this point on, explosions formed ash plumes that were visually darker and more ash-rich, which occasionally generated pyroclastic flows (Global Volcanism Program, 2015). From February to September 2015 (Fig. 4.2g), these explosions became progressively less frequent (decreasing towards <10 per day; Lamb *et al.*, 2019), with average repose intervals of ≥2 hours, as their magnitude increased synchronously (up to 8.8 x $10^3$ MJ). The time delays between seismic and infrasound signals during this phase were the same as those recorded for pre-2015 explosions. Although few thermal satellite anomalies were detected during this period (likely due to cloud coverage), there was no apparent change in the heat flux (Fig. 4.2g).

#### *4.4.1.3. Phase 2: September 2015–March 2016*

From September 2015, the number of explosions per day was at its minimum (<10 per day) and remained so for the following year (Fig. 4.2g; Lamb *et al.*, 2019). Explosions in December 2015 produced ash plumes up to 7 km above sea level (a.s.l.) with ash fall reported >10 km away from the vent. Intense explosions on 7$^{th}$ February 2016 produced dense ash plumes up to 6 km a.s.l, ballistics and pyroclastic flows (Global Volcanism Program, 2016). These explosions continued to produce similar time arrival delays for the seismic and infrasound signals with those in pre-2015 and phase 1 (Fig. 4.2h); however, occasional high thermal anomalies were detected (up to 54.2 MW; Fig. 4.2g), which were not observed in phase 1. Similar large, irregular and ash-rich explosions and pyroclastic flows continued in early 2016, with ash falling on villages up to 20 km away from the active vent, often interspersed by small explosions. Repose intervals during this phase often increased to ~12 hours as explosions became more energetic (avg. ~ 9.0 x $10^2$ MJ; Fig. 4.2g).

#### *4.4.1.4. Phase 3: March–October 2016*

Explosions throughout mid-2016 continued to be irregular, ash-rich and plumes up to several kilometres above the active vent (Fig. 4.2c). However, explosions in April and May 2016 were the largest reported throughout the 2015–2016 eruptive period (Fig. 4.2g; up to 1.3 x $10^5$ MJ), and completely excavated the summit crater (Fig. 4.2d; ~300 m width and ~175 m depth). Metre sized blocks and bombs were ejected up to 3 km away from the El Caliente vent. Similar activity continued until October 2016 (Fig. 4.2e), accompanied by irregular pyroclastic flows, although no explosions exceeded 9 x $10^3$ MJ after May and their frequency

remained at <10 per day. Irregular spikes in the detected heat flux persisted throughout this period (Fig. 4.2g), with the largest recorded in mid-April (up to 114.5 MW) which coincided with the explosions that excavated the crater. The time delay in arrivals between the seismic and infrasound signals within this period overlap with those in phase 1 and 2 (i.e., ~6 seconds); however, some explosions during this high-energy phase have up to a 17 second delay (Fig. 4.2h). Amongst the many primary hazards generated during the phase, heavy rainfall from May to September 2016 led to erratic lahars (Global Volcanism Program, 2016).

#### *4.4.1.5. Phase 4: October 2016–January 2018*

From October 2016 onwards, no large explosions were reported, and activity gradually returned to regular, small-to-moderate regular explosions (>30 per day). Contemporaneously, the extrusion of lava began to fill the excavated El Caliente summit crater leading to the growth of a new dome (Fig. 4.2f). By March 2017, lava had completely filled the excavated crater and began to overflow generating block-and-ash flows down the flank of the dome. The thermal data during this time detected no anomalous heat flux, although the satellite did detect an anomaly in April 2017 (Fig. 4.2g) that was notably larger than those detected during phase 3. By late-2017 and early-2018, weak gas-and-ash explosions continued to emerge from the infilled Caliente crater (~14 per day), with ash plumes rarely exceeding 1 km above the vent (Global Volcanism Program, 2018).

### 4.4.2. Eruptive products

#### *4.4.2.1. Ash componentry*

Ash erupted from explosion events during phases 2 and 3 of the 2014–2017 eruptive period comprised eight clast types: dense brown (DB), transparent (TC), dense grey, white vesicular, dull lithic, hydrothermally altered, and single felsic and mafic crystals. DB clasts have a brown, glossy surface texture that is glass-rich, has angular edges and no apparent vesicularity (Fig. 4.3a). BSE images of DB clasts often contain varying abundance of mafic microlites in the groundmass (Fig. 4.3b). TC clasts are grey to transparent with a glossy surface texture (i.e., glass-rich) and have a similar low vesicularity to the DB clasts; however, bubble walls are often observed at the edges of TC fragments (Fig. 4.3c). Unlike the DB clasts, the TC clasts consistently contain a lower abundance of mafic microlites in the groundmass (Fig. 4.3d). As DB and TC clasts are glass-rich, we refer to these as the juvenile components (representing freshest material). The dense grey, dull lithic and white vesicular clasts reveal no fresh glass, which has degraded to $SiO_2$ phases (Fig. A3.1), and thus are regarded as non-

juvenile. Dense bombs ejected during an explosion on 7th February 2016 are texturally similar to TC clasts, while bombs from an explosion on 21st April 2016 consist of discrete domains of dark- and light-coloured groundmass (Fig. 4.3e), comparable to the textures in DB and TC clasts, respectively (Fig. 4.3b, d and f). The lighter domains are macro-vesicular (up to 500 µm diameter), consistent with bubble walls observed at the edges of the TC clasts (Fig. 4.3c), while the darker domains are significantly less vesicular. Quantification of the temporal changes in the ash components are displayed in Figure 4.3g. Ash from explosions during phase 2 (December 2015 and February 2016) are dominated by DB clasts (~60–70 %), which switch to TC dominated (up to 60 %) during the highest energy explosions in phase 3 (April 2016). Ash from explosion events during May and June 2016 contain a higher amount of dense grey clasts (up to 30%), which coincides with a reduction in the amount of TC clasts. Ash ejected form a small explosion event in January 2018 has a similar componentry to ash from large explosions in April 2016, although contains more hydrothermally altered fragments.

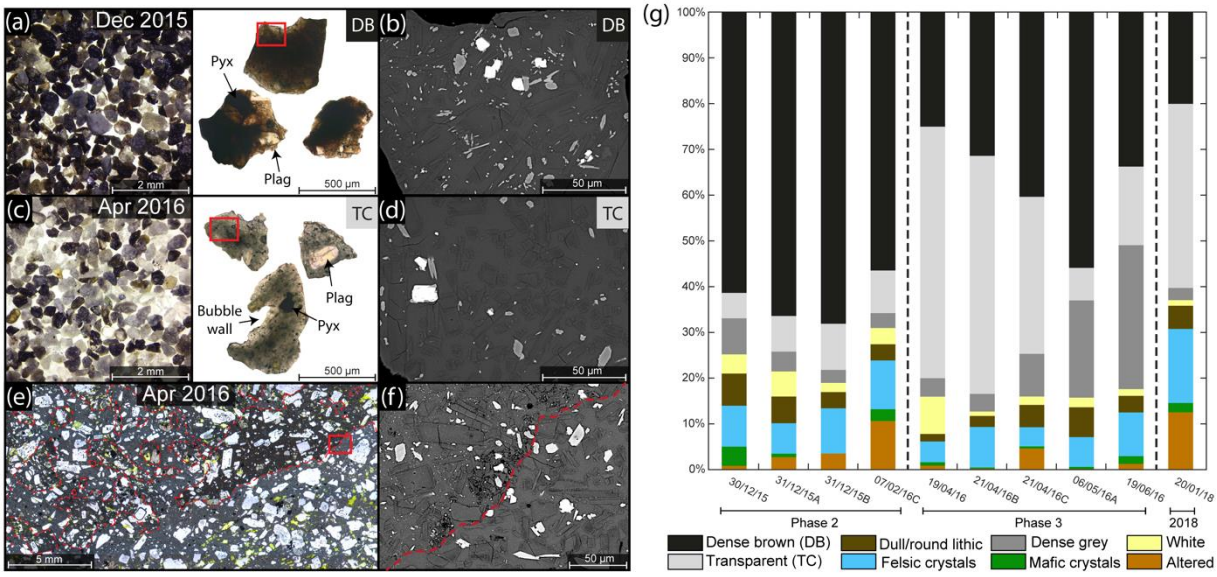


***Figure 4.3*** *– Ash and bomb characteristics from 2015–2016 explosions. (a) Image of ash (250–500 µm size) from 31st December 2015 displaying the dominance of dense brown (DB) clasts, along with a representative BSE image of the DB groundmass textures (b). (c) Image of ash (250–500 µm size) from 21st April 2016 show a change in ash componentry to a dominance in transparent clasts (TC) and representative groundmass textures (d). (e) Photomicrograph of a bomb ejected during an explosion on 21st April 2016, revealing two distinct domains, dark and light-coloured groundmass, mingled together (outlined in red). Note the high vesicularity of the light-coloured groundmass. (f) Groundmass texture of the contact between the two domains showing distinct microlite textures, akin to the DB and TC ash. (g) Quantitative component analysis across for the 2015–2016 ash (on the 250–500 µm fraction), measuring >300 ash particles per sample.*

#### *4.4.2.2. Mineralogy*

All erupted samples are porphyritic with phenocrysts of plagioclase, clinopyroxene, orthopyroxene, amphibole and titanomagnetite. Quartz is rare, although, when present, takes the form of resorbed fragments. The groundmass contains microlites (<50 μm in length) of plagioclase, pyroxene, titanomagnetite, and minor apatite, situated with an interstitial rhyolitic glass. Silica-rich phases are present in the groundmass of the non-juvenile ash clasts and are locally found in clusters in the dark, dense domains of the bombs. QEMSCAN mineral maps were collected on raw ash samples (Fig. 4.4a–f) and bombs (Fig. A3.2). The mineralogy is broadly consistent across all samples (Fig. 4.4g), although subtle differences are observed between the ratio in Si-rich phases (Si polymorph) and glass that are consistent with the ash componentry. For example, the increase in silica polymorphs in ash samples in May and June 2016 is in agreement to the increased abundance of dense grey lithic clasts, and the higher glass content of the bombs indicates they are exceptionally juvenile. XRD further confirms an increase in silica polymorphs in ash from late-2015 to mid-2016, identified as tridymite (Fig. 4.4h).

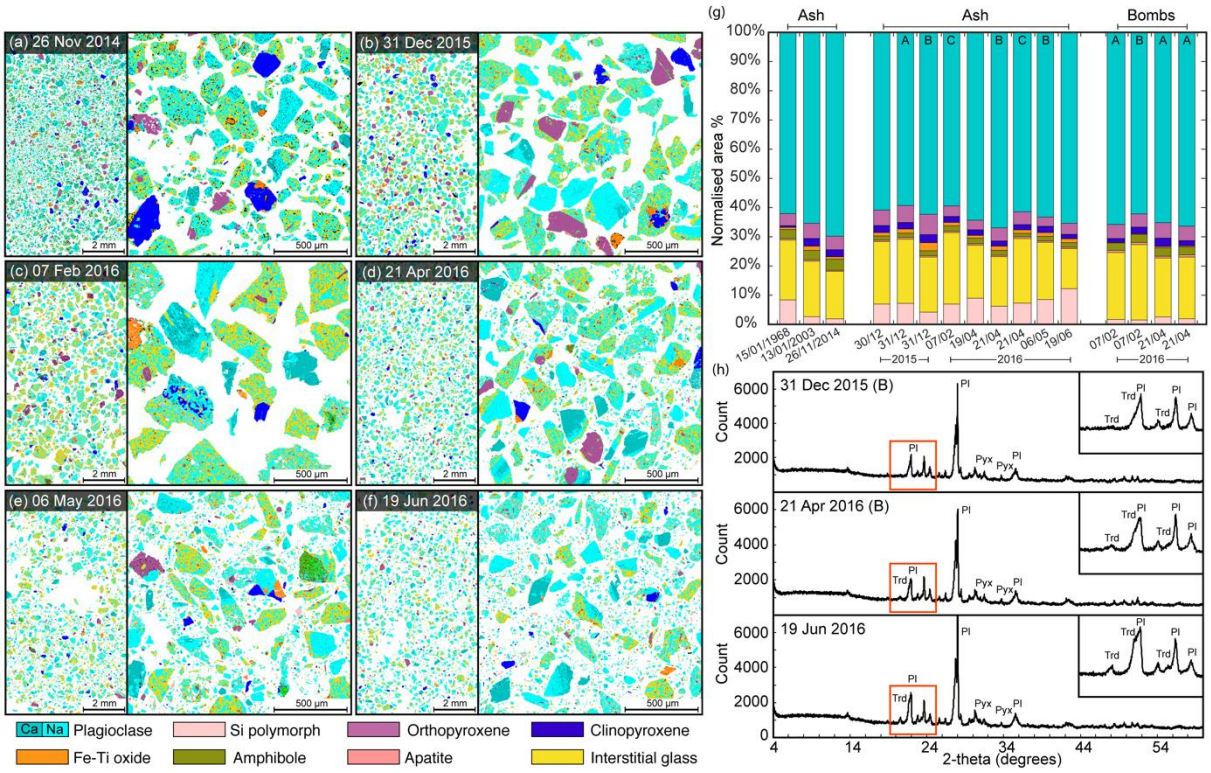


***Figure 4.4*** *– Quantitative mineral modal abundance of explosive products from pre-2015 (1968, 2003 and 2014) and across the 2015–2016 transition period. (a–f) QEMSCAN maps of unsieved ash particles from explosions between November 2014 and June 2016. (g) Temporal variations in mineral abundance derived from QEMSCAN, including ash from January 1968 and 2003, and bombs from February and April 2016. Letters A–C denote different samples with the same eruption date. (h) XRD spectra for powdered ash samples confirming the mineralogy detected by QEMSCAN. The insets are close-ups of the spectra heighted by the red box, displaying the detection of silica polymorph tridymite in ash in April and June 2016.*

***Table 4.1*** *– Whole rock chemical composition of major and trace elements for ash and bombs collected between 2015–2016, along with eruption date and collection location. Sample locations include El Caliente (El), VIP camp (VC), El Brujo (EB), La Mitad (LM), El Palmar (EP), Monte Bello Farm (MBF), OVSAN and Llano de Pinal (see Fig. 4.1).*

| **Eruption Date:** | 26/11 2014 | 30/12 2015 | 31/12 2015 | 07/02 2016 | | | 19/04 2016 | 21/04 2016 | | | | 06/05 2016 | | 25/05 2016 | 19/06 2016 |
|---|---|---|---|---|---|---|---|---|---|---|---|---|---|---|---|
| **Location:** | EC | VC | EB | LM | | | EP | EP | MBF | OVSAN | | EP | OVSAN | MBF | LdP |
| **Lithology:** | L. Flow | Ash | Ash | Ash | Bomb | | Ash | Ash | Ash | Vesicular-domain bomb | Dense-domain bomb | Ash | Ash | Ash | Ash |
| **Sample no.:** | 261114 | 301215 | 311125C | 070216C | 070216A | 070216B | 190416 | 210416B | 210416C | 210416A | 210416A | 060516A | 060516B | 250516 | 190616 |
| *(wt.%)* | | | | | | | | | | | | | | | |
| **$SiO_2$** | 62.65 | 61.37 | 61.30 | 61.84 | 61.68 | 61.51 | 61.57 | 61.62 | 61.56 | 61.57 | 62.10 | 61.64 | 61.42 | 61.96 | 62.27 |
| **$TiO_2$** | 0.48 | 0.60 | 0.63 | 0.58 | 0.58 | 0.58 | 0.57 | 0.57 | 0.60 | 0.59 | 0.57 | 0.60 | 0.57 | 0.58 | 0.52 |
| **$Al_2O_3$** | 17.17 | 17.65 | 16.97 | 17.31 | 17.79 | 17.70 | 17.93 | 17.92 | 17.32 | 17.78 | 17.86 | 16.97 | 17.98 | 17.18 | 18.08 |
| **$Fe_2O_3$*** | 5.13 | 5.79 | 6.48 | 5.61 | 5.54 | 5.63 | 5.50 | 5.49 | 6.13 | 5.70 | 5.58 | 6.09 | 5.50 | 5.73 | 5.15 |
| **MnO** | 0.15 | 0.14 | 0.17 | 0.15 | 0.14 | 0.14 | 0.14 | 0.14 | 0.16 | 0.14 | 0.14 | 0.17 | 0.14 | 0.15 | 0.14 |
| **MgO** | 1.72 | 2.29 | 2.77 | 2.33 | 2.20 | 2.19 | 2.10 | 2.11 | 2.65 | 2.26 | 2.24 | 2.62 | 2.09 | 2.35 | 1.88 |
| **CaO** | 5.42 | 5.75 | 5.49 | 5.44 | 5.69 | 5.70 | 5.73 | 5.73 | 5.57 | 5.73 | 5.64 | 5.39 | 5.78 | 5.34 | 5.61 |
| **$Na_2O$** | 4.76 | 4.42 | 4.28 | 4.43 | 4.50 | 4.47 | 4.52 | 4.52 | 4.37 | 4.54 | 4.57 | 4.36 | 4.55 | 4.42 | 4.55 |
| **$K_2O$** | 1.36 | 1.55 | 1.53 | 1.57 | 1.53 | 1.54 | 1.49 | 1.49 | 1.50 | 1.54 | 1.57 | 1.58 | 1.46 | 1.61 | 1.46 |
| **$P_2O_5$** | 0.23 | 0.22 | 0.23 | 0.21 | 0.22 | 0.22 | 0.22 | 0.21 | 0.23 | 0.22 | 0.22 | 0.23 | 0.21 | 0.23 | 0.21 |
| **LOI** | 0.08 | -0.04 | -0.02 | 0.06 | -0.06 | -0.04 | 0.01 | 0.04 | 0.03 | 0.02 | -0.05 | -0.03 | 0.05 | 0.10 | 0.06 |
| **Total** | 99.14 | 99.76 | 99.85 | 99.55 | 99.81 | 99.67 | 99.79 | 99.83 | 100.15 | 100.09 | 100.45 | 99.62 | 99.76 | 99.67 | 99.95 |
| *(ppm)* | | | | | | | | | | | | | | | |
| **Ba** | 780 | 728 | 729 | 755 | 758 | 752 | 759 | 760 | 730 | 743 | 751 | 766 | 756 | 774 | 765 |
| **Ce** | 28 | 26 | 27 | 26 | 29 | 26 | 26 | 25 | 30 | 29 | 27 | 25 | 23 | 24 | 23 |
| **Cu** | 20 | 22 | 27 | 24 | 24 | 24 | 23 | 25 | 22 | 32 | 26 | 26 | 25 | 24 | 19 |
| **La** | 14 | 13 | 13 | 15 | 14 | 14 | 14 | 14 | 14 | 15 | 14 | 15 | 16 | 13 | 14 |
| **Nb** | 4 | 4 | 4 | 5 | 4 | 4 | 4 | 4 | 4 | 6 | 5 | 4 | 4 | 5 | 4 |
| **Rb** | 30 | 29 | 30 | 30 | 29 | 29 | 28 | 28 | 30 | 29 | 29 | 30 | 27 | 31 | 28 |
| **Sc** | 9 | 12 | 13 | 12 | 15 | 12 | 14 | 14 | 12 | 14 | 13 | 13 | 12 | 14 | 12 |
| **Sr** | 501 | 492 | 474 | 475 | 498 | 501 | 512 | 509 | 492 | 499 | 494 | 460 | 513 | 469 | 517 |
| **V** | 74 | 91 | 106 | 94 | 90 | 90 | 91 | 96 | 95 | 104 | 96 | 103 | 92 | 95 | 84 |
| **Y** | 19 | 20 | 20 | 20 | 19 | 20 | 20 | 19 | 20 | 19 | 18 | 20 | 19 | 21 | 19 |
| **Zn** | 72 | 71 | 82 | 82 | 69 | 71 | 75 | 74 | 124 | 76 | 74 | 85 | 71 | 80 | 70 |
| **Zr** | 150 | 145 | 148 | 150 | 145 | 146 | 143 | 143 | 146 | 145 | 148 | 149 | 141 | 153 | 141 |

## 4.4.3. Geochemical signatures

### *4.4.3.1. Bulk-rock compositional differences*

All erupted products are andesites (61.3–62.7 wt.% $SiO_2$; Table 4.1) that abide to Santiaguito's historical mafic trend (Fig. 4.5a). However, subtle variabilities exist across the 2014–2017 eruptive period (Fig. 4.5b). The 2014 lava flow is the most evolved with 62.7 wt.% $SiO_2$ and a Mg # of 57.1. Ash and bombs erupted during phase 2 record a significant decrease in $SiO_2$ (by 1.0–1.5 wt.%) and increase in Mg # (by 4.0–6.0). During the high energy explosions in phase 3 the bulk-ash composition remained similarly more mafic, as in phase 2, although it became progressively less mafic during explosions in May and June 2016. The vesicular domains within the April 2016 bombs, which display groundmass textures similar to the TC clasts, are compositionally more mafic (61.57 wt.% $SiO_2$) than the denser domains (62.10 wt.% $SiO_2$).

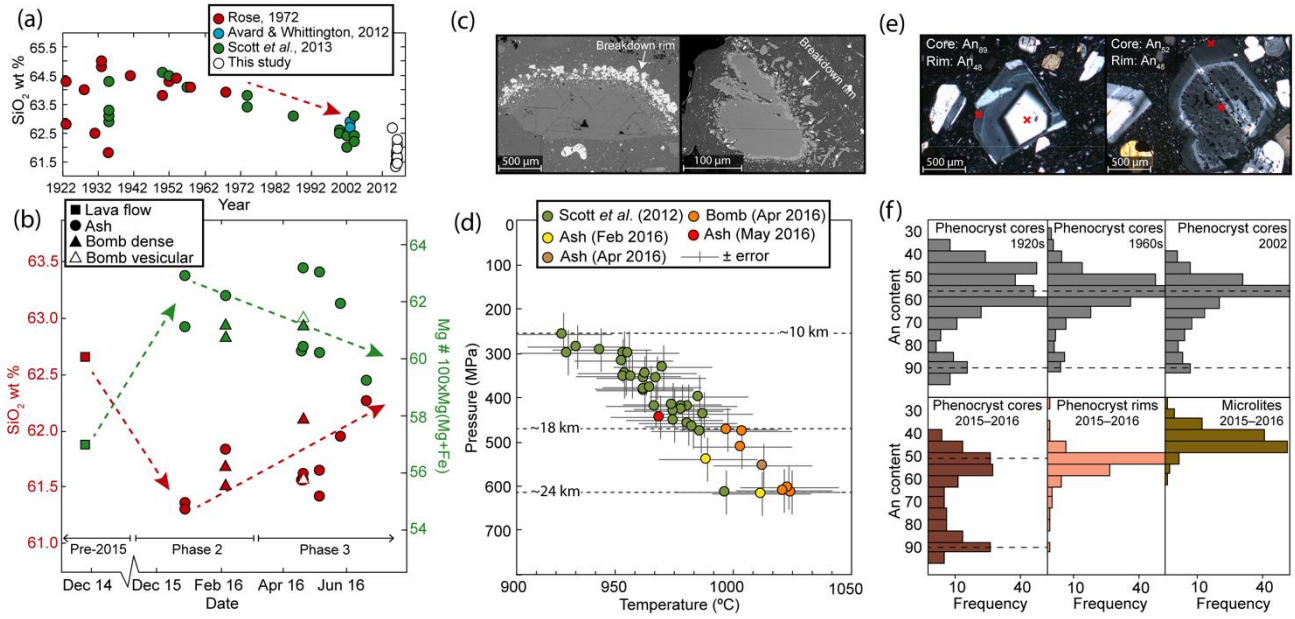


***Figure 4.5*** *– Geochemical signatures of the eruptive products. (a) Historical bulk-rock $SiO_2$ trend for Santiaguito from 1922–2016. (b) Bulk-rock compositional changes across collected samples from November 2014 to June 2016. (c) BSE images of amphibole phenocrysts displaying variations in breakdown rim texture indicative of multiple interacting processes. (d) Amphibole geothermobarometry from the method of Ridolfi et al. (2010) for amphiboles pre-2002 (Scott et al., 2012) and those from 2015–2016. (e) Plagioclase phenocrysts textures and respective An content of core and rim from the 21st April 2016 bomb. (f) Histogram displaying the evolution of plagioclase phenocryst cores An content for pre-2002 lavas (Scott et al., 2013) and 2015–2016 ash and bombs, along with phenocryst rim and microlite compositions.*

#### *4.4.3.2. Amphibole phenocrysts*

Amphibole crystals in the eruptive products from 2015–2016 are sparse (≤2 area %), and are found as clusters or individual phenocrysts. They typically display breakdown rims of anhydrous mineral phases, including plagioclase, orthopyroxene, clinopyroxene and titanomagnetite. Rims textures vary from thin, fine grained symplectitic laths consisting of anhydrous crystals to thick, coarse-grained crystals in the rim (Fig. 4.5c). In some cases, amphibole crystals are completely broken down resulting in pseudomorphs. Their remnant core compositions of different pressure-sensitive (e.g., Al) and temperature-sensitive (e.g., Si and Ti) elements can be used to estimate the conditions in which they crystallised (Ridolfi *et al.*, 2010; Ridolfi & Renzulli, 2012; Andrews, 2014; Kiss *et al.*, 2014). By employing the empirical amphibole geothermobarometer of Ridolfi *et al.* (2010), the amphiboles from large explosions in 2016 were estimated to crystallise at temperatures between ~965 and ~1024 ºC (±22 ºC) and pressures from ~446 to ~619 MPa (±50), which represents conditions at the higher temperature and pressure end of the previously constrained storage region (Fig. 4.5d; Scott *et al.*, 2012). The Ridolfi *et al.* (2010) model also provides formulations for a hygrometer (primarily influenced by Al content), with estimated dissolved magma $H_2O$ contents of between 6 and 8%.

#### *4.4.3.3. Plagioclase phenocrysts*

Plagioclase phenocryst core compositions from Santiaguito lavas between 1922 and 2002 record a temporal evolution based on An content (Fig. 4.5f; Scott *et al.*, 2012), which reveals a diminishing bimodal (peaks at $An_{40–50}$ and $An_{60}$) to a final unimodal distribution (single $An_{50–55}$ peak) through time. A small $An_{85–90}$ peak was recorded in all of Santiaguito's pre-2002 lavas (<10% of the phenocryst population). Plagioclase phenocryst core compositions from the explosive deposits in 2015–2016 (Fig. 4.5e and f; see Electronic Appendix 3) have a similar An peak to the early lavas ($An_{45–55}$, accounting 42% of the phenocrysts), although an additional strong peak at $An_{85–95}$ accounts 30% of the total plagioclase phenocryst population. Plagioclase phenocryst rim compositions record a single, strong unimodal distribution with a peak at $An_{50–55}$, while microlites reveal still lower An contents ($An_{22–57}$).

### 4.4.4. Groundmass textures and composition

#### *4.4.4.1. Interstitial glass chemistry*

The compositions of the interstitial groundmass glass for the ash and bombs pre-, during and post-2015–2016 are dominantly rhyolitic, although glass compositions for samples from 2015–2016 and 2018 are more heterogeneous with some extending to dacitic and trachytic (see Electronic Appendix 3). DB clasts have $SiO_2$ concentrations ranging 74–79 wt.%, while TC clasts show a larger range in glass $SiO_2$ content from 66–79 wt.%. Glass composition of the 2016 bombs reveal a similar heterogeneous $SiO_2$ range (69–79 wt.%), although negligible chemical differences were recorded for the dark and vesicular domains in the April 2016 bomb. Projecting the glass compositions onto the haplogranitic plot of Cashman and Blundy (2000), which uses An-corrected normative Qz-Ab-Or, provides an approximate assessment of the glasses' equilibrium state and kinetics of crystallisation (Fig. 4.6a). Liquid lines of descent show progressively higher glass equilibrium pressures through time, with the bomb in April 2016 and ash in January 2018 revealing significant disequilibrium between the melt and microlites at lower pressures.

Magmatic temperatures and water contents of the erupted products were estimated using the plagioclase-melt geothermometer and hygrometer of Putirka (2008). An average of the glass chemistry from each clast type was used as the melt composition along with the coexisting plagioclase microlites. These estimates show the TC clasts were hotter (~1000–1010 ºC) and more $H_2O$-rich (~2.4–2.7 %) than the DB clasts, which was significantly cooler (~920–930 ºC) and degassed (≤1 % $H_2O$), consistent with the vesicular texture of the bombs and pore shaped geometry of the TC clasts.

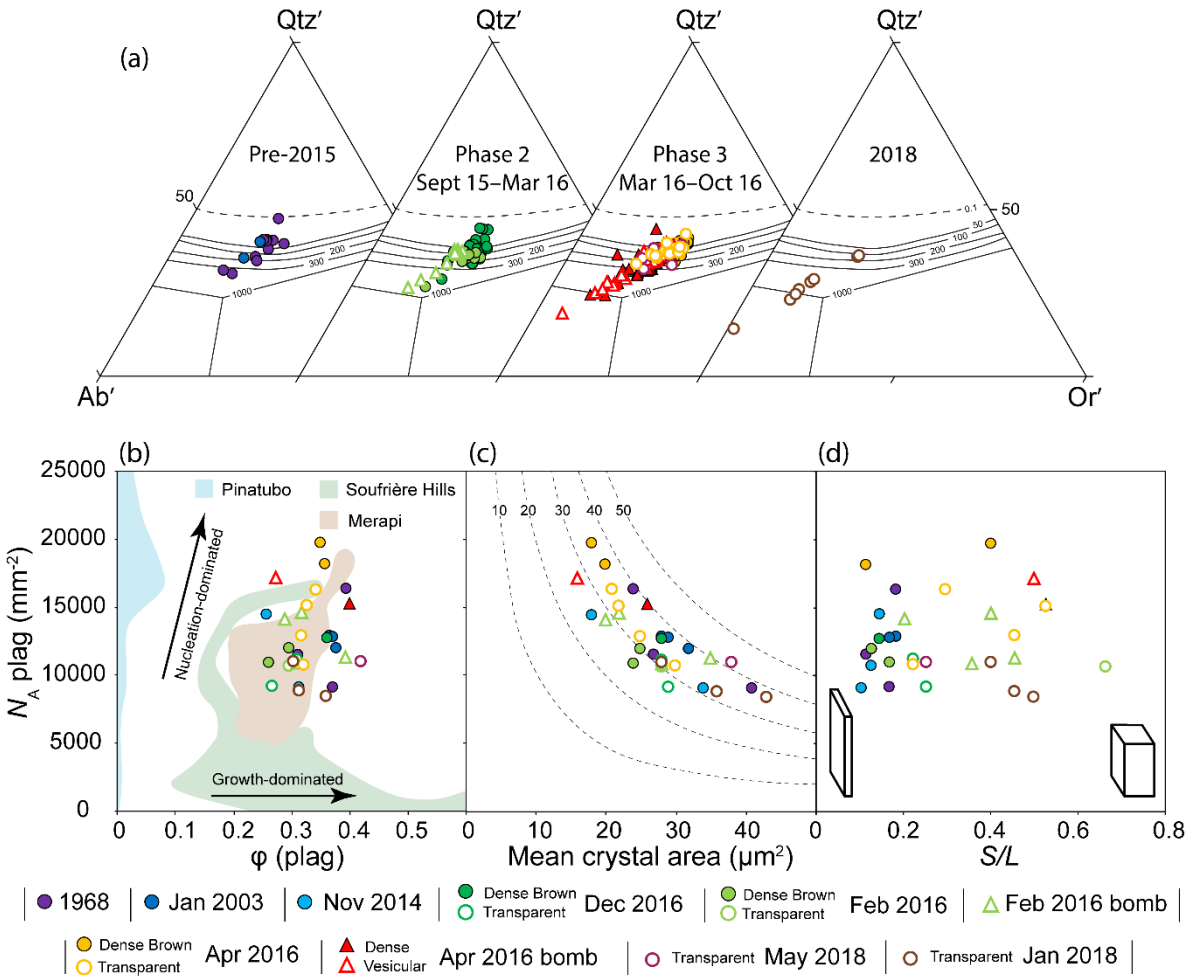


***Figure 4.6*** *– Interstitial glass composition and microlite textures. (a) Projection of glass composition on the haplogranitic plot after Cashman and Blundy (2000), revealing a temporal change to less evolved glass compositions. The phases represent albite (Ab), quartz (Qtz) and orthoclase (Or). (b–d) Quantitative assessment of plagioclase microlite textures and groundmass glass chemistry. Microlite number density ($N_A$) against (b) microlite crystallinity (φ), (c) mean crystal size and (d) aspect ratio using short/long axis (S/L) calculated from CSDSlice (Morgan & Jerram, 2006). Shaded areas in (a) show composition with other well characterised systems including Pinatubo (Hammer et al., 1999), Soufrière Hills Volcano (Clarke et al., 2007) and Merapi (Preece et al., 2013).*

***Table 4.2*** *– Quantitative textural analysis of groundmass plagioclase microlites for different juvenile clast types in the ash (transparent, TC, and dense brown, DB) and bombs from explosions in 2015–2016, compared to ash from 1968, 2003, 2014 and 2018 (n denotes number of crystals analysed). Crystals aspect ratios (short:intermediate:long axes) were calculated using the 3D stereological correction program CSDSlice (Morgan & Jerram, 2006). Growth rates and nucleation rates were calculated from equations of Marsh (1988). Ascents rates were calculated using the water exsolution rate meter of Toramaru et al. (2008).*

| Explosion date | Sample-grain/area no. | Clast type | 2D areal measurements | | | | | 3D volumetric measurements | | Calculated aspect ratio ($R^2$) | Average growth rates, $G$ (mm $s^{-1}$) | Average nucleation rates, $J$ ($mm^{-3}$ $s^{-1}$) | Ascent rate (m $s^{-1}$) |
|---|---|---|---|---|---|---|---|---|---|---|---|---|---|
| | | | $n$ | $N_A$ ($mm^{-2}$) | Area % | $\varphi$ | Mean crystal area ($\mu m^2$) | $S/L$ | Nv ($mm^{-3}$) | | | | |
| 15/01/1968 | 150168-1 | DB | 162 | 16,344 | 38.82 | 0.396 | 24.00 | 0.18 | 3,212,401 | 1.00:1.60:5.50 (0.6578) | – | – | 2.6E-05 |
| | 150168-2 | DB | 88 | 9,090 | 36.06 | 0.372 | 41.00 | 0.17 | 1,236,048 | 1.00:1.40:6.00 (0.6457) | – | – | 1.4E-05 |
| | 150168-3 | DB | 113 | 11,509 | 30.52 | 0.312 | 27.00 | 0.11 | 1,943,297 | 1.00:2.00:9.00 (0.5789) | – | – | 1.8E-05 |
| 13/01/2003 | 131103-1 | DB | 120 | 12,864 | 34.02 | 0.365 | 28.00 | 0.18 | 1,799,670 | 1.00:1.70:5.50 (0.6207) | – | – | 5.9E-05 |
| | 131103-2 | DB | 113 | 11,932 | 35.78 | 0.378 | 32.00 | 0.13 | 4,640,812 | 1.00:1.40:8.00 (0.5751) | – | – | 1.1E-04 |
| | 131103-3 | DB | 123 | 12,782 | 35.74 | 0.372 | 29.00 | 0.17 | 1,958,538 | 1.00:1.90:6.00 (0.4447) | – | – | 6.2E-05 |
| 26/11/2014 | 261114-1 | DB | 103 | 10,737 | 28.69 | 0.298 | 28.00 | 0.13 | 1,528,740 | 1.00:1.50:8.00 (0.5023) | 1.38E-06 | 270 | 3.5E-05 |
| | 261114-2 | DB | 86 | 9,067 | 29.74 | 0.313 | 34.00 | 0.10 | 1,645,045 | 1.00:2.00:10.00 (0.3931) | 7.76E-07 | 290 | 3.7E-05 |
| | 261114-3 | DB | 126 | 14,461 | 24.52 | 0.256 | 18.00 | 0.14 | 2,083,549 | 1.00:1.10:7.00 (0.4566) | 1.50E-06 | 368 | 4.3E-05 |
| 31/12/2015 | 311215A-1 | TC | 108 | 11,154 | 30.04 | 0.310 | 28.00 | 0.22 | 2,973,955 | 1.00:1.40:4.50 (0.7052) | 3.50E-08 | 33 | 2.1E-04 |
| | 311215A-2 | DB | 124 | 12,718 | 33.40 | 0.362 | 28.00 | 0.14 | 1,493,738 | 1.00:1.30:7.00 (0.4808) | 6.11E-08 | 17 | 1.0E-05 |
| | 311215A-3 | TC | 85 | 9,123 | 24.81 | 0.267 | 29.00 | 0.25 | 1,071,510 | 1.00:1.10:4.00 (0.6790) | 8.31E-08 | 12 | 1.2E-04 |
| 07/02/2016 | 070216-1 | TC | 98 | 10,608 | 27.32 | 0.295 | 28.00 | 0.67 | 3,152,877 | 1.00:1.40:1.50 (0.6809) | 2.54E-08 | 35 | 1.7E-04 |
| | 070216-2 | DB | 104 | 10,912 | 24.75 | 0.260 | 24.00 | 0.17 | 2,018,066 | 1.00:1.60:6.00 (0.8513) | 2.70E-08 | 23 | 1.3E-05 |
| | 070216-3 | DB | 108 | 11,942 | 28.97 | 0.296 | 25.00 | 0.13 | 1,289,272 | 1.00:1.40:8.00 (0.4383) | 1.26E-07 | 14 | 1.1E-05 |
| | 070216A-1 | Bomb | 107 | 10,853 | 30.49 | 0.309 | 28.00 | 0.36 | 3,327,415 | 1.00:1.50:2.80 (0.7703) | 2.62E-08 | 37 | 1.5E-05 |
| | 070216A-2 | Bomb | 128 | 14,126 | 27.75 | 0.288 | 20.00 | 0.20 | 3,971,338 | 1.00:1.15:5.00 (0.4969) | 1.51E-08 | 45 | 1.7E-05 |
| | 070216B-3 | Bomb | 109 | 11,268 | 38.07 | 0.393 | 35.00 | 0.45 | 1,974,087 | 1.00:1.30:2.20 (0.6027) | 2.87E-08 | 22 | 1.0E-05 |
| | 070216B-4 | Bomb | 136 | 14,574 | 29.60 | 0.316 | 22.00 | 0.40 | 3,425,310 | 1.00:1.50:2.50 (0.6194) | 1.29E-08 | 39 | 1.5E-05 |
| 19/04/2016 | 190416-1 | TC | 145 | 15,076 | 31.53 | 0.328 | 22.00 | 0.53 | 6,251,354 | 1.00:1.40:1.90 (0.7008) | 1.29E-08 | 70 | 6.8E-04 |
| | 190416-2 | DB | 190 | 19,699 | 33.77 | 0.351 | 18.00 | 0.40 | 6,488,447 | 1.00:1.60:2.50 (0.7163) | 1.75E-08 | 73 | 1.5E-05 |
| | 190416-3 | TC | 123 | 12,885 | 30.06 | 0.317 | 25.00 | 0.45 | 3,886,170 | 1.00:1.30:2.20 (0.6092) | 8.38E-09 | 44 | 2.7E-04 |
| 21/04/2016 | 210416B-1 | DB | 173 | 18,136 | 34.14 | 0.358 | 20.00 | 0.11 | 2,484,393 | 1.00:1.40:9.00 (0.7163) | 6.91E-08 | 28 | 2.4E-05 |
| | 210416B-2 | TC | 102 | 10,740 | 30.55 | 0.321 | 30.00 | 0.22 | 852,169 | 1.00:1.25:4.50 (0.7605) | 3.53E-08 | 10 | 8.2E-05 |
| | 210416B-3 | TC | 148 | 16,291 | 33.36 | 0.342 | 21.00 | 0.29 | 3,762,548 | 1.00:1.50:3.40 (0.6509) | 2.28E-08 | 42 | 1.4E-04 |
| | 210416A-1 | Vesicular bomb | 163 | 17,171 | 25.81 | 0.272 | 16.00 | 0.50 | 4,268,243 | 1.00:1.40:2.00 (0.8289) | 4.14E-08 | 48 | 1.5E-03 |
| | 210416A-2 | Dense bomb | 146 | 15,167 | 37.42 | 0.395 | 26.00 | 0.53 | 4,775,529 | 1.00:1.50:1.90 (0.7181) | 2.97E-08 | 54 | 2.7E-05 |
| 06/05/2016 | 060516-1 | TC | 106 | 10,944 | 40.72 | 0.421 | 38.00 | 0.25 | 1,182,184 | 1.00:1.15:4.00 (0.5013) | 7.84E-08 | 13 | 1.4E-04 |
| 20/01/2018 | 200118-1 | TC | 83 | 8,414 | 35.44 | 0.361 | 43.00 | 0.50 | 1,317,677 | 1.00:1.25:2.00 (0.6718) | 3.62E-07 | 107 | 8.5E-04 |
| | 200118-2 | TC | 103 | 10,985 | 29.17 | 0.305 | 28.00 | 0.40 | 2,746,636 | 1.00:1.25:2.50 (0.7892) | 2.40E-07 | 223 | 1.6E-03 |
| | 200118-3 | TC | 88 | 8,834 | 31.08 | 0.314 | 36.00 | 0.45 | 1,237,069 | 1.00:1.20:2.20 (0.7054) | 2.19E-07 | 100 | 3.4E-03 |

*4.4.4.2. Plagioclase microlite textures*

The groundmass of the ash and bombs across the 2015–2016 eruptive transition consists of 25–40% plagioclase, 1–8% mafic crystals (combined pyroxene and titanomagnetite), 55–70 % interstitial glass and <1 % porosity (Fig. 4.3b and d). Textural characterisation of groundmass microlites can provide a quantitative assessment of the style of late-stage crystallisation. We focus exclusively on quantification of plagioclase microlites between the DB and TC clasts, as well as the bombs (Fig. 4.3a–f, Fig. A3.3; Table 4.2).

Both DB and TC clasts have similar overlapping microlite number densities ($N_A$) (9067–19699 $mm^{-2}$ and 8414–16291 $mm^{-2}$, respectively). Similarly, fractal plagioclase crystallinities for both clasts ($\varphi$) fall within a similar range (0.25–0.41) and show negligible correlation with $N_A$ (Fig. 4.6b). However, $N_A$ for both DB and TC clasts correlate with crystal size and fit along isopleth lines for crystallinity, with smaller crystals having a higher $N_A$ and larger crystals having a lower $N_A$ (Fig. 4.6c). Although negligible 2D textural variations exist between $N_A$ and $\varphi$ for the DB and TC clasts, 3D crystal morphologies (determined using *CSDSlice*) reveal a distinct divide between the clast types (Fig 4.6d). Plagioclase microlite aspect ratios (*S/L*) for DB clasts were typically less than 0.2 (i.e., elongate/acicular), while microlites' aspect ratios in TC clasts were consistently higher (0.2–0.7; i.e., more equant).

3D crystal size distributions (CSDs) correct for the errors obtained by using 2D slices, which can provide a more quantitative assessment of the style of late-stage magma ascent (see Fig. A3.4 for all CSD curves). Using the slope ($\alpha$) and y-intercept ($n_o$) of the steepest portion of the CSD curves (smallest microlites representing late-crystallisation), volumetric number densities ($N_v$), microlite growth rates (*G*) and nucleation rates (*J*) were calculated (Marsh, 1988; Blundy and Cashman, 2008) and temporally assessed (Fig. 4.7a–d). $N_v$ for pre-2015 ash were typically $<3 \times 10^6$ $mm^{-3}$ (except for an anomalous high $N_v$ in ash from 2013), which show a progressive increase in the upper limit through 2015–2016 (up to $6.5 \times 10^6$ $mm^{-3}$) that returned to $<3 \times 10^6$ $mm^{-3}$ in 2018 (Fig. 4.7a). The temporal evolution in *S/L* values also show an increase for explosions in 2015–2016, which remain high in 2018 (Fig. 4.7b). *G* values (Fig. 4.7c) and *J* values (Fig. 4.7d) show large ranges owing to the uncertainty of crystallisation timescales ($\tau$), thus should be taken with caution. However, by using repose times as the minimum $\tau$, and the time difference between the explosion and the start of phase 1 as the maximum $\tau$, an average *G* and *J* can be calculated which provides an approximate, realistic estimate. Average growth rates for microlites in 2014 are $\sim 1.2 \times 10^{-6}$ mm $s^{-1}$, drop to $\sim 4.0 \times 10^{-8}$ mm $s^{-1}$ in 2015–2016, and increase again in 2018 ($2.7 \times 10^{-8}$ mm $s^{-1}$); similar trend is calculated for the average *J* (~300 $mm^{-3}$ $s^{-1}$ in 2014, ~35 $mm^{-3}$ $s^{-1}$ in 2015–2016, and ~140 $mm^{-3}$ $s^{-1}$ in 2018), yet no clear differences in *G* and *J* were calculated for DB and TC clasts.

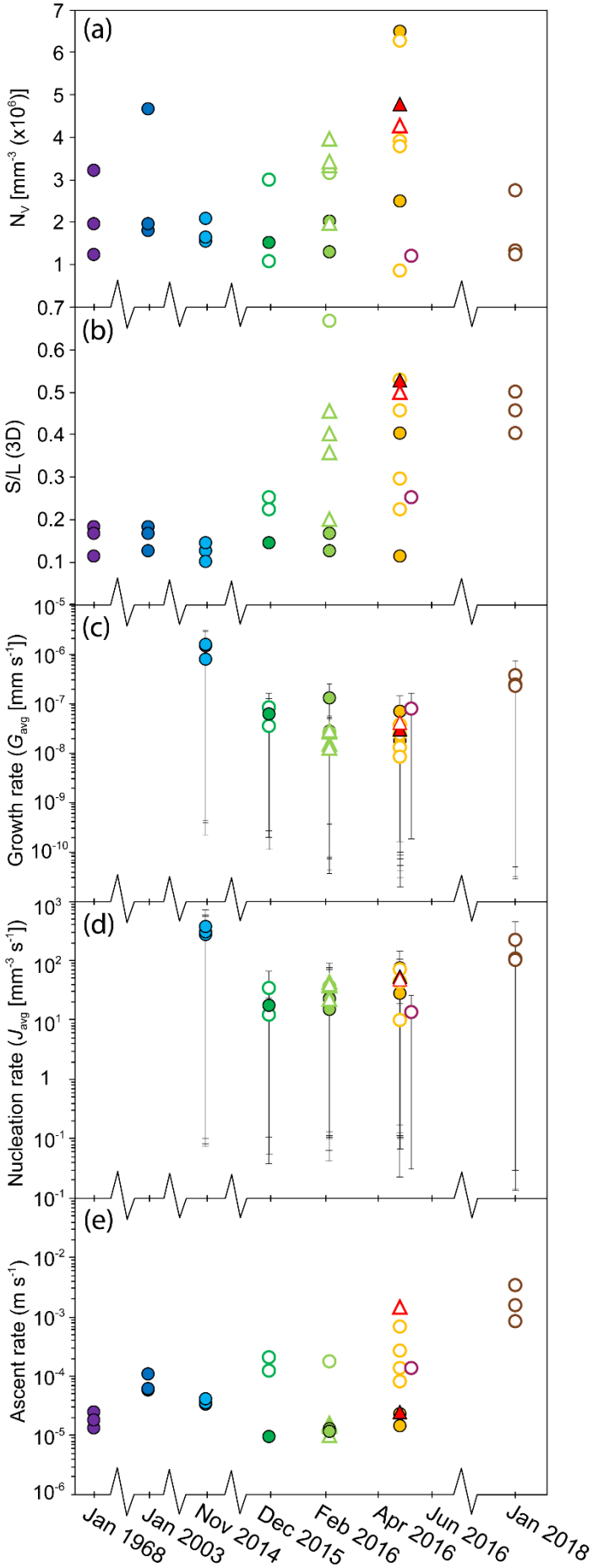


***Figure 4.7*** *– Temporal evolution of 3D plagioclase microlite textural characteristics for ash and bombs samples over the eruptive period. (a) Volumetric number densities ($N_v$), (b) short/long axes (S/L) determined using CSDSlice (Morgan & Jerram, 2006), (c) average growth rates (G) and (d) nucleation rates (J), and (e) calculated ascent rates using the water exsolution rate meter (Toramaru et al., 2008). Error bars in (c) and (d) represent minimum and maximum rates. Symbols are the same as those in Figure 4.6.*

*4.4.4.3. Ascent rates*

In order to assess whether a variation in magma ascent rate took place during microlite crystallisation, ascent rates were estimated using the water exsolution rate meter of Toramaru *et al.* (2008). Firstly, decompression rates ($dP_w/dt$) were calculated as:

$$\left|\frac{dP_w}{dt}\right| = \frac{c}{b}\left(\frac{N}{a}\right)^{\frac{2}{3}} \quad (4.2)$$

where $c$ is a function of the water content, $b$ is a constant (40 for plagioclase), $N$ is the microlite number volume and $a$ is a calculation combining both glass $SiO_2$ and water content. Water contents of 1% and 2.5% were used for the DB and TC clasts, respectively, as derived from the plagioclase-melt hygrometer of Putirka (2008), although the most sensitive factors are the volumetric number densities and glass composition. An ascent rate ($V_n$) was then calculated from the following:

$$V_n = \frac{1}{\rho g}\left|\frac{dP}{dz}\right|_{z=zn} \quad (4.3)$$

where $\rho$ is the density (2500 kg $m^{-3}$), $g$ is gravity and $dP/dz$ is the decompression rate at a given water content at a given depth (i.e., onset of microlite crystallisation). Estimated ascent rates (Fig. 4.7e) for the DB clasts are between 1.0–3.5 x $10^{-5}$ m $s^{-1}$ (Fig. 4.7e), while the TC clasts from 2015–2016 and 2018, along with the vesicular domains in the bombs, ascended up to 2 orders of magnitude faster (3.4 x $10^{-3}$ m $s^{-1}$).

## 4.5. DISCUSSION AND INTERPRETATION

The explosive eruption intensification during 2015–2016 coincided with systematic shifts in the geophysical, geochemical and petrological (i.e., microtextural and mineralogical) signals. Previous eruption intensifications at other systems have been attributed to deep magmatic process, particularly the injection of new magma (e.g., Sparks *et al.*, 1977; Pallister *et al.*, 1992; Venezky & Rutherford, 1999; Murphy *et al.*, 2000), fluctuations in volatile content (e.g., Edmonds & Herd, 2007; Williamson *et al.*, 2010; Costa *et al.*, 2013; Parmigiani *et al.*, 2016), changes in ascent style and rate (e.g., Hammer *et al.*, 1999; Noguchi *et al.*, 2008b; Preece *et al.*, 2013; Cassidy *et al.*, 2015) or cyclic pressure accumulation and release (e.g., Voight *et al.*, 1999; Melnik & Sparks, 2002; Johnson *et al.*, 2014) within a high-viscosity plug. Thus, identifying the cause requires an understanding of the magma plumbing system from source to surface.

### 4.5.1. Architecture of the 2015–2016 magma storage region

Amphiboles are ubiquitous hydrous minerals found in many intermediate volcanic systems, which provide a useful tool for assessing the conditions and processes occurring during magma storage and ascent owing to their sensitivity to different intensive variables (e.g., Rutherford & Hill, 1993; Browne & Gardner, 2006; Ridolfi *et al.*, 2010; De Angelis *et al.*, 2015). Our data suggest that amphibole crystals in the ash and bombs erupted explosively in 2015–2016 were derived from a hottest (~965–1024 ºC), deepest (~446–619 MPa) and volatile-rich (6–8 wt.% $H_2O$) region of the pre-constrained magmatic plumbing system (~940–980 ºC, ~330–615 MPa, 5–7 wt.% $H_2O$; Fig. 4.8a; Scott *et al.* (2012)). The use of amphiboles as geothermometers is generally well accepted, however their use as a reliable geobarometer remains controversial (e.g., Putirka, 2016), despite being used widely to reconstruct magma source conditions (e.g., Shane & Smith, 2013; Kiss *et al.*, 2014) that agree with depths constrained by seismicity (e.g., Nagasaki *et al.*, 2017). The shift to a less evolved bulk-rock composition for the ash and bombs during 2015–2016 (Fig. 4.5b) further supports the geothermobarometry, which also abides to the hypothesised chemically stratified storage region beneath Santiaguito (e.g., Scott *et al.*, 2013).

Compositions of plagioclase phenocrysts, in particular growth zonations from core to rim (Fig. 4.5e), can provide useful insights into deeper magmatic processes as they are influenced by the composition of the surrounding parent melt, along with pressure, temperature and volatile contents (Fig. 4.5e). Although plagioclase phenocrysts' core compositions from lava extruded since the 1940's have retained a homogenous peak at $An_{45–45}$, which took over from the two peaks from the 1920's attributed to magma mixing (Scott *et al.*, 2013), the increase of high An cores ($An_{85–95}$) in the 2015–2016 eruptive products suggests remobilisation and/ or convection of a relatively thick mush zone at ~17–24 km depth (e.g., Kratzmann *et al.*, 2009; Burgisser & Bergantz, 2011). This mush zone likely contained crystals formed from a more primitive melt (e.g., Stock *et al.*, 2018), which got incorporated as antecrysts (e.g., Larrea *et al.*, 2013; Cashman *et al.*, 2017; Holness *et al.*, 2019) during ascent and followed a similar path through the shallow system as confirmed by the near-homogenous plagioclase rim compositions (Fig. 4.5f and 4.8a).

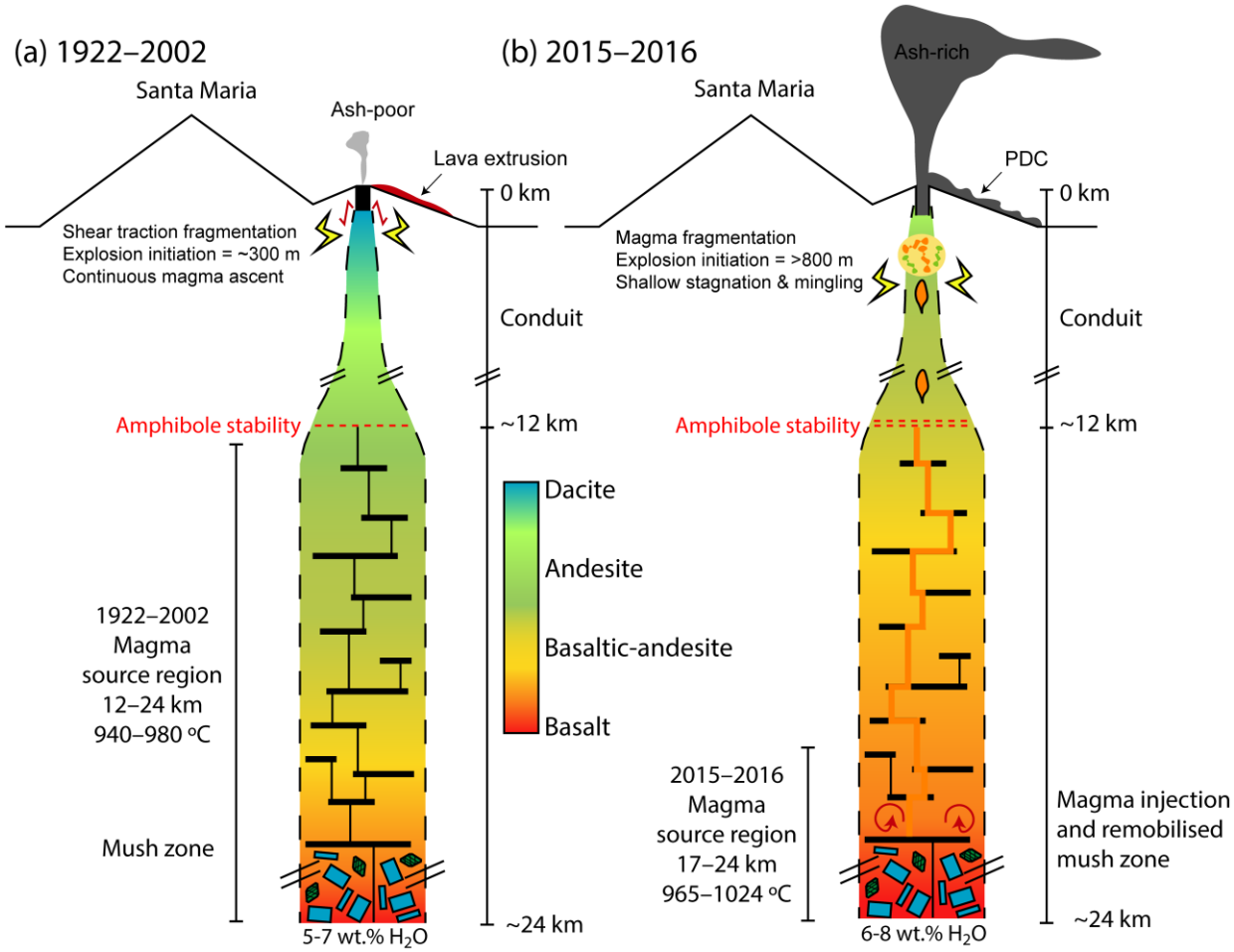


***Figure 4.8*** *– Conceptual model for the change in explosivity during 2015–2016. (a) An interpretative model for the magma plumbing system from 1922–2015 modified from Scott et al. (2013). Coloured-gradation reflects the degree of magma evolution from dacitic to basaltic. The storage region was constrained by amphibole thermobarometry to reside at 12–24 km depth. Slow, continuous magma ascent from the deep to shallow system would have taken place, with crystallisation and volatile exsolution leading to the formation of blocky lava flows and generation of a plug. Shallow shear and friction-driven fragmentation likely resulted in small (<1 km high) ash-poor plumes. (b) Injection of new magma into the shallow magmatic system from depth, which passed through an extensive mush zone. Magma likely ascended as volatile-rich pulses that experienced a relatively fast ascent towards the surface, stalling beneath the dome which facilitated mingling with pre-2015 magma. Overpressure from rising magma and gases from beneath led to the gradual excavation of the 2014 lava flow that plugged the vent causing greater delays in the arrival times in seismic and acoustic signals (as fragmentation depth increased), resulting in high energy, ash-rich explosions and pyroclastic flows.*

### 4.5.2. Magma ascent

Textural characterisation of groundmass microlites can provide a quantitative assessment of the style of crystallisation, which may thus be used to constrain pre-eruptive magmatic process and ascent paths in the shallow volcanic conduit (e.g., Cashman & Blundy, 2000; Hammer *et al.*, 2000; Noguchi *et al.*, 2008b; Toramaru *et al.*, 2008; Miwa *et al.*, 2009; Preece *et al.*, 2013; Cassidy *et al.*, 2015; Preece *et al.*, 2016; Bain *et al.*, 2019). Plagioclase microlites reflect the degree of undercooling ($\Delta T$) and thus ascent rate (e.g., Hammer & Rutherford, 2002; Brugger & Hammer, 2010). Theoretically, a larger $\Delta T$ favours a nucleation-dominated regime with the formation of many small microlites, whereas a smaller $\Delta T$ would result in a growth-dominated regime and the growth of fewer large crystals (Mollo & Hammer, 2017). The overlapping microlite number densities ($N_A$), mean crystal sizes and crystallinities ($\varphi$) for the DB and TC ash fragments across the eruptive transition period makes such an interpretation challenging. Yet, the differences in the crystal morphology (*S/L*) for the two clast types (Fig. 4.6c and 4.7b) can also be related to the style of crystallisation (e.g., Hammer & Rutherford, 2002; Couch *et al.*, 2003); these experimental studies have shown that crystals change from equant/tabular to acicular with an increasing $\Delta T$. Microlites in TC clasts have a consistently higher *S/L* values than the DB clasts, suggesting these clasts experienced a lower $\Delta T$. Apply these results to the experimentally calibrated model linking crystal morphology with final crystallisation pressures (Hammer & Rutherford, 2002), DB clasts suggest continued crystallisation to ~10 MPa in the conduit (~400 m depth) as previously estimated for pre-2002 lavas (Scott *et al.*, 2012), while TC clasts suggest final pressures of ≥50 MPa (~2 km depth). This is supported by the observation that TC microlites show more pronounced growth zones (Fig. 4.3b and d). Furthermore, the broad range in plagioclase microlite An contents ($An_{22–57}$; Fig. 4.5f) suggests microlites in both clast types formed at different temperatures, pressures and water-contents indicative of multi-step decompression (e.g., Cassidy *et al.*, 2015; Bain *et al.*, 2019).

The higher estimated $H_2O$ content and temperatures of the TC magma and vesicular domains in the bombs (from plagioclase-melt hygrometer) suggests limited degassing in the shallow conduit, which is supported by the higher equilibrium pressures of the interstitial glass (Fig. 4.6a) and faster ascent rates relative to degassed DB clasts (Fig. 4.7e). This is consistent with the pore shaped edges of the TC clasts (Fig. 4.3c). Several lines of evidence thus demonstrate that the TC clasts and vesicular bomb domains were derived from a new magma source that influenced final ascent style and thus the differentiation of the groundmass microlite textures and glass composition. Consequently, the mingling of the volatile-rich, vesicular domains and degassed dense-domains in April 2016, which appear to represent the TC and DC clasts, respectively, likely interacted at a shallow level in the conduit following

groundmass crystallisation (e.g., Cimarelli *et al.*, 2010). During such mingling at shallow levels, it is likely that the eruptive products entrained material that had coupled to the conduit margin wall-rock. The systemically more evolved composition of ash from the large explosions in May and June 2016 (Fig. 4.5b), which coincides with increased content of lithic clasts (Fig. 4.3g) comprising increased silica polymorphs (Fig. 4.4g and h), suggests entrainment of the more evolved conduit wall-rock. The presence of clast with silica polymorphs suggests that these clasts had resided at high temperatures and shallow depths for a long duration causing subsequent glass devitrification (e.g., Couch *et al.*, 2003; Scott *et al.*, 2012; Horwell *et al.*, 2013).

### 4.5.3. Explosion mechanisms: Linking geophysical and petrological observations

Early interpretations of Santiaguito's regular, weak explosive activity suggested magma-water interaction may be responsible (i.e., phreatomagmatic) owing to a combination of heavy rainfall and the active vent residing in the centre of the 1902 crater (Rose, 1972). However, more recent observations have led to different mechanisms being proposed. Geophysical monitoring of the dome using tilt meters revealed regular (every ~26 minutes) inflation and deflation cycles throughout 2012–2014 (Johnson *et al.*, 2014; Lavallée *et al.*, 2015a; Lamb *et al.*, 2019). Intermittent Very Long Period (VLP) earthquakes (Johnson *et al.*, 2014) accompanied explosions which occurred during the most rapid inflation-deflation cycles; whereas steady, slower inflation-deflation cycles resulted in passive degassing at the vent, no explosion and no VLP earthquakes. These cycles have been attributed to gas accumulation from a pressure source (Sanderson *et al.*, 2010; Johnson *et al.*, 2014), either beneath a plug or within a shallow reservoir, during times of temporal sealing of permeable pathways, followed by its sudden release, rapid decompression and deflation of the surface with a corresponding gas flux of ~$10^1$ kg $s^{-1}$ (Johnson *et al.*, 2008; Johnson *et al.*, 2014). Combined seismic, acoustic and thermal monitoring of these explosions provided depth constraints for the source of these explosions, occurring 100–620 metres beneath the vent (Sahetapy-Engel *et al.*, 2008; Johnson *et al.*, 2014). The dominance of DB clasts in ash generated during similar events pre-2015 suggests fragmentation of a completely degassed magma plug that resided at <400 m depth in the conduit (Fig. 4.8a). The low energy of these explosions (Fig. 4.2g) and relatively short delays in the time arrivals between the seismic and acoustic infrasound signals observed here support a shallow explosion source, likely representing fragmentation of the 2014 lava that filled the conduit. The capping of open-system volcanic conduits with a high viscosity plug is a common phenomenon observed at many silicic volcanoes that show persistent explosive activity (e.g., Volcán de Colima, Lavallée *et al.* (2013); Sakurajima, Miwa *et al.* (2009); Soufrière Hills, Clarke *et al.* (2007)).

Conduit flow modelling suggests shear-induced fragmentation is a likely process in such cases (Gonnermann & Manga, 2003), owing to pulsatory ascent and subsequent localised failure near the conduit margins (e.g., Goto, 1999; Papale, 1999; Bluth & Rose, 2004; Neuberg *et al.*, 2006). At Santiaguito, this model is supported by the gas-rich, ash-poor nature of the 2014 eruption plumes (De Angelis *et al.*, 2016), along with rapid outgassing along arcuate fractures (Bluth & Rose, 2004; Johnson *et al.*, 2008; Sahetapy-Engel *et al.*, 2008). Furthermore, $SO_2$ gas fluxing during explosions in 2008–2009 have provided further evidence for localised shear fracturing, in which monitored $SO_2$ degassing remained continuous throughout repose intervals, suggesting no significant sealing of the permeable network took place for pressure to accumulate (Holland *et al.*, 2011). We thus infer that the trigger mechanism for explosions up until phase 1 (Fig. 4.2g) were driven primarily by shear-induced fragmentation at shallow depth (Fig. 4.8a). The detectable, low heat flux from satellite data in pre-2015 supports this shallow fragmentation that failed to excavate the crater to access fresh magma; as such the heat flux likely derived from incandescence of fractures within the infilled crater.

The gradual increase in the repose intervals and energy of explosions from phase 1 to phase 2 likely reflects a change in magma ascent, evolution and eruption mechanism influenced by the injection of volatile-rich magma (likely a low volume) modifying the pressure source in the conduit and the outgassing efficiency of the high-viscosity magma (Fig. 4.8a). During this time, the development and destruction of outgassing pathways, including fracture networks (e.g., Tuffen *et al.*, 2003), tuffisite veins (e.g., Castro *et al.*, 2012; Kendrick *et al.*, 2016) and other permeable networks (e.g., Heap *et al.*, 2015; Farquharson *et al.*, 2016b), would play a non-trivial role. However, the new magma would not have the same permeable mature outgassing pathways as the old magma (e.g., Kennedy *et al.*, 2016). The largest explosions recorded in phase 3 (April 2016) coincided with the high abundance of TC clasts in the ash and mingled bombs, contemporaneous with the excavation of the crater. The longer delay in the seismic and acoustic time arrivals for some explosion events during this period suggests a potential deeper fragmentation source, which is consistent with the higher final crystallisation pressures (lower degree of undercooling, $\Delta T$) and more equant shaped (high *S/L* values) microlites in the TC clasts. It thus suggests a switch from shallow-shear fragmentation to deeper overpressure-driven fragmentation may have been triggered by a small injection pulse of magma entering the shallow system causing an evolution from phase 1 to 4 (Fig. 4.2g and 4.8b). Interestingly, although activity returned to regular, small-to-moderate explosions in phase 4 (late-2016) and the crater subsequently refilled, ash from January 2018 was abundant in TC clasts, leaving questions on the future state of Santiaguito's eruptive activity.

## 4.6. CONCLUSION

The shift in eruption style at Santiaguito from early-2015 to late-2016 has been explored by combining petrological, geochemical, geophysical and thermal observations. In this study, we show a unique dataset that documents this escalation in explosivity using a multiparametric approach. Multiple lines of evidence, including a shift to less evolved magma, geothermobarometry estimates, influx of plagioclase antecrysts, higher estimated dissolved $H_2O$ contents, and a shift in ash componentry suggests eruption intensification in 2015–2016 was influenced by the injection of new magma. Monitored seismic and acoustic signals suggest that this caused fewer, more erratic (i.e., less regular), larger explosions, generated from generally deeper fragmentation levels. These larger explosions disrupted the dome, excavated a crater and exposed the hot interior of the dome as observed by satellite-based thermal imagery. Although many questions regarding the processes taking place during 2015–2016 at Santiaguito remain (e.g., the role of volatiles), we highlight the importance of long-term multiparametric monitoring techniques coupled with detailed investigation of the erupted products. Such efforts will assist in improving our understanding of pre-eruptive volcanic processes, the monitored signals these processes produce and shifts in eruption style at intermediate volcanic systems, ultimately to mitigate the threats to local communities.

# Chapter 5 Conclusions and outlook

## 5.1. SUMMARY OF RESULTS

The enigmatic behaviour of lava dome eruptions and associated hazards arises from the complex interplay and feedback between deep and shallow magmatic processes that can alter the rheological, physical and chemical properties of the magma. The dynamic relationship between rheological transitions of magma during ascent, shallow mechanical processes and petrological signatures of the eruptive products demonstrates the importance of multidisciplinary studies. In this thesis, I have investigated the impact of strain localisation during magma ascent, including the role of shearing (Chapter 2) and friction (Chapter 3) in the upper conduit preceding and contributing to eruption. Furthermore, I investigated the cause of a shift in eruption intensification at Santiaguito dome complex, Guatemala (Chapter 4), where explosive activity has previously been attributed to faulting and shear-driven processes at the conduit margins. For each chapter, I elucidate how the impact of shear, friction and magma recharge can regulate intermediate–silicic volcanism, particularly at lava domes, with this thesis contributing new insights on processes that can have an essential role in regulating eruptive activity.

In Chapter 2, I assessed the evidence for and role of strain localisation during magma ascent at Unzen volcano, Japan, through a detailed, systematic petrological survey of a marginal shear zone of the 1994–95 lava spine. I deployed a multidisciplinary approach combining field observations, petrology, microstructures, crystallography, magnetics and experimentation to constrain the impact of shear on the architecture of the magmatic column. Based on the understanding of a magma's rheological behaviour from extensive experimental investigations (e.g., Caricchi *et al.*, 2007; Lavallée *et al.*, 2007; Costa *et al.*, 2009), shear zone development was attributed to the shear thinning, non-Newtonian rheology of the magma, which facilitated in localising stress and strain near the conduit margins, favouring plug style ascent (Hale, 2007; Hale *et al.*, 2007). I demonstrated that crystals can monitor stress conditions as magma ascends through the viscous–brittle transition, from viscous remobilisation and crystal alignment to brittle failure and comminution in regions of most strain. Previous work on Mount St. Helens (Washington, USA) lava spines revealed evidence for only brittle deformation at the conduit margins, suggesting fault traction was the main processes involved (Cashman *et al.*, 2008; Kennedy *et al.*, 2009; Pallister *et al.*, 2013). However, at Unzen volcano I showed that lava spine extrusion involved a complex interplay between viscous, plastic and brittle deformation mechanisms. I highlighted for the first time for extrusive lavas at outcrop scale, that crystals can accommodate strain by deforming plastically, wherein I revealed an increase in crystal plasticity towards the spine margin

associated with shear intensity. Naturally, crystal plasticity may be used as an outlet for strain as magma ascends through the viscous–brittle transition, which may even delay the onset of brittle failure. Brittle failure manifested primarily as cataclasis and comminution of the main phenocryst phases (plagioclase and amphiboles), which caused a reduction in crystal size towards the spine margin. The crystal textures observed with increased strain conditions are similar to those reported by Cordonnier *et al.* (2009). Owing to intense comminution of these phases in the high shear zone, some finer crystal fragments were excavated from cataclastic bands causing a shift in mineral modal abundance across the shear zone.

Disequilibrium conditions were also shown to be associated with magmatic shearing in the form of amphibole reaction rims. Processes that are known to contribute to amphibole breakdown are decompression (e.g., Rutherford & Hill, 1993; Browne & Gardner, 2006), heating (e.g., Murphy *et al.*, 2000; Rutherford & Devine, 2003; De Angelis *et al.*, 2015) or oxidation (e.g., Garcia & Jacobson, 1979). I showed that the amphibole reaction rims in the magmatic shear zone become more pronounced with shear intensity. Two types of rims were displayed, a granular rim exclusive to the high shear zone and gouge, which was attributed to shear heating, and a symplectitic rim related to late-stage oxidation of the spine. The localised granular reaction rims coupled with viscous remobilisation, compaction of the porous network and distinct magnetic properties in the high shear zone indicated a thermal input due to shear and frictional heating. I further suggested that this temperature increase may also have contributed to the increase in crystal plasticity towards the spine margin, owing to yield stresses required for crystal plasticity being lower at high temperatures (Poirier, 1995). These deformation textures would facilitate in reducing permeability in the shear zone, enabling gas accumulation and favouring explosive behaviour. However, it appears that due to Unzen's relatively high connected porosity, sufficient pressure was unable to accumulate to trigger an explosion, yet it remains a factor that needs to be considered when assessing shifts in eruption style during future eruptions at Unzen and at other intermediate volcanic systems.

The processes taking place during magma shearing in the volcanic conduit were simulated by performing the first (to our knowledge) high ambient temperature, high-velocity rotary shear experiment on the lava from Unzen. This experiment provided a temperature constraint for shearing by recreating natural spine textures through frictional heating and thermal dissipation away from the slip zone, including viscous deformation, pore compaction and amphibole reaction rim textures. I also showed that the lava spine experienced a chemical and textural overprint in the form of devitrification of the interstitial glass as a result of the prolonged exposure to higher temperatures. In particular, the gouge displays intense breakdown of the glass to silica-rich phases, which implied continuous decoupling from the

spine, along with magnetic signatures that suggest fluid and gas fluxing at high temperatures following emplacement.

The high strain conditions at the conduit margins, as demonstrated in Chapter 2, can lead to seismogenic magma failure that promotes faulting and slip along fracture planes (e.g., Iverson *et al.*, 2006; Neuberg *et al.*, 2006; Lavallée *et al.*, 2008; Lensky *et al.*, 2008; Kendrick *et al.*, 2014b; Lavallée *et al.*, 2015b). Frictional melting of the adjoining slip surfaces, associated with extreme frictional heat, can have a profound effect on the style of slip, which may dictate magma ascent dynamics in the upper conduit (Kendrick *et al.*, 2014a). The mechanical behaviour of a frictional melt is determined by its shear resistance during slip, acting as either a lubricant (e.g., McKenzie & Brune, 1972; Tsutsumi & Shimamoto, 1997) or viscous brake (e.g., Koizumi *et al.*, 2004; Kendrick *et al.*, 2014b), which is dependent on its rheological properties (e.g., Hirose & Shimamoto, 2005; Lavallée *et al.*, 2012a; Hornby *et al.*, 2015). In Chapter 3, I provide a detailed, systematic, experimental investigation to assess the geochemical, textural and rheological evolution of a frictional melt and demonstrate the contribution of the host-rock mineral assemblage to slip properties via selective phase melting (Spray, 1992). High-velocity rotary shear experiments were performed on three mineralogically contrasting intermediate lavas collected from active lava dome volcanoes. These included an amphibole-bearing andesite from Soufrière Hills Volcano, Montserrat, an amphibole-pore dacite from Santiaguito dome complex, Guatemala, and an amphibole-free andesite from Volcán de Colima, Mexico. I report in detail the textural evolution of the slip-zone frictional melts with increasing slip distance. At the early stages of melting, comminution dominates leading to the formation of ultra-fine crystal fragments that subsequently melt due to frictional heating. The first melts to form on the slip surface cause an initial increase in shear stress, which continues to climb to a maximum until a full melt layer has formed. With increasing slip, the frictional melts exhibit a shear-weakening response leading to steady-state conditions. At this point, comminution is replaced by tearing of large crystals along the slip interface, attributed to a switch from frictional heating to shear heating (i.e., viscous energy dissipation).

I showed that the mechanical behaviour during frictional melting is dependent on the mineral assemblage of the precursor material, in particular, the presence or absence of amphibole. Frictional melting of the amphibole-bearing andesite generated the lowest shear resistance during slip, had a pronounced shear-weakening stage that preceded steady-state conditions and experienced only minor sample shortening (i.e., the wear rate and subsequent melting were slow). However, the amphibole-poor dacite and amphibole-free andesite displayed a stronger shear resistance during slip, had a negligible shear-weakening stage and experienced a faster rate of sample shortening. I demonstrate that these differences in

mechanical properties are primarily a result of preferential amphibole melting, due to its lower melting temperature (Allen, 1979; Spray, 1992), influencing the compositional heterogeneity and viscosity of the frictional melt layer. Microstructural investigation revealed that selective melting initially form isolated melt filaments, which begin to stretch and fold as melting and mixing efficiency increased with time, eventually homogenising by double-diffusion convection. Owing to preferential amphibole melting, frictional melting of the amphibole-bearing andesite generates progressively more mafic melts with lower viscosities. This finding opposes the theoretical assumption of Jiang *et al.* (2015), who suggested frictional melts will progressively become less mafic if hydrous minerals are present. Additionally, amphibole decomposition can contribute $H_2O$ to the frictional melt, leading to ubiquitous bubble formation, and lowering the melt viscosity further. In contrast, frictional melting of the amphibole-pore dacite and amphibole-free andesite primarily involved melting of plagioclase and softening/remobilising of glass (i.e., phases with higher melting temperatures), causing the melt to homogenise continuously towards the bulk-rock composition and generate frictional melts with increasingly higher viscosities. As frictional melting temperatures did not exceed melting temperatures of the entire mineral assemblage, restite fragments of some minerals remained in the melt zone. I thus also modelled the impact of crystal suspensions on frictional melt rheology (Caricchi *et al.*, 2007; Costa *et al.*, 2009), which caused a relative increase in viscosity. I highlight the importance of a glass phase to frictional melt composition due its kinetic nature and glass transition temperature ($T_g$) being lower than mineral melting temperatures. However, owing to the high heating rates involved, it would have limited the timescales available for structural relaxation of the glass, and likely shifted the $T_g$ to temperatures beyond that of some mineral melting temperatures (e.g., amphibole). As a result, I suggest that during the frictional melting of volcanic materials, hydrous minerals are more influential to slip properties than a glass phase.

In nature, slip velocities are rarely constant (Kendrick *et al.*, 2014b; Lavallée *et al.*, 2015b). As slip velocity wanes, the strain rates within the melt zone would simultaneously decrease, causing less frictional heat, which decreased temperature and, in addition to the non-Newtonian nature of suspensions (whose viscosity decreases with strain rate), increased the frictional melt apparent viscosity. I suggest that during deceleration in the presence of amphibole, the frictional melts' lower viscosity would still enable slip to progress, while in the absence of amphibole, the higher melt viscosities would eventually cause the melt to fail. Consequently, this study (Chapter 3) demonstrates the importance of mineral assemblage on frictional melting dynamics, which can impact the style of magma ascent and activity at the surface (Fig. 5.1). These results also provide new constraints for the modelling of the

velocities and run-out distances of granular flows during collapse events (e.g., landslides, block-and-ash flows and debris-avalanches).

The scarce observations (and arguably, the lack of *in-situ* preservation) of frictional melts and pseudotachylytes in volcanic environments is attributed to the high ambient background temperatures causing chemical, textural and physical overprints (e.g., Kendrick *et al.*, 2012; Kirkpatrick & Rowe, 2013). Yet, in addition to a number of collapse-related pseudotachylytes, evidence of pseudotachylyte formation during eruption has been observed in blocks from block-and-ash flow deposits that represent the dome interior at Soufrière Hills Volcano (Kendrick *et al.*, 2014a), on the lava spine margin at Mount St. Helens (Kendrick *et al.*, 2012) and in volcanic ash fragments from explosive activity at Santiaguito dome complex (Lavallée *et al.*, 2015a). For the last century, Santiaguito dome complex has been characterised by cyclic lava effusion interspersed by regular, small gas-and-ash explosions (e.g., Harris *et al.*, 2003; Bluth & Rose, 2004). Monitoring data of the active Caliente dome over the past decade suggests that these explosions are a consequence of strain localisation and fault friction at the conduit margins during ascent of a magma plug (e.g., Bluth & Rose, 2004; Holland *et al.*, 2011; Lavallée *et al.*, 2015a). However, in Chapter 4 I report a unique dataset that marks a shift in eruption intensification in 2015–2016, transitioning from these small, regular ash-poor explosions (ash plumes <1 km high) to larger, less frequent ash-rich explosions (ash plumes up to 7 km high), which returned to regular activity by late 2016. Here, I employed a multiparametric approach that combined petrological, geochemical and geophysical observations to constrain the cause behind this shift in activity. An integration of the seismic signals and visual observations of dome activity from November 2014 to April 2017 revealed a gradual increase in the repose intervals between explosions, while the magnitude of the events increased simultaneously that peaked in April and May 2016. Satellite thermal data during the period of largest explosions detected an elevated heat flux, which was concordant with the excavation of the crater. The geophysical data revealed a change in the time arrivals between the seismic and infrasound signals, with some explosions during the heightened activity having a longer delay between the two, indicative of the explosion source situated deeper in the conduit.

The ash componentry also changed during these larger explosions, noted by an increase in the juvenile transparent clasts and decrease in dense brown clasts. Surface textures of the transparent ash fragments displayed evidence for fragmentation of a vesicular magma (i.e., bubble wall geometry), while textures of the dense brown clasts suggested these were derived from a degassed magma. Composition of the explosive products (ash and bombs) revealed a decrease in bulk-rock $SiO_2$ compared to the lava previously extruded, along with amphibole geothermobarometry and plagioclase phenocrysts suggesting a deeper, higher

temperature and more mafic magma injection was involved. Microlite textures for the two clast types revealed contrasting degassing histories, associated with the combined effect of undercooling and magma ascent rates. The dense brown clasts ascended at a slow rate in the conduit to low pressures, allowing extensive degassing; however, I showed evidence that the transparent clasts ascended relatively faster and experienced less degassing, which likely stalled beneath the degassed plug. Mingling textures within the bombs (representing the two clasts types) further support the proposed different ascent styles prior to eruption. These observations are supported by the shift in fragmentation depth suggested by the geophysical data, where the transparent clasts were excavated from deeper in the conduit by fragmentation due to gas overpressures, while the dense clasts were a result of shallow shear-driven fragmentation of the plug (e.g., Gonnermann & Manga, 2003; Lavallée *et al.*, 2015a). Thus, I suggest ash componentry can provide a means for indicating fragmentations depths in the volcanic conduit. These integrated observations highlight the importance of using multiparametric datasets to infer eruption dynamics, particularly to constrain the cause for shifts from effusive-explosive activity as observed at many active lava domes. This unique dataset is anticipated to advance our understanding of long-standing dome activity and assist in mitigating the risks associated with rapid transitions in eruption styles.

## 5.2. IMPLICATIONS FOR EFFUSIVE–EXPLOSIVE ACTIVITY

As described in Chapter 1, the explosive potential of a volcanic system is regulated by magma's ability to outgas efficiently and prevent pressure accumulation following degassing (e.g., Lavallée *et al.*, 2013; Gaunt *et al.*, 2014; Ashwell *et al.*, 2015; Cassidy *et al.*, 2018). Conduit margins are typically assigned as ideal outgassing pathways as a response high strain conditions and creating porosity via the development of fracture networks that increase permeability, favouring effusive activity (Fig. 5.1a; e.g., Eichelberger, 1995; Tuffen & Dingwell, 2005; Kendrick *et al.*, 2013a; Heap *et al.*, 2015; Farquharson *et al.*, 2016a). The porosity of magma can also be a defining factor, which may compact or dilate during shear (e.g., Heap *et al.*, 2015), and as such, determines whether the magma seals or creates degassing pathways, which can contribute to the explosivity. In Chapter 2, I showed evidence for increased stress and temperature causing the original porous network within a shear zone to partially close, reducing permeability. In the event of densification via shear at the conduit margins, I suggest that pore connectivity and permeability anisotropy of the magma has a non-trivial role in determining eruptive activity by shifting the location of outgassing, either through the wall-rock or a relatively undeformed magma core (e.g., Ashwell *et al.*, 2015; Heap *et al.*, 2015; Farquharson *et al.*, 2016b). Consequently, the effect of shear and shear heating

during magma ascent may temporally seal gas pathways in high strain regions in the volcanic conduit by compacting the porous network and creating isolated porosity, facilitating pressure build up that can drive explosive activity (Fig. 5.1b). A magma's response to strain localisation may thus be responsible for rapid shifts from effusive–explosive activity as observed at many intermediate-silicic volcanoes.

Magma shearing can lead to seismogenic failure as magma encounters the viscous-brittle transition (e.g., Lavallée *et al.*, 2008; Coats *et al.*, 2018). The high strain rates developed near the conduit margins can promote slip along fault and fracture planes, leading to the formation of a frictional melt (Fig. 5.1), which may influence the style of ascent and overall dome morphology (e.g., Lavallée *et al.*, 2008; Kendrick *et al.*, 2014b; Lavallée *et al.*, 2015b). In Chapter 3, I demonstrated that the role of a frictional melt is highly dependent on mineral assemblage, which may change over time due to long term magmatic evolution (e.g., Scott *et al.*, 2013) or magma recharge events (e.g., Murphy *et al.*, 2000). In particular, the introduction of amphibole by the injection of hydrous magma at depth (e.g., Luhr & Carmichael, 1990; Luhr, 2002; Savov *et al.*, 2008; Saucedo *et al.*, 2010) may have a profound effect on fault rheology and other mechanical processes occurring in the upper conduit. The frictional melting of amphibole-bearing magmas can reduce the frictional resistance during slip, facilitating continuous lubrication of the fault surface that is less likely to result in failure than more silicic, viscous melts. Consequently, frictional melting in amphibole-bearing systems (which may onset rapidly during frictional sliding) can assist in sealing fracture planes, reducing permeability and favouring higher gas overpressures that can result in explosive activity (Fig. 5.1b). Furthermore, the observations that these melts can form faster than frictional melting of an amphibole-free material may also prove non-trivial. However, the frictional melting of amphibole-free material is likely to have an opposing effect by having a higher melt viscosity and thus stronger shear resistance during slip, producing shear zones that are more prone to failure. Whilst this phenomenon generates local fragmentation events, it may also create fracture networks that could facilitate outgassing and reduce the explosive potential, causing magma to ascend in a stick-slip manner owing to cyclic slip and fracturing along the fault plane, as deemed responsible for characteristic, shallow drumbeat seismicity (e.g., Tuffen *et al.*, 2003; Iverson *et al.*, 2006; Neuberg *et al.*, 2006; Lensky *et al.*, 2008; Kendrick *et al.*, 2014b).

Although shearing and friction may trigger shifts in eruption style, in Chapter 4 I suggest deeper magmatic processes can temporally overprint these processes, causing a shift in explosion mechanism (Fig. 5.1a–b). I used a multiparametric approach to examine the cause for a switch from regular, small-to-moderate explosions to less frequent, large explosions at Santiaguito dome complex, Guatemala, by integrating geophysical monitoring signals with

petrological and geochemical signatures of the eruptive products. I showed that deeper magma injection caused a shift in the componentry, mineralogy and geochemistry of ash particles, whilst seismicity provided a proxy for the explosion source at depth, demonstrating a switch from shallow, shear-driven explosions (e.g., Goto, 1999; Papale, 1999; Bluth & Rose, 2004; Lavallée *et al.*, 2015a) to deeper overpressure driven explosions. This thesis thus highlights the importance of characterising and understanding the way magmas respond to strain localisation during magma ascent in the shallow volcanic conduit, but also demonstrates that deeper magmatic processes can have an important impact on the style of activity and dome growth. An integration of these factors into current models of magma ascent is vital for understanding shifts from effusive-explosive activity (Cassidy *et al.*, 2018), which can assist in mitigating risks associated with the hazards that proceed.

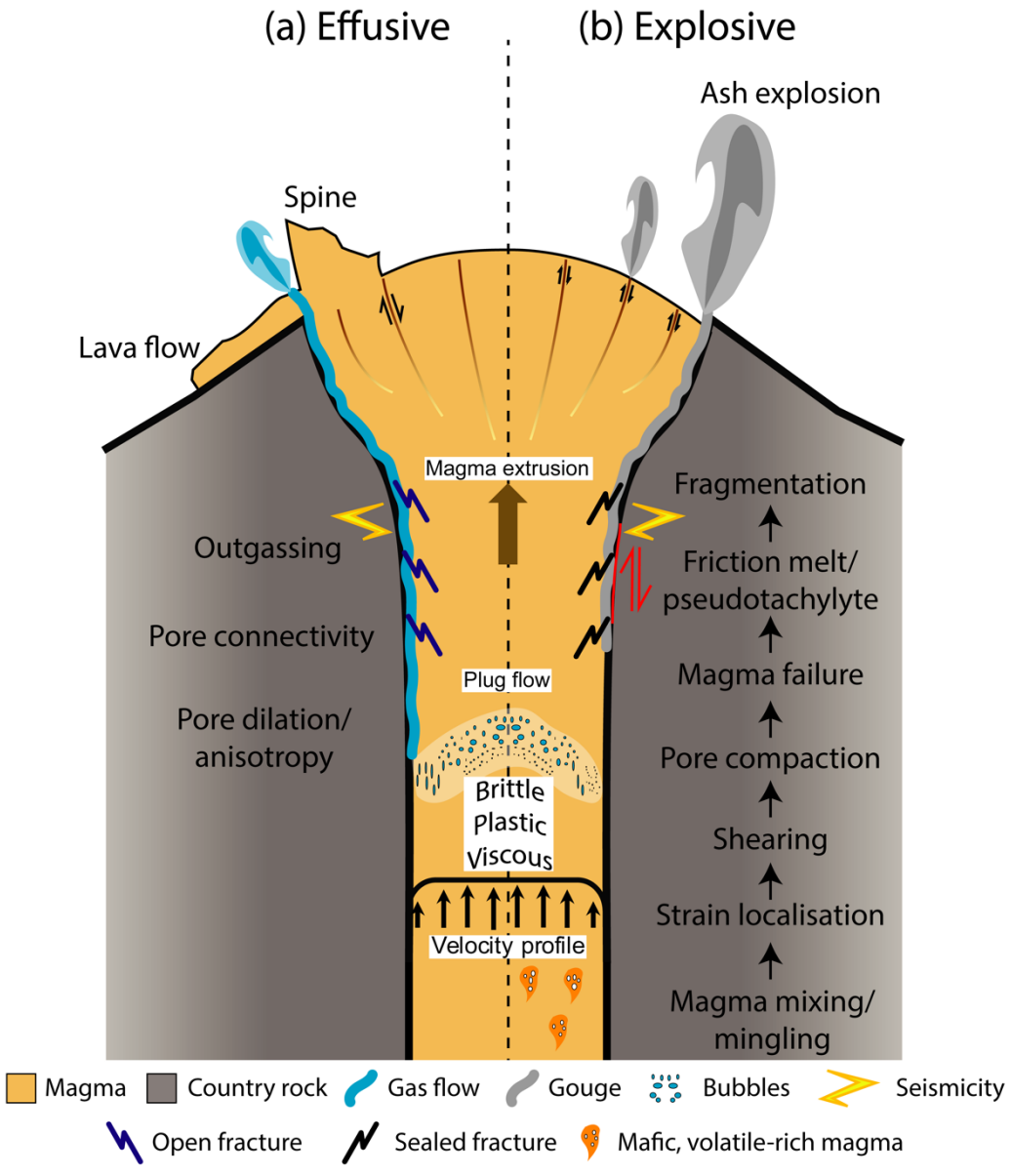

***Figure 5.1*** *– A conceptual model of volcanic conduit processes that can regulate eruptive activity at the surface and the different eruptive regimes: (a) effusive and (b) explosive. As magma ascends in the conduit, volatile exsolution and crystallisation causes a rheological transition where the magma adopts a non-Newtonian behaviour, facilitating in localising stress and strain near the conduit margins. An increase strain in such regions leads to the development of localised shear zones, where magma deformation transitions from viscous to brittle behaviour, with the boundary between the two being marked by crystal-plastic deformation. Deformation in these shear zones can generate a permeable network of connected porosity and open fractures that allow efficient outgassing leading to effusive activity (a), in the form as degassing, lava flow extrusion or spine growth. However, shear heating during strain localisation may compact the porous network and generate gas overpressures causing an explosion (b). As magma ascends further, plug flow and subsequently brittle failure and faulting at the conduit margins can regulate activity. Frictional melting during faulting can influence slip dynamics, which depending on the mineral assemblage may promote slip, causing an explosion, or prevent slip leading to failure, causing seismicity. Explosive activity (b) can also be triggered by deep magma injection. Magma recharge events can introduce more mafic, volatile-rich magma into the shallow volcanic system that are highly susceptible to generate gas overpressures beneath an overlying plug. Deep gas overpressures can alter shallower processes (e.g., faulting and friction), by causing deeper fragmentation and resulting in explosive products (ash and bombs) displaying mixing or mingling textures between the recharged magma and plug material.*

## 5.3. SUGGESTIONS FOR FUTURE STUDIES

In this thesis, I highlight the importance of strain localisation during magma ascent and the role of shearing and friction on petrological and rheological instabilities in the volcanic conduit. The thermo-mechanical response due to shear and frictional heating requires an assessment of the thermal budget of magma. Although I have eluded to the role of shear on petrological disequilibrium textures, further investigation is needed to fully constrain its role.

In particular, although I related microlite textures to decompression induced degassing, thermal instabilities in the volcanic conduit can also drive volatile exsolution (e.g., Lavallée *et al.*, 2015a). An increase in temperature may lower the degree of undercooling experienced by the melt, thus influencing the style of crystallisation and resultant groundmass textures. Constraining the impact of shear and resultant heating on the kinetics of crystallisation (i.e., nucleation and growth) and crystal textures (size and shape) may provide

important insights into the competition between changes in pressure and temperature during final magma ascent in the shallow conduit, which is yet to be addressed.

Additionally, evidence of the impact of shear on amphibole stability was shown in this study in a qualitative perspective. In order for this to be applied quantitatively to future investigations it requires a more extensive experimental investigation of shear and shear heating on mineral stability. Development of a calibrated model is thus required, enabling discrimination between heating-induced reactions rims and other processes that may drive mineral reactions (e.g., decompression, $CO_2$ flushing). Furthermore, hydrous mineral destabilisation at shallow depths in the conduit may affect many physical and chemical processes due to the release of $H_2O$ during the reactions. For example, fracture healing is a process that is dependent on diffusion timescales (Lamur *et al.*, 2019), which may be enhanced by amphibole releasing water into the system during dehydration, and may also influence the timescales of sintering of comminuted crystal and glass fragments during gouge lithification (e.g., Ryan *et al.*, 2018).

Crystal deformation, as discussed in Chapter 2, provides useful information on stress conditions in the volcanic conduit. In particular, crystal plasticity can contribute to the non-Newtonian behaviour of magma. The observation that crystal plastic deformation increases with shear intensity demonstrates the importance of incorporating this deformation mechanism into rheological models. In order to provide a quantitative model linking strain rates and degree of crystal plastic deformation, required for rheological models, future experimental investigations are required to build on the work of Kendrick *et al.* (2017). Additionally, different crystal phases would have different internal yield strengths (e.g., Poirier, 1995), thus the conditions required for these to deform plastically would vary. To fully investigate this, experiments could be performed under a range of temperature and stress/strain conditions to induce internal crystal deformation in suspensions with different crystal cargos, followed by EBSD analysis to quantify the degree of crystal plasticity. Other constraints on stress conditions in the volcanic conduit may be found in mafic enclaves, which are highly deformed within the Unzen shear zone (Chapter 2). Although no detailed analysis was performed to constrain their mode and extent of deformation it may give greater insights into strain conditions inside the volcanic conduit.

In Chapter 3, I demonstrated the importance of mineral assemblage on frictional melting and slip progression. However, the role of porosity on frictional properties is likely an essential factor that requires greater consideration, as higher porosity material would reduce the contact area available for friction, thus concentrating stresses and potentially succumbing to failure more readily (as strength is largely porosity dependent). Frictional melts are often poorly preserved due to their formation at high ambient temperature, likely due to their

chemical and textural overprints (e.g., Kendrick *et al.*, 2012; Kirkpatrick & Rowe, 2013). Yet, it is also likely that the lack of evidence for such features is due to their formation in high strain regions. As pseudotachylytes form on pre-existing fracture planes within high strain regions (i.e., shear zones), continuous deformation accompanied by repetitive healing and re-fracturing in the same location is common. Consequently, fracturing and fragmentation of pseudotachylytes to fine ash is likely a common process. A typical limitation of many ash studies is that they discard non-juvenile fragments, yet I anticipate that evidence for frictional melting may be more likely preserved in such fragments.

As shown in Chapter 4, multiparametric observations are the most robust means for assessing shifts in eruptive activity. At Santiaguito, activity was inferred to come to a close between 2014–2024 based on the long-term chemical trend of the magma and the decrease in cyclic extrusion rates (Harris *et al.*, 2003), which suggested gradual depressurisation and exhaustion of the source region. However, the eruption intensification in 2015–2016 raised new questions about the plumbing system and the processes regulating activity. Coupling the geophysical and petrological findings with gas fluxing data during this eruptive period (i.e., $SO_2$ and $CO_2$) may further enhance our understanding of eruptive activity, particularly during repose intervals. Another consideration that needs to be taken into account is the role of volatiles. An assessment of melt inclusions to track volatiles through the magmatic system are required to understand the importance of $CO_2$ and $H_2O$ fluctuations on eruptive activity (Cashman & Blundy, 2013; Cassidy *et al.*, 2016). Furthermore, the eruptive products of Santiaguito often contain mafic enclaves. A detailed evaluation of the chemistry and type of enclaves in Santiaguito's eruptive products may provide greater information on magma storage processes (e.g., Murphy *et al.*, 2000), and even provide constraints on magma residence time owing to their re-equilibration as they ascend to lower pressures (e.g., Sato *et al.*, 2017). However, the current state and future of Santiaguito remains elusive, thus it is vital that active monitoring of Santiaguito, and other active lava domes, continues from both a geophysical and petrological standpoint.

# Bibliography


Adams, N. K., Houghton, B. F. & Hildreth, W. (2006). Abrupt transitions during sustained explosive eruptions: examples from the 1912 eruption of Novarupta, Alaska. *Bulletin of Volcanology* **69**, 189–206.

Allen, A. R. (1979). Mechanism of frictional fusion in fault zones. *Journal of Structural Geology* **1**, 231–237.

Allen, S. R. & McPhie, J. (2003). Phenocryst fragments in rhyolitic lavas and lava domes. *Journal of Volcanology and Geothermal Research* **126**, 263–283.

Andrews, B. J. (2014). Magmatic storage conditions, decompression rate, and incipient caldera collapse of the 1902 eruption of Santa Maria Volcano, Guatemala. *Journal of Volcanology and Geothermal Research* **282**, 103–114.

Ashwell, P. A., Kendrick, J. E., Lavallée, Y., Kennedy, B. M., Hess, K. U., von Aulock, F. W., Wadsworth, F. B., Vasseur, J. & Dingwell, D. B. (2015). Permeability of compacting porous lavas. *Journal of Geophysical Research: Solid Earth* **120**, 1605–1622.

Auker, M. R., Sparks, R. S. J., Siebert, L., Crosweller, H. S. & Ewert, J. (2013). A statistical analysis of the global historical volcanic fatalities record. *Journal of Applied Volcanology* **2**, 1–24.

Avard, G. & Whittington, A. G. (2012). Rheology of arc dacite lavas: experimental determination at low strain rates. *Bulletin of Volcanology* **74**, 1039–1056.

Ayling, B., Rose, P., Petty, S., Zemach, E. & Drakos, P. (2012). QEMSCAN (quantitative evaluation of minerals by scanning electron microscopy): capability and application to fracture characterization in geothermal systems. *Thirty-Seventh Workshop on Geothermal Reservoir Engineering*. Stanford, California, USA, 30 January–1 February, 2012.

Bagdassarov, N. S. & Dingwell, D. B. (1992). A rheological investigation of vesicular rhyolite. *Journal of Volcanology and Geothermal Research* **50**, 307–322.

Bain, A. A., Calder, E. S., Cortes, J. A., Cortes, G. P. & Loughlin, S. (2019). Textural and geochemical constraints on andesitic plug emplacement prior to the 2004–2010 vulcanian explosions at Galeras volcano, Colombia. *Bulletin of Volcanology* **81**, 1–25.

Barclay, J., Rutherford, M. J., Carroll, M. R., Murphy, M. D., Devine, J. D., Gardner, J. & Sparks, R. S. J. (1998). Experimental phase equilibria constraints on pre-eruptive storage conditions of the Soufriere Hills magma. *Geophysical Research Letters* **25**, 3437–3440.

Baxter, P. J., Bonadonna, C., Dupree, R., Hards, V. L., Kohn, S. C., Murphy, M. D., Nichols, A., Nicholson, R. A., Norton, G., Searl, A., Sparks, R. S. J. & Vickers, B. P. (1999). Cristobalite in Volcanic Ash of the Soufriere Hills Volcano, Montserrat, British West Indies. *Science* **283**, 1142–1145.

Ben-Zion, Y. & Sammis, C. G. (2003). Characterization of Fault Zones. *Pure and Applied Geophysics* **160**, 677–715.

Bergantz, G. W., Schleicher, J. M. & Burgisser, A. (2015). Open-system dynamics and mixing in magma mushes. *Nature Geoscience* **8**, 793–796.

Bernard, K. & de Vries, B. V. (2017). Volcanic avalanche fault zone with pseudotachylite and gouge in French Massif Central. *Journal of Volcanology and Geothermal Research* **347**, 112–135.

Bloemendal, J., King, J. W., Hall, F. R. & Doh, S. J. (1992). Rock Magnetism of Late Neogene and Pleistocene Deep-Sea Sediments: Relationship to Sediment Source, Diagenetic Processes, and Sediment Lithology. *Journal of Geophysical Research* **97**, 4361–4375.

Blundy, J. & Cashman, K. (2001). Ascent-driven crystallisation of dacite magmas at Mount St Helens, 1980-1986. *Contributions to Mineralogy and Petrology* **140**, 631–650.

Blundy, J. & Cashman, K. (2005). Rapid decompression-driven crystallization recorded by melt inclusions from Mount St. Helens volcano. *Geology* **33**, 793–796.
Blundy, J., Cashman, K. & Humphreys, M. (2006). Magma heating by decompression-driven crystallization beneath andesite volcanoes. *Nature* **443**, 76–80.
Blundy, J. & Cashman, K. (2008). Petrologic Reconstruction of Magmatic System Variables and Processes. *Minerals, Inclusions and Volcanic Processes* **69**, 179–239.
Bluth, G. J. S. & Rose, W. I. (2004). Observations of eruptive activity at Santiaguito volcano, Guatemala. *Journal of Volcanology and Geothermal Research* **136**, 297–302.
Bouligand, C., Glen, J. M. G. & Blakely, R. J. (2014). Distribution of buried hydrothermal alteration deduced from high-resolution magnetic surveys in Yellowstone National Park. *Journal of Geophysical Research: Solid Earth* **119**, 2595–2630.
Brewer, L. N., Othon, M. A., Young, L. M. & Angeliu, T. M. (2006). Misorientation mapping for visualization of plastic deformation via electron back-scattered diffraction. *Microscopy and Microanalysis* **12**, 85–91.
Brown, S. K., Auker, M. R. & Sparks, R. S. J. (2015). Populations around Holocene volcanoes and development of a Population Exposure Index. In: Loughlin, S. C., Sparks, R. S. J., Brown, S. K., Jenkins, S. F. & Vye-Brown, C. (eds.) *Global Volcanic Hazards and Risk*. Cambridge: Cambridge University Press, 223–232.
Browne, B. L. & Gardner, J. E. (2006). The influence of magma ascent path on the texture, mineralogy, and formation of hornblende reaction rims. *Earth and Planetary Science Letters* **246**, 161–176.
Brugger, C. R. & Hammer, J. E. (2010). Crystallization kinetics in continuous decompression experiments: Implications for interpreting natural magma ascent processes. *Journal of Petrology* **51**, 1941–1965.
Buckley, V. J. E., Sparks, R. S. J. & Wood, B. J. (2006). Hornblende dehydration reactions during magma ascent at Soufriere Hills Volcano, Montserrat. *Contributions to Mineralogy and Petrology* **151**, 121–140.
Burgisser, A., Poussineau, S., Arbaret, L., Druitt, T. H., Giachetti, T. & Bourdier, J.-L. (2010). Pre-explosive conduit conditions of the 1997 vulcanian explosions at Soufrière Hills Volcano, Montserrat: I. Pressure and vesicularity distributions. *Journal of Volcanology and Geothermal Research* **194**, 27–41.
Burgisser, A. & Bergantz, G. W. (2011). A rapid mechanism to remobilize and homogenize highly crystalline magma bodies. *Nature* **471**, 212–215.
Calder, E. S., Cole, P. D., Dade, W. B., Druitt, T. H., Hoblitt, R. P., Huppert, H. E., Ritchie, L., Sparks, R. S. J. & Young, S. R. (1999). Mobility of pyroclastic flows and surges at the Soufriere Hills Volcano, Montserrat. *Geophysical Research Letters* **26**, 537–540.
Calder, E. S., Lavallée, Y., Kendrick, J. E. & Bernstein, M. (2015). Lava Dome Eruptions. In: Sigurdsson, H., Houghton, B., McNutt, S., Rymer, H. & Stix, J. (eds.) *The Encyclopedia of Volcanoes*: Elsevier Science, 343–362.
Caricchi, L., Burlini, L., Ulmer, P., Gerya, T., Vassalli, M. & Papale, P. (2007). Non-Newtonian rheology of crystal-bearing magmas and implications for magma ascent dynamics. *Earth and Planetary Science Letters* **264**, 402–419.
Carmichael, I. S. E. (2002). The andesite aqueduct: perspectives on the evolution of intermediate magmatism in west-central (105-99 degrees W) Mexico. *Contributions to Mineralogy and Petrology* **143**, 641–663.
Carslaw, H. S. & Jaeger, J. C. (1959). *Conduction of heat in solids*. Oxford,: Clarendon Press.
Cashman, K. & Blundy, J. (2000). Degassing and Crystallization of ascending andesite and dacite. *Philosophical transactions of the Royal Society of London* **358** 1487–1513.
Cashman, K. & Blundy, J. (2013). Petrological cannibalism: the chemical and textural consequences of incremental magma body growth. *Contributions to Mineralogy and Petrology* **166**, 703–729.

Cashman, K., Sparks, R. S. J. & Blundy, J. D. (2017). Vertically extensive and unstable magmatic systems: A unified view of igneous processes. *Science* **355**, eaag3055.
Cashman, K. V. (1988). Crystallization of Mount-St-Helens 1980-1986 Dacite - a Quantitative Textural Approach. *Bulletin of Volcanology* **50**, 194–209.
Cashman, K. V. (1992). Groundmass Crystallization of Mount St Helens Dacite, 1980-1986 - a Tool for Interpreting Shallow Magmatic Processes. *Contributions to Mineralogy and Petrology* **109**, 431–449.
Cashman, K. V., Thornber, C. R. & Pallister, J. S. (2008). From Dome to Dust: Shallow Crystallization and Fragmentation of Conduit Magma During the 2004-2006 Dome Extrusion of Mount St. Helens, Washington. In: Sherrod, D. R., Scott, W. E. & Stauffer, P. H. (eds.) *A Volcano Rekindled: The Renewed Eruption of Mount St. Helens, 2004-2006. Professional Paper 1750.*: U.S. Geological Survey, 387–413.
Cashman, K. V. & Sparks, R. S. J. (2013). How volcanoes work: A 25 year perspective. *Geological Society of America Bulletin* **125**, 664–690.
Cassidy, M., Cole, P. D., Hicks, K. E., Varley, N. R., Peters, N. & Lerner, A. H. (2015). Rapid and slow: Varying magma ascent rates as a mechanism for Vulcanian explosions. *Earth and Planetary Science Letters* **420**, 73–84.
Cassidy, M., Castro, J. M., Helo, C., Troll, V. R., Deegan, F. M., Muir, D., Neave, D. A. & Mueller, S. P. (2016). Volatile dilution during magma injections and implications for volcano explosivity. *Geology* **44**, 1027–1030.
Cassidy, M., Manga, M., Cashman, K. & Bachmann, O. (2018). Controls on explosive-effusive volcanic eruption styles. *Nature Communications* **9**, 2839.
Castro, J., Manga, M. & Cashman, K. (2002). Dynamics of obsidian flows inferred from microstructures: insights from microlite preferred orientations. *Earth and Planetary Science Letters* **199**, 211–226.
Castro, J., Schipper, C. I., Mueller, S. P., Militzer, A. S., Amigo, A., Parejas, C. S. & Jacob, D. (2013). Storage and eruption of near-liquidus rhyolite magma at Cordón Caulle, Chile. *Bulletin of Volcanology* **75**, 1–17.
Castro, J. M., Cordonnier, B., Tuffen, H., Tobin, M. J., Puskar, L., Martin, M. C. & Bechtel, H. A. (2012). The role of melt-fracture degassing in defusing explosive rhyolite eruptions at volcán Chaitén. *Earth and Planetary Science Letters* **333–334**, 63–69.
Chen, X. F., Madden, A. S. E. & Reches, Z. (2017). Friction evolution of granitic faults: Heating controlled transition from powder lubrication to frictional melt. *Journal of Geophysical Research: Solid Earth* **122**, 9275–9289.
Cichy, S. B., Botcharnikov, R. E., Holtz, F. & Behrens, H. (2011). Vesiculation and Microlite Crystallization Induced by Decompression: a Case Study of the 1991-1995 Mt Unzen Eruption (Japan). *Journal of Petrology* **52**, 1469–1492.
Cimarelli, C., Di Traglia, F. & Taddeucci, J. (2010). Basaltic scoria textures from a zoned conduit as precursors to violent Strombolian activity. *Geology* **38**, 439–442.
Cimarelli, C., Costa, A., Mueller, S. & Mader, H. M. (2011). Rheology of magmas with bimodal crystal size and shape distributions: Insights from analog experiments. *Geochemistry, Geophysics* **12**, Q07024.
Clarke, A. B., Stephens, S., Teasdale, R., Sparks, R. S. J. & Diller, K. (2007). Petrologic constraints on the decompression history of magma prior to Vulcanian explosions at the Soufrière Hills volcano, Montserrat. *Journal of Volcanology and Geothermal Research* **161**, 261–274.
Coats, R., Kendrick, J. E., Wallace, P. A., Miwa, T., Hornby, A. J., Ashworth, J. D., Matsushima, T. & Lavallée, Y. (2018). Failure criteria for porous dome rocks and lavas: a study of Mt. Unzen, Japan. *Solid Earth* **9**, 1299–1328.
Cole, P. D., Calder, E. S., Sparks, R. S. J., Clarke, A. B., Druitt, T. H., Young, S. R., Herd, R. A., Harford, C. L. & Norton, G. E. (2002). Deposits from dome-collapse and fountain-collapse pyroclastic flows at Soufrière Hills Volcano, Montserrat. *Geological Society, London, Memoirs* **21**, 231–262.

Colombier, M., Wadsworth, F. B., Gurioli, L., Scheu, B., Kueppers, U., Muro, A. D. & Dingwell, D. B. (2017). The evolution of pore connectivity in volcanic rocks. *Earth and Planetary Science Letters* **462**, 99–109.

Cooper, K. M. & Kent, A. J. R. (2014). Rapid remobilization of magmatic crystals kept in cold storage. *Nature* **506**, 480–483.

Cordonnier, B., Hess, K.-U., Lavallée, Y. & Dingwell, D. B. (2009). Rheological properties of dome lavas: Case study of Unzen volcano. *Earth and Planetary Science Letters* **279**, 263–272.

Cordonnier, B., Caricchi, L., Pistone, M., Castro, J., Hess, K.-U., Gottschaller, S., Manga, M., Dingwell, D. B. & Burlini, L. (2012). The viscous-brittle transition of crystal-bearing silicic melt: Direct observation of magma rupture and healing. *Geology* **40**, 611–614.

Costa, A. & Macedonio, G. (2003). Viscous heating in fluids with temperature-dependent viscosity: implications for magma flows. *Nonlinear Processes in Geophysics* **10**, 545–555.

Costa, A., Melnik, O. & Vedeneeva, E. (2007). Thermal effects during magma ascent in conduits. *Journal of Geophysical Research: Solid Earth* **112**.

Costa, A., Caricchi, L. & Bagdassarov, N. (2009). A model for the rheology of particle-bearing suspensions and partially molten rocks. *Geochemistry, Geophysics* **10**, Q03010.

Costa, F., Andreastuti, S., de Maisonneuve, C. B. & Pallister, J. S. (2013). Petrological insights into the storage conditions, and magmatic processes that yielded the centennial 2010 Merapi explosive eruption. *Journal of Volcanology and Geothermal Research* **261**, 209–235.

Couch, S., Sparks, R. S. J. & Carroll, M. R. (2001). Mineral disequilibrium in lavas explained by convective self-mixing in open magma chambers. *Nature* **411**, 1037–1039.

Couch, S., Harford, C. L., Sparks, R. S. J. & Carroll, M. R. (2003). Experimental constraints on the conditions of formation of highly calcic plagioclase microlites at the Soufrière Hills Volcano, Montserrat. *Journal of Petrology* **44**, 1455–1475.

Daly, R. A. (1911). The Nature of Volcanic Action. *Proceedings of the American Academy of Arts and Sciences* **47**, 47–122.

Day, R., Fuller, M. & Schmidt, V. A. (1977). Hysteresis properties of titanomagnetites: Grain-size and compositional dependence. *Physics of the Earth and Planetary Interiors* **13**, 260–267.

De Angelis, S. & Henton, S. M. (2011). On the feasibility of magma fracture within volcanic conduits: Constraints from earthquake data and empirical modelling of magma viscosity. *Geophysical Research Letters* **38**, L19310.

De Angelis, S., Lamb, O. D., Lamur, A., Hornby, A. J., von Aulock, F. W., Chigna, G., Lavallee, Y. & Rietbrock, A. (2016). Characterization of moderate ash- and- gas explosions at Santiaguito volcano, Guatemala, from infrasound waveform inversion and thermal infrared measurements. *Geophysical Research Letters* **43**, 6220–6227.

De Angelis, S. H., Larsen, J., Coombs, M., Dunn, A. & Hayden, L. (2015). Amphibole reaction rims as a record of pre-eruptive magmatic heating: An experimental approach. *Earth and Planetary Science Letters* **426**, 235–245.

De Campos, C. P., Perugini, D., Ertel-Ingrisch, W., Dingwell, D. B. & Poli, G. (2011). Enhancement of magma mixing efficiency by chaotic dynamics: an experimental study. *Contributions to Mineralogy and Petrology* **161**, 863–881.

Deubelbeiss, Y., Kaus, B. J. P., Connolly, J. A. D. & Caricchi, L. (2011). Potential causes for the non-Newtonian rheology of crystal-bearing magmas. *Geochemistry, Geophysics, Geosystems* **12**, Q05007.

Di Toro, G., Hirose, T., Nielsen, S., Pennacchioni, G. & Shimamoto, T. (2006). Natural and experimental evidence of melt lubrication of faults during earthquakes. *Science* **311**, 647–649.

Di Toro, G., Han, R., Hirose, T., De Paola, N., Nielsen, S., Mizoguchi, K., Ferri, F., Cocco, M. & Shimamoto, T. (2011). Fault lubrication during earthquakes. *Nature* **471**, 494–498.

Dieterich, J. H. (1979). Modeling of rock friction. 2. Simulation of pre-seismic slip. *Journal of Geophysical Research* **84**, 2169–2175.

Diller, K., Clarke, A. B., Voight, B. & Neri, A. (2006). Mechanisms of conduit plug formation: implications for vulcanian explosions. *Geophysical Research Letters* **33**, L20302.

Dingwell, D. B. & Webb, S. L. (1989). Structural relaxation in silicate melts and Non-Newtonian melt rheology in geologic processes. *Physics and Chemistry of Minerals* **16**, 508–516.

Dingwell, D. B. (1996). Volcanic dilemma: Flow or blow? *Science* **273**, 1054–1055.

Dingwell, D. B., Romano, C. & Hess, K. U. (1996). The effect of water on the viscosity of a haplogranitic melt under P-T-X conditions relevant to silicic volcanism. *Contributions to Mineralogy and Petrology* **124**, 19–28.

Dingwell, D. B., Lavallee, Y., Hess, K. U., Flaws, A., Marti, J., Nichols, A. R. L., Gilg, H. A. & Schillinger, B. (2016). Eruptive shearing of tube pumice: pure and simple. *Solid Earth* **7**, 1383–1393.

Dunlop, D. J. (2002). Theory and application of the Day plot (Mrs/Ms versus Hcr/Hc) 1. Theoretical curves and tests using titanomagnetite data. *Journal of Geophysical Research* **107**, 2056.

Edmonds, M., Oppenheimer, C. M., Pyle, D. M., Herd, R. A. & Thompson, G. (2003). SO2 emissions from Soufrière Hills Volcano and their relationship to conduit permeability, hydrothermal interaction and degassing regime. *Journal of Volcanology and Geothermal Research* **124**, 23–43.

Edmonds, M. & Herd, R. A. (2007). A volcanic degassing event at the explosive-effusive transition. *Geophysical Research Letters* **34**, L21310.

Edmonds, M. (2008). New geochemical insights into volcanic degassing. *Philosophical Transactions of the Royal Society a-Mathematical Physical and Engineering Sciences* **366**, 4559–4579.

Edmonds, M., Gerlach, T. M. & Herd, R. A. (2009). Halogen degassing during ascent and eruption of water-poor basaltic magma. *Chemical Geology* **263**, 122–130.

Eichelberger, J. C. (1995). Silicic Volcanism - Ascent of Viscous Magmas from Crustal Reservoirs. *Annual Review of Earth and Planetary Sciences* **23**, 41–63.

Einstein, A. (1906). Eine neue Bestimmung der Moleküldimensionen *Annalen der Physik* **19**, 289–306.

Esri. (2009) “World Imagery (Basemap)”. "World Imagery Map". Source: Esri, DeLorme Publishing Company, Inc. https://services.arcgisonline.com/ArcGIS/rest/services/World_Imagery/MapServer. September 13, 2018

Esri. (2015) “World Countries (Generalized)”. "World Countries”. Source: Esri, DigitalGlobe, GeoEye, Earthstar Geographics, CNES/Airbus DS, USDA, USGS, AeroGRID, IGN, and the GIS User Community https://services.arcgis.com/P3ePLMYs2RVChkJx/arcgis/rest/services/World__Countries_Generalized_analysis_trim/FeatureServer. September 13, 2018

Fabian, K. (2003). Some additional parameters to estimate domain state from isothermal magnetization measurements. *Earth and Planetary Science Letters* **213**, 337–345.

Farquharson, J. I., Heap, M. J. & Baud, P. (2016a). Strain-induced permeability increase in volcanic rock. *Geophysical Research Letters* **43**, 11603–11610.

Farquharson, J. I., Heap, M. J., Lavallee, Y., Varley, N. R. & Baud, P. (2016b). Evidence for the development of permeability anisotropy in lava domes and volcanic conduits. *Journal of Volcanology and Geothermal Research* **323**, 163–185.

Ferré, E. C., Zechmeister, M. S., Geissman, J. W., MathanaSekaran, N. & Kocak, K. (2005). The origin of high magnetic remanence in fault pseudotachylites: Theoretical

considerations and implication for coseismic electrical currents. *Tectonophysics* **402**, 125–139.
Fialko, Y. & Khazan, Y. (2005). Fusion by earthquake fault friction: Stick or slip? *Journal of Geophysical Research: Solid Earth* **110**, B12407.
Fink, J. H., Anderson, S. W. & Manley, C. R. (1992). Textural Constraints on Effusive Silicic Volcanism: Beyond the Permeable Foam Model. *Journal of Geophysical Research* **97**, 9073–9083.
Fink, J. H. & Bridges, N. T. (1995). Effects of eruption history and cooling rate on lava dome growth. *Bulletin of Volcanology* **57**, 229–239.
Fink, J. H. & Griffiths, R. W. (1998). Morphology, eruption rates, and rheology of lava domes: Insights from laboratory models. *Journal of Geophysical Research: Solid Earth* **103**, 527–545.
Forien, M., Arbaret, L., Burgisser, A. & Champallier, R. (2011). Experimental constrains on shear-induced crystal breakage in magmas. *Journal of Geophysical Research: Solid Earth* **116**.
Fourcade, S. & Allègre, C. J. (1981). Trace-elements behavior in granite genesis - a case-study the calc-alkaline plutonic association from the Querigut Complex (Pyrenees, France). *Contributions to Mineralogy and Petrology* **76**, 177–195.
Francis, P. W. (1972). The pseudotachylyte problem. *Comments Earth Science and Geophysics* **3**, 35–53.
Freund, F., Salgueiro da Silva, M. A., Lau, B. W. S., Takeuchi, A. & Jones, H. H. (2007). Electric currents along earthquake faults and the magnetization of pseudotachylite veins. *Tectonophysics* **431**, 131–141.
Garcia, M. & Jacobson, S. (1979). Crystal clots, amphibole fractionation and the evolution of calc-alkaline magmas. *Contributions to Mineralogy and Petrology* **69**, 319–327.
Gaunt, H. E., Sammonds, P. R., Meredith, P. G., Smith, R. & Pallister, J. S. (2014). Pathways for degassing during the lava dome eruption of Mount St. Helens 2004–2008. *Geology* **42**, 947–950.
Geschwind, C. H. & Rutherford, M. J. (1995). Crystallization of microlites during magma ascent: the fluid mechanics of 1980-1986 eruptions at Mount St Helens. *Bulletin of Volcanology* **57**, 356–370.
Geuna, S. E., Lagorio, S. L. & Vizán, H. (2014). Oxidation processes and their effects on the magnetic remanence of Early Cretaceous subaerial basalts from Sierra Chica de Córdoba, Argentina. *Geological Society, London, Special Publications* **396**, 239–263.
Giordano, D., Romano, C., Dingwell, D. B., Poe, B. & Behrens, H. (2004). The combined effects of water and fluorine on the viscosity of silicic magmas. *Geochimica et Cosmochimica Acta* **68**, 5159–5168.
Giordano, D., Russell, J. K. & Dingwell, D. B. (2008). Viscosity of magmatic liquids: A model. *Earth and Planetary Science Letters* **271**, 123–134.
Global Volcanism Program. (2015). Report on Santa Maria (Guatemala) – 2015. In: Venzke, E. (ed.) *Bulletin of the Global Volcanism Network*. Washington, DC: Smithsonian Institution.
Global Volcanism Program. (2016). Report on Santa Maria (Guatemala) – 2016. In: Venzke, E. (ed.) *Bulletin of the Global Volcanism Network*. Washington, DC: Smithsonian Institution.
Global Volcanism Program. (2018). Report on Santa Maria (Guatemala) – 2018. In: Venzke, E. (ed.) *Bulletin of the Global Volcanism Network*. Washington, DC: Smithsonian Institution.
Goncalves, P., Oliot, E., Marquer, D. & Connolly, J. A. D. (2012). Role of chemical processes on shear zone formation: an example from the Grimsel metagranodiorite (Aar massif, Central Alps). *Journal of Metamorphic Geology* **30**, 703–722.
Gonnermann, H. M. & Manga, M. (2003). Explosive volcanism may not be an inevitable consequence of magma fragmentation. *Nature* **426**, 432–435.

Gonnermann, H. M. & Manga, M. (2005). Flow banding in obsidian: A record of evolving textural heterogeneity during magma deformation. *Earth and Planetary Science Letters* **236**, 135–147.
Gonnermann, H. M. (2015). Magma Fragmentation. *Annual Review of Earth and Planetary Sciences* **43**, 431–458.
Gonnermann, H. M., Giachetti, T., Fliedner, C., Nguyen, C. T., Houghton, B. F., Crozier, J. A. & Carey, R. J. (2017). Permeability During Magma Expansion and Compaction. *Journal of Geophysical Research: Solid Earth* **122**, 9825–9848.
Goto, A. (1999). A new model for volcanic earthquake at Unzen Volcano: Melt rupture model. *Geophysical Research Letters* **26**, 2541–2544.
Goto, Y., Nakada, S., Kurokawa, M., Shimano, T., Sugimoto, T., Sakuma, S., Hoshizumi, H., Yoshimoto, M. & Uto, K. (2008). Character and origin of lithofacies in the conduit of Unzen volcano, Japan. *Journal of Volcanology and Geothermal Research* **175**, 45–59.
Gottlieb, P., Wilkie, G., Sutherland, D., Ho-Tun, E., Suthers, S., Perera, K., Jenkins, B., Spencer, S., Butcher, A. & Rayner, J. (2000). Using quantitative electron microscopy for process mineralogy applications. *Journal of the Minerals, Metals & Materials Society* **52**, 24–25.
Gottsmann, J., Giordano, D. & Dingwell, D. B. (2002). Predicting shear viscosity during volcanic processes at the glass transition: a calorimetric calibration. *Earth and Planetary Science Letters* **198**, 417–427.
Grunewald, U., Sparks, R. S. J., Kearns, S. & Komorowski, J. C. (2000). Friction marks on blocks from pyroclastic flows at the Soufrière Hills volcano, Montserrat: Implications for flow mechanisms. *Geology* **28**, 827–830.
Gualda, G. A. R., Ghiorso, M. S., Lemons, R. V. & Carley, T. L. (2012). Rhyolite-MELTS: a Modified Calibration of MELTS Optimized for Silica-rich, Fluid-bearing Magmatic Systems. *Journal of Petrology* **53**, 875–890.
Hagerty, M. T., Schwartz, S. Y., Garces, M. A. & Protti, M. (2000). Analysis of seismic and acoustic observations at Arenal Volcano, Costa Rica, 1995-1997. *Journal of Volcanology and Geothermal Research* **101**, 27–65.
Hale, A. J. (2007). Magma flow instabilities in a volcanic conduit: Implications for long-period seismicity. *Physics of the Earth and Planetary Interiors* **163**, 163–178.
Hale, A. J., Wadge, G. & Muhlhaus, H. B. (2007). The influence of viscous and latent heating on crystal-rich magma flow in a conduit. *Geophysical Journal International* **171**, 1406–1429.
Hale, A. J. & Wadge, G. (2008). The transition from endogenous to exogenous growth of lava domes with the development of shear bands. *Journal of Volcanology and Geothermal Research* **171**, 237–257.
Hammer, J. E., Cashman, K. V., Hoblitt, R. P. & Newman, S. (1999). Degassing and microlite crystallization during pre-climactic events of the 1991 eruption of Mt. Pinatubo, Philippines. *Bulletin of Volcanology* **60**, 355–380.
Hammer, J. E., Cashman, K. V. & Voight, B. (2000). Magmatic processes revealed by textural and compositional trends in Merapi dome lavas. *Journal of Volcanology and Geothermal Research* **100**, 165–192.
Hammer, J. E. & Rutherford, M. J. (2002). An experimental study of the kinetics of decompression-induced crystallization in silicic melt. *Journal of Geophysical Research: Solid Earth* **107**, ECV 8-1–ECV 8-24.
Harbord, C. W. A., Nielsen, S. B., De Paola, N. & Holdsworth, R. E. (2017). Earthquake nucleation on rough faults. *Geology* **45**, 931–934.
Harford, C. L., Sparks, R. S. J. & Fallick, A. E. (2003). Degassing at the Soufrière Hills Volcano, Montserrat, recorded in matrix glass compositions. *Journal of Petrology* **44**, 1503–1523.
Harris, A. J. L., Rose, W. I. & Flynn, L. P. (2003). Temporal trends in lava dome extrusion at Santiaguito 1922-2000. *Bulletin of Volcanology* **65**, 77–89.

Hayman, N. W., Housen, B. A., Cladouhos, T. T. & Livi, K. (2004). Magnetic and clast fabrics as measurements of grain-scale processes within the Death Valley shallow crustal detachment faults. *Journal of Geophysical Research: Solid Earth* **109**.

Heap, M. J., Farquharson, J. I., Baud, P., Lavallee, Y. & Reuschle, T. (2015). Fracture and compaction of andesite in a volcanic edifice. *Bulletin of Volcanology* **77**, 55.

Heap, M. J., Violay, M., Wadsworth, F. B. & Vasseur, J. (2017). From rock to magma and back again: The evolution of temperature and deformation mechanism in conduit margin zones. *Earth and Planetary Science Letters* **463**, 92–100.

Hendrasto, M., Eto, T., Kimata, F., Matsushima, T. & Ishihara, K. (1997). Magma transport at Mt. Unzen associated with the 1990–1995 activity inferred from levelling data. *Disaster Prevention Research Institute Annuals* **40**, 61–72.

Henkel, O. (1964). Remanenzverhalten und Wechselwirkungen in hartmagnetischen Teilchenkollektiven. *physica status solidi (b)* **7**, 919–929.

Herrmann, W. & Berry, R. F. (2002). MINSQ - a least squares spreadsheet method for calculating mineral proportions from whole rock major element analyses. *Geochemistry: Exploration, Environment, Analysis* **2**, 361–368.

Hess, K. U. & Dingwell, D. B. (1996). Viscosities of hydrous leucogranitic melts: a non-Arrhenian model. *American Mineralogist* **81**, 1297–1300.

Hess, K. U., Cordonnier, B., Lavallee, Y. & Dingwell, D. B. (2008). Viscous heating in rhyolite: An in situ experimental determination. *Earth and Planetary Science Letters* **275**, 121–126.

Hetzel, R., Altenberger, U. & Strecker, M. R. (1996). Structural and chemical evolution of pseudotachylytes during seismic events. *Mineralogy and Petrology* **58**, 33–50.

Higgins, M. D. (2000). Measurement of crystal size distributions. *American Mineralogist* **85**, 1105–1116.

Hirose, T. & Shimamoto, T. (2003). Fractal dimension of molten surfaces as a possible parameter to infer the slip-weakening distance of faults from natural pseudotachylytes. *Journal of Structural Geology* **25**, 1569–1574.

Hirose, T. & Shimamoto, T. (2005). Growth of molten zone as a mechanism of slip weakening of simulated faults in gabbro during frictional melting. *Journal of Geophysical Research: Solid Earth* **110**, B05202.

Holland, A. S. P., Watson, I. M., Phillips, J. C., Caricchi, L. & Dalton, M. P. (2011). Degassing processes during lava dome growth: Insights from Santiaguito lava dome, Guatemala. *Journal of Volcanology and Geothermal Research* **202**, 153–166.

Holland, T. & Blundy, J. (1994). Nonideal Interactions in Calcic Amphiboles and Their Bearing on Amphibole-Plagioclase Thermometry. *Contributions to Mineralogy and Petrology* **116**, 433–447.

Holness, M. B., Stock, M. J. & Geist, D. (2019). Magma chambers versus mush zones: constraining the architecture of sub-volcanic plumbing systems from microstructural analysis of crystalline enclaves. *Philosophical Transactions of the Royal Society A: Mathematical, Physical and Engineering Sciences* **377**, 1–28.

Holtz, F., Sato, H., Lewis, J., Behrens, H. & Nakada, S. (2005). Experimental petrology of the 1991-1995 Unzen dacite, Japan. Part I: Phase relations, phase composition and pre-eruptive conditions. *Journal of Petrology* **46**, 319–337.

Hornby, A. J., Kendrick, J. E., Lamb, O. D., Hirose, T., De Angelis, S., von Aulock, F. W., Umakoshi, K., Miwa, T., Henton De Angelis, S., Wadsworth, F. B., Hess, K. U., Dingwell, D. B. & Lavallée, Y. (2015). Spine growth and seismogenic faulting at Mt. Unzen, Japan. *Journal of Geophysical Research: Solid Earth* **120**, 4034–4054.

Horwell, C., Williamson, B., Llewellin, E., Damby, D. & Blond, J. (2013). The nature and formation of cristobalite at the Soufrière Hills volcano, Montserrat: implications for the petrology and stability of silicic lava domes. *Bulletin of Volcanology* **75**, 1–19.

Hoshizumi, H., Uto, K. & Watanabe, K. (1999). Geology and Eruptive History of Unzen Volcano, Shimabara Peninsula, Kyushu, SW Japan. *Journal of Volcanology and Geothermal Research* **89**, 81–94.

Hu, W., Huang, R. Q., McSaveney, M., Zhang, X. H., Yao, L. & Shimamoto, T. (2018). Mineral changes quantify frictional heating during a large low-friction landslide. *Geology* **46**, 223–226.

Humphreys, M. C. S., Edmonds, M., Christopher, T. & Hards, V. (2009). Chlorine variations in the magma of Soufriere Hills Volcano, Montserrat: Insights from Cl in hornblende and melt inclusions. *Geochimica et Cosmochimica Acta* **73**, 5693–5708.

Huppert, H. E., Turner, J. S. & Sparks, R. S. J. (1982). Replenished Magma Chambers - Effects of Compositional Zonation and Input Rates. *Earth and Planetary Science Letters* **57**, 345–357.

Huppert, H. E. & Sparks, S. J. (1984). Double-diffusive convection due to crystallization in magmas. *Annual Review of Earth and Planetary Sciences* **12**, 11–37.

Iverson, R. M., Dzurisin, D., Gardner, C. A., Gerlach, T. M., LaHusen, R. G., Lisowski, M., Major, J. J., Malone, S. D., Messerich, J. A., Moran, S. C., Pallister, J. S., Qamar, A. I., Schilling, S. P. & Vallance, J. W. (2006). Dynamics of seismogenic volcanic extrusion at Mount St Helens in 2004-05. *Nature* **444**, 439–443.

Iverson, R. M. (2008). Dynamics of seismogenic volcanic extrusion resisted by a solid surface plug, Mount St. Helens, 2004-2005. In: Sherrod, D. R., Scott, W. E. & Stauffer, P. H. (eds.) *A Volcano Rekindled: The Renewed Eruption of Mount St. Helens, 2004-2006. Professional Paper 1750.*: U.S. Geological Survey 425–460.

Jiang, H. H., Lee, C. T. A., Morgan, J. K. & Ross, C. H. (2015). Geochemistry and thermodynamics of an earthquake: A case study of pseudotachylites within mylonitic granitoid. *Earth and Planetary Science Letters* **430**, 235–248.

Johnson, J. B., Harris, A. J. L., Sahetapy-Engel, S. T. M., Wolf, R. & Rose, W. I. (2004). Explosion dynamics of pyroclastic eruptions at Santiaguito Volcano. *Geophysical Research Letters* **31**, L06610.

Johnson, J. B. & Aster, R. C. (2005). Relative partitioning of acoustic and seismic energy during Strombolian eruptions. *Journal of Volcanology and Geothermal Research* **148**, 334–354.

Johnson, J. B., Lees, J. M., Gerst, A., Sahagian, D. & Varley, N. (2008). Long-period earthquakes and co-eruptive dome inflation seen with particle image velocimetry. *Nature* **456**, 377–381.

Johnson, J. B., Lyons, J. J., Andrews, B. J. & Lees, J. M. (2014). Explosive dome eruptions modulated by periodic gas-driven inflation. *Geophysical Research Letters* **41**, 6689–6697.

Kendrick, J. E., Lavallée, Y., Ferk, A., Perugini, D., Leonhardt, R. & Dingwell, D. B. (2012). Extreme frictional processes in the volcanic conduit of Mount St. Helens (USA) during the 2004–2008 eruption. *Journal of Structural Geology* **38**, 61–76.

Kendrick, J. E., Lavallée, Y., Hess, K. U., Heap, M. J., Gaunt, H. E., Meredith, P. G. & Dingwell, D. B. (2013a). Tracking the permeable porous network during strain-dependent magmatic flow. *Journal of Volcanology and Geothermal Research* **260**, 117–126.

Kendrick, J. E., Smith, R., Sammonds, P., Meredith, P. G., Dainty, M. & Pallister, J. S. (2013b). The influence of thermal and cyclic stressing on the strength of rocks from Mount St. Helens, Washington. *Bulletin of Volcanology* **75**, 1–12.

Kendrick, J. E., Lavallée, Y., Hess, K. U., De Angelis, S., Ferk, A., Gaunt, H. E., Meredith, P. G., Dingwell, D. B. & Leonhardt, R. (2014a). Seismogenic frictional melting in the magmatic column. *Solid Earth* **5**, 199–208.

Kendrick, J. E., Lavallée, Y., Hirose, T., Di Toro, G., Hornby, A., De Angelis, S. & Dingwell, D. B. (2014b). Volcanic drumbeat seismicity caused by stick-slip motion and magmatic frictional melting. *Nature Geoscience* **7**, 438–442.

Kendrick, J. E., Lavallee, Y., Varley, N. R., Wadsworth, F. B., Lamb, O. D. & Vasseur, J. (2016). Blowing Off Steam: Tuffisite Formation As a Regulator for Lava Dome Eruptions. *Frontiers in Earth Science* **4**, 1–15.

Kendrick, J. E., Lavallée, Y., Mariani, E., Dingwell, D. B., Wheeler, J. & Varley, N. R. (2017). Crystal plasticity as an indicator of the viscous-brittle transition in magmas. *Nature Communications* **8**, 1926.

Kennedy, B. M., Jellinek, A. M., Russell, J. K., Nichols, A. R. L. & Vigouroux, N. (2010). Time-and temperature-dependent conduit wall porosity: A key control on degassing and explosivity at Tarawera volcano, New Zealand. *Earth and Planetary Science Letters* **299**, 126–137.

Kennedy, B. M., Wadsworth, F. B., Vasseur, J., Schipper, C. I., Jellinek, A. M., von Aulock, F. W., Hess, K.-U., Russell, J. K., Lavallée, Y., Nichols, A. & Dingwell, D. B. (2016). Surface tension driven processes densify and retain permeability in magma and lava. *Earth and Planetary Science Letters* **433**, 116–124.

Kennedy, L. A., Russell, J. K. & Nelles, E. (2009). Origins of Mount St. Helens cataclasites: Experimental insights. *American Mineralogist* **94**, 995–1004.

Kirkpatrick, J. D. & Rowe, C. D. (2013). Disappearing ink: How pseudotachylytes are lost from the rock record. *Journal of Structural Geology* **52**, 183–198.

Kirkpatrick, R. J. (1981). Kinetics of crystallization of igneous rocks. In: C., L. A. & J., K. R. (eds.) *Mineralogical Society of America. Rev Mineral*, 321–398.

Kiss, B., Harangi, S., Ntaflos, T., Mason, P. R. D. & Pal-Molnar, E. (2014). Amphibole perspective to unravel pre-eruptive processes and conditions in volcanic plumbing systems beneath intermediate arc volcanoes: a case study from Ciomadul volcano (SE Carpathians). *Contributions to Mineralogy and Petrology* **167**, 1–27.

Klemetti, E. W. & Clynne, M. A. (2014). Localized Rejuvenation of a Crystal Mush Recorded in Zircon Temporal and Compositional Variation at the Lassen Volcanic Center, Northern California. *Plos One* **9**, e113157.

Klug, C. & Cashman, K. V. (1996). Permeability development in vesiculating magmas: Implications for fragmentation. *Bulletin of Volcanology* **58**, 87–100.

Kohno, Y., Matsushima, T. & Shimizu, H. (2008). Pressure sources beneath Unzen Volcano inferred from leveling and GPS data. *Journal of Volcanology and Geothermal Research* **175**, 100–109.

Koizumi, Y., Otsuki, K., Takeuchi, A. & Nagahama, H. (2004). Frictional melting can terminate seismic slips: Experimental results of stick-slips. *Geophysical Research Letters* **31**, L21605.

Krása, D. & Herrero-Bervera, E. (2005). Alteration induced changes of magnetic fabric as exemplified by dykes of the Koolau volcanic range. *Earth and Planetary Science Letters* **240**, 445–453.

Kratzmann, D. J., Carey, S., Scasso, R. & Naranjo, J. A. (2009). Compositional variations and magma mixing in the 1991 eruptions of Hudson volcano, Chile. *Bulletin of Volcanology* **71**, 419–439.

Kueppers, U., Scheu, B., Spieler, O. & Dingwell, D. B. (2005). Field-based density measurements as tool to identify preeruption dome structure: set-up and first results from Unzen volcano, Japan. *Journal of Volcanology and Geothermal Research* **141**, 65–75.

Lacroix, A. (1904). *La Montagne Pelée et ses eruptions*. Paris: Masson et Cie.

Lamb, O. D., De Angelis, S., Umakoshi, K., Hornby, A. J., Kendrick, J. E. & Lavallee, Y. (2015). Repetitive fracturing during spine extrusion at Unzen volcano, Japan. *Solid Earth* **6**, 1277–1293.

Lamb, O. D., Lamur, A., Diaz-Moreno, A., De Angelis, S., Hornby, A. J., Von Aulock, F. W., Kendrick, J. E., Wallace, P. A., Gottschammer, E., Rietbrock, A., Alvarez, I., Chigna, G. & Lavallee, Y. (2019). Disruption of Long-Term Effusive-Explosive Activity at Santiaguito, Guatemala. *Frontiers in Earth Science* **6**, 1–14.

Lamur, A., Kendrick, J. E., Eggertsson, G. H., Wall, R. J., Ashworth, J. D. & Lavallee, Y. (2017). The permeability of fractured rocks in pressurised volcanic and geothermal systems. *Scientific Reports* **7**.

Lamur, A., Wadsworth, F. B., Kendrick, J. E. & Lavallee, Y. (2019). Timescales of fracture healing and strength recovery in magmatic liquids. *Geology* **47**, 195–198.

Larrea, P., Franca, Z., Lago, M., Widom, E., Gale, C. & Ubide, T. (2013). Magmatic Processes and the Role of Antecrysts in the Genesis of Corvo Island (Azores Archipelago, Portugal). *Journal of Petrology* **54**, 769–793.

Laumonier, M., Arbaret, L., Burgisser, A. & Champallier, R. (2011). Porosity redistribution enhanced by strain localization in crystal-rich magmas. *Geology* **39**, 715–718.

Lavallée, Y., Hess, K. U., Cordonnier, B. & Dingwell, D. B. (2007). Non-Newtonian rheological law for highly crystalline dome lavas. *Geology* **35**, 843–846.

Lavallée, Y., Meredith, P. G., Dingwell, D. B., Hess, K. U., Wassermann, J., Cordonnier, B., Gerik, A. & Kruhl, J. H. (2008). Seismogenic lavas and explosive eruption forecasting. *Nature* **453**, 507–510.

Lavallée, Y., Mitchell, T. M., Heap, M. J., Vasseur, J., Hess, K. U., Hirose, T. & Dingwell, D. B. (2012a). Experimental generation of volcanic pseudotachylytes: Constraining rheology. *Journal of Structural Geology* **38**, 222–233.

Lavallée, Y., Varley, N., Alatorre-Ibargüengoitia, M., Hess, K. U., Kueppers, U., Mueller, S., Richard, D., Scheu, B., Spieler, O. & Dingwell, D. (2012b). Magmatic architecture of dome-building eruptions at Volcán de Colima, Mexico. *Bulletin of Volcanology* **74**, 249–260.

Lavallée, Y., Benson, P. M., Heap, M. J., Hess, K. U., Flaws, A., Schillinger, B., Meredith, P. G. & Dingwell, D. B. (2013). Reconstructing magma failure and the degassing network of dome-building eruptions. *Geology* **41**, 515–518.

Lavallée, Y., Hirose, T., Kendrick, J. E., De Angelis, S., Petrakova, L., Hornby, A. J. & Dingwell, D. B. (2014). A frictional law for volcanic ash gouge. *Earth and Planetary Science Letters* **400**, 177–183.

Lavallée, Y., Dingwell, D. B., Johnson, J. B., Cimarelli, C., Hornby, A. J., Kendrick, J. E., von Aulock, F. W., Kennedy, B. M., Andrews, B. J., Wadsworth, F. B., Rhodes, E. & Chigna, G. (2015a). Thermal vesiculation during volcanic eruptions. *Nature* **528**, 544–547.

Lavallée, Y., Hirose, T., Kendrick, J. E., Hess, K. U. & Dingwell, D. B. (2015b). Fault rheology beyond frictional melting. *Proceedings of the National Academy of Sciences of the United States of America* **112**, 9276–9280.

Lee, S. K., Han, R., Kim, E. J., Jeong, G. Y., Khim, H. & Hirose, T. (2017). Quasi-equilibrium melting of quartzite upon extreme friction. *Nature Geoscience* **10**, 436–441.

Legros, F., Cantagrel, J. M. & Devouard, B. (2000). Pseudotachylyte (frictionite) at the base of the Arequipa volcanic landslide deposit (Peru): Implications for emplacement mechanisms. *The Journal of Geology* **108**, 601–611.

Lejeune, A. M. & Richet, P. (1995). Rheology of Crystal-Bearing Silicate Melts - An Experimental study at High Viscosities. *Journal of Geophysical Research* **100**, 4215–4229.

Lejeune, A. M., Bottinga, Y., Trull, T. W. & Richet, P. (1999). Rheology of bubble-bearing magmas. *Earth and Planetary Science Letters* **166**, 71–84.

Lensky, N. G., Sparks, R. S. J., Navon, O. & Lyakhovsky, V. (2008). Cyclic activity at Soufrière Hills Volcano, Montserrat: degassing-induced pressurization and stick-slip extrusion. *Geological Society, London, Special Publications* **307**, 169–188.

Leonhardt, R. (2006). Analyzing rock magnetic measurements: The RockMagAnalyzer 1.0 software. *Computers & Geosciences* **32**, 1420–1431.

Lin, A. M. & Shimamoto, T. (1998). Selective melting processes as inferred from experimentally generated pseudotachylytes. *Journal of Asian Earth Sciences* **16**, 533–545.

Lin, A. M. (1999). Roundness of clasts in pseudotachylytes and cataclastic rocks as an indicator of frictional melting. *Journal of Structural Geology* **21**, 473–478.

Llewellin, E. W. & Manga, M. (2004). Bubble suspension rheology and implications for conduit flow. *Journal of Volcanology and Geothermal Research* **143**, 205–217.

Lockner, D. A., Kilgore, B. D., Beeler, N. M. & Moore, D. E. (2017). The transition from frictional sliding to shear melting in laboratory stick- slip experiments. In: Thomas,

M., Mitchell, T. & Bhat, H. (eds.) *Fault zone dynamic processes: Evolution of fault properties during seismic rupture*. Washington, DC: American Geophysical Union, 105–132.
Luhr, J. F. & Carmichael, I. S. E. (1990). Petrological monitoring of cyclical eruptive activity at Volcán Colima, Mexico. *Journal of Volcanology and Geothermal Research* **42**, 235–260.
Luhr, J. F. (2002). Petrology and geochemistry of the 1991 and 1998-1999 lava flows from Volcán de Colima, México: implications for the end of the current eruptive cycle. *Journal of Volcanology and Geothermal Research* **117**, 169–194.
Lynch, J. S. & Stephens, G. (1996). Mount Pinatubo: A satellite perspective of the June 1991 eruptions. In: Newhall, C. G. & Punongbayan, R. S. (eds.) *Fire and Mud: eruptions and lahars of Mount Pinatubo, Phillipines*. Quezon City, PHIVOLCS: Seattle, University of Washington Press, 637–645.
Macedonio, G. & Martini, M. (2010). Motivations for muon radiography of active volcanoes. *Earth, Planets and Space* **62**, 139–143.
Macias, J. L., Sosa-Ceballos, G., Arce, J. L., Gardner, J. E., Saucedo, R. & Valdez-Moreno, G. (2017). Storage conditions and magma processes triggering the 1818 CE Plinian eruption of Volcán de Colima. *Journal of Volcanology and Geothermal Research* **340**, 117–129.
Mader, H., Llewellin, E. & Mueller, S. (2013). The rheology of two-phase magmas: A review and analysis. *Journal of Volcanology and Geothermal Research* **257**, 135–158.
Magloughlin, J. F. (1992). Microstructural and chemical-changes associated with cataclasis and frictional melting at shallow crustal levels - the cataclasite pseudotachylyte connection. *Tectonophysics* **204**, 243–260.
Magloughlin, J. F. & Spray, J. G. (1992). Frictional Melting Processes and Products in Geological-Materials - Introduction and Discussion. *Tectonophysics* **204**, 197–206.
Manga, M., Castro, J., Cashman, K. V. & Loewenberg, M. (1998). Rheology of bubble-bearing magmas. *Journal of Volcanology and Geothermal Research* **87**, 15–28.
Mariani, E., Mecklenburgh, J., Wheeler, J., Prior, D. J. & Heidelbach, F. (2009). Microstructure evolution and recrystallization during creep of MgO single crystals. *Acta Materialia* **57**, 1886–1898.
Marsh, B. D. (1988). Crystal Size Distribution (CSD) in Rocks and the Kinetics and Dynamics of Crystallization .1. Theory. *Contributions to Mineralogy and Petrology* **99**, 277–291.
Mason, R. M., Starostin, A. B., Melnik, O. E. & Sparks, R. S. J. (2006). From Vulcanian explosions to sustained explosive eruptions: The role of diffusive mass transfer in conduit flow dynamics. *Journal of Volcanology and Geothermal Research* **153**, 148–165.
Mastin, L. G. (2005). The controlling effect of viscous dissipation on magma flow in silicic conduits. *Journal of Volcanology and Geothermal Research* **143**, 17–28.
Maxwell, J. C. (1867). On the dynamical theory of gases. *Philosophical transactions of the Royal Society of London* **157**, 49–88.
McKenzie, D. & Brune, J. N. (1972). Melting on fault planes during large earthquakes. *Geophysical Journal of the Royal Astronomical Society* **29**, 65–78.
Melnik, O. & Sparks, R. S. J. (2002). Dynamics of magma ascent and lava extrusion at Soufrière Hills Volcano, Montserrat. *Geological Society, London, Memoirs* **21**, 153–171.
Michaut, C., Bercovici, D. & Sparks, R. S. J. (2009). Ascent and compaction of gas rich magma and the effects of hysteretic permeability. *Earth and Planetary Science Letters* **282**, 258–267.
Michaut, C., Ricard, Y., Bercovici, D. & Sparks, R. S. J. (2013). Eruption cyclicity at silicic volcanoes potentially caused by magmatic gas waves. *Nature Geosci* **6**, 856–860.

Miwa, T., Toramaru, A. & Iguchi, M. (2009). Correlations of volcanic ash texture with explosion earthquakes from vulcanian eruptions at Sakurajima volcano, Japan. *Journal of Volcanology and Geothermal Research* **184**, 473–486.
Miyabuchi, Y. (1999). Deposits associated with the 1990-1995 eruption of Unzen volcano, Japan. *Journal of Volcanology and Geothermal Research* **89**, 139–158.
Moitra, P. & Gonnermann, H. M. (2015). Effects of crystal shape- and size-modality on magma rheology. *Geochemistry, Geophysics, Geosystems* **16**, 1–26.
Mollo, S. & Hammer, J. E. (2017). Dynamic crystallization in magmas. *Mineral Reaction Kinetics: Microstructures, Textures, Chemical and Isotopic Signatures* **16**, 373–418.
Monzawa, N. & Otsuki, K. (2003). Comminution and fluidization of granular fault materials: implications for fault slip behavior. *Tectonophysics* **367**, 127–143.
Morgan, D. J. & Jerram, D. A. (2006). On estimating crystal shape for crystal size distribution analysis. *Journal of Volcanology and Geothermal Research* **154**, 1–7.
Morgavi, D., Perugini, D., De Campos, C. P., Ertel-Ingrisch, W. & Dingwell, D. B. (2013). Time evolution of chemical exchanges during mixing of rhyolitic and basaltic melts. *Contributions to Mineralogy and Petrology* **166**, 615–638.
Moskowitz, B. M. (1981). Methods for Estimating Curie Temperatures of Titanomaghemites from Experimental Js-T Data. *Earth and Planetary Science Letters* **53**, 84–88.
Mueller, S., Melnik, O., Spieler, O., Scheu, B. & Dingwell, D. B. (2005). Permeability and degassing of dome lavas undergoing rapid decompression: An experimental determination. *Bulletin of Volcanology* **67**, 526–538.
Mueller, S., Scheu, B., Spieler, O. & Dingwell, D. B. (2008). Permeability control on magma fragmentation. *Geology* **36**, 399–402.
Mueller, S., Llewellin, E. W. & Mader, H. M. (2010). The rheology of suspensions of solid particles. *Proceedings of the Royal Society of London A: Mathematical, Physical and Engineering Sciences* **466**, 1201–1228.
Mueller, S., Llewellin, E. W. & Mader, H. M. (2011). The effect of particle shape on suspension viscosity and implications for magmatic flows. *Geophysical Research Letters* **38**, L13316.
Murphy, M. D., Sparks, R. S. J., Barclay, J., Carroll, M. R. & Brewer, T. S. (2000). Remobilization of andesite magma by intrusion of mafic magma at the Soufrière Hills Volcano, Montserrat, West Indies. *Journal of Petrology* **41**, 21–42.
Murray, J. D. (1979). Outlines of the structure and emplacement history of a tonalite plutons in the Peninsular Ranges batholith, northern Baja California, Mexico. In: Abbott, P. L. & Todd, V. R. (eds.) *Mesozoic crystalline rocks: Peninsular ranges batholith and pegmatites, Point Sal Ophiolite*. San Diego State University, San Diego, California, 163–176.
Nagasaki, S., Ishibashi, H., Suwa, Y., Yasuda, A., Hokanishi, N., Ohkura, T. & Takemura, K. (2017). Magma reservoir conditions beneath Tsurumi volcano, SW Japan: Evidence from amphibole thermobarometry and seismicity. *Lithos* **278**, 153–165.
Nakada, S. & Fujii, T. (1993). Preliminary-Report on the Activity at Unzen Volcano (Japan), November 1990 November 1991 - Dacite Lava Domes and Pyroclastic Flows. *Journal of Volcanology and Geothermal Research* **54**, 319–333.
Nakada, S., Miyake, Y., Sato, H., Oshima, O. & Fujinawa, A. (1995). Endogenous growth of dacitic dome at Unzen Volcano (Japan), 1993-1994. *Geology* **23**, 157–160.
Nakada, S. & Motomura, Y. (1999). Petrology of the 1991-1995 eruption at Unzen: effusion pulsation and groundmass crystallization. *Journal of Volcanology and Geothermal Research* **89**, 173–196.
Nakada, S., Shimizu, H. & Ohta, K. (1999). Overview of the 1990-1995 eruption at Unzen Volcano. *Journal of Volcanology and Geothermal Research* **89**, 1–22.
Nakamura, M. (1995). Continuous Mixing of Crystal Mush and Replenished Magma in the Ongoing Unzen Eruption. *Geology* **23**, 807–810.
Nakamura, N., Hirose, T. & Borradaile, G. J. (2002). Laboratory verification of submicron magnetite production in pseudotachylytes: relevance for paleointensity studies. . *Earth and Planetary Science Letters* **201**, 13–18.

Neuberg, J., Tuffen, H., Collier, L., Green, D., Powell, T. & Dingwell, D. (2006). The trigger mechanism of low-frequency earthquakes on Montserrat. *Journal of Volcanology and Geothermal Research* **153**, 37–50.

Neuberg, J. W., Collinson, A. S. D., Mothes, P. A., Ruiz, M. C. & Aguaiza, S. (2018). Understanding cyclic seismicity and ground deformation patterns at volcanoes: Intriguing lessons from Tungurahua volcano, Ecuador. *Earth and Planetary Science Letters* **482**, 193–200.

Nielsen, S., Di Toro, G., Hirose, T. & Shimamoto, T. (2008). Frictional melt and seismic slip. *Journal of Geophysical Research-Solid Earth* **113**, B01308.

Nielsen, S., Di Toro, G. & Griffith, W. A. (2010). Friction and roughness of a melting rock surface. *Geophysical Journal International* **182**, 299–310.

Niemeijer, A. R., Di Toro, G., Nielsen, S. & Di Felice, F. (2011). Frictional melting of gabbro under extreme experimental conditions of normal stress, acceleration and sliding velocity. *Journal of Geophysical Research: Solid Earth* **116**, B07404.

Noguchi, S., Toramaru, A. & Nakada, S. (2008a). Groundmass crystallization in dacite dykes taken in Unzen Scientific Drilling Project (USDP-4). *Journal of Volcanology and Geothermal Research* **175**, 71–81.

Noguchi, S., Toramaru, A. & Nakada, S. (2008b). Relation between microlite textures and discharge rate during the 1991-1995 eruptions at Unzen, Japan. *Journal of Volcanology and Geothermal Research* **175**, 141–155.

O'Hara, K. D. (1992). Major- and trace-element constraints on the petrogenesis of a fault-related pseudotachylyte, western Blue Ridge Province, North Carolina. *Tectonophysics* **204**, 279–288.

Ockendon, H. (1979). Channel Flow with Temperature-Dependent Viscosity and Internal Viscous Dissipation. *Journal of Fluid Mechanics* **93**, 737–746.

Ohmura, A. & Kawamura, H. (2007). Rate- and state-dependent friction law and statistical properties of earthquakes. *Europhysics Letters* **77**, 69001.

Okumura, S., Nakamura, M., Takeuchi, S., Tsuchiyama, A., Nakano, T. & Uesugi, K. (2009). Magma deformation may induce non-explosive volcanism via degassing through bubble networks. *Earth and Planetary Science Letters* **281**, 267–274.

Pallister, J. S., Hoblitt, R. P., Crandell, D. R. & Mullineaux, D. R. (1992). Mount St. Helens a decade after the 1980 eruptions: magmatic models, chemical cycles, and a revised hazards assessment. *Bulletin of Volcanology* **54**, 126–146.

Pallister, J. S., Thornber, C. R., Cashman, K. V., Clynne, M. A., Lowers, H. A., Mandeville, C. W., Brownfield, I. K. & Meeker, G. P. (2008). Petrology of the 2004-2006 Mount St Helens lava dome - implications for magmatic plumbing and eruption triggering. In: Sherrod, D. R., Scott, W. E. & Stauffer, P. H. (eds.) *A Volcano Rekindled: The Renewed Eruption of Mount St. Helens, 2004-2006. Professional Paper 1750.*: U.S. Geological Survey, 647–703.

Pallister, J. S., Cashman, K. V., Hagstrum, J. T., Beeler, N. M., Moran, S. C. & Denlinger, R. P. (2013). Faulting within the Mount St. Helens conduit and implications for volcanic earthquakes. *Geological Society of America Bulletin* **125**, 359–376.

Papale, P. (1999). Strain-induced magma fragmentation in explosive eruptions. *Nature* **397**, 425–428.

Papale, P., Moretti, R. & Barbato, D. (2006). The compositional dependence of the saturation surface of H2O+CO2 fluids in silicate melts. *Chemical Geology* **229**, 78–95.

Parmigiani, A., Faroughi, S., Huber, C., Bachmann, O. & Su, Y. (2016). Bubble accumulation and its role in the evolution of magma reservoirs in the upper crust. *Nature* **532**, 492–495.

Paulatto, M., Annen, C., Henstock, T. J., Kiddle, E., Minshull, T. A., Sparks, R. S. J. & Voight, B. (2012). Magma chamber properties from integrated seismic tomography and thermal modeling at Montserrat. *Geochemistry Geophysics Geosystems* **13**.

Perugini, D., Poli, G. & Mazzuoli, R. (2003). Chaotic advection, fractals and diffusion during mixing of magmas: evidence from lava flows. *Journal of Volcanology and Geothermal Research* **124**, 255–279.
Perugini, D., Petrelli, M. & Poli, G. (2006). Diffusive fractionation of trace elements by chaotic mixing of magmas. *Earth and Planetary Science Letters* **243**, 669–680.
Perugini, D., De Campos, C. R., Dingwell, D. B., Petrelli, M. & Poli, G. (2008). Trace element mobility during magma mixing: Preliminary experimental results. *Chemical Geology* **256**, 146–157.
Perugini, D. & Poli, G. (2012). The mixing of magmas in plutonic and volcanic environments: Analogies and differences. *Lithos* **153**, 261–277.
Perugini, D., De Campos, C. P., Dingwell, D. B. & Dorfman, A. (2013). Relaxation of concentration variance: A new tool to measure chemical element mobility during mixing of magmas. *Chemical Geology* **335**, 8–23.
Petford, N. (2009). Which effective viscosity? *Mineralogical Magazine* **73**, 167–191.
Picard, D., Arbaret, L., Pichavant, M., Champallier, R. & Launeau, P. (2011). Rheology and microstructure of experimentally deformed plagioclase suspensions. *Geology* **39**, 747–750.
Pirrie, D., Butcher, A. R., Power, M. R., Gottlieb, P. & Miller, G. L. (2004). Rapid quantitative mineral and phase analysis using automated scanning electron microscopy (QEMSCAN®); potential applications in forensic geoscience. In: Pye, K. & Croft, D. J. (eds.) *Forensic Geoscience, Principles, Techniques and Applications*. London: Geological Society Special Publication, 123–136.
Plechov, P. Y., Tsai, A. E., Shcherbakov, V. D. & Dirksen, O. V. (2011). Opacitization conditions of hornblende in Bezymyannyi volcano andesites (March 30, 1956 eruption). *Petrology* **16**, 19–35.
Poirier, J. P. (1995). Plastic rheology of crystals. *Mineral Physics & Crystallography: A Handbook of Physical Constants*. Washington, DC: AGU, 237–247.
Polacci, M., Papale, P. & Rosi, M. (2001). Textural heterogeneities in pumices from the climactic eruption of Mount Pinatubo, 15 June 1991, and implications for magma ascent dynamics. *Bulletin of Volcanology* **63**, 83–97.
Popov, V. L., Grzemba, B., Starcevic, J. & Popov, M. (2012). Rate and state dependent friction laws and the prediction of earthquakes: What can we learn from laboratory models? *Tectonophysics* **532**, 291–300.
Pouchou, J. L. & Pichoir, F. (1984). A new model for quantitative X-ray-microanalysis .1. Application to the analysis of homogeneous samples. *La Recherche Aérospatiale*, 167–192.
Preece, K., Barclay, J., Gertisser, R. & Herd, R. A. (2013). Textural and micro-petrological variations in the eruptive products of the 2006 dome-forming eruption of Merapi volcano, Indonesia: Implications for sub-surface processes. *Journal of Volcanology and Geothermal Research* **261**, 98–120.
Preece, K., Gertisser, R., Barclay, J., Charbonnier, S. J., Komorowski, J. C. & Herd, R. A. (2016). Transitions between explosive and effusive phases during the cataclysmic 2010 eruption of Merapi volcano, Java, Indonesia. *Bulletin of Volcanology* **78**.
Prior, D. J., Boyle, A. P., Brenker, F., Cheadle, M. C., Day, A., Lopez, G., Peruzzo, L., Potts, G. J., Reddy, S., Spiess, R., Timms, N. E., Trimby, P., Wheeler, J. & Zetterstrom, L. (1999). The application of electron backscatter diffraction and orientation contrast imaging in the SEM to textural problems in rocks. *American Mineralogist* **84**, 1741–1759.
Prior, D. J., Mariani, E. & Wheeler, J. (2009). EBSD in the earth sciences: applications, common practice, and challenges. In: Schwartz, A. J., Kumar, M., Adams, B. L. & Field, D. P. (eds.) *Electron Backscatter Diffraction in Materials Science*. New York: Springer Science, 345–360.
Putirka, K. (2016). Amphibole thermometers and barometers for igneous systems and implications for eruption mechanisms of felsic magmas at arc volcanoes. *American Mineralogist* **101**, 841–858.

Putirka, K. D. (2008). Thermometers and Barometers for Volcanic Systems. *Minerals, Inclusions and Volcanic Processes* **69**, 61–120.
Reches, Z. & Lockner, D. A. (2010). Fault weakening and earthquake instability by powder lubrication. *Nature* **467**, 452–455.
Reid, M. E., Keith, T. E. C., Kayen, R. E., Iverson, N. R., Iverson, R. M. & Brien, D. L. (2010). Volcano collapse promoted by progressive strength reduction: new data from Mount St. Helens. *Bulletin of Volcanology* **72**, 761–766.
Reubi, O. & Blundy, J. (2008). Assimilation of plutonic roots, formation of high-K 'exotic' melt inclusions and genesis of andesitic magmas at Volcán De Colima, Mexico. *Journal of Petrology* **49**, 2221–2243.
Rhodes, E., Kennedy, B., Lavallee, Y., Hornby, A., Edwards, M. & Chigna, G. (2018). Textural Insights Into the Evolving Lava Dome Cycles at Santiaguito Lava Dome, Guatemala. *Frontiers in Earth Science* **6**.
Rice, J. R., Lapusta, N. & Ranjith, K. (2001). Rate and state dependent friction and the stability of sliding between elastically deformable solids. *Journal of the Mechanics and Physics of Solids* **49**, 1865–1898.
Richet, P. & Ottonello, G. (2010). Thermodynamics of Phase Equilibria in Magma. *Elements* **6**, 315–320.
Ridolfi, F., Renzulli, A. & Puerini, M. (2010). Stability and chemical equilibrium of amphibole in calc-alkaline magmas: An overview, new thermobarometric formulations and application to subduction-related volcanoes. *Contributions to Mineralogy and Petrology* **160**, 45–66.
Ridolfi, F. & Renzulli, A. (2012). Calcic amphiboles in calc-alkaline and alkaline magmas: thermobarometric and chemometric empirical equations valid up to 1,130A degrees C and 2.2 GPa. *Contributions to Mineralogy and Petrology* **163**, 877–895.
Roscoe, R. (1952). The viscosity of suspensions of rigid spheres. *British Journal of Applied Physics* **3**, 267.
Rose, W. I. (1972). Santiaguito Volcanic Dome, Guatemala. *Geological Society of America Bulletin* **83**, 1413–1434.
Rosenberg, C. L. & Handy, M. R. (2005). Experimental deformation of partially melted granite revisited: implications for the continental crust. *Journal of Metamorphic Geology* **23**, 19–28.
Rosi, M., Landi, P., Polacci, M., Di Muro, A. & Zandomeneghi, D. (2004). Role of conduit shear on ascent of the crystal-rich magma feeding the 800-year-BP Plinian eruption of Quilotoa Volcano (Ecuador). *Bulletin of Volcanology* **66**, 307–321.
Rossi, S., Petrelli, M., Morgavi, D., Gonzalez-Garcia, D., Fischer, L. A., Vetere, F. & Perugini, D. (2017). Exponential decay of concentration variance during magma mixing: Robustness of a volcanic chronometer and implications for the homogenization of chemical heterogeneities in magmatic systems. *Lithos* **286**, 396–407.
Rust, A. C. & Manga, M. (2002). Bubble Shapes and Orientations in Low Re Simple Shear Flow. *Journal of Colloid and Interface Science* **249**, 476–480.
Rutherford, M. J. & Hill, P. M. (1993). Magma Ascent Rates from Amphibole Breakdown - an Experimental-Study Applied to the 1980-1986 Mount St-Helens Eruptions. *Journal of Geophysical Research: Solid Earth* **98**, 19667–19685.
Rutherford, M. J. & Devine, J. D. (2003). Magmatic conditions and magma ascent as indicated by hornblende phase equilibria and reactions in the 1995-2002 Soufriere Hills magma. *Journal of Petrology* **44**, 1433–1454.
Ryan, A. G., Friedlander, E. A., Russell, J. K., Heap, M. J. & Kennedy, L. A. (2018). Hot pressing in conduit faults during lava dome extrusion: Insights from Mount St. Helens 2004-2008. *Earth and Planetary Science Letters* **482**, 171–180.
Saar, M. O., Manga, M., Cashman, K. V. & Fremouw, S. (2001). Numerical models of the onset of yield strength in crystal-melt suspensions. *Earth and Planetary Science Letters* **187**, 367–379.

Sahetapy-Engel, S. T., Harris, A. J. L. & Marchetti, E. (2008). Thermal, seismic and infrasound observations of persistent explosive activity and conduit dynamics at Santiaguito lava dome, Guatemala. *Journal of Volcanology and Geothermal Research* **173**, 1–14.

Saito, T., Ishikawa, N. & Kamata, H. (2007). Magnetic petrology of the 1991-1995 dacite lava of Unzen volcano, Japan: Degree of oxidation and implications for the growth of lava domes. *Journal of Volcanology and Geothermal Research* **164**, 268–283.

Saito, T. & Shikawa, N. (2007). Magnetic petrology and its implication for magma mixing of the 1991-1995 dacite at Unzen volcano, Japan. *Earth Planets and Space* **59**, 863–870.

Sakuma, S., Kajiwara, T., Nakada, S., Uto, K. & Shimizu, H. (2008). Drilling and logging results of USDP-4 - Penetration into the volcanic conduit of Unzen Volcano, Japan. *Journal of Volcanology and Geothermal Research* **175**, 1–12.

Salaun, A., Villemant, B., Gerard, M., Komorowski, J. C. & Michel, A. (2011). Hydrothermal alteration in andesitic volcanoes: Trace element redistribution in active and ancient hydrothermal systems of Guadeloupe (Lesser Antilles). *Journal of Geochemical Exploration* **111**, 59–83.

Sanderson, R. W., Johnson, J. B. & Lees, J. M. (2010). Ultra-long period seismic signals and cyclic deflation coincident with eruptions at Santiaguito volcano, Guatemala. *Journal of Volcanology and Geothermal Research* **198**, 35–44.

Sato, H., Fujii, T. & Nakada, S. (1992). Crumbling of Dacite Dome Lava and Generation of Pyroclastic Flows at Unzen Volcano. *Nature* **360**, 664–666.

Sato, H., Nakada, S., Fujii, T., Nakamura, M. & Suzuki-Kamata, K. (1999). Groundmass pargasite in the 1991-1995 dacite of Unzen volcano: phase stability experiments and volcanological implications. *Journal of Volcanology and Geothermal Research* **89**, 197–212.

Sato, H., Holtz, F., Botcharnikov, R. E. & Nakada, S. (2017). Intermittent generation of mafic enclaves in the 1991-1995 dacite of Unzen Volcano recorded in mineral chemistry. *Contributions to Mineralogy and Petrology* **172**, 22.

Saucedo, R., Macias, J. L., Gavilanes, J. C., Arce, J. L., Komorowski, J. C., Gardner, J. E. & Valdez-Moreno, G. (2010). Eyewitness, stratigraphy, chemistry, and eruptive dynamics of the 1913 Plinian eruption of Volcán de Colima, México. *Journal of Volcanology and Geothermal Research* **191**, 149–166.

Savov, I. P., Luhr, J. F. & Navarro-Ochoa, C. (2008). Petrology and geochemistry of lava and ash erupted from Volcán Colima, Mexico, during 1998–2005. *Journal of Volcanology and Geothermal Research* **174**, 241–256.

Schneider, C. A., Rasband, W. S. & Eliceiri, K. W. (2012). NIH Image to ImageJ: 25 years of image analysis. *Nature Methods* **9**, 671–675.

Schwarzkopf, L. M., Schmincke, H. U. & Troll, V. R. (2001). Pseudotachylite on impact marks of block surfaces in block-and-ash flows at Merapi volcano, Central Java, Indonesia. *International Journal of Earth Sciences* **90**, 769–775.

Scott, J. A. J., Mather, T. A., Pyle, D. M., Rose, W. I. & Chigna, G. (2012). The magmatic plumbing system beneath Santiaguito Volcano, Guatemala. *Journal of Volcanology and Geothermal Research* **237**, 54–68.

Scott, J. A. J., Pyle, D. M., Mather, T. A. & Rose, W. I. (2013). Geochemistry and evolution of the Santiaguito volcanic dome complex, Guatemala. *Journal of Volcanology and Geothermal Research* **252**, 92–107.

Scott, J. S. & Drever, H. I. (1953). Frictional fusion along a Himalayan thrust. *Proceedings of the Royal Society of Edinburgh* **658**, 121–142.

Self, S., Wilson, L. & Nairn, I. A. (1979). Vulcanian Eruption Mechanisms. *Nature* **277**, 440–443.

Selverstone, J., Axen, G. J. & Luther, A. (2012). Fault localization controlled by fluid infiltration into mylonites: Formation and strength of low-angle normal faults in the midcrustal brittle-plastic transition. *Journal of Geophysical Research: Solid Earth* **117**.

Shand, S. J. (1916). The pseudotachylyte of Parijs (Orange Free State), and its relation to "trap-shotten gneiss" and "flinty crush-rock". *Quarterly Journal of the Geological Society* **72**, 198–221.
Shane, P. & Smith, V. C. (2013). Using amphibole crystals to reconstruct magma storage temperatures and pressures for the post-caldera collapse volcanism at Okataina volcano. *Lithos* **156**, 159–170.
Sherrod, D. R., Scott, W. E. & Stauffer, P. H. (2008). A Volcano Rekindled: the Renewed Eruption of Mount St. Helens, 2004-2006. . *U.S.Geological Survey Professional Paper 1750*, 856 pp.
Shimamoto, T. & Lin, A. (1994). Is frictional melting equilibrium melting, or non-equilibrium melting? *Structural Geology-Journal of the Tectonic Research Group of Japan* **39**, 79–84.
Shimamoto, T. & Tsutsumi, A. (1994). A new rotary-shear high-speed frictional testing machine: its basic design and scope of research. *Structural Geology: Journal of the Tectonic Research Group of Japan* **39**, 65–78.
Sibson, R. H. (1975). Generation of pseudotachylyte by ancient seismic faulting. *Journal of Royal Astronomical Society of London* **43**, 775–794.
Siebert, L., Simkin, T. & Kimberly, P. (2010). *Volcanoes of the World: Third Edition*: University California Press.
Small, C. & Naumann, T. (2001). *The global distribution of human population and recent volcanism, Global Environmental Change Part B: Environmental Hazards*.
Smith, J. V., Miyake, Y. & Oikawa, T. (2001). Interpretation of porosity in dacite lava domes as ductile-brittle failure textures. *Journal of Volcanology and Geothermal Research* **112**, 25–35.
Smith, R., Sammonds, P. R., Tuffen, H. & Meredith, P. G. (2011). Evolution of the mechanics of the 2004-2008 Mt. St. Helens lava dome with time and temperature. *Earth and Planetary Science Letters* **307**, 191–200.
Spagnuolo, E., Nielsen, S., Violay, M. & Di Toro, G. (2016). An empirically based steady state friction law and implications for fault stability. *Geophysical Research Letters* **43**, 3263–3271.
Sparks, R. S. J. (1978). The dynamics of bubble formation and growth in magmas: A review and analysis. *Journal of Volcanology and Geothermal Research* **3**, 1–37.
Sparks, R. S. J. & Marshall, L. A. (1986). Thermal and mechanical constraints on mixing between mafic and silicic magmas. *Journal of Volcanology and Geothermal Research* **29**, 99–124.
Sparks, R. S. J. (1997). Causes and consequences of pressurisation in lava dome eruptions. *Earth and Planetary Science Letters* **150**, 177–189.
Sparks, R. S. J., Murphy, M. D., Lejeune, A. M., Watts, R. B., Barclay, J. & Young, S. R. (2000). Control on the emplacement of the andesite lava dome of the Soufriere Hills volcano, Montserrat by degassing-induced crystallization. *Terra Nova* **12**, 14–20.
Sparks, R. S. J. & Young, S. R. (2002). The eruption of Soufriere Hills Volcano, Montserrat (1995-1999): overview of scientific results. In: Druitt, T. H. & Kokelaar, B. P. (eds.) *The Eruption of Soufriere Hills Volcano, Montserrat, from 1995 to 1999*. London: Geological Society, 45–69.
Sparks, R. S. J. (2003a). Forecasting Volcanic Eruptions. *Earth and Planetary Science Letters* **210**, 1–15.
Sparks, R. S. J. (2003b). Dynamics of magma degassing. In: Oppenheimer, C., Pyle, D. M. & Barclay, J. (eds.) *Volcanic Degassing*: Geological Society, 5–22.
Sparks, S. R. J., Sigurdsson, H. & Wilson, L. (1977). Magma Mixing - Mechanism for Triggering Acid Explosive Eruptions. *Nature* **267**, 315–318.
Spieler, O., Kennedy, B., Kueppers, U., Dingwell, D. B., Scheu, B. & Taddeucci, J. (2004). The fragmentation threshold of pyroclastic rocks. *Earth and Planetary Science Letters* **226**, 139–148.
Spray, J. G. (1992). A physical basis for the frictional melting of some rock-forming minerals. *Tectonophysics* **204**, 205–221.

Spray, J. G. (2010). Frictional melting processes in planetary materials: From hypervelocity impact to earthquakes. *Annual Review of Earth and Planetary Sciences* **38**, 221–254.

Stechern, A., Just, T., Holtz, F., Blume-Oeste, M. & Namur, O. (2017). Decoding magma plumbing and geochemical evolution beneath the Lastarria volcanic complex (Northern Chile) Evidence for multiple magma storage regions. *Journal of Volcanology and Geothermal Research* **338**, 25–45.

Stevenson, R. J., Dingwell, D. B., Webb, S. L. & Sharp, T. G. (1996). Viscosity of microlite-bearing rhyolitic obsidians: An experimental study. *Bulletin of Volcanology* **58**, 298–309.

Stix, J., Zapata, J. A., Calvache, M., Cortes, G. P., Fischer, T. P., Gomez, D., Narvaez, L., Ordonez, M., Ortega, A., Torres, R. & Williams, S. N. (1993). A Model of Degassing at Galeras Volcano, Colombia, 1988-1993. *Geology* **21**, 963–967.

Stix, J., Torres, R., Narvaez, L., Cortes, G. P., Raigosa, J., Gomez, D. & Castonguay, R. (1997). A model of vulcanian eruptions at Galeras volcano, Colombia. *Journal of Volcanology and Geothermal Research* **77**, 285–303.

Stock, M. J., Bagnardi, M., Neave, D. A., Maclennan, J., Bernard, B., Buisman, I., Gleeson, M. L. M. & Geist, D. (2018). Integrated Petrological and Geophysical Constraints on Magma System Architecture in the Western Galapagos Archipelago: Insights From Wolf Volcano. *Geochemistry Geophysics Geosystems* **19**, 4722–4743.

Swanson, D. A. & Holcomb, R. T. (1990). Regularities in Growth of the Mount St Helens Dacite Dome, 1980-1986. In: Fink, J. H. (ed.) *Lava Flows and Domes: Emplacement Mechanisms and Hazard Implications*: Springer Verlag, 3–24.

Tait, S., Jaupart, C. & Vergniolle, S. (1989). Pressure, Gas Content and Eruption Periodicity of a Shallow, Crystallizing Magma Chamber. *Earth and Planetary Science Letters* **92**, 107–123.

Tanaka, H. K. M. (2016). Instant snapshot of the internal structure of Unzen lava dome, Japan with airborne muography. *Scientific Reports* **6**.

Tanguy, J. C. (2004). Rapid dome growth at Montagne Pelee during the early stages of the 1902-1905 eruption: a reconstruction from Lacroix's data. *Bulletin of Volcanology* **66**, 615–621.

Tepley, F. J., Davidson, J. P., Tilling, R. I. & Arth, J. G. (2000). Magma mixing, recharge and eruption histories recorded in plagioclase phenocrysts from El Chichon Volcano, Mexico. *Journal of Petrology* **41**, 1397–1411.

Tilling, R. I. (2005). Volcano Hazards. In: Martí, J. & Ernst, G. (eds.) *Volcanoes and the Environment*. Cambridge: Cambridge University Press, 56–89.

Tilling, R. I. (2008). The critical role of volcano monitoring in risk reduction. *Advances in Geosciences* **14**, 3–11.

Toramaru, A., Noguchi, S., Oyoshihara, S. & Tsune, A. (2008). MND(microlite number density) water exsolution rate meter. *Journal of Volcanology and Geothermal Research* **175**, 156–167.

Tsutsumi, A. & Shimamoto, T. (1997). High-velocity frictional properties of gabbro. *Geophysical Research Letters* **24**, 699–702.

Tuffen, H., Dingwell, D. B. & Pinkerton, H. (2003). Repeated fracture and healing of silicic magma generate flow banding and earthquakes? *Geology* **31**, 1089–1092.

Tuffen, H. & Dingwell, D. B. (2005). Fault textures in volcanic conduits: evidence for seismic trigger mechanisms during silicic eruptions. *Bulletin of Volcanology* **67**, 370–387.

Tuffen, H., Smith, R. & Sammonds, P. R. (2008). Evidence for seismogenic fracture of silicic magma. *Nature* **453**, 511–514.

Tuffen, H., James, M. R., Castro, J. & Schipper, C. I. (2013). Exceptional mobility of an advancing rhyolitic obsidian flow at Cordón Caulle volcano in Chile. *Nature Communications* **4**, 2709.

Ubide, T. & Kamber, B. S. (2018). Volcanic crystals as time capsules of eruption history. *Nature Communications* **9**.

Ui, T., Matsuwo, N., Sumita, M. & Fujinawa, A. (1999). Generation of block and ash flows during the 1990-1995 eruption of Unzen Volcano, Japan. *Journal of Volcanology and Geothermal Research* **89**, 123–137.

Umakoshi, K., Shimizu, H. & Matsuwo, N. (2001). Volcano-tectonic seismicity at Unzen Volcano, Japan 1985-1999. *Journal of Volcanology and Geothermal Research* **112**, 117–131.

Umakoshi, K., Takamura, N., Shinzato, N., Uchida, K., Matsuwo, N. & Shimizu, H. (2008). Seismicity associated with the 1991-1995 dome growth at Unzen Volcano, Japan. *Journal of Volcanology and Geothermal Research* **175**, 91–99.

Varley, N., Arámbula-Mendoza, R., Reyes-Dávila, G., Sanderson, R. & Stevenson, J. (2010). Generation of Vulcanian activity and long-period seismicity at Volcán de Colima, Mexico. *Journal of Volcanology and Geothermal Research* **198**, 45–56.

Vedeneeva, E. A., Melnik, O. E., Barmin, A. A. & Sparks, R. S. J. (2005). Viscous dissipation in explosive volcanic flows. *Geophysical Research Letters* **32**.

Venezky, D. Y. & Rutherford, M. J. (1999). Petrology and Fe-Ti oxide reequilibration of the 1991 Mount Unzen mixed magma. *Journal of Volcanology and Geothermal Research* **89**, 213–230.

Vernon, R. H. & Paterson, S. R. (1993). The Ardara Pluton, Ireland - Deflating All Expanded Intrusion. *Lithos* **31**, 17–32.

Vernon, R. H. (2000). Review of Microstructural Evidence of Magmatic and Solid-State Flow. *Visual Geosciences* **5**, 1–23.

Violay, M., Di Toro, G., Gibert, B., Nielsen, S., Spagnuolo, E., Del Gaudio, P., Azais, P. & Scarlato, P. G. (2014). Effect of glass on the frictional behavior of basalts at seismic slip rates. *Geophysical Research Letters* **41**, 348–355.

Voight, B., Sparks, R. S., Miller, A. D., Stewart, R. C., Hoblitt, R. P., Clarke, A., Ewart, J., Aspinall, W. P., Baptie, B., Calder, E. S., Cole, P., Druitt, T. H., Hartford, C., Herd, R. A., Jackson, P., Lejeune, A. M., Lockhart, A. B., Loughlin, S. C., Luckett, R., Lynch, L., Norton, G. E., Robertson, R., Watson, I. M., Watts, R. & Young, S. R. (1999). Magma Flow Instability and Cyclic Activity at Soufriere Hills Volcano, Montserrat, British West Indies. *Science* **283**, 1138–1142.

Voight, B. (2000). Structural stability of andesite volcanoes and lava domes. *Philosophical transactions of the Royal Society of London* **358** 1663–1703.

Voight, B., Young, K. D., Hidayat, D., Subandrio, M. A., Purbawinata, M. A., Ratdomopurbo, A., Suharna, Panut, Sayudi, D. S., LaHusen, R., Marso, J., Murray, T. L., Dejean, M., Iguchi, M. & Ishihara, K. (2000). Deformation and seismic precursors to dome-collapse and fountain-collapse nuees ardentes at Merapi Volcano, Java, Indonesia, 1994-1998. *Journal of Volcanology and Geothermal Research* **100**, 261–287.

von Aulock, F. W., Kennedy, B. M., Maksimenko, A., Wadsworth, F. B. & Lavallée, Y. (2017). Outgassing from Open and Closed Magma Foams. *Frontiers in Earth Science* **5**, 1–7.

Wadge, G., Robertson, R. E. A. & Voight, B. (2014). The Eruption of Soufrière Hills Volcano, Montserrat from 2000 to 2010. *The Geological Society Memoir 39 London.* **39**, 1–40.

Wallace, P. A., Kendrick, J. E., Miwa, T., Ashworth, J. D., Coats, R., Utley, J. E. P., Henton De Angelis, S., Mariani, E., Biggin, A., Kendrick, R., Nakada, S., Matsushima, T. & Lavallée, Y. (2019). Petrological architecture of a magmatic shear zone: A multidisciplinary investigation of strain localisation during magma ascent at Unzen Volcano, Japan. *Journal of Petrology* **60**, 791–826.

Wallace, P. J. (2005). Volatiles in subduction zone magmas: concentrations and fluxes based on melt inclusion and volcanic gas data. *Journal of Volcanology and Geothermal Research* **140**, 217–240.

Watts, R. B., Herd, R. A., Sparks, R. S. J. & Young, S. R. (2002). Growth patterns and emplacement of the andesitic lava dome at Soufrière Hills Volcano, Montserrat. *Geological Society, London, Memoirs* **21**, 115–152.

Webb, S. L. & Dingwell, D. B. (1990). Non-Newtonian rheology of igneous melts at high stresses and strain rates: experimental results for rhyolite, andesite, basalt and nephelinite. *Journal of Geophysical Research* **95**, 15695–15701.
Wibberley, C. (1999). Are feldspar-to-mica reactions necessarily reaction-softening processes in fault zones? *Journal of Structural Geology* **21**, 1219–1227.
Williamson, B. J., Di Muro, A., Horwell, C. J., Spieler, O. & Llewellin, E. W. (2010). Injection of vesicular magma into an andesitic dome at the effusive-explosive transition. *Earth and Planetary Science Letters* **295**, 83–90.
Wohlfarth, E. P. (1958). Relations between different modes of acquisition of the remanent magnetization of ferromagnetic particles. *Journal of Applied Physics* **29**, 595–596.
Woods, A. W. & Koyaguchi, T. (1994). Transitions between Explosive and Effusive Eruptions of Silicic Magmas. *Nature* **370**, 641–644.
Wright, H. M. N. & Weinberg, R. F. (2009). Strain localization in vesicular magma: Implications for rheology and fragmentation. *Geology* **37**, 1023–1026.
Wright, R. (2016). MODVOLC: 14 years of autonomous observations of effusive volcanism from space. *Detecting, Modelling and Responding to Effusive Eruptions* **426**, 23–53.
Wright, R., Lucey, P., Crites, S., Garbeil, H., Wood, M., Pilger, E., Gabrieli, A. & Honniball, C. (2016). TIRCIS: thermal infrared compact imaging spectrometer for small satellite applications. *Multispectral, Hyperspectral, and Ultraspectral Remote Sensing Technology, Techniques and Applications Vi* **9880**.
Yamamoto, H., Takayama, K. & Kedrinskii, V. (2008). An analog experiment of magma fragmentation: behavior of rapidly decompressed starch sirup. *Shock Waves* **17**, 371–385.
Yamamoto, T., Takarada, S. & Suto, S. (1993). Pyroclastic Flows from the 1991 Eruption of Unzen Volcano, Japan. *Bulletin of Volcanology* **55**, 166–175.
Yamashina, K., Matsushima, T. & Ohmi, S. (1999). Volcanic deformation at Unzen, Japan, visualized by a time-differential stereoscopy. *Journal of Volcanology and Geothermal Research* **89**, 73–80.
Yonkee, W. A., Czeck, D. M., Nachbor, A. C., Barszewski, C., Pantone, S., Balgord, E. A. & Johnson, K. R. (2013). Strain accumulation and fluid-rock interaction in a naturally deformed diamictite, Willard thrust system, Utah (USA): Implications for crustal rheology and strain softening. *Journal of Structural Geology* **50**, 91–118.
Zibra, I., Kruhl, J. H., Montanini, A. & Tribuzio, R. (2012). Shearing of magma along a high-grade shear zone: Evolution of microstructures during the transition from magmatic to solid-state flow. *Journal of Structural Geology* **37**, 150–160.

# Appendix I: Supplementary Figures (Chapter 2)

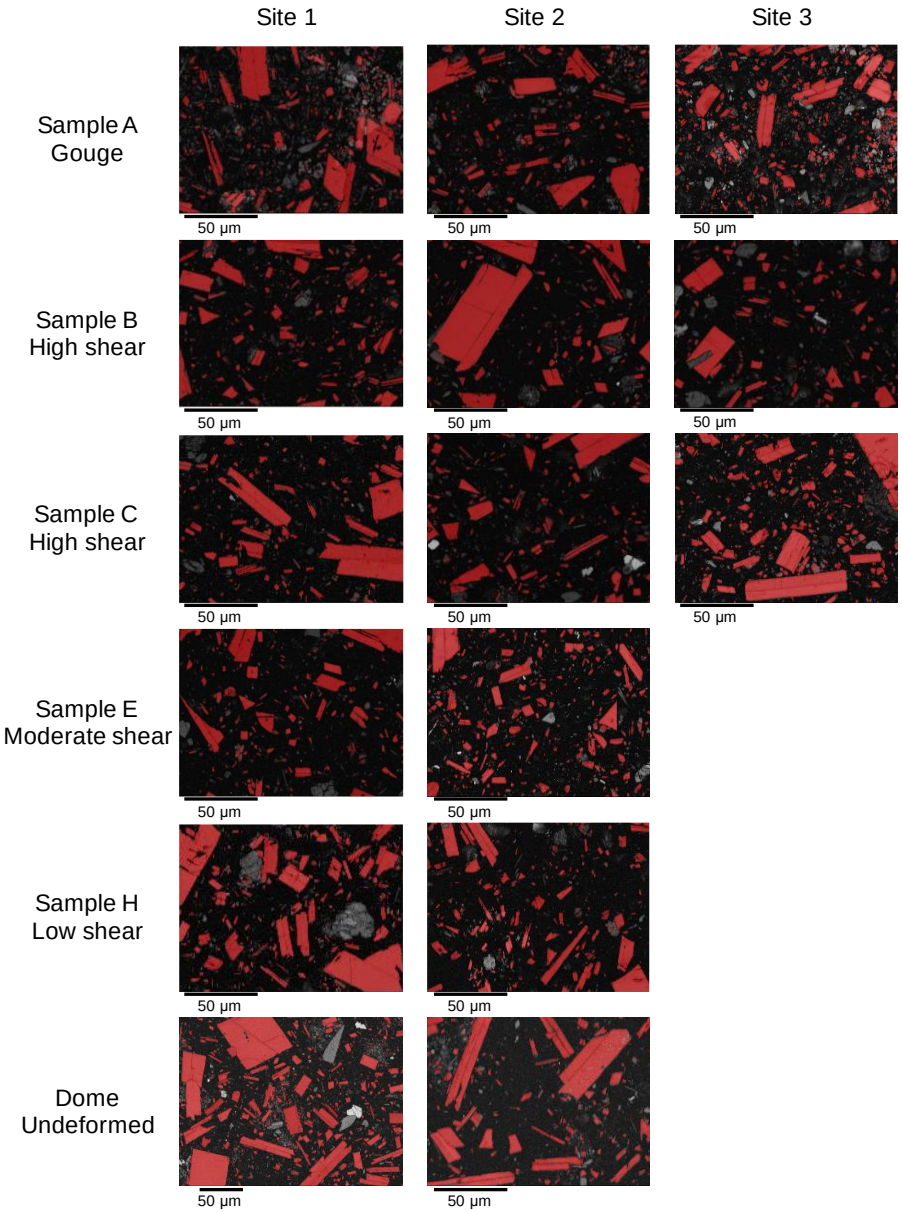


***Figure A1.1*** *– Band contrast images of areas for plagioclase microlite EBSD analysis (Fig. 2.9), with all plagioclase highlighted in red. All other phases are the non-highlighted grey areas. Black represents either glass, pore space or any crystals that were not successfully indexed. The crystals quantified for plastic deformation were those with good indexing to ensure quality and accuracy. Measurements from each sample were compiled in terms of section of the shear zone (i.e., gouge (A), high shear (B & C), moderate shear (E), low shear (H) from outcrop 1 and the undeformed dome rock. Note the higher abundance of small grey patches (~5–10 µm in diameter) in the gouge relative to the low, moderate and higher shear zones. These correspond to silica phases in the groundmass and are therefore crystalline* $SiO_2$ *polymorphs.*

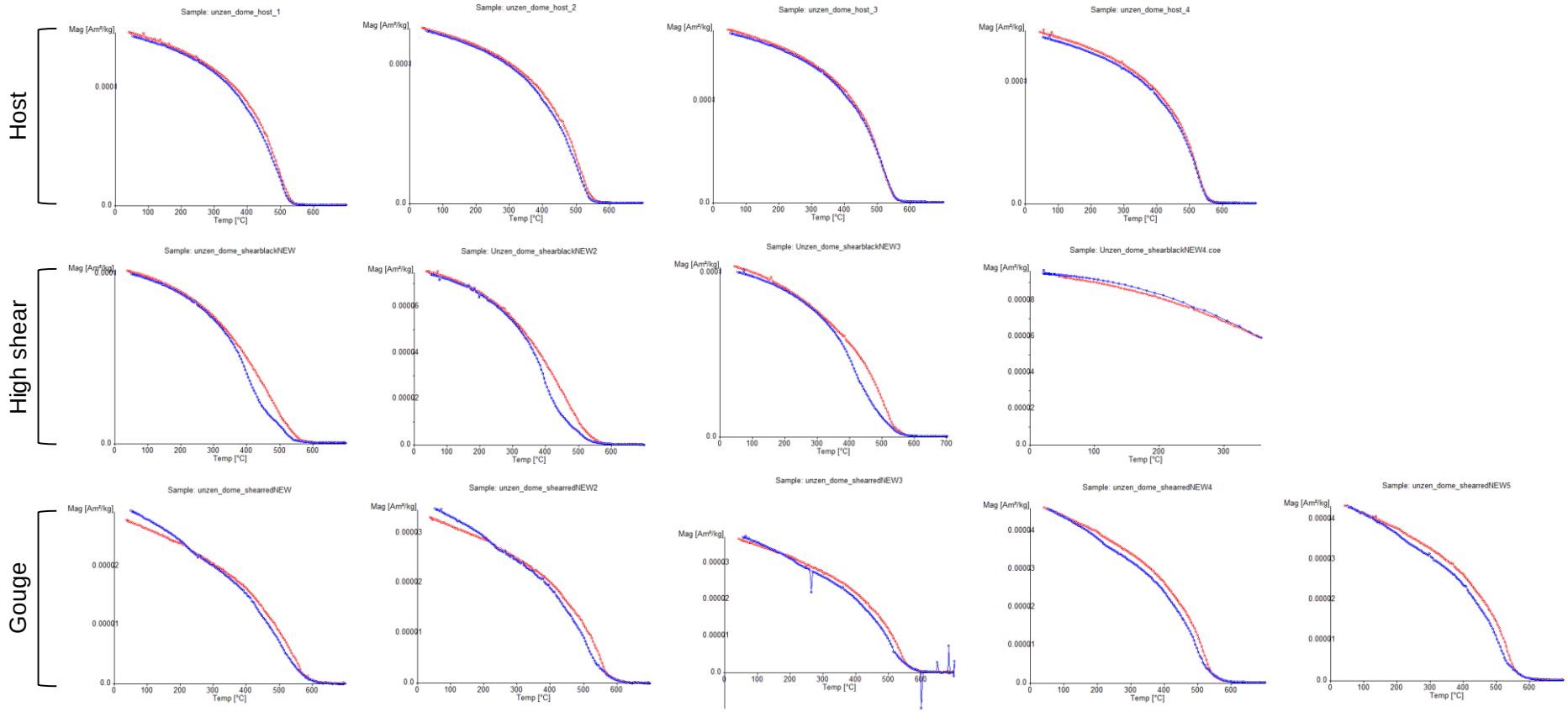


***Figure A1.2*** *– Thermomagnetic heating (red) and cooling (blue) curves used to derive Curie temperatures from Outcrop 2 shear zone. For each sample set one Curie temperature was identified using the method of Moskowitz (Moskowitz, 1981) from the heating curves and produced averages of 521 ºC in the undeformed host rock, 507 ºC in the highly sheared rock and 544 ºC in the gouge, corresponding well with the demagnetisation of bulk susceptibility (Fig. 2.10d). Notably, the least reversible behaviour is seen in the highly sheared samples. A minor inflection is observed at 230–240 ºC during cooling in the gouge suggesting the incipient formation of a new phase after heating to 700 ºC in the laboratory.*

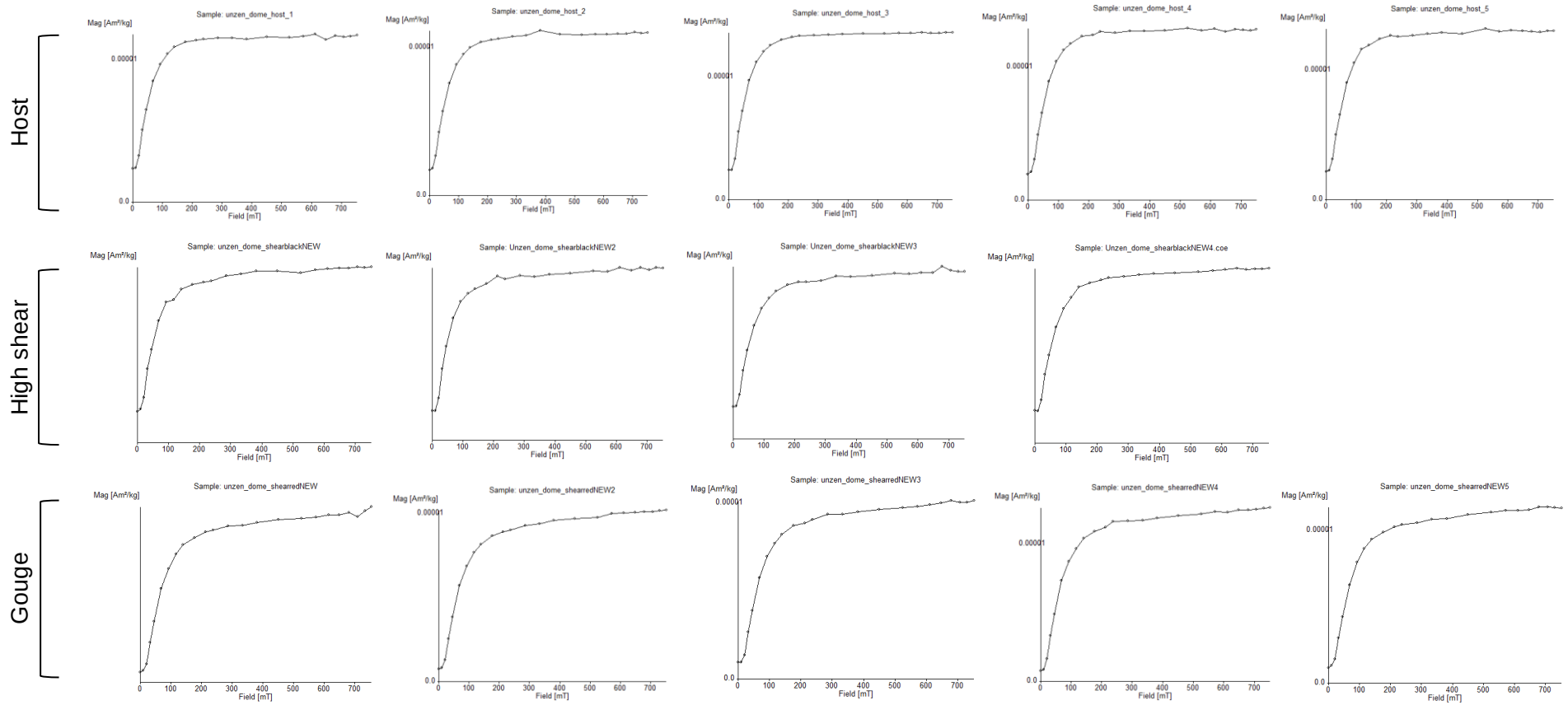


***Figure A1.3*** *– Isothermal Remanent Magnetisation (IRM) curves for each sample of Outcrop 2. The shape of the lines indicates that the host material is almost fully saturated at ~ 200 mT, whereas, in the gouge, the IRM is still increasing above 700 mT; the highly sheared material is intermediate. All sample sets show very repeatable behaviour.*

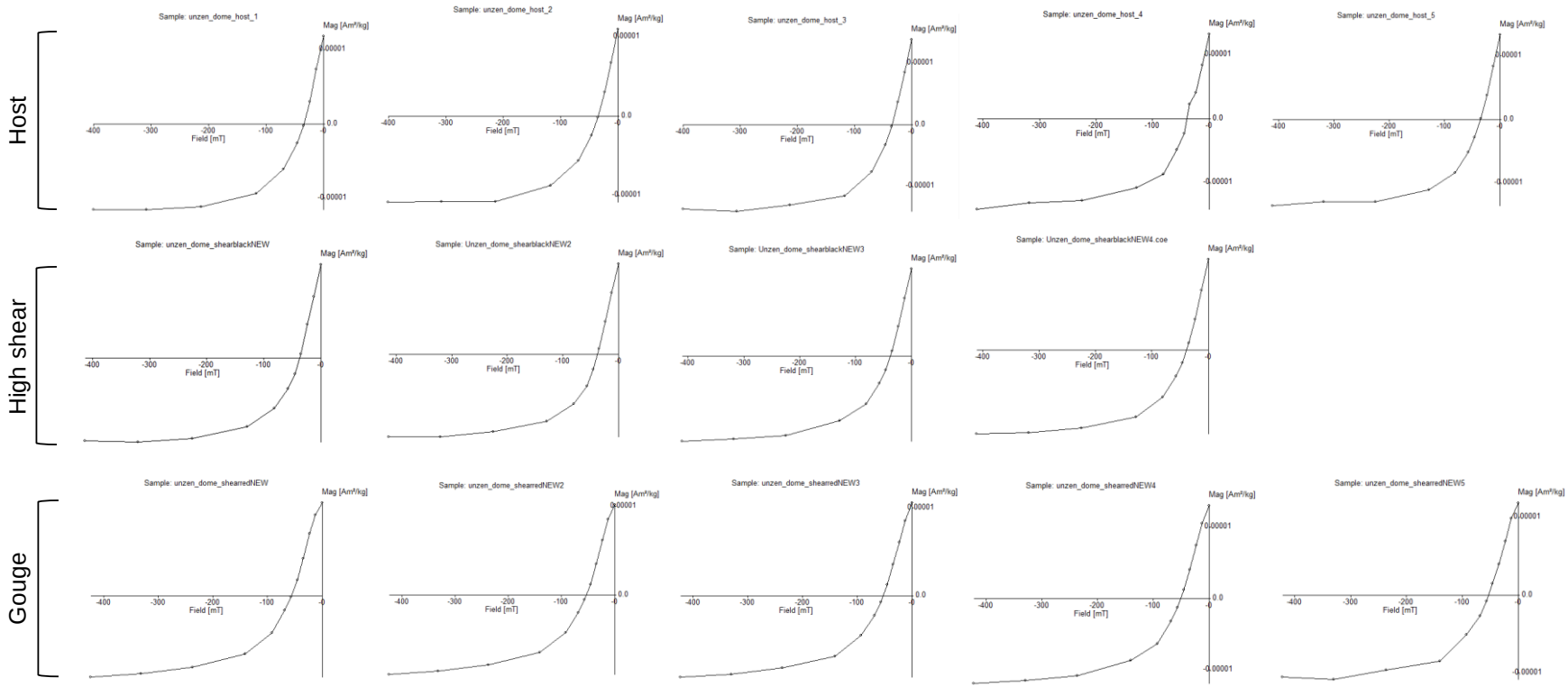


***Figure A1.4*** *– Backfield curves used to characterise the coercivity of the different samples. Similar to Fig. A1.3, the morphology of the curves demonstrates gradational changes from the host, to high shear, to gouge samples.*

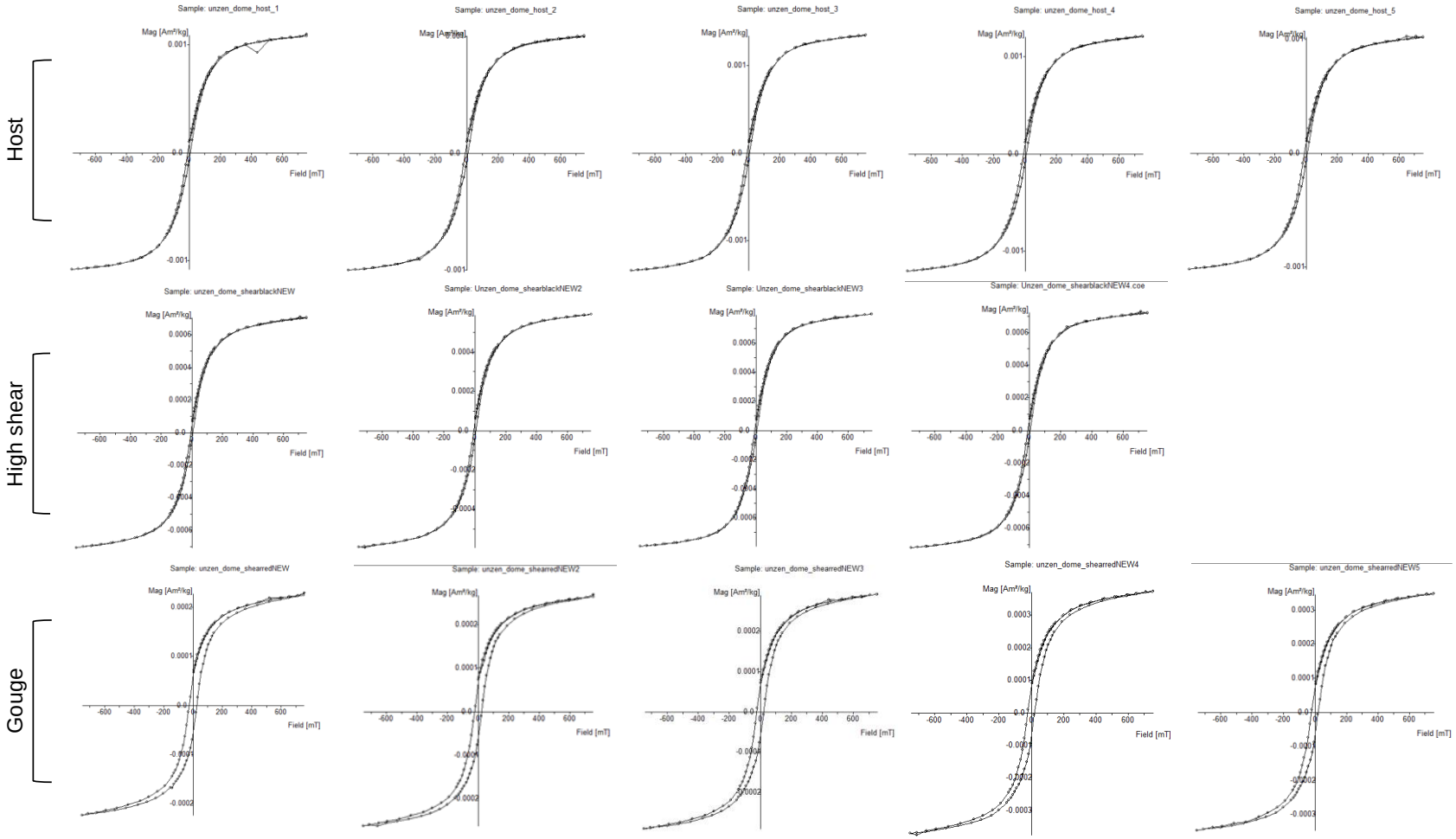


***Figure A1.5*** *– Hysteresis plots indicating the presence of low coercivity minerals, the samples are all "potbellied", but the gouge samples show the broadest hysteresis loop, indicative of the presence of higher coercivity minerals.*

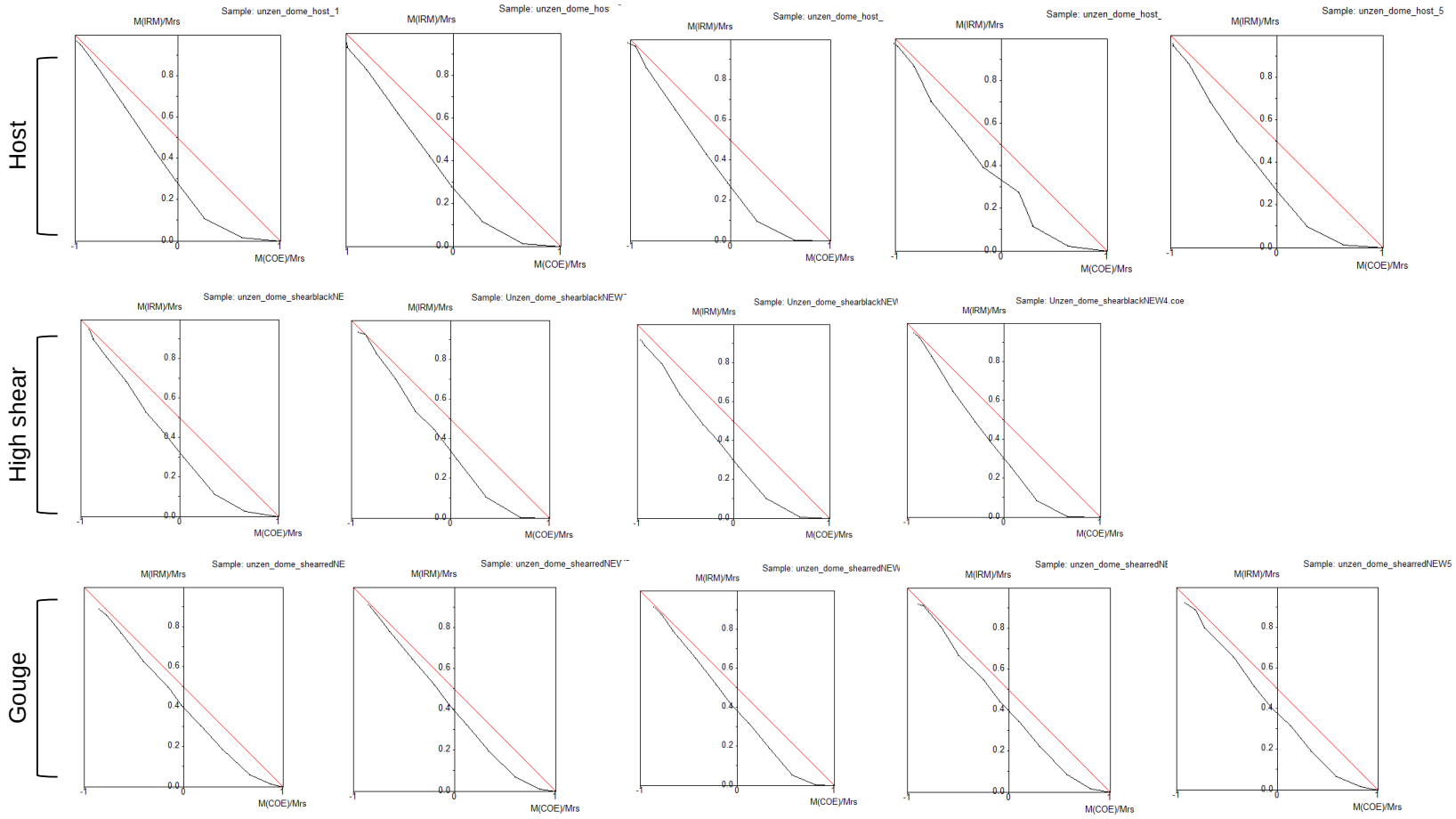


***Figure A1.6*** *– Henkel plots which combine backfield and IRM data to identify the presence of a demagnetising field. Sample data are plotted (in black) versus the behaviour (in red) of uniaxial non-interacting single-domain particles (i.e., ideal Stoner-Wohlfarth particles; Wohlfarth, 1958). The remanence carriers for all samples deviate from this ideal behaviour, though the host rock is furthest, and gouge is closest (the high shear being intermediate).*

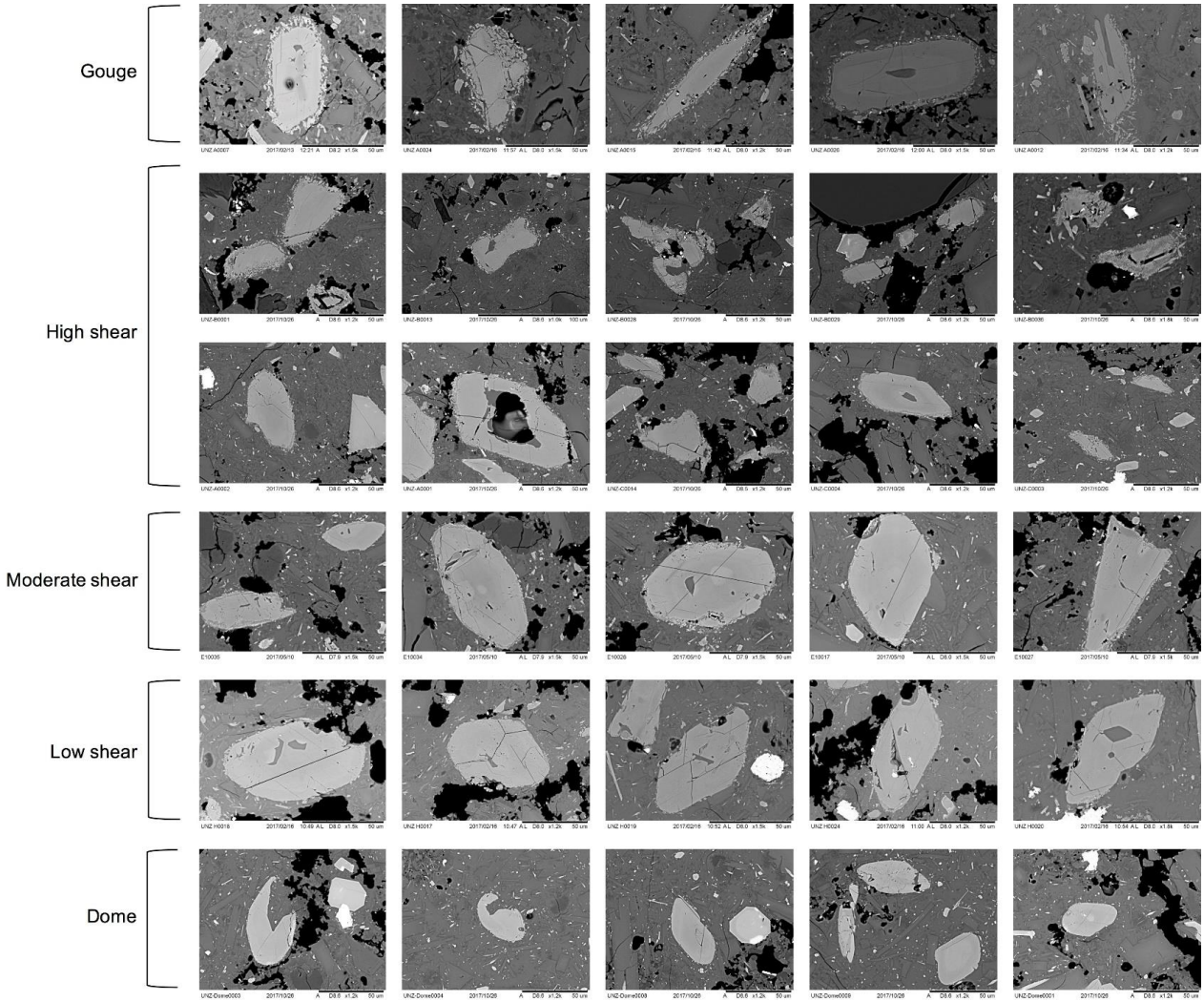


***Figure A1.7*** *– Representative examples of pargasite crystals in the groundmass across outcrop 1 shear zone and those from the undeformed dome block, an extension of examples shown in Fig. 2.11a. Pargasite in the dome and low shear zone show either no or very thin reaction rims in the form of a symplectitic decay. The moderate shear zone hosts pargasites with thicker symplectitic rims. In the high shear zone, symplectitic pargasite rims are more pronounced with the occasional presence of a coarser, detached granular rim. Pargasite rims in the gouge are all granular, with minor symplectitic patches between the granular rims and unaltered pargasite cores.*

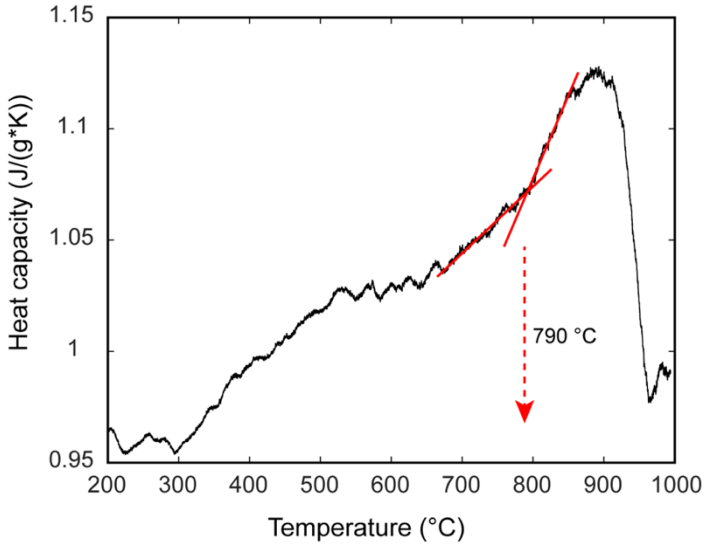


***Figure A1.8*** *– Heat capacity ($C_p$) for the low shear zone sample H, displaying the heating curve at a rate of 10 ºC.min$^{-1}$. The deviation from linear of the $C_p$ curve at ~790 ºC is interpreted to be the glass transition temperature ($T_g$). This temperature is consistent with modelled values of $T_g$ using measured glass chemistry.*

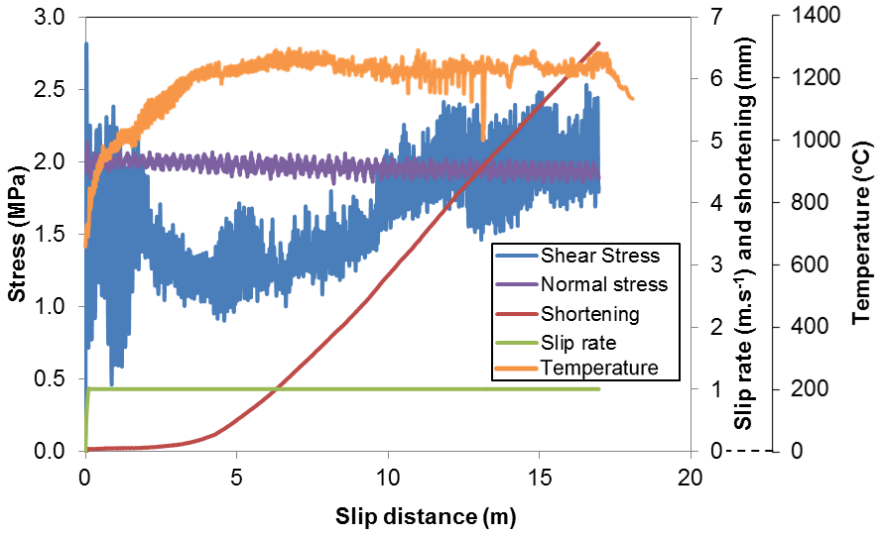


***Figure A1.9*** *– The mechanical data for the high-temperature, high-velocity rotary shear (HVR) experiment. The data shows the constant slip rate of 1 m s$^{-1}$, a controlled axial stress of 2 MPa and resulting shear stress, shortening (corresponding to melt expelled from the slip zone) and maximum temperature evolution.*

# Appendix II: Supplementary Figures (Chapter 3)

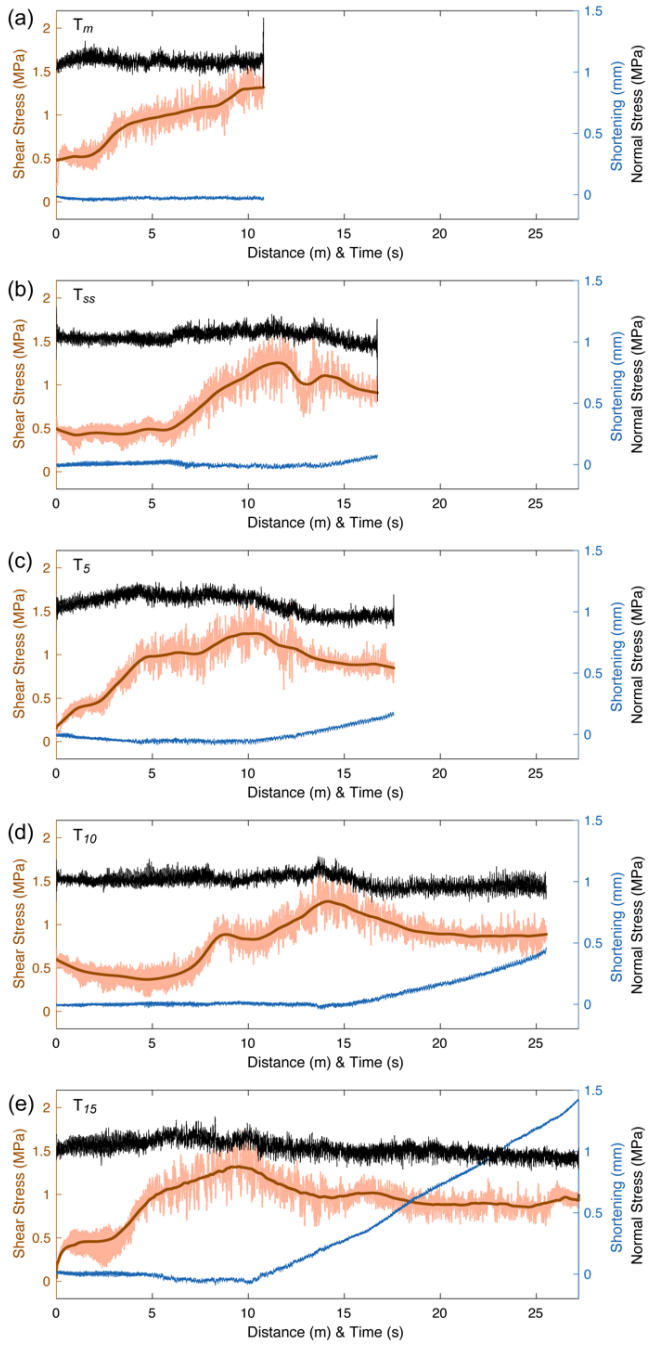


***Figure A2.1*** *– Mechanical data for the five high-velocity rotary shear (HVR) experiments performed on the Soufrière Hills Volcano (SHV) andesite. Each panel represents the evolution in frictional properties (i.e., shear stress, normal stress and sample shortening) monitored during experiments that were terminated at: (a) onset of melting ($T_m$), (b) formation of full frictional melt and attainment of steady-state condition ($T_{ss}$), (c) after 5 m of slip at steady-state conditions ($T_5$), (d) after 10 m of slip at steady-state conditions ($T_{10}$), and (e) after 15 m of slip at steady-state conditions ($T_{15}$).*

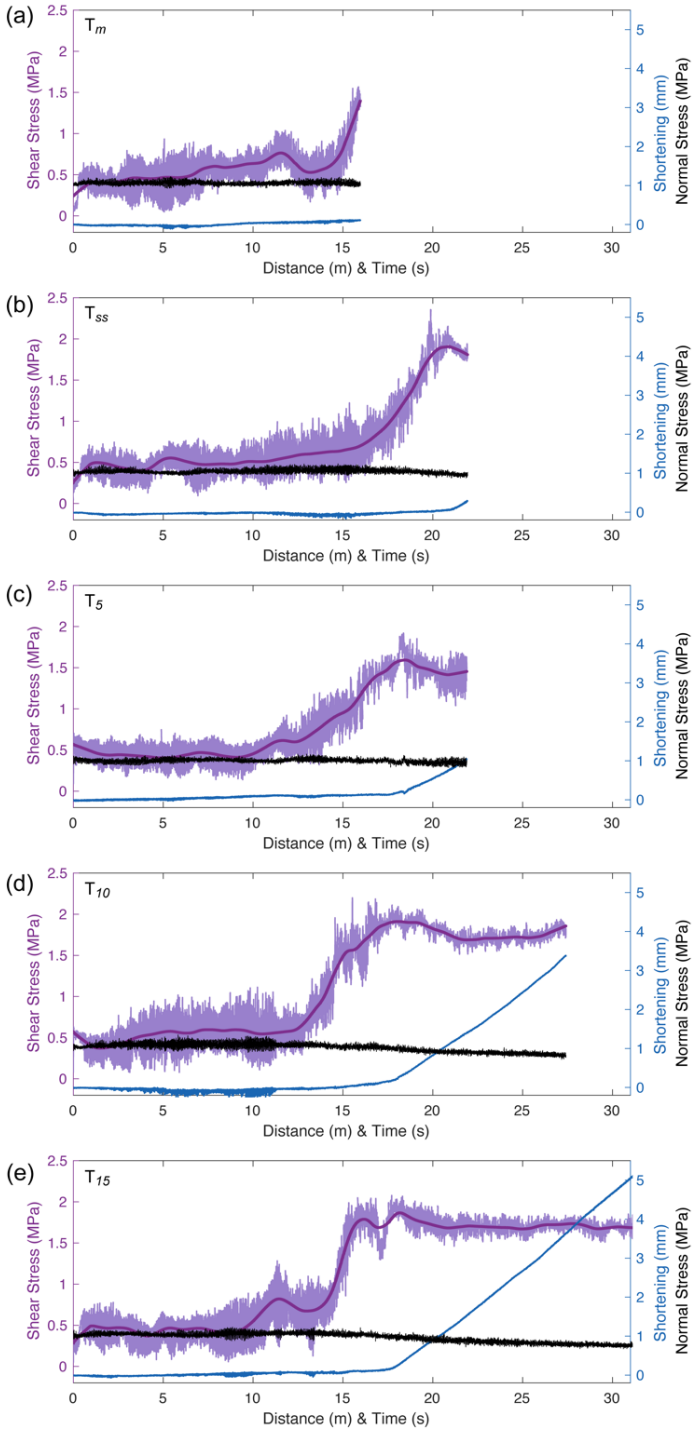


***Figure A2.2*** *– Mechanical data for the five high-velocity rotary shear (HVR) experiments performed on the Santiaguito dome complex (SG) dacite. Each panel represents the evolution in frictional properties (i.e., shear stress, normal stress and sample shortening) monitored during experiments that were terminated at: (a) onset of melting ($T_m$), (b) formation of full frictional melt and attainment of steady-state condition ($T_{ss}$), (c) after 5 m of slip at steady-state conditions ($T_5$), (d) after 10 m of slip at steady-state conditions ($T_{10}$), and (e) after 15 m of slip at steady-state conditions ($T_{15}$).*

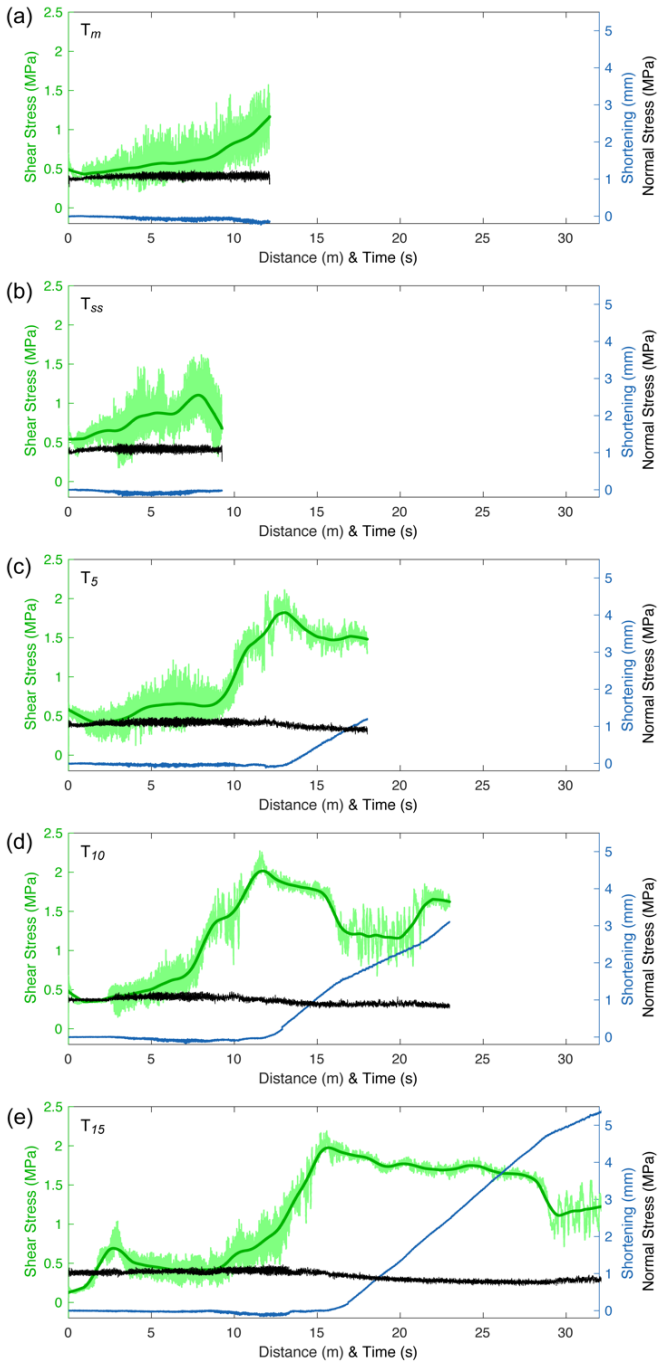


***Figure A2.3*** *– Mechanical data for the five high-velocity rotary shear (HVR) experiments performed on the Volcán de Colima (COL) andesite. Each panel represents the evolution in frictional properties (i.e., shear stress, normal stress and sample shortening) monitored during experiments that were terminated at: (a) onset of melting ($T_m$), (b) formation of full frictional melt and attainment of steady-state condition ($T_{ss}$), (c) after 5 m of slip at steady-state conditions ($T_5$), (d) after 10 m of slip at steady-state conditions ($T_{10}$), and (e) after 15 m of slip at steady-state conditions ($T_{15}$). Note that steady-state melting in (b) occurred at a shorter slip distance than the onset of melting in (a), which demonstrates the natural variability of a single sample.*

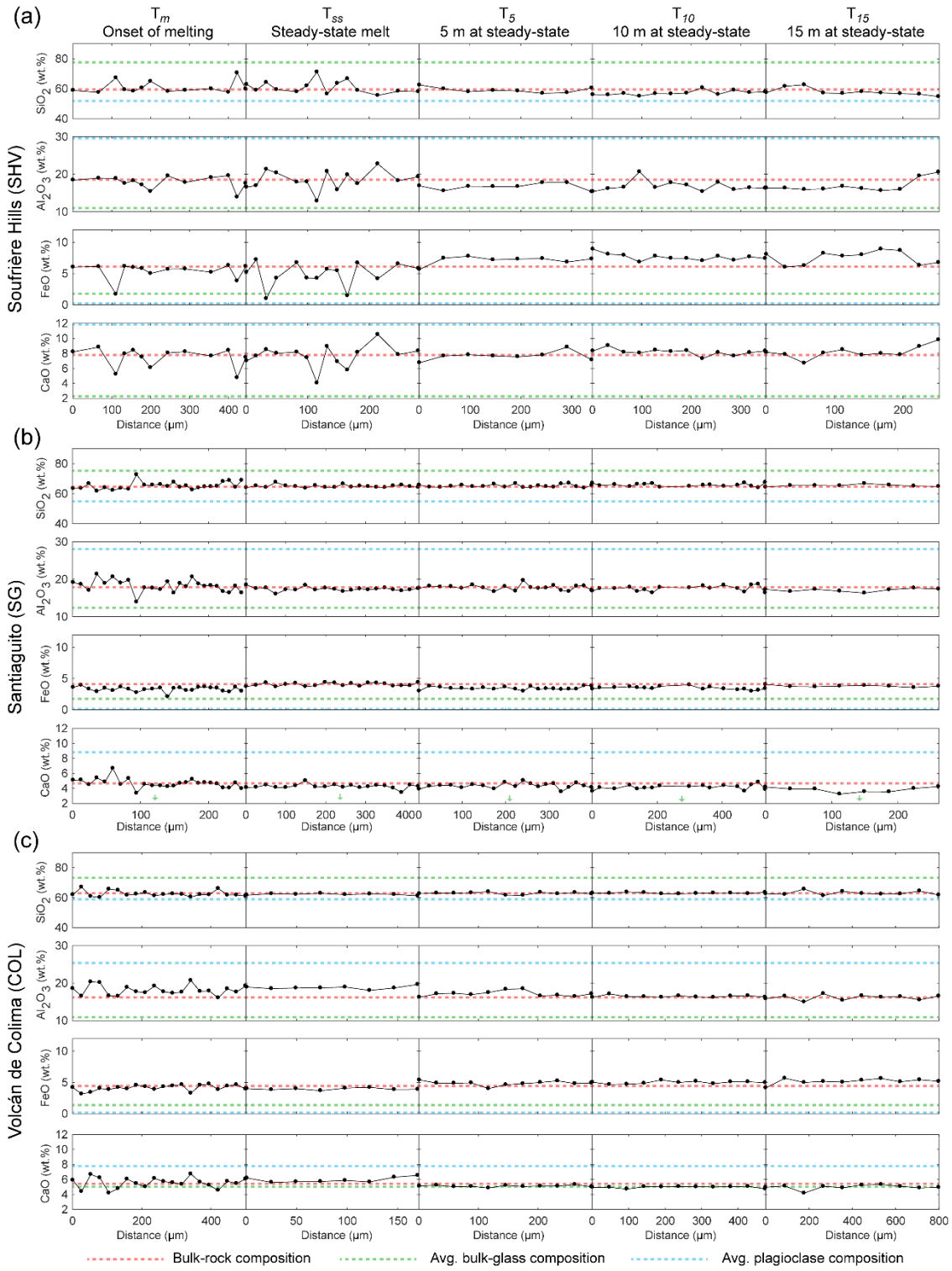


***Figure A2.4*** *– Major element chemical transects across the experimental melt zone (i.e., perpendicular to the slip plane) following melting of the (a) Soufrière Hills Volcano (SHV) andesite, (b) Santiaguito dome complex (SG) dacite and (c) Volcán de Colima (COL) andesite at: onset of melting ($T_m$), formation of full frictional melt and attainment of steady-state condition ($T_{ss}$), and after 5 m ($T_5$), 10 m ($T_{10}$), and 15 m of slip at steady-state conditions ($T_{15}$). The composition of the bulk-rock along with averages of the bulk-rock interstitial glass and plagioclase crystals have been labelled for reference.*

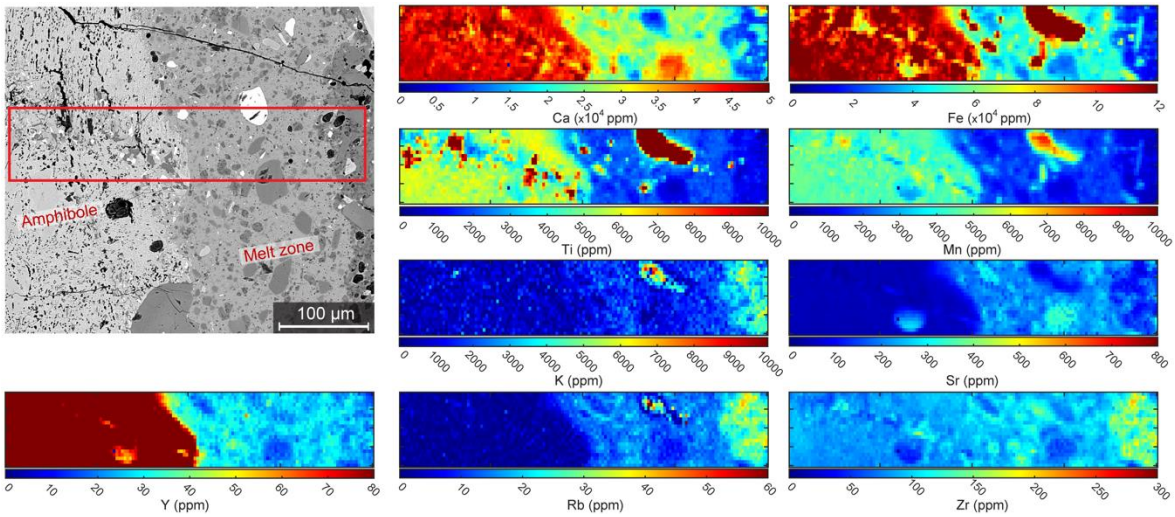


***Figure A2.5*** *– Synchrotron X-ray element maps of Soufrière Hills Volcano (SHV) frictional melt formed after 5 m of slip at steady-state conditions ($T_5$) displaying the contribution of amphibole to frictional melt composition. Elements that are high in concentration in amphiboles include: Ca, Fe and Y; amphibole incompatible elements include: K, Sr, Rb, and Zr.*

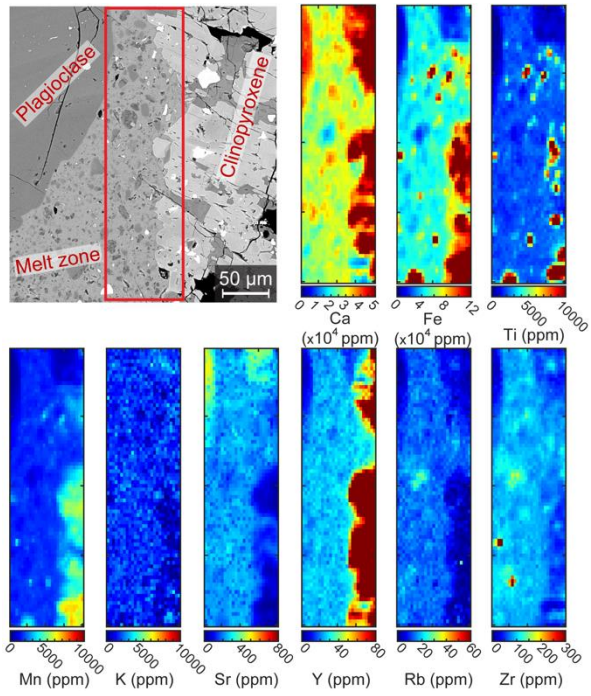


***Figure A2.6*** *– Synchrotron X-ray element maps of Soufrière Hills Volcano (SHV) frictional melt upon reaching steady-state conditions ($T_{ss}$) displaying the contributions of plagioclase (left of maps) and clinopyroxene (augite; right of maps) to frictional melt composition.*

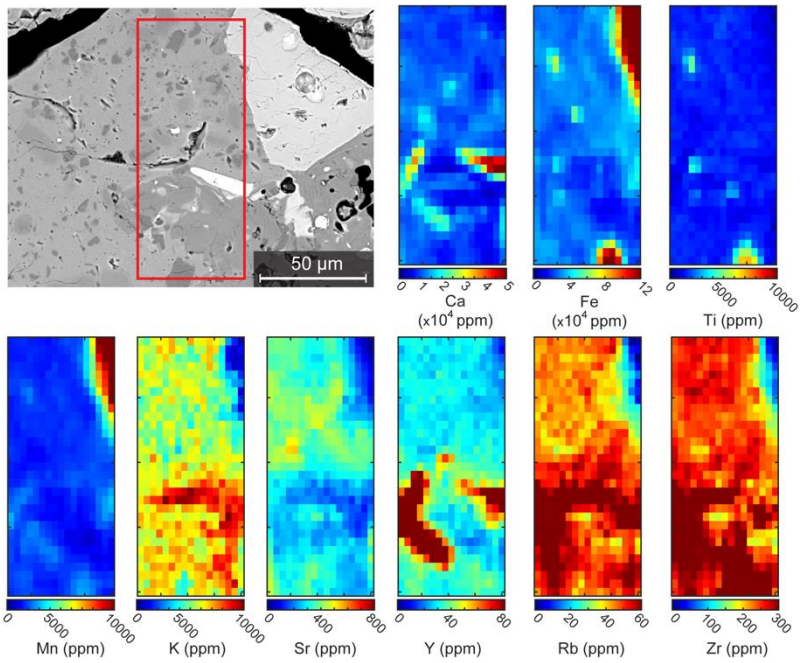


***Figure A2.7*** *– Synchrotron X-ray element maps of Santiaguito dome complex (SG) frictional melt upon reaching steady-state conditions ($T_{ss}$) displaying the contributions of orthopyroxene (OPX, hypersthene; top right of map) and interstitial glass (bottom of maps) to frictional melt composition.*

# Appendix III: Supplementary Figures (Chapter 4)

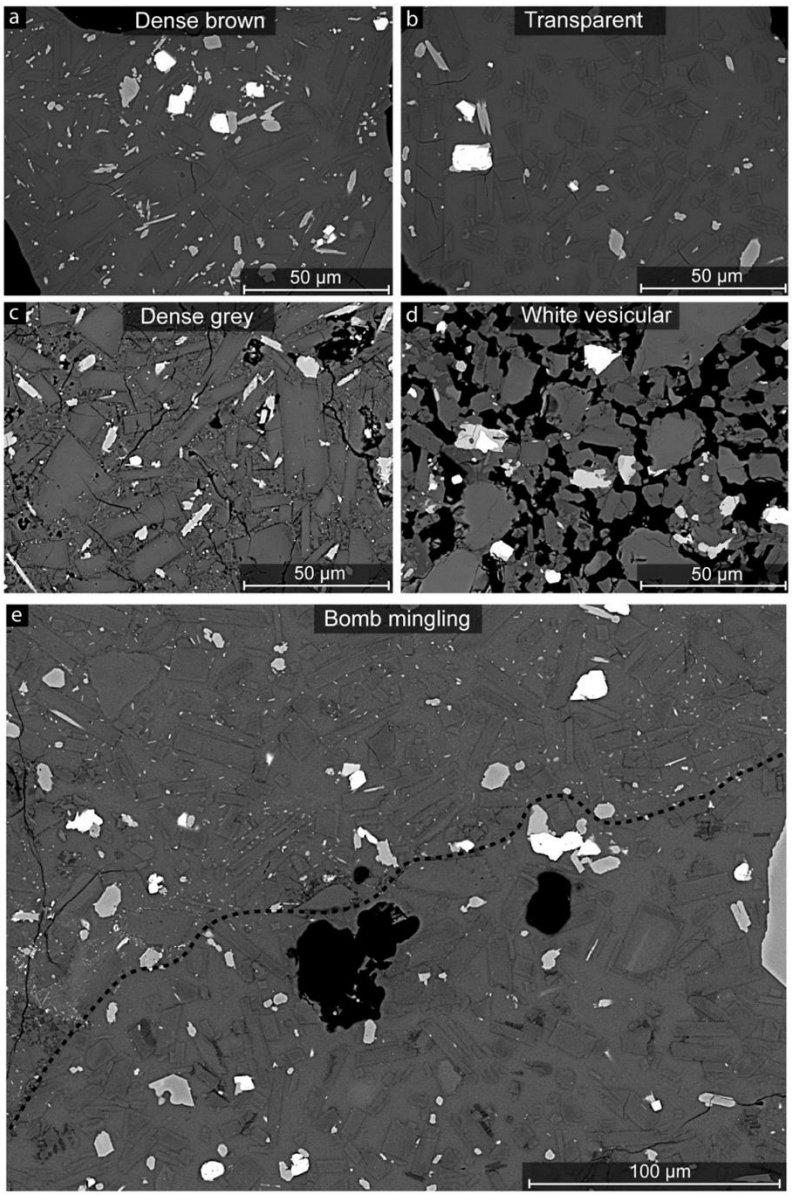


***Figure A4.1*** *– Backscattered electron (BSE) images of the groundmass textures for the different components of the ash. (a) Juvenile dense brown (DB) clasts displaying abundant mafic microlites (lighter grey crystals) and elongated plagioclase microlites (darker grey crystals). (b) Juvenile transparent clasts (TC) displaying less mafic microlites and more equant plagioclase microlites. (c) Non-juvenile dense grey clasts showing elongated plagioclase microlites (similar to DB clasts) and abundant Si-rich phases (darkest grey) as a result of glass devitrification. (d) Non-juvenile vesicular white clasts showing abundant vesicles but no glass. (e) Mingling textures with the 21$^{st}$ April 2016 bomb revealing different groundmass textures between the two vesicular-domains (bottom half) and dense-domains (top half).*

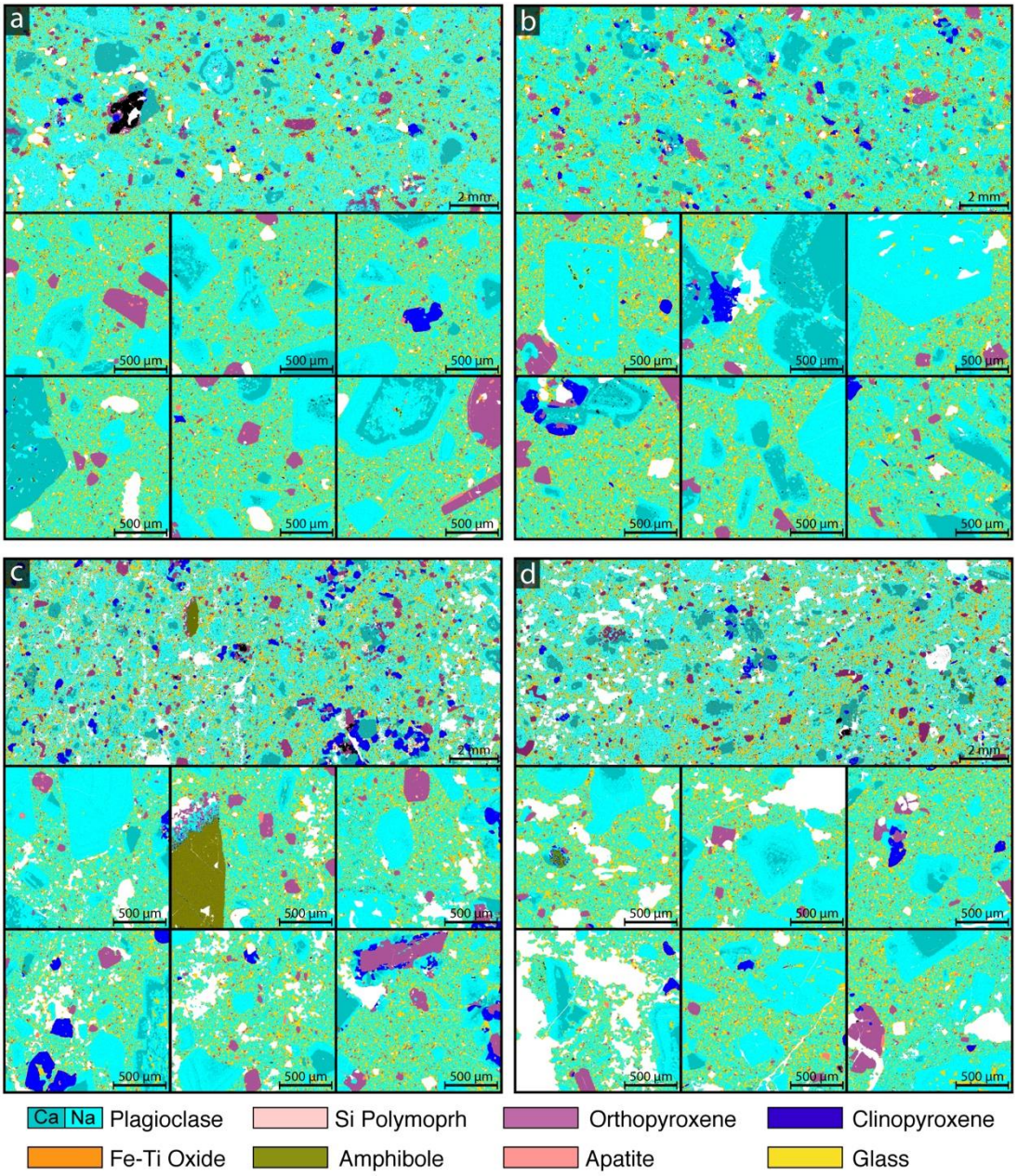


***Figure A4.2*** *– QEMSCAN maps of volcanic bombs erupted on 7th February (a–b) and 21st April (c–d) 2016. In each panel, the top map provides an overview of the bomb textures, and the six inset maps below them are high resolution close-ups. Mingling textures with vesicular and dense domains can be observed in the 21st April 2016 bomb (c–d).*

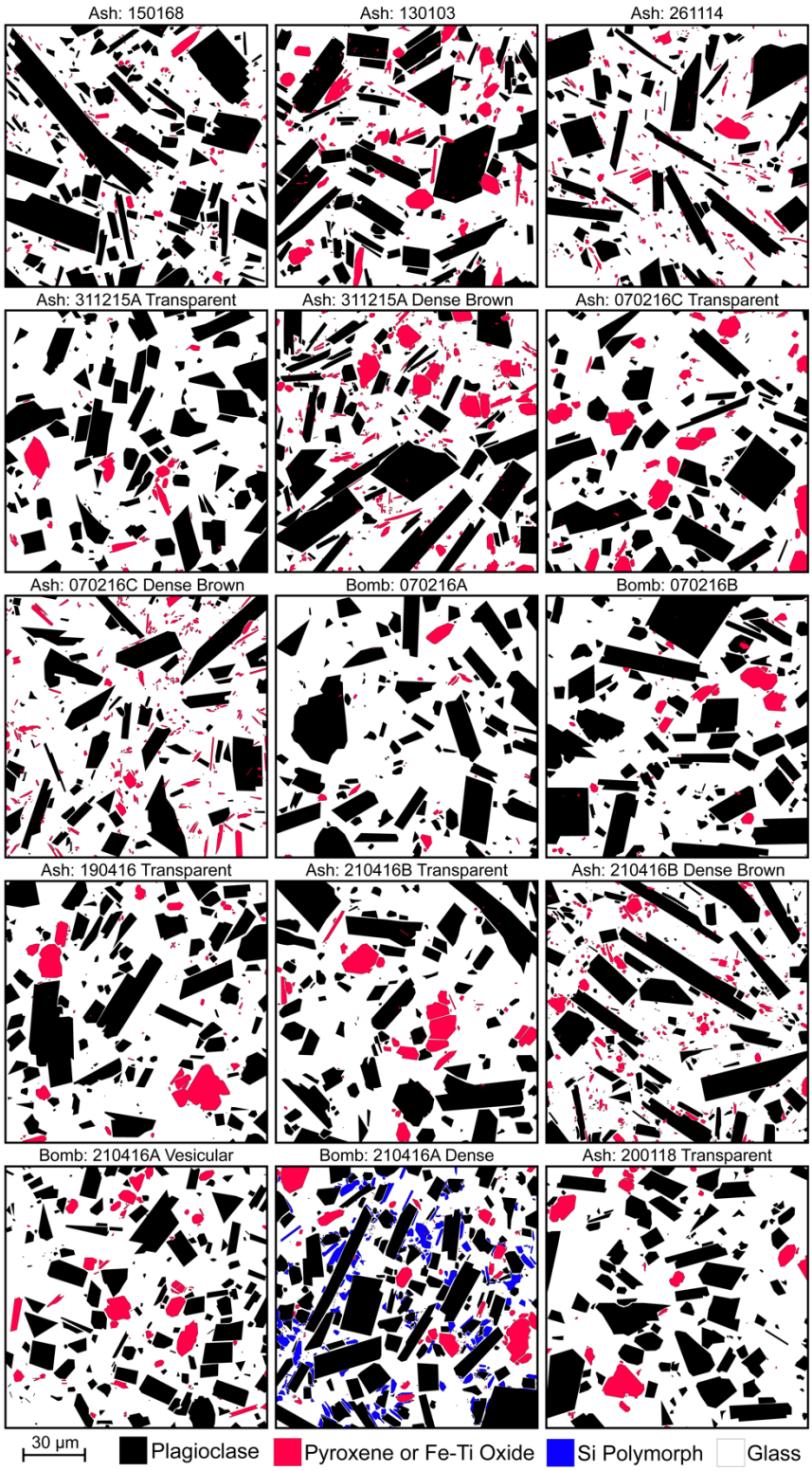


***Figure A4.3*** *– Examples of manually outlined microlites used for 2D and 3D textural analysis in Figures 4.6, 4.7 and Table 4.2. Note the variations in aspect ratios for plagioclase microlite between the samples.*

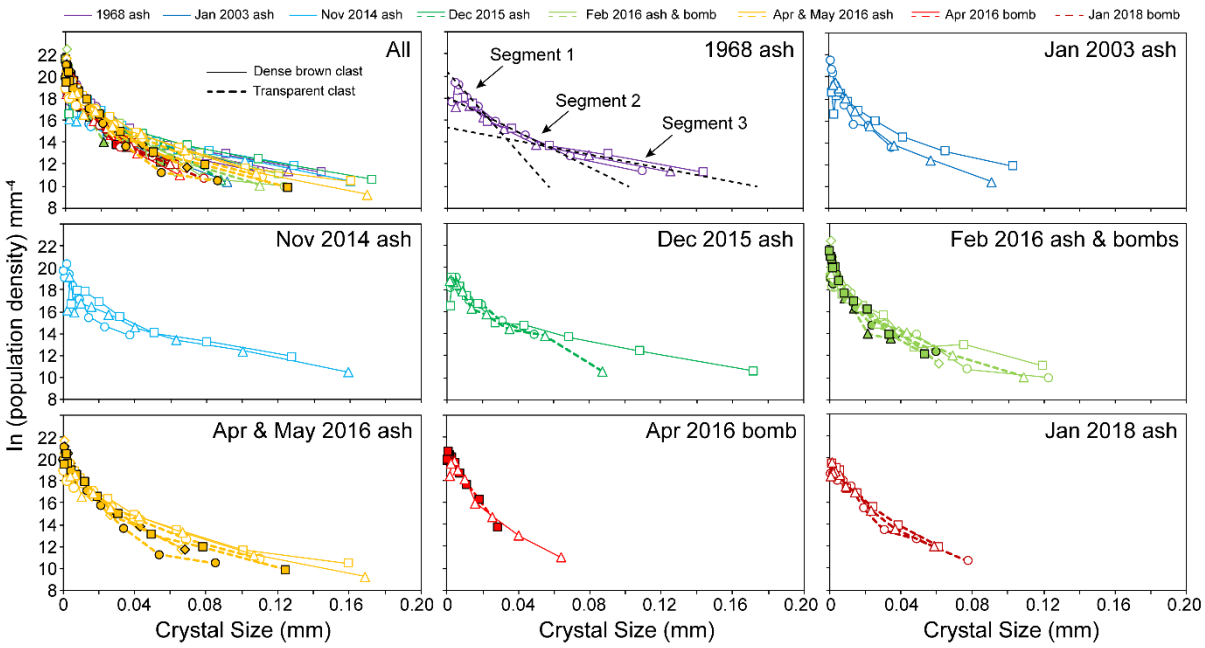


***Figure A4.4*** *– Three-dimensional crystal size distribution (CSD) plots of plagioclase microlites for the time-constrained ash and bomb samples used for 3D textural analysis using CSDCorrections (Higgins, 2000). Population density refers to the number of crystals per volume per length. The CSD curves can be separated into 3 segments as shown in the 1968 ash panel. The steepest segment (segment 1) for each CSD curve was used for the calculations of growth and nucleation rates (Fig. 4.7), representing the last microlites to form before eruption.*

# Electronic Appendix 1–3 (see CD)

Included in the Electronic Appendix are:

- **Electronic Appendix 1.1** – Plagioclase phenocrysts size and shape data from Unzen lava spine shear zone (Chapter 2)
- **Electronic Appendix 1.2** – Plagioclase microlite crystal plasticity data from Unzen lava spine shear zone (Chapter 2)
- **Electronic Appendix 1.3** – Amphibole reaction rim thickness measurements from Unzen lava spine shear zone (Chapter 2)
- **Electronic Appendix 2** – Electron probe microanalysis (EPMA) data of host-rock phases (minerals and glass) and frictional melt compositions, including standards used for calibration of the spectrometers, working standards for calculations of accuracy and precision, and detection limits for both EPMA and XRF (Chapter 3)
- **Electronic Appendix 3** – Electron probe microanalysis (EPMA) data of glass and mineral (plagioclase and amphibole) compositions for Santiaguito ash and bomb samples (Chapter 4)
- **PDF copy of the thesis**
- **Published papers as formatted by the journal (Chapters 2 and 3)**